Sensorless Adaptive Optics in Advanced Microscopy Techniques

by

Marie Caroline Müllenbroich

A thesis presented in partial fulfillment of the requirements for the degree of Doctor of Philosophy

Institute of Photonics

December 2012

Declaration of Authenticity

This thesis is the result of the author's original research. It has been composed by the author and has not been previously submitted for examination which has lead to the award of a degree.

Signed: Date:

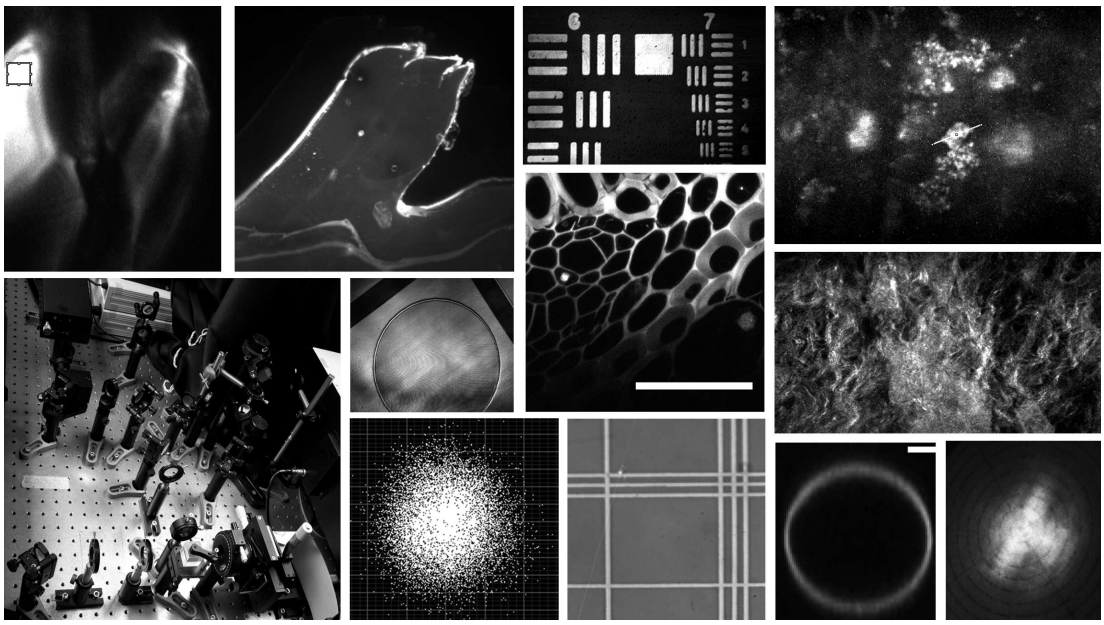

Frontispiece. Clockwise starting top left: SHG image of urea crystals, fluorescence image of quantum dots embedded in host polymer, confocal scan of resolution test chart, two-photon fluorescence image of fibroblast cells, SHG image of mouse basement membrane, image of the central actuators of the MEMS mirror, XZ image of a 15 µm fluorescent bead, calibration grid, Brownian motion of an optically trapped 1 µm diameter bead, adaptive optics setup, confocal scan of a microLED, two-photon fluorescence image of *convallaria*.

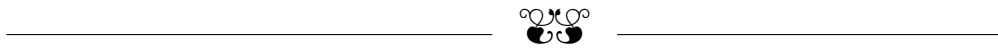

“Die Wissenschaft hat das mit der Kunst gemein, daß ihr das Alltäglichste völlig neu und anziehend, ja wie durch die Macht einer Verzauberung als eben geboren und jetzt zum ersten Male erlebt erscheint.

Das Leben ist wert, gelebt zu werden, sagt die Kunst, die schönste Verführerin; das Leben ist wert, erkannt zu werden, sagt die Wissenschaft.

Friedrich Wilhelm Nietzsche ”

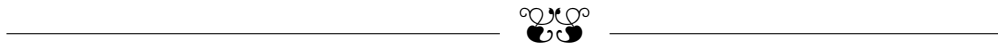

Abstract

Adaptive optics is a technique that is able to restore diffraction limited performance in optical systems that are adversely affected by optical aberrations. In this doctoral thesis adaptive optics technology has been implemented in systems for imaging and micromanipulation whose performance degrade with increasing penetration depth due to refractive index mismatch. With a focus on optical trapping and nonlinear microscopy, the combination of a deformable membrane mirror and a random search optimisation algorithm is used to improve system performance at depth by pre-shaping the incoming wavefront with aberrations that are equal but opposite to those that degrade quality. The approach used in this work does not require the use of a wavefront sensor but instead the optimisation algorithm randomly alters the shape of the deformable membrane mirror until a specifically chosen merit factor is satisfactorily improved.

This work demonstrates the improvement of the specific quality that is chosen as the merit factor by factors ranging from 1.2 to 8 fold. Specifically, the lateral trapping strength of an optical trap was improved by an average factor of 3.8 at a depth of 131 µm by optimising on a merit factor that is directly proportional to lateral trapping strength. In the nonlinear microscope, signal intensity is increased more than 7 fold when imaging fibroblast cells at a depth of 92 µm by optimising on the fluorescence intensity. Limitations and pitfalls in the implementation of sensorless adaptive optics are examined and possible solutions are investigated. Optical systems that have been optimised in this way reduce the risk of photo-induced damage by reducing the necessary incident laser power and therefore improve sample viability.

List of Figures

List of Tables

Contents

Chapter 1

Preface

1.1 Introduction

Life scientists have always desired to study the structure and function or dysfunction of intact tissues and their cellular constituents. Optical microscopy has been at the heart of this research due to its ability to perform non-invasive observations on living tissue at relatively high spatial resolution. The foundations of modern light microscopes were established over a century ago by Ernst Abbe [1,2] and since that time, optical microscopy techniques have been constantly adapted and developed and the quality of optical components and indeed entire imaging systems have become so exquisite that often diffraction is the ultimate limiting factor. Technical improvements have been made in the fields of light delivery and detection, optimisation of fluorophores and dyes, price, simplicity and system miniaturisation amongst others.

When trying to understand the functional behaviour of viable cells it is considered crucial to investigate them in their natural environment. The life scientist therefore needs to image deeper into a specimen so as to visualise biological functions in context. With the invention of confocal microscopy by Marvin Minski in 1961 [3, 4], the first efforts towards overcoming this problem were rewarded with increased resolution and contrast at depth. The major concept in confocal microscopy is to focus signal photons onto a detector pinhole which rejects scattered and out-of-focus light. With the advent of digital data acquisition, storage, processing and, most importantly, stable laser sources came the first practical applications of confocal laser scanning microscopy. The major advantage of confocal microscopy is also an apparent drawback: photon absorption happens all along

the optical axis but only ballistic signal photons originating from the focal point are detected. Especially in fluorescence microscopy where imaging of live tissue is always limited by the destruction of the fluorophore (photobleaching) or the photodynamic damage to the tissue mediated by fluorophores (photodamage), this wasteful excitation all along the optical axis is a cause for major concern.

Laser scanning microscopy made another important step towards the goal of imaging at depth with the successful demonstration of two photon excited fluorescence in 1990 by the group around Winfried Denk [5]. The possibility of multiphoton absorption during a single quantum event was predicted as early as 1931 by Maria Göppert-Mayer in her doctoral dissertation [6] but experimental confirmation was only made possible with the invention of lasers and later their mode-locked operation [7]. The nonlinear dependence between fluorescence signal and excitation intensity gives multiphoton excitation fluorescence its optical sectioning properties because fluorescence is only generated in the close vicinity of the focal point rather than all along the optical axis. Signal photon detection can therefore be simple and efficient because every fluorescence photon, whether on a ballistic or scattered trajectory, counts as useful signal against virtually no background. Tissue penetration depth is further aided by the use of longer wavelengths which are roughly twice the wavelength necessary for single photon absorption.

Imaging at depth, however, is always accompanied with a degradation of resolution and contrast. This degradation is caused by increased scattering due to inhomogeneities in refractive index which are present to some degree in every tissue worth imaging; with only few exceptions, biological tissues strongly scatter light. Another reason for imaging degradation are optical aberrations that progressively become more severe with increasing penetration depth until high resolution imaging eventually becomes impossible. Whereas scattering and absorption are inevitable characteristics of the tissue, the amount of optical aberrations introduced by the sample can be manipulated in various ways. The purpose of adaptive optics is to compensate for distortions introduced by the optical system and the sample under investigation and restore diffraction limited imaging where possible.

1.2 Motivation and objectives

The work presented in this thesis has a very broad scope and aims to implement sensorless adaptive optics (AO) technology in three different systems, two for optical imaging and one for micromanipulation. Work was carried out in the design, implementation, alignment and characterisation of those optical systems, including a confocal laser-scanning microscope, a nonlinear microscope and an optical trap.

Another focus was the development and optimisation of software code for hardware control and communication, optimisation algorithms for sensorless aberration correction, data acquisition and particle tracking all of which have been written in the LabVIEW programming language. The aim was to develop a versatile and intuitive, yet highly functional user interface that could serve as test bed for future system development and testing, involving all relevant tasks and commands in a single front panel.

This doctoral thesis concentrated on sensorless AO technology for aberration correction at depth using deformable membrane mirrors (DMMs) in combination with optimisation algorithms. This means that the necessary commands for the DMM needed to be determined without prior knowledge of the aberrations, which are usually measured by wavefront sensors. Instead a metric that is only maximised in the absence of optical aberrations is optimised with an algorithm. The choice of this metric, called merit factor (MF), and the implementation of the optimising algorithm were highly specific to each application and represent the root of complexity in such adaptive optics systems. This calls for a number of strategies to make the implementation of sensorless adaptive optics novel and competitive with other work carried out in this field. Table 1.1 summarises the targets that were met in this work.

Table 1.1: Objectives of the work presented in this doctoral thesis. OT: optical trap, NLM: nonlinear microscopy, CLSM: confocal laser scanning microscopy.

Target	CLSM	NLM	OT
Chapter	4	6	8
System built from scratch	✓		✓
Software development	✓	✓	✓
Successful implementation of AO	✓	✓	✓
Aberration correction at depth		✓	✓
Presented at conference		✓	✓

1.3 Main contributions

My contribution to this field has been to develop a robust system for wavefront sensorless AO which corrects for aberrations that arise mainly at high penetration depths in systems for optical imaging and micromanipulation. This was done relying solely on the readout of detectors that were already present in each system, that is an avalanche photodiode, a photomultiplier tube and a scientific CMOS camera. This research furthers the idea of wavefront sensorless AO in a range of applications and the main contribution of this thesis can be summarised for each application as follows.

Confocal laser scanning microscopy The confocal setup doubled as confocal scanner and as test bed for AO system development. Optimisations were performed on a resolution test chart and a sample containing photoluminescent quantum dots. The effect of the optimisation on signal intensity and spatial resolution was analysed as well as repeatability of improvements by previously acquired DMM shapes. Some improvement in signal intensity could be achieved in both reflective and fluorescent imaging modalities with improvement factors ranging from 1.2 to 8 fold.

Nonlinear microscopy PSF engineering by means of a DMM was employed to improve image quality at depth and the benefits of wavefront compensation for system- and sample induced aberrations in a variety of samples was demonstrated. The aberration correction was determined in a wavefront sensorless approach by rapidly altering the mirror shape with a RSA until the two photon excited fluorescence or second harmonic signal intensity was satisfactorily improved. The imaging of fluorescent test samples, nonlinear crystals and intermediate tissue culture systems in form of organotypic collagen I assays were compared with and without aberration correction. Some significant improvement in signal intensity was achieved in TPEF and SHG imaging modalities with improvement factors ranging from 1.2 to 8.5 fold.

The possibility of optimising on an intrinsic second harmonic signal was investigated, an approach providing an optimisation procedure which is not limited by photobleaching therefore allowing many algorithm iterations. This optimised mirror shape was then stored in a look-up table and called upon for multiphoton imaging at a specific depth.

High quality beam profiles and stable focusing at depth are important not only in high-resolution microscopy but are also central to other applications in optical and photonic engineering, for example, in the fields of laser micro/ nanofabrication [8–10].

Optical Tweezers The use of a DMM to increase the lateral trapping force at depth was demonstrated in a wavefront sensorless approach. The optimum shape of the DMM was determined with a random search algorithm (RSA) using lateral bead displacement from equilibrium due to a viscous drag force applied through motion of the sample stage as a MF. This wavefront sensorless approach had several distinctive advantages in the application of micromanipulation described in this work. The most important point, however, is that the MF used in the optimisation routine was chosen such that it was directly proportional to the specific quantity that was to be improved. By minimising the lateral bead displacement, the spring constant was increased and the trapping strength directly improved.

The success of the AO implementation was quantified by a study of spring constants with and without aberration correction at varying depths. The stiffness of the trap could be improved throughout the trapping range of a conventional optical trap and beyond. At a depth of 131 μm the trapping stiffness was improved by a factor of 4.37 and 3.31 for the x- and y- axis respectively, demonstrating the pronounced power of optimisation algorithm based AO for micromanipulation.

Achieving a stronger trapping force at depth without having to increase incident laser power is especially beneficial when working with cells where prolonged exposure to high power laser radiation can affect their viability [11]. Uniform trapping strength throughout depth is also a critical issue when the optical trap is used as a force transducer, investigating mechanical properties such as elasticity, stiffness, rigidity and torque of cells, intracellular structures, single molecules and their suspending fluids [12, 13].

1.4 Synopsis

The work presented in this thesis relates to the implementation of adaptive optics in three different applications: optical trapping, nonlinear microscopy and confocal microscopy. Therefore, this thesis is subdivided into three segments, each comprised of two chapters, one concerned with a general introduction to the applied field and one presenting the original results obtained in this work.

There are, however, overlaps in underlying theory and literature reviews which are pointed out as cross-references throughout the thesis.

Chapter 2 outlines the key working principles of adaptive optics and aberration correction. The underlying concepts of image formation are introduced and serve as a starting point for the definition of image quality, such as spatial resolution, signal content and the depth at which meaningful images can still be generated. These concepts provide the frame of reference for the following discussion of image degradation through optical aberrations of the wavefront and their mathematical description. The remainder of this chapter examines the main components of adaptive optics, the wavefront correcting elements, the wavefront sensing devices and optimisation algorithms for wavefront sensorless applications.

Chapter 3 reviews confocal microscopy and galvanometer-based point scanners. The confocal pinhole and the concept of telecentricity are covered. Refractive index mismatch in the form of a plain dielectric interface is discussed in detail and various compensation strategies for the resulting spherical aberrations are surveyed.

Chapter 4 describes the design and implementation of a custom built confocal laser scanning system with incorporated adaptive optics for aberration correction. The calibration of the optical system in terms of spatial resolution, magnification and sampling frequency is examined. The microscope was tested in reflection mode and in fluorescent mode. Optimisations on reflective and photoluminescent samples were performed and the outcome was quantified through improvement in signal intensity and resolution.

Chapter 5 provides an overview of nonlinear microscopy techniques, with two photon excitation fluorescence (TPEF) and second harmonic generation (SHG) being a main focus. Advances and applications of nonlinear imaging are surveyed and the optical aberrations that limit the penetration depth are examined.

Chapter 6 presents experiments conducted in an adaptive nonlinear microscope. The experimental details are given in the first section and the original results are presented in the second section. Details are given on the implementation and alignment of the adaptive optics, the adaptation of the optimisation algorithm to be applicable to samples which are prone to photobleaching and the calibration and characterisation of the optical system. Optimisations, which were performed on fluorescent beads and SHG signal generating urea crystals, are presented and their improvements in image resolution and signal intensity

are discussed. Optimisations performed on organotypic tissue cultures explore the possibility of using AO to optimise on SHG, a process which is not prone to bleaching, these results were then used to image TPEF structures.

Chapter 7 covers an introduction to optical trapping and the underlying physics to micromanipulation. The forces acting on trapped particles are discussed and ways in which they can be calibrated. This is essential if the optical trap is used as a force transducer as is the case in many biological applications. A review of recent advances in optical trapping and their multiple applications is presented. The chapter concludes with a description of the the problems that arise when optical aberrations limit the performance of the optical trap at depth inside a medium.

Chapter 8 presents experiments performed with an aberration correction system in optical trapping. The first section gives the experimental details including the optical setup and methodology of experimentation, whereas the second section examines the original results obtained from the experiments. The adaptation of the optimisation algorithm to this specific task is discussed and the degradation of lateral trapping strength with penetration depth is mapped qualitatively and quantitatively. The outcome of the aberration correction is analysed in terms of reduction in Brownian motion of the trapped bead, increased trapping strength and uniformity of the optical trap at depth and a Zernike mode decomposition.

Chapter 9 provides a summary of the work presented in this thesis and concludes with the outline of further work that could be carried out to complement and continue this research.

❦

Two lists containing the acronyms (Appendix C) and symbols (Appendix D) commonly used through out this thesis are located in the appendices for ease of reference.

Chapter 2

Adaptive Optics

2.1 Adaptive optics and aberration correction

The general principle of operation in adaptive optics (AO) [14, 15] is straightforward and depicted in Figure 2.1. It consists in many cases of just three key elements; a wavefront sensor (WFS) that measures the distortions in the wavefront causing the image degradation and an active element that compensates for these distortions. The operation of the whole system in a closed loop is controlled by a suitable computing system which drives the active element so that the error in the wavefront is minimised.

AO originates from astronomy where atmospheric turbulence degraded images acquired with ground-based telescopes. The deleterious impact of atmospheric "tremors" on telescope imaging was noticed by Newton in 1730 [16], but only in 1953 did Horace Babcock propose a closed loop AO system as a method to correct for optical aberrations induced by the turbulences of the atmosphere [17]. The first application of AO to astronomy is accredited to Buffington [18] and shortly after Hardy [19, 20]. As a result, image quality of ground-based telescopes in astronomy is improved, as examples from the Keck telescope impressively demonstrate [21].

A closely related problem has lead to the implementation of AO into ophthalmology where it has now become a integral element over the years. Ophthalmology suffers in a similar way to astronomy from image degradation. The optical aberrations are this time induced by the the human eye, mainly by the lens and the cornea. As far as human vision is concerned, the so called lower aberrations, e.g. myopia /hyperopia (defocus) and astigmatism are usually readily corrected

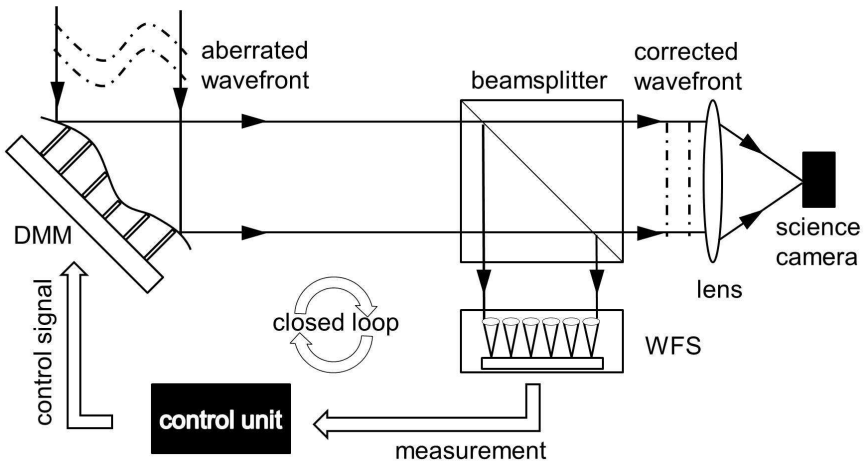

Figure 2.1: Schematic of AO operating in closed loop. The incoming, aberrated wavefront is phase modulated by the wavefront corrector, here a deformable membrane mirror (DMM). The outcoming wavefront is then divided with a beam splitter. One part serves as a signal for the wavefront sensor (WFS), here a Hartman Shack WFS, which acts like a null sensor, measuring the residual deviation from a perfectly flat wavefront. This information is passed on to the control unit which applies the conjugate deformation onto the DMM. The flat output wavefront from the beam splitter is imaged onto a scientific camera.

by spectacles or contact lenses. However, these and other aberrations that reduce the quality of vision also hamper the resolution and contrast of retinal imaging in ophthalmoscopy since the dioptric apparatus of the eye acts like an objective lens [22].

From 1982 onwards, Bille *et al.* were the first to adapt AO to ophthalmology by implementing an active optical system into a laser tomographic scanner [23,24]. However, the theoretical diffraction limit could not be achieved with this setup, since the AO system lacked a WFS to close the loop. Precise measurements of the aberrations of the human eye with a Shack-Hartmann WFS and the demonstration of a closed loop AO system was demonstrated in 1997 by Liang *et al.* [25,26]. Many later studies have built upon the implementation of AO into ophthalmology, for example in the field of colour vision. Perception of color in the human retina depends on three different classes of cones, each with a different maximum in wavelength sensitivity. Using AO, the spatial scale of the probing laser beam can be reduced to sizes smaller than the diameter of a cone such that the necessary limits to colour blindness within normal colour vision subjects can be explored and the relative number and spacial arrangement of the cone classes can be investigated. Roorda *et al.* combined an AO system with retinal densitometry

to obtain the first images of the arrangement of the three cone classes in the living human eye [27]. With increased quality in retinal imaging, AO developed its potential in the diagnosis and early stage detection of retinal pathologies through AO scanning laser ophthalmoscopes and optical coherence tomography (OCT) systems. Several studies have implemented AO into spectral domain and Fourier domain OCT systems in order to improve the lateral resolution while maintaining the high axial resolution inherent to OCT [28, 29].

The analogy of astronomical imaging through the turbulences of the atmosphere and ophthalmological imaging of the retina through the aberrations introduced by the human cornea made AO an obvious choice for aberration correction in vision science and from there it was only a short step to the introduction of AO concepts into broader life science research. In 1998, Booth *et al.* proposed the use of an active optical element in a confocal microscope to preshape the input beam in order to overcome the previously measured spherical aberrations induced by a refractive index-mismatched sample [30]. The incorporation of AO in microscopy applications would allow the user to compensate for optical aberrations at large imaging depths and thus restore resolution and signal strength to surface quality [31, 32]. AO techniques have since been applied to confocal microscopy [30,33] (reviewed in section 3.4.3) and nonlinear microscopy (reviewed in section 5.4.4) such as two photon excited fluorescence microscopy [34, 35], higher harmonic generation microscopy [36,37] and coherent anti-Stokes Raman scattering microscopy [38].

The direct measurement of aberrations in microscopy, however, is not straightforward. Due to the nature of epi-illumination typically employed in optical microscopy, light passes the aberrating optical system and the tissue under investigation twice and hence the direct measurement of the wavefront like in astronomy applications is not possible. Therefore alternative methods have been suggested which make the exact knowledge of the wavefront aberrations redundant. These, so called, wavefront sensorless applications rely on a search algorithm to find the appropriate control signal to actuate the corrective element.

Figure 2.2 illustrates the concept of aberration correction in microscopy applications. Microscope objectives are assemblies of highly corrected lenses which produce, under ideal conditions, a diffraction limited focal spot (a). They are, however, corrected for a certain immersion medium and any deviation from that specific refractive index anywhere along the optical path introduces aberrations (b). Most of the time, a certain amount of refractive index mismatch is unavoid-

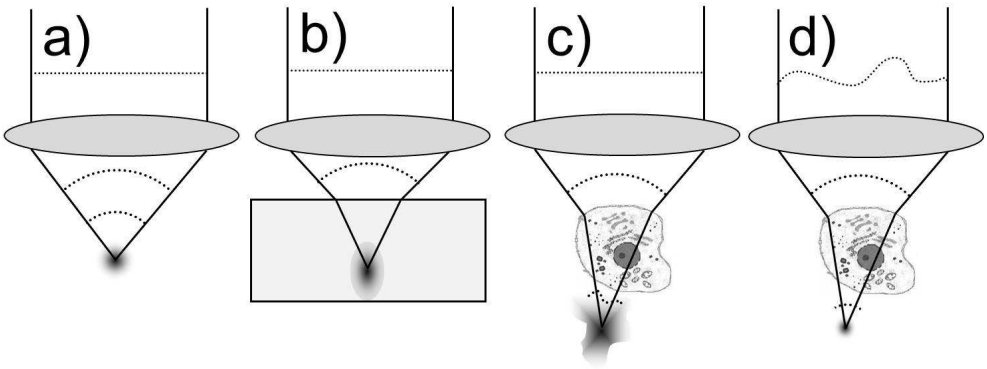

Figure 2.2: Aberration correction in tissue imaging. **(a)** In imaging, a microscope objective converts a perfectly planar wavefront into a converging, spherical wavefront thereby producing a diffraction limited focal spot. **(b)** A simple dielectric interface, for example, a microscope slide or coverslip, introduces optical aberrations and causes the focal spot to broaden and elongate. **(c)** The situation is aggravated when imaging through a biological specimen exhibiting multiple mismatches in refractive index. **(d)** A wavefront that has been pre-shaped so as to exhibit the optically conjugated aberrations can restore the diffraction limited focal spot at depth.

able as, for example, most biological tissues are mainly water based but imaged with oil-immersion objectives since they achieve the highest NA which is often essential for high resolution imaging. In any case, the inhomogeneities of the specimens in terms of refractive index will cause the focal spot to broaden and elongate (c). The resolution of the microscope is then no longer given by the diffraction limit but by the aberrations introduced by the system and the sample under investigation. A preshaped wavefront which introduces the exact optical conjugated aberrations can restore the diffraction limited focal spot at depth (d).

2.2 Image formation

Only for an infinitely small wavelength will any optical system image a point-like object onto a perfect image point. For finite wavelengths, however, diffraction will inevitably smear the image point which analytically leads to the point spread function (PSF). The PSF is the diffraction pattern in intensity due to the circular aperture of a lens at its focus and can be interpreted as the impulse response of an imaging system to the delta function. The three-dimensional PSF depends on the wavelength and the numerical aperture (NA) and for an aberration-free lens with circular aperture is given by:

$$\mathrm{PSF}(u,v) = \left| 2 \int_0^1 P(\rho) J_0(\nu\rho) \exp \frac{iu\rho^2}{2} \rho d\rho \right| \tag{2.1}$$

where J_0 denotes the zero-order Bessel function, $\sqrt{-1} = i$, v, u are the normalised optical coordinates defined in section 2.2 and ρ is the normalised radial coordinate. $P(\rho)$ denotes the complex pupil function that can be expressed in terms of its amplitude A and phase ϕ as:

$$P(\rho) = A(\rho) \exp\left(i\phi(\rho)\right). \tag{2.2}$$

An image is obtained by convolution (denoted $\otimes$) of the object with the PSF, and this convolution can be simplified to multiplication in Fourier space:

$$\mathrm{object} \otimes \mathrm{PSF} = \mathrm{image} \quad \overset{FT}{\Longleftrightarrow} \quad \mathscr{F}(\mathrm{object}) \cdot \mathrm{OTF} = \mathscr{F}(\mathrm{image}) \tag{2.3}$$

where $\mathscr{F}$ denotes the Fourier transform and OTF the optical transfer function with OTF$= \mathscr{F}$(PSF). For incoherent imaging, the OTF depends on the spatial frequency f and is a complex variable whose normalised modulus is the modulation transfer function (MTF) and phase is the phase transfer function (PTF):

$$\mathrm{OTF(f)} = \mathrm{MTF(f)} \exp\left(i\mathrm{PTF(f)}\right). \tag{2.4}$$

The OTF represents the ratio of image contrast to specimen contrast when plotted as a function of spatial frequency, taking into account the phase shift between positions occupied by the actual and ideal image. The MTF (see also Fig 2.3a and section 4.1.5 on page 50) is a measure for the ability of the imaging system to transfer contrast from the specimen to the intermediate image plane. When imaging a precisely defined target having a repeating structure with 100 % contrast with a diffraction limited microscope the image will have sinusoidal intensity with reduced contrast. The objective quality will affect the modulation response as a function of spatial frequency f (mostly quoted as a number of spacings per unit interval, e.g. line pairs per mm) up to a cut-off frequency f_c at which contrast reaches zero:

$$f_c = \frac{2\mathrm{NA}}{\lambda}. \tag{2.5}$$

where NA is the numerical aperture of the lens. Resolution in this context becomes the highest spatial frequency at which the contrast is above a somewhat

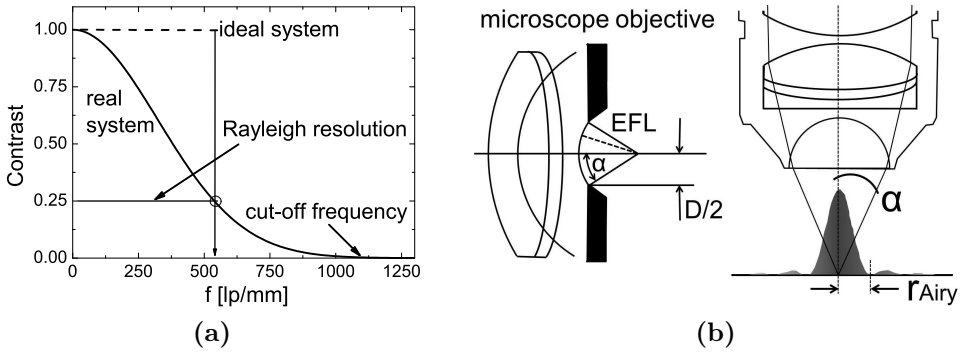

Figure 2.3: **(a)** Modulation transfer function. **(b)** Numerical aperture NA = $n \sin \alpha$ and effective focal length of a microscope objective. The radius of the first dark fringe in the diffraction pattern of a lens defines the Airy disc.

arbitrarily chosen value. In accordance to the Rayleigh criterion a contrast of 25 % is often chosen as the limit [39]. However, this does not mean that all spatial frequencies up to this limit are equally visible, rather that the contrast in the image is proportional to the contrast in the sample as degraded by the MTF of the imaging system and the contrast of smaller features is much lower than that of larger features.

The NA of a microscope objective quantifies its light gathering ability by giving a measure of the amount of highly diffracted, image forming light rays captured (Fig. 2.3b). The NA is given by NA = $n \sin \alpha$ where n is the refractive index and α the half-angle of the maximum cone of light that can enter the objective or is converging to an illumination spot. The NA describes the angular behaviour of a light cone; the higher the NA of a microscope objective the higher the amount of increasingly oblique rays which can enter the objective and therefore contribute to a highly resolved image. The practical limitation of the angular aperture is $\alpha \approx 72°$ and beyond this the NA of an objective can only be increased further by using an immersion medium of higher refractive index n, for example water or oil.

For the further discussion it is convenient to define the optical unit u along the optical axis and v for the lateral direction using the modified wavenumber $k' = \frac{2n\pi}{\lambda} = nk_0$:

$$u(z) = \frac{2\pi}{n\lambda} \mathrm{NA}^2 z = z k' \sin^2(\alpha), \tag{2.6a}$$

$$v(r) = \frac{2\pi}{\lambda} \mathrm{NA} r = r k' \sin(\alpha). \tag{2.6b}$$

These dimensionless, generalised coordinates are frequently employed in the treatment of diffraction in systems with low angular aperture [40] as they are conveniently proportional to the resolution of diffraction limited systems.

2.3 Image quality

The optical performance of any imaging system for biological tissues can be quantified and assessed by three distinctive parameters. The maximum spatial (lateral and axial) resolution, the maximum penetration depth and the depth dependent signal to noise ratio.

2.3.1 Spatial resolution

The spatial resolution is determined by the dimensions of the effective (detected) PSF of a subresolution, point-like object. The lateral PSF p(u,v) in the focal plane of the objective with circular aperture is commonly calculated for the approximation of paraxial optics (small NA) to be [41]:

$$p(0, v) = \frac{2J_1^2(v)}{v^2} \tag{2.7}$$

where J_1 denotes the first order Bessel function of the first kind. This diffraction pattern is also known as the Airy disc (Fig. 2.3b). The radius of the first dark fringe in the diffraction pattern is given by [42]:

$$r_{\text{Airy}} = 0.61\frac{\lambda}{\text{NA}} \tag{2.8}$$

where λ denotes the wavelength and NA stands for the numerical aperture. The image of two incoherently radiating points will only be resolved if these two points are far enough apart for their PSFs to be distinct, which means an appreciable dip needs to appear between the two peaks. According to the Rayleigh criterion, two objects are resolved if the distance between their intensity peaks is greater than the radius of the Airy disc, which means the PSF maximum of the second point falls on the first minimum of the PSF of the first point. This leads to a dip between the two peaks of approximately 25 % [41]. However, it has become common practice to fit a one-dimensional Gaussian to the lateral and axial profiles of the point spread function and use the full-width half- maximum (FWHM) as a measure for resolution.

In the axial direction, the PSF is given in a paraxial approximation by:

$$p(u,0) = \left(\frac{\sin\left(\frac{u}{4}\right)}{\frac{u}{4}} \right)^2 . \tag{2.9}$$

In analogy to the lateral resolution limit, the axial resolution can also be defined by the distance from the centre of the 3D diffraction pattern to the first axial minimum. This distance must be derived from wave optics and is given by [42]:

$$z_{min} = \frac{2n\lambda}{\left(\mathrm{NA}^2\right)} \tag{2.10}$$

where n refers to the refractive index of the object medium.

2.3.2 Signal and noise

The resolution criterion according to Rayleigh relies on the distinction of separate peaks by a reasonable dip between their respective PSF maxima. This means resolution is dependent on contrast and noise content in the image because these parameters influence the visibility of such a dip. According to the Rose Criterion, a dark feature contained in a single pixel must have an intensity that differs from that of the white background by at least five times the noise level of the background in order to be visible [43].

The imaging performance of every photon sensor is fundamentally limited by noise that is due to the random arrival times of photons according to Poisson statistics, termed quantum- or shot noise. The noise of such a quantum-limited detector is given by the square root of the detected photons:

$$\text{noise} = \sqrt{\#\text{photons}}. \tag{2.11}$$

The signal to noise ratio (SNR) is a dimensionless ratio of signal power to noise power contained in a signal and commonly used as a measure to quantify how much an image has been corrupted by noise. For a digital image, the SNR can be simply calculated by [44]:

$$\mathrm{SNR} = \frac{\mu_g}{\sigma_g} \tag{2.12}$$

where μ_g stands for the mean signal intensity in terms of grey value of a region of interest (ROI) and σ_g for the standard deviation in grey value of that same

ROI. Contrast of an image is defined by [41]:

$$c = \frac{n_b - n_d}{2n_{\text{avg}}} \tag{2.13}$$

where n_b and n_d denote the intensity on the bright and dark side of the ROI respectively. This definition of contrast is dependent on the the ROI, as noise decreases with averaging.

The quality of an image and the information content that can be deduced from it is thus dependent on two factors, contrast and the illumination level. The number of detected photons depends on the illumination power of the source and the efficiency of the detection, whereas contrast is determined by the object modulation and the ability of the imaging system to exclude stray light that is additive without contributing to the signal. Many methods have been developed in order to improve the contrast in microscopy, such as fluorescence microscopy (increase in contrast through detection of Stoke's shifted wavelengths only) or confocal microscopy, which only detects light that originates from a volume in the sample that is optically conjugate to the source and the detector (see also chapter 3 of this thesis).

2.3.3 Sampling

Digital data acquisition of an analog signal introduces effects which are determined by the sampling aperture A and sampling distance Δ of the digitiser. The sampling distance or pixel pitch, Δ, is the spatial interval at which the analog signal is discretely sampled and defines the Nyquist frequency:

$$f_N = \frac{1}{2\Delta}. \tag{2.14}$$

Mathematically, the process of sampling involves the reduction of a continuous (analog) signal to a discrete signal by multiplying the analog signal with a row of δ-functions (the comb function) separated by Δ. The δ-function is infinitesimally small (with zero width) and therefore sampling occurs at infinitively small points along the analog signal. In practice, however, sampling occurs over a finite sampling aperture A of the analog signal for each pixel. This causes a blurring that can be calculated by the convolution of the analog signal and the aperture response function over the width A [45]. More details on the effect of various digital parameters, such as the sampling aperture, sampling distance on

the MTF of digital systems can be found in Giger *et al.* [46]. The presampled MTFs calculated in chapter 4 of this thesis include the effect of aperture blurring but do not take aliasing effects due to the discrete sampling of an analogue signal into account.

Aliasing describes an effect in which features of the object might be distorted or displaced in the image and features that are not present in the object appear as artifacts in the data [39]. According to the Nyquist Criterion, the discrete sampling of an analog signal is free of aliasing effects if the analog signal contains no frequencies higher than the Nyquist frequency. For microscopy applications, this means that the finest spatial structure, the radius of the Airy disk, should be imaged by at least two pixels. Changing the zoom magnification in a microscope usually does not alter the number of pixels used but the pixel size. It follows that for a given optical system only one pixel size and therefore zoom factor matches the Nyquist Criterion. Zoom settings with smaller pixel size necessarily oversample the sample with an increased risk of photobleaching and a reduced field of view. Conversely, lower zoom settings are not able to resolve finer structures in the sample and can cause aliasing.

2.3.4 Light scattering in biological tissue

Many relevant biological processes happen at a considerable depth within highly scattering biological tissues and in order to investigate those effects within their natural environment it is important to have an understanding of the maximum penetration depth at which useful dynamic, high-resolution images can still be acquired. The maximum penetration depth is defined as the imaging depth at which the signal decreases to the level of the background noise and therefore becomes indistinguishable. That is, at the maximum penetration depth SNR := 1 by definition [47].

In most biological tissues light scattering outweighs absorption, particularly in the near-infrared (NIR) region. Scattering is the deflection of light rays due to the heterogeneous mixture of cells and sub-cellular structures with varying molecular polarisabilities and is commonly quantified by the mean free path length $\iota(\lambda)$ which depends on the wavelength and determines the average distance between scattering events. Rayleigh scattering describes the nearly isotropic and strongly wavelength dependent ($\propto \lambda^{-4}$) scattering of light by particles that are much smaller than the wavelength. In biological tissue scattering also decreases with

wavelength albeit less than expected for Rayleigh scattering [48]. Cellular structures such as organelles and other refractive structures which are larger than the wavelength of light contribute to Mie scattering [49]. Mie scattering has a sharper forward lobe similar to an antenna pattern, is not strongly wavelength dependent and the intensity of the scattered light is proportional to the square of the ratio of the refractive indices of the feature and the media [50].

The power of ballistic, non-scattered, photons is given by a Lambert-Beer exponential decay with imaging depth z:

$$P_{ball} = P_0 \exp\left(\frac{-z}{\iota}\right) \tag{2.15}$$

where P_0 is the incident power. In non-linear microscopy only this fraction can contribute to signal generation in the focal volume and due to its quadratic dependency on excitation, two-photon excited fluorescence decreases as $\propto \exp\frac{-2z}{\iota}$ [51]. In the visible spectrum, the scattering of fluorescence photons is dominant over ballistic fluorescence such that for sufficient imaging depth, multiply scattered fluorescence light leaves the sample from a region on the surface spanning an area that is wider than the focus is deep [52].

2.4 Image degradation

2.4.1 Optical aberrations

The electric field vector of a monochromatic light wave is given by

$$\vec{E}(\vec{r},t) = \vec{E}(\vec{r})e^{i[(\vec{k}\vec{r}+\epsilon(\vec{r}))-\omega t]} \tag{2.16}$$

where $|k| = \frac{2\pi}{\lambda}$, $\omega = 2\pi f$ is the angular frequency, $\vec{E}(\vec{r})$ is the amplitude and $\phi(\vec{r}) = \vec{k}\vec{r} + \epsilon(\vec{r})$ denotes the phase. Wavefronts are defined as surfaces of equal phase, *i.e.*

$$\phi(\vec{r}) = \phi_0 = \text{const.} \tag{2.17}$$

Any departure from a perfectly flat or spherical wavefront caused either by the optical system or the specimen under investigation is called an optical aberration. Aberrations can be included as phase variations into the pupil function of the objective lens ($P(\rho)$ in eq.2.2) and thus allow for the calculation of aberrated

PSFs [30, 32]. Aberrations can be grouped into either monochromatic, that is wavelength-independent aberrations or chromatic aberrations and a short introduction to the most important aberrations is given in the next sections.

Monochromatic aberrations

Spherical aberrations Spherical aberrations (SA) (see Fig. 7.3 on p.149) are caused by peripheral rays not being brought to focus at the same spot as paraxial rays when a dielectric interface is introduced in the image space of an optical system leading to a sequence of focal spots along the optical axis [53]. One approach to avoid SA is to employ water-immersion lenses, however these lenses cannot be made with NAs of much above 1.25 due to the 1.33 refractive index of water [42]. Also, the collection of 3D data stacks requires the movement of the specimen with respect to the lens, and if this is not to produce motion of the specimen, a coverslip must be used. Olympus hold a patent on "cytop", a coverslip material which has a refractive index of 1.34 almost that of water, intended for that application [54].

Although high-end optical components like oil immersion objectives are designed to provide almost perfect correction for SA if focused near the coverslip surface, more and more aberrations are introduced the deeper the focus is moved into a aqueous sample due to the refractive index mismatch (RIM) between the oil /glass ($n_1 = 1.51$) and the water ($n_2 = 1.33$). The results are increasing focal spot size, additional side-maxima, decrease in maximum intensity, focal shift and decaying intensity gradients [55]. As the peripheral parts of the focusing beam have to traverse more material, they are attenuated to a higher degree than the paraxial rays which leads to a substantial decrease in the effective NA with increasing imaging depth [51]. Therefore the effect of SA increases rapidly with the RIM ($n_1 - n_2$), the NA and the imaging depth.

The effects of SA and strategies to compensate for them will make an appearance in almost every chapter of this thesis. In section 7.5 the detrimental effects of SA in optical trapping are examined and methods for their compensation are surveyed in section 8.3.3. In the case of nonlinear microscopy, SA and other aberrations are sometimes limiting factors for deep imaging (section 5.4.2) and have therefore caused a lot of research into methods of compensating for them to be undertaken (section 5.4.3). RIM is covered in more detail in section 3.4.1 with the following two sections exploring efforts in aberration correction.

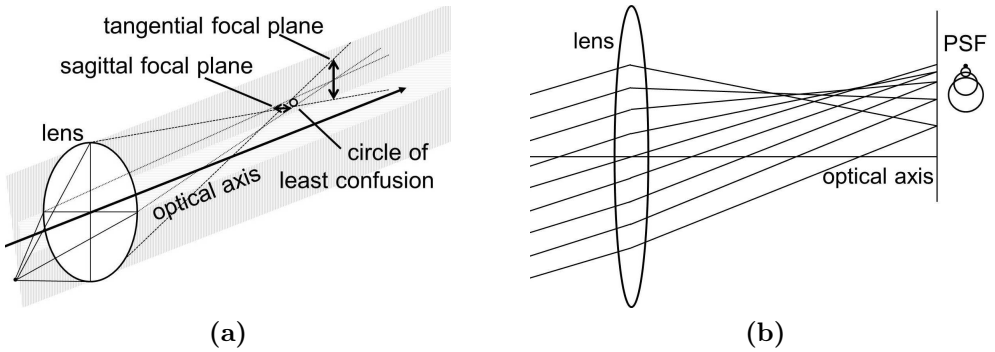

Figure 2.4: **(a)** Schematic of astigmatic aberration. Rays in perpendicular planes have different foci. **(b)** Schematic of comatic aberration. Magnification varies over the entrance pupil.

Finally, high NA objectives also affect the applicability of certain formulas. All physical equations derived from a paraxial approximation assume that light rays pass through an optical element in proximity to the optical axis such that the small angle approximation $\sin\alpha \approx \alpha$ can be applied, *i.e.* for opening angles $\alpha \leq 0.5\,\text{rad} \approx 28°$. The use of high NA objective lenses is essential for applications like optical trapping or multiphoton microscopy (see chapters 7 and 5 of this thesis). The paraxial approximation no longer holds true for such cases as high NA lenses are specifically designed to collect the largest possible cone of light/ transmit peripheral rays with large incident angle. This improves the contribution of marginal rays in the focal spot leading to an increase in resolution, however, it also introduces optical aberrations into the system which can deteriorate and/or deform the quality of an image.

Astigmatism When astigmatism is present in an optical system marginal rays in two orthogonal cross-sections through the imaging wavefront (tangential and sagittal) have different focal distances (Fig. 2.4a). The circle of least confusion denotes the position of compromise between the tangential and sagittal extremes and placing the focal spot there results in a four-lobed Airy disc.

Coma Coma is an off-axis aberration and therefore pronounced in beam scanning instruments. The name hints to the shape of a PSF from a lens with comatic aberrations which exhibits a tail similar to a comet. Coma can be described as a variation of magnification over the entrance pupil (Fig. 2.4b). In severe cases peripheral rays focus on the image plane closer to the optical axis than do rays

passing near the central part of the lens: the peripheral rays then produce the smallest image with the least magnification (negative coma).

Chromatic aberrations

The main cause for a wavelength dependency of aberrations is due to the wavelength dependency of the refractive index of every material caused by dispersion. In longitudinal (axial) chromatic aberration, the image plane is only in sharp focus for one wavelength and for every other wavelength a shift in focal length Δf occurs. The image plane is slightly defocused for different colours, creating greenish or purple fringes on images of sharp edges. Some degree of correction can be achieved with apochromat objectives which replace single lenses with doublets containing both materials with normal and anomalous dispersion and are used to cancel out chromatic effects at two or more wavelength.

Axial chromatic aberrations, described above, arise because the focal length of a lens is dependent on the wavelength of the light. The magnification of a lens is inversely proportional to the focal length and this causes magnification to be dependent on wavelength too. This aberration is termed lateral chromatic aberration and causes intensity loss at the pinhole.

2.4.2 Zernike representation

An aberrated wavefront can be conveniently decomposed over a series of Zernike polynomials [56], a complete set of orthonormal polynomials defined over the unit circle [57–59]. In the continuous numeration with single index k the Zernike polynomials $Z_k(\rho, \theta)$ are related to the classical aberrations like astigmatism, coma and spherical aberration. In Appendix A the first 15 Zernike polynomials are formulated and illustrated graphically and an equation for the change from single index notation to double index notation is given.

Each wavefront $\phi(\rho, \theta)$ can be decomposed using this set of polynomials using the coefficients c_k according to:

$$\phi(\rho, \theta) = \sum_{k=0}^{\infty} c_k Z_k(\rho, \theta). \tag{2.18}$$

Higher order aberrations that contain higher spatial frequencies require higher order Zernike polynomials for their description. In imaging applications, high NA lenses are often preferred because of their superior light collection efficiency

and resolution. By using such lenses a greater range of the same wavefront or phase content can be captured and therefore larger NAs lead to higher spatial frequencies in the pupil function [60]. Aberrations can be modeled as phase variations in the pupil of the objective lens (see eq. 2.2) and thus correction is, in principle, possible by introducing an equal but opposite phase aberration into this pupil or its optical conjugate using an appropriate correction element [32]. The next section is concerned with such correction elements.

2.5 Corrective elements

Deformable membrane mirrors (DMMs) essentially consist of a mirrored surface whose shape can be controlled by means of actuators. The wavefront is corrected upon reflection of that surface by acting on the optical path difference. Alternatively spatial light modulators (SLMs) which act directly on the phase can be employed.

2.5.1 Deformable membrane mirrors

The optical path difference OPD is given by:

$$OPD = n\Delta z \tag{2.19}$$

where n is the refractive index, and Δz is the physical distance traveled by the wave. OPD is related to the phase ϕ as:

$$\phi = \frac{2\pi}{\lambda}\mathrm{OPD} = kn\Delta z \tag{2.20}$$

where k denotes the wavenumber. DMMs correct for aberrations by modulation of Δz upon reflection off their surface.

Many different methods of deforming the membrane have been implemented including electrostatic [61–63], magnetic [64], piezoelectric [65], bimorph [66], thermal [67], vacuum [68], fluidic [69] and ferromagnetic [70] actuation. Several publications focus on the characterisation and comparison of DMMs in order to estimate the range of aberration correction that is achievable in particular correction tasks, mostly the fitting of ocular and atmospheric wavefronts [71–73]. DMMs with highly reflective membranes are particularly useful for fluorescence microscopy because their high optical efficiency means that optical losses are low.

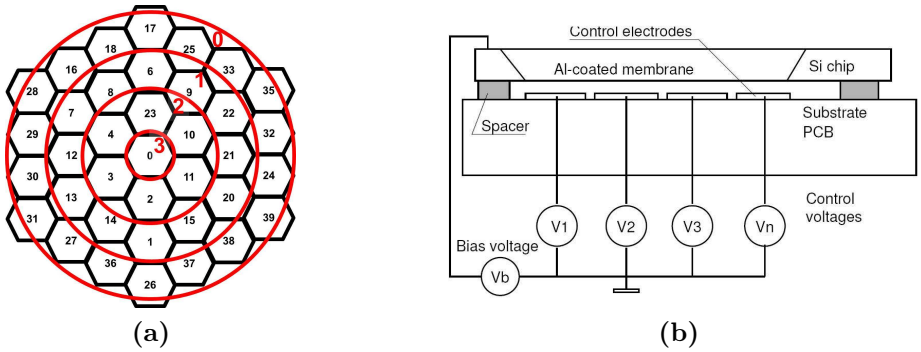

(a) **(b)**

Figure 2.5: **(a)**Actuator layout of the OKO37 and mapping of the 37 control channels. The red circles indicate the rings of actuators that have been weighted with a Gaussian function to speed up optimisation convergence (see section 2.6.2). **(b)** Electrostatic actuation principle.

DMMs are modal correction elements which use a set of smooth functions, the influence functions (IF), to approximate the required wavefront. IFs correspond to the response of the membrane to the action of every isolated actuator, activated with a known voltage. IFs are generally measured with an interferometer [74] and grouped in the IF matrix $\bar{M}$ given by:

$$\phi = \bar{M}v. \tag{2.21}$$

The inverse problem of calculating a set of actuator voltages v for the generation of a given wavefront ϕ_m is solved by inverting the IF matrix $\bar{M}$ to obtain the control matrix:

$$v = \bar{M}^{-1}\phi_m. \tag{2.22}$$

The control matrix of the membrane is the function that translates required surfaces to sets of voltages. As the IF matrix is generally neither square nor regular and thus non-invertible, the pseudo-inverse is calculated through singular value decomposition [64]. The size and shape of the IFs of a given DMM have a great influence on its performance in aberration correction, with wide IFs reducing the DMMs spatial correcting abilities [75]. In the following the three DMMs used in this work are introduced and their specifications are summarised and compared in Table 2.1.

OKOtech37

The OKO37 from Flexible Optical Technology (former OKOTech) [76] was the first, cheap micromachined deformable membrane mirror to hit the market. It consists of 37 hexagonal electrostatic actuators mounted underneath a thin silicon nitride membrane coated with a highly reflective aluminium layer (Fig 2.5) [62, 77,78]. The membrane is stretched over a frame with circular aperture and bound at the edges. The optical pupil has a diameter of 15 mm, although studies have shown that only a reduced region of 63 % equivalent to 9.5 mm is ideally used as optical pupil because this leaves a ring of actuators outside the optical pupil and hence improves the correction of the pupil edge [74]. According to Vdovin *et al.* any DMM described by the Poisson equation requires at least two actuators to be placed outside the working aperture per period of the azimuthal aberration of the highest expected order [79].

The deformation of the membrane is caused by the electrostatic forces applied by the actuators. For a plate capacitor of capacitance $C = \epsilon\frac{A}{d}$, where A is the area over an individual actuator and d denotes the distance between the actuator and the membrane, the electric field is given by $E = \frac{CV}{\epsilon A}$ where V represents the voltage between actuator and membrane. This field leads to an electrostatic pressure $p = \epsilon E^2 = \epsilon\frac{V^2}{d^2}$ where $\epsilon = \epsilon_r\epsilon_0$ is the permittivity. The electrostatic force is given by:

$$F_{el} = pA = \epsilon\frac{A}{d^2}V^2. \tag{2.23}$$

The deformation is not linear with the applied voltage but follows a quadratic dependence with good approximation.

With the membrane of the mirror being on ground only positive voltages can be applied to the actuators (Fig 2.5b). Hence, the membrane deflection is always directed towards the electrode structure producing concave shapes. A bi-directional operation becomes possible by applying a bias voltage V_B to all actuators. By applying a control voltage V_C with $V_C \ll V_B$ the sensitivity of the mirror becomes linear:

$$F = \epsilon\frac{A}{d^2}(V_B + V_C)^2 \Leftrightarrow \frac{F}{V_C} \approx 2\epsilon\frac{A}{d^2}V_B. \tag{2.24}$$

A maximum voltage of 200 V can be applied to each and every actuator, however, the mirror is controlled via a 8 bit scale with values ranging from 0 to

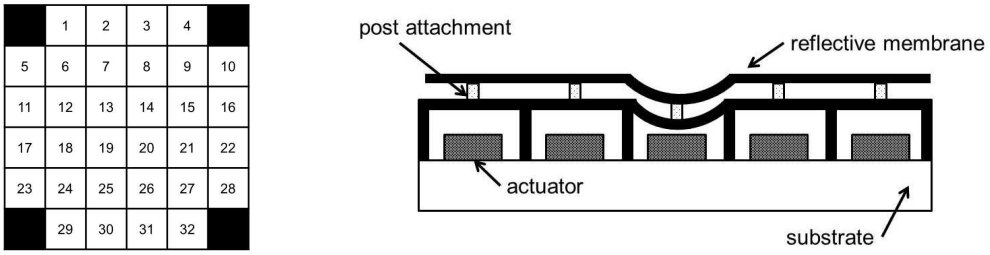

Figure 2.6: **(a)** Actuator layout of the BMC mini. **(b)** Electrostatic actuation principle.

255. A disadvantage of the biased operation is that it introduces a considerable amount of defocus on any collimated beam upon reflection from the DMM. This defocus has to be compensated for by axially displacing the preceding lens to ensure that collimated light enters the back aperture of the microscope objective. A common problem encountered with this continuous DMMs is the dependency of the membrane on not only the actuator directly underneath it but also on actuators in the direct vicinity. This is referred to as cross-talk or mode-coupling and occurs when the IFs of the actuators are not orthogonal.

The OKO37 was used for aberration correction in a custom-built confocal laser scanning microscope as described in chapter 4 of this thesis.

BMC mini

Microelectrical mechanical systems (MEMS) technology has been a driving force in the production of a number of DMM systems [63, 80]. Using microstructured silicon, a supporting structure below the reflective membrane ensures that the influence of each actuator is spatially confined to minimise cross-talk. The actuation in this DMM also uses electrostatic forces to shape the membrane, but this time to mechanically displace the actuators instead. This approach, commercialised by Boston Micromachines with models having 32, 140 and 1024 actuators, allows for high packing ratios, high linearity and low cost per actuator.

The BMC mini from Boston Micromachines Corporation is actuated by 32 pistons (6x6 array without the 4 corners, Fig. 2.6). Similarly to the OKO37, the BMC is also operated biased to its mid-range in order to allow for bi-directional operation. This mirror was used in a nonlinear microscope setup and the results obtained by this experiment are presented in chapter 6 of this thesis.

Table 2.1: Comparison of the DMMs employed in this work. CLSM: confocal laser scanning microscopy, OT: optical trapping, NLM: nonlinear microscopy.

Specification	OKO37	Mirao52	BMCmini
in Chapter	4	8	6
Application in thesis	CLSM	OT	NLM
Technology	el.-static	el.-magnetic	el.-static
Actuators	37	52	32
Optical pupil [mm]	15	15	1.5
Optimal aperture [%]	63	100	100
Actuator pitch [mm]	1.8	2.5	0.3
Max voltage [V]	200	25	215
Response rate [kHz]	1	0.25	3.5
Max stroke [µm]	8	100	-
Actuator stroke [µm]	0.6- 0.8	10-15	3.5
Coating	Al	Ag	Au
Correction [radial order n]	3rd	5th	-
Price (approx.)	£3.2k	£16.5k	£5.4k

Mirao52

The Mirao52 DMM from Image Optic uses 52 push-and-pull, magnetic actuators to deform a highly reflective, silver-coated membrane (Fig. 2.7). Actuation of the membrane is achieved by applying a voltage to underlying coils which creates a magnetic field that can either push or pull small magnets attached to the back of the membrane. The exerted force from the actuators is linearly dependent on the current applied to the DMM. The IFs of this DMM have been shown to exhibit a linear response with voltage with virtual no mode coupling and a high fidelity in the generation of Zernike polynomials [64]. This DMM was employed for aberration correction in an optical trapping setup as described in chapter 8 of this thesis.

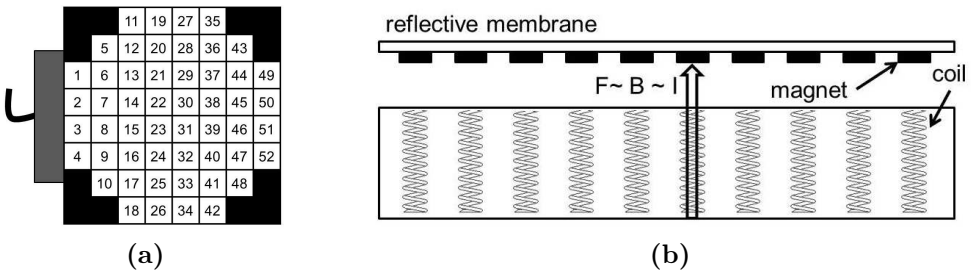

Figure 2.7: **(a)** Actuator layout of the Mirao52. **(b)** Magnetic actuation principle.

2.5.2 Spatial light modulators

The development of liquid crystals panels for displays has led to spatial light modulators (SLM) being increasingly available for research applications, for example in optical trapping (see section 7.3 of this thesis) or as correction elements in AO [81]. In response to changes in the applied electrical field, changes in the refractive index in the nematic liquid crystal are generated which modulate the phase of the wavefront [82, 83]. The main advantage of SLMs over DMM is large stroke and high density of independent pixels, however drawbacks include a reduced speed of response and a relatively low optical efficiency. The calculation of a hologram to change the shape of the beam is computational intensive but can be done in real time. The update rate of SLMs, however, is generally only at around $15 - 30\,\mathrm{Hz}$ in comparison to kHz update speeds which are possible with DMMs. Additionally SLMs are polarisation and wavelength dependent which makes them incompatible with fluorescence confocal microscopy.

An SLM from Boulder Nonlinear Systems XY series consisting of 512 x 512 individually addressable pixels was used to trap beads of $3\,\mu\mathrm{m}$ diameter in chapter 8 of this thesis. Holograms are calculated and displayed on the SLM by the Red Tweezers software developed by the Optics Group at Glasgow University [84, 85].

2.6 Wavefront sensing and algorithm based optimisation

A number of methods have been used in AO systems to measure wavefronts. Shearing interferometers [86], pyramid sensors [87], and Shack-Hartmann Sensors [88] all measure the wavefront slope directly whereas curvature sensors [89] and phase diversity [90] are used to measure the wavefront curvature. Other methods include modal sensing [91–93] and common path interferometry [94]. It is beyond the scope of this work to give a detailed review of each method.

2.6.1 Shack-Hartmann WFS

Here, we will only discuss the principle of the Shack-Hartmann sensor , the most common wavefront sensor (WFS) in AO applications [95, 96]. The principle of operation is illustrated in Figure 2.8. In a Shack-Hartmann sensor, the incoming wavefront is sampled with a dense array of microlenses. Each of these lenses

produces a focal spot F onto a CCD array which is positioned a focal distance f behind the microlens array. A perfectly plain wavefront W(x,y) produces focal spots precisely relating to the matrix determined by the dimensions of the lenslet array and the position of the centroids of each focal spot can be found by computation. An aberrated wavefront which is incident on an individual microlens will cause a shift in the position of the focal spot F' which is proportional to the wavefront slope α averaged over the subaperture of the microlens.

Let α_{ix} and α_{iy} be the mean wavefront slopes over a subaperture of one lenslet i in the array:

$$\alpha_x = \frac{\partial W(x,y)}{\partial x}; \qquad \alpha_y = \frac{\partial W(x,y)}{\partial y}. \tag{2.25}$$

For an aberrated wavefront the focal spots of each individual lenslet i will be shifted laterally by:

$$\Delta_{ix} = f\alpha_{x,i}; \qquad \Delta_{iy} = f\alpha_{y,i} \tag{2.26}$$

where $W(x,y)$ is the deviation from the plane wavefront. Due to the expression of the trigonometric function as a Taylor expansion this is only valid for small aberrations. For large aberration the exact equation $\frac{\partial W(x,y)}{\partial x} = \arctan(\frac{\Delta_{xi}}{f})$ has to be used. The centroid of each shifted focal spot is now given by the wavefront slope averaged over each subaperture and by calculating the displacement from the unaberrated case the incident wavefront can be reconstructed by least square fitting [97].

It should be noted that extremely large aberrations can cause the focal spot

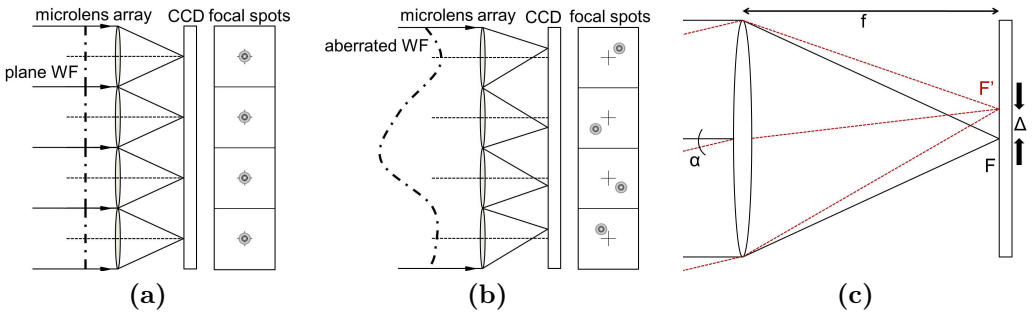

Figure 2.8: **(a)** Plane wavefront incident on a lenslet array and the resulting spot pattern on the CCD sensor. **(b)** Aberrated incident wavefront, the lateral displacement is proportional to the wavefront slope averaged over the subaperture of the microlens. **(c)** Shack-Hartmann lenslet principle.

to be displaced by more than the diameter of a subaperture on the CCD camera causing the wavefront reconstruction to fail. The spatial resolution of the Hartman Shack wavefront sensor is obviously limited by the size of the microlenses in the lenslet array. Ideally the resolution of the WFS is closely matched to the correction abilities of the wavefront corrector, therefore appropriate spatial and temporal sampling need to be considered.

2.6.2 Optimisation algorithms

In some AO applications the required wavefront for aberration correction is not directly measured with a WFS but instead a particular optimisation algorithm is used to sequentially reconfigure the correction element by maximising a feedback signal, the merit function (MF). Selecting a feature of interest in the image like brightness, contrast or resolution, an optimisation algorithm is employed that applies a range of shapes to the mirror accepting those that improve the MF and then making variations to further improve the image, stopping when a plateau has been reached. Sensorless AO have been employed in confocal fluorescence and reflection microscopy [33], two photon fluorescence microscopy [35,98], second harmonic generation imaging [99], intracavity aberration correction in lasers [100], optical tweezers [101, 102] and coupling laser light into optical fibers [103]. A variety of optimisation algorithms have been implemented to drive the corrective element, mostly based on genetic algorithms [35, 98, 99, 103], hill climbing algorithms [100, 101] and random search algorithms [102]. Wright *et al.* have compared the relative merits of several forms of algorithm [104], including genetic, hill climbing and random search, and methods to reduce the search space and hence speed up the time required to find the optimal solution have been indicated by Booth *et al.* [105]. A comparison and evaluation of possible MFs is given in Poland *et al.* [106].

A disadvantage of this approach is that it tends to require a relatively large number of iterations that might not be practical for applications where high speed or low photon exposure is paramount. A solution to this problem is the use of look-up tables that store preoptimised DMM shapes for certain depths [38, 107].

Random search algorithm

A flowchart relating to the custom written random search algorithm (RSA) and its optimisation routine can be seen in Fig. 2.9. Starting from a flat DMM shape, one

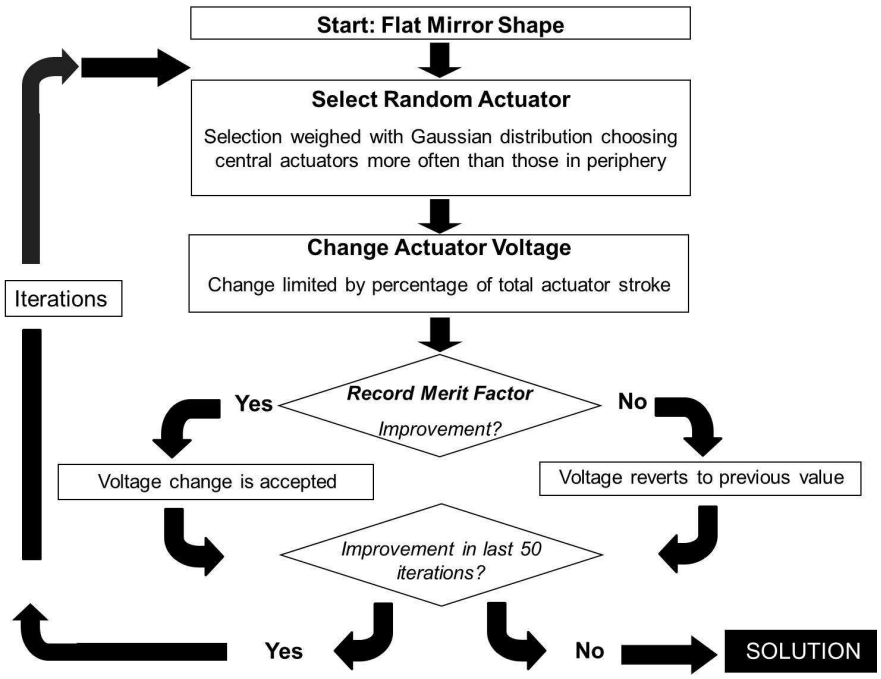

Figure 2.9: Random search algorithm flow chart.

actuator is randomly selected. The selection process is weighted with a Gaussian function to preferentially select the central actuators of the active area of the DMM (see for example Fig 2.5). The central actuators have a greater influence on the DMM shape than those in the periphery hence selecting them more often speeds up the optimisation process. The voltage on the selected actuator is then randomly changed within a user defined percentage range of the maximum permitted control voltage for one actuator. The MF is consequently measured in order to determine the acceptance or rejection of the voltage change. If the MF has improved by a certain percentage which is chosen to be above the noise level of the system, the actuator voltage change is accepted and if it has not improved the change is automatically reversed and the actuator is set back to its original value. After a certain number of iterations the algorithm is stopped by the user and the DMM shape which has produced the lowest MF is determined.

The efficiency of wavefront sensorless AO depends not only on the optimisation algorithm but also on the parameters used in its implementation. These parameters are usually highly specific to the chosen application and need to be carefully considered. The RSA described above was implemented in the LabVIEW programming language and used in three distinct applications of AO: confocal laser scanning microscopy (chapter 4), nonlinear microscopy (chapter 6, section 6.2.2) and optical trapping (chapter 8, section 8.2.2).

Chapter 3

Confocal Laser-Scanning Microscopy

3.1 Introduction

In confocal laser scanning microscopy (CLSM), the sample is sequentially illuminated by a diffraction limited spot and the signal from this spot is registered by a detector masked by a small pinhole [108]. The CLSM is a serial sampling instrument and the 3D image needs to be reconstructed digitally. Confocal microscopy increases the contrast in images by restricting the observed volume such that light emitted from areas nearby the focal spot cannot contribute to the detected signal.

Invented and patented by Marvin Minsky [3, 4] ahead of its time in 1955 and after pioneering work by a group in Oxford [109–113], confocal microscopy was demonstrated experimentally by the Cremer brothers and Brakenhoff *et al.* some 20 years later [114,115]. Several labs picked up the development of the technique, verified the theory of confocal imaging and expanded its application to biological research [116–118]. Accompanied by the rapid advances of video microscopy and digital image processing, the development of confocal laser scanning microscopy (CLSM) followed shortly afterwards by several groups [119–121] as well as the launch of commercial systems onto the market in the 1980s by BioRad, Olympus, Zeiss and Leitz.

CLSM has been widely applied over decades in cutting-edge biological and clinical research due its ability to produce three-dimensional, high-resolution images [122–125]. Employed by every bio-medical institution, the use of CLSM is taken for granted in countless scientific publications [126].

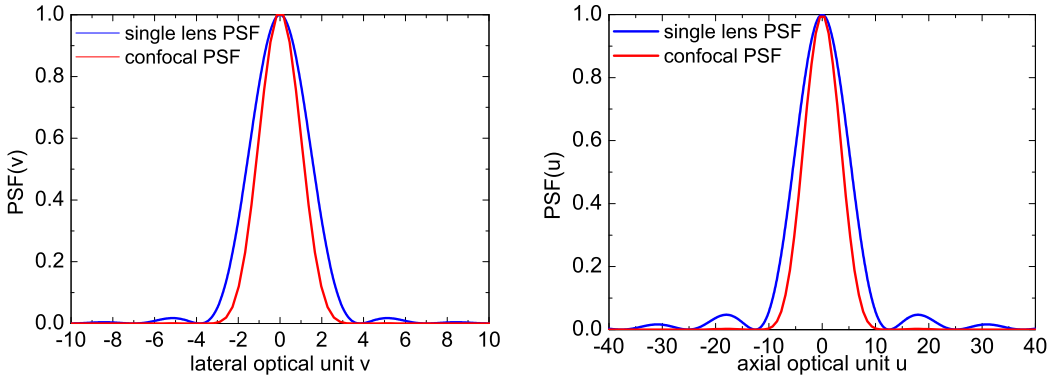

(a) **(b)**

Figure 3.1: PSF for a single lens and a confocal system **(a)** laterally and **(b)** axially. The normalised optical coordinates v and u are calculated for $\lambda_{exc} = \lambda_{em}$.

3.2 Physical background

The illumination volume is determined by the illumination PSF $p_{\text{ill}}(u, v)$ (eq.2.1) and can be interpreted as the probability that an illumination photon will reach the point (u, v) in the sample (see p.13 for the normalised optical units v and u) [41]. The detection volume is determined by the detection PSF $p_{\text{det}}(u, v)$ and can be interpreted as the probability that a photon will be able to propagate from this point (u, v) to the point detector. If epitaxial illumination is used, the light falls onto the object from the observation side, which means the same objective is used twice, once to focus the illumination spot into the sample and then again to collect the detection signal. The volume observed by a confocal microscope is then simply the product of the two PSFs (assuming $\lambda_{exc} = \lambda_{em}$):

$$p_{\text{conf}}(u, v) = p_{\text{ill}}(u, v) \cdot p_{\text{det}}(u, v) = p^2(u, v) \tag{3.1}$$

and can be interpreted as the product of the two independent probabilities. The confocal PSF $p_{\text{conf}}(u, v)$ exhibits a sharper peak and suppressed side lobes than the single lens PSF $p(u, v)$ (Fig. 3.1). This leads to an improvement in lateral resolution by a factor of $\sqrt{2} \approx 1.4$ in terms of the Rayleigh criterion compared to conventional microscopy [108, 126]. In CLSM, the lateral resolution is [41]

$$\Delta r_{\text{conf}} = 0.72 r_{\text{Airy}} = 0.44 \frac{\lambda}{\text{NA}}. \tag{3.2}$$

where r_{Airy} is half the diameter of the Airy disk, λ is the wavelength of the light used and NA is the numerical aperture of the lens. Two bright points are

axially resolved if they are separated by [41]:

$$\Delta z_{\text{conf}} = 1.5\frac{n\lambda}{\text{NA}^2}. \tag{3.3}$$

Axial resolution is commonly measured by moving a surface through the focal plane of the microscope objective while plotting the measured signal as a function of depth. The FWHM of this plot is related to the axial resolution through [41]:

$$\text{FWHM} = 0.84\Delta z_{\text{conf}}. \tag{3.4}$$

The optical sectioning effect is a result of the response of the CLSM to a fluorescent point source falling off approximately according to an inverse fourth-power rule with distance from the plane of focus [126].

3.3 Components of a CLSM

3.3.1 Scanner

Scanning is the sequential illumination of small areas on the sample. To this end, either the specimen can be scanned mechanically through movement of the stage, a slow and vibration-sensitive approach, or the laser focus can be scanned across the sample. Due to the increased speed and stability of this approach, it has become the method of choice in commercial, state-of-the-art confocal systems [127].

From this point on, several laser scanning mechanisms have been developed and successfully employed in CLSM, including line scanning using cylindrical lenses to focus the beam to a line on the specimen and multiple spot scanning for example spinning disk scanning microscopy [128]. Axial scanning can be achieved either by movement of the microscope objective or the specimen. The galvanometric scanning with a single spot is the most straightforward mechanism and will be discussed in more detail in the next section. Typically imaging speeds of ≈ 1 frames/s for a 512 x 512 image can be achieved. The accuracy of closed-loop galvanometric scanning, where the precise angular position of the rotating shaft is detected by an optical sensor and fed back to the device electronics, comes at the expense of slow scan rates.

Faster scanning, capable of video scan rates (≈ 30 frames/s), can be achieved with rotating polygon mirrors [129, 130],scanning with the use of acousto-optic devices (AOD) [131] or resonant scanning [132–134] (see references [127] for an

overview). However, the downside of resonant scanner is that they run at only one fixed frequency, their resonant frequency ($\approx 8\,\mathrm{kHz}$), the x-scan is sinusoidal rather than linear and it is not possible to zoom, pan or rotate. A fundamental limitation of AOD scanning is its wavelength dependency, so that fluorescence emission cannot be descanned.

In an attempt to miniaturise the size of CLSM, microelectromechanical system (MEMS) -based scanning mirrors [135] and vibrational optical fibers for fast endoscopic scanning have emerged [136–139]. A review of scanning techniques and further details are given in [140].

Galvanometers

The most common scanning design in CLSM is arguably the non-resonant point scanner in which the beam scanners are small mirrors mounted on galvanometers, commonly called galvos. Historically, galvos were used to sense electric currents which would cause the galvo and mirror mounted on it to rotate and deflect a light beam onto a meter to act as a pointer to read out the applied electric current. In CLSM, galvos are used in a reversed way: a known current is applied so as to deflect a light beam with a specific angle [140]. There are three main elements in a closed loop galvo system, the positioning actuator, the positioning detector and the closed-loop servo control electronics board. The positioning actuator is most commonly realised by a permanent magnet motor interacting with the magnetic field created by a current in a wire coil. This interaction results in a rotary torque and force on the actuator's rotor which is suspended on a set of bearings [141]. The actual angular position of the rotor is sensed and reported by the position detector, often realised optically involving a laser light source, a blocking element secured to the rotor and the photocell detection of the transmitted light. The final element, the servo circuitry compares the command position with the detected position and drives the actuator to minimise any discrepancies in a closed-loop fashion.

The focused beam can be scanned accurately in a rasterlike fashion through the specimen with an adjustable scan speed. One direction, (in this work the vertical direction) is scanned 100 to 1000 times faster than the other (horizontal direction). This enables 'digital zooming', a variable apparent magnification by scanning a smaller region more slowly. For example, decreasing the amplitude of the galvo movement by half and reducing the step size by a factor of two as well

while keeping the number of pixels in the image the same results in an apparent two-fold zoom into the specimen. Of great use is the ability to park the beam stably at a specific position on the sample by applying a constant voltage to the galvos and thus enabling point measurements. In AO applications, this allows for the optimisation of the entire image based on the improvement of a single pixel value, typically in the centre of the field of view [107, 142].

Telecentricity

In a scanning setup, the light traverses the optics mostly off-axis: a change of position in an object plane is realised by a change of angle in an aperture plane (Fig. 3.2a). This is achieved with a telecentric system in which two lenses are spaced the sum of their focal lengths apart such that the magnification depends only on the ratio of their respective focal lengths. Such systems are linear and space invariant; the lateral and longitudinal magnification are constant throughout the whole space and the shape of the PSF is independent of the absolute location of the point source [143]. Scan mirrors need to be positioned in planes that are optically conjugate to the back focal plane of the microscope objective, the primary telecentric plane. The scan system has pivot points at pupilary planes, where it is simplest to keep the beam collimated whereas the beam is focused in image planes and the object plane.

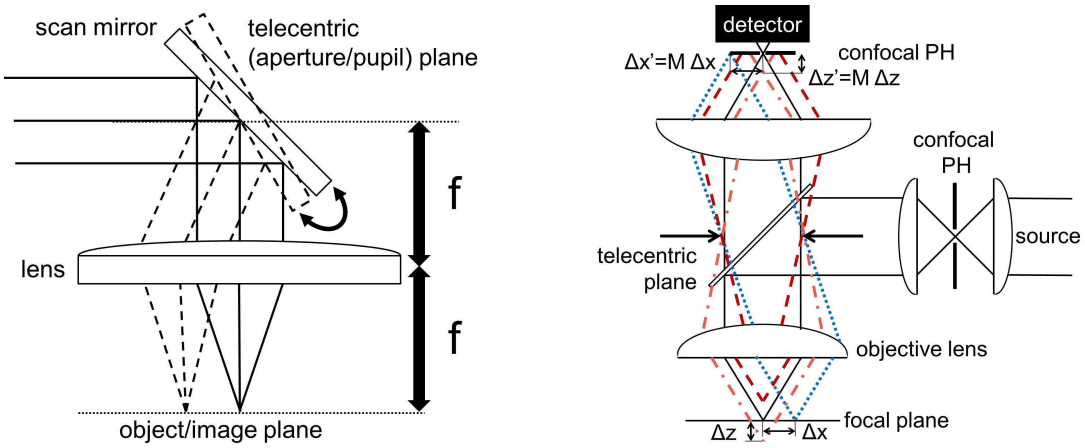

Figure 3.2: **(a)** Schematic of Telecentricity. **(b)** Confocal pinhole (PH). The beam must fill the back aperture of the objective lens, the primary telecentric plane, at all times and rotate around a point in this aperture plane to produce a corresponding translation of the focused spot in the object plane.

3.3.2 Pinhole

The pinhole in a CLSM prevents light originating from anywhere but the focal spot from reaching the detector (Fig. 3.2b). Light that is emitted from an area that is laterally displaced by Δx from the focal area (blue dotted line) is focused a distance $\Delta x' = M\Delta x$ from the pinhole, where M is the magnification of the system, such that it is effectively blocked from reaching the detector. Light that is emitted from an area that is axially displaced by Δz either above or below the focal plane (red dashed lines) is focused a distance $\Delta z' = M\Delta z$ before or after the pinhole such that it is effectively attenuated because only a small fraction can reach the detector.

The pinhole is mounted in an image plane and it is the image of the pinhole in the object plane that describes the area from which photons will be collected. Typically pinhole diameters of 1-2 Airy units are employed; a smaller diameter does not improve resolution, it just reduces the number of photons reaching the detector whereas a larger pinhole will smear the detection PSF over the pinhole's image in the object plane, a process that is described by the convolution of the detection PSF and the pinhole [41].

3.4 Aberration correction in CLSM

The relationship between the phase aberrations in the pupil plane and the final form of the PSF is complex. However, generally speaking, aberrations lead to a spreading of the focal spot. The fluorescence generation in a CLSM depends linearly on focal intensity but the imaging of this fluorescence onto the confocal pinhole is also affected by the same aberrations. Therefore CLSM signal levels are similarly affected by the degree of aberrations as TPEF (see section 5.4.2).

Illumination photons not reaching the sample are easily replaced as the available laser power is generally sufficient for biological applications. Fluorescent photons on the other side are valuable because they carry information bought at the price of causing photobleaching to the tissue. Therefore increasing the excitation power might restore signal levels by compensating for lower focal intensities but at the expense of phototoxic effects. The resolution, however, cannot be improved in this way but requires strategies for aberration compensation.

3.4.1 Refractive index mismatch

The transition between the cover glass and the specimen represents a dielectric interface at which the light will be partially reflected and partially refracted. The refracted light undergoes a change in phase and amplitude when passing through the interface resulting in an aberration of the wavefront and apodisation, respectively.

The effect of refractive index mismatch (RIM) on image quality has been investigated in numerous publications [144–147]. The effect of oil-immersion objectives focusing through a dielectric slab of lower refractive index on the spatial extent of the confocal volume has been investigated theoretically [148–150] and experimentally [151] exposing the problem of decreasing spatial resolution, dropping signal intensity and increasing focal shifts when the probing beam penetrates deeper parts of the object.

A rigorous examination using full vectorial electromagnetic theory has shown that the diffraction of light focused by a high NA lens from a first medium into a second medium with RIM is the origin of spherical aberrations (SA) [152–155]. Wiersma *et al.* derived an alternative theoretical description and found that moving the lens a distance d towards the interface does not result in an equal shift of the intensity profile. Only if $n_{\text{medium}} = n_{\text{sample}}$ does the peak follow the movement of the lens precisely. For $n_{\text{sample}} < n_{\text{medium}}$ the peak shifts less than the movement of the lens [156]. A comprehensive review of studies dating before 1998 is provided by Egener *et al.* [157].

A group of co-workers in Oxford show in a plethora of publications that SA reduce the high spatial frequency response of a confocal microscope [158]. They also show that the presence of very small amounts of SA are sufficient to produce a substantial degradation of the imaging performance and far more so in the axial than in the lateral direction. This asymmetric distribution along the optical axis of a high NA lens was predicted with full vectorial Kirchhoff theory by Visser *et al.* [159]. For high NA systems, this apodisation gives rise to an asymmetric axial response [160].

In Schwertner *et al.*, a different aspect of specimen induced aberrations is studied; defocus, tip and tilt, commonly referred to as geometrical distortions, introduce a significant three dimensional focal shift [60].

3.4.2 Compensation strategies

SA can be avoided by using water immersion objectives for imaging aqueous specimen and sometimes these objectives come with adjustable cover glass correction to allow for the usage of different cover glass thicknesses.

Several strategies have been suggested to compensate for SA in practice [161]. Sheppard *et al.* investigated the effect of varying the effective tube length by introducing a weak correction lens into the optical system, the position of which could be altered to vary the amount of correction provided [162]. Alternatively the reduction of the effective aperture of the objective has been shown to improve axial resolution at the expense of signal intensity as the effect of aberrations can become less strong for lower NA systems [163]. In Sieracki *et al.*, a two-level binary phase mask partially corrects for RIM induced SA improving axial resolution [164]. Compensation of SA by varying the refractive index of the immersion fluid and the thickness of the coverslip has also been proposed [165]. The drawback of these attempts however, is that they only statically correct for aberrations, the correction is not readily changed while imaging and potentially only applicable for lower order aberrations.

3.4.3 Adaptive optics

In 1992, O'Byrne *et al.* proposed a closed-loop AO setup to correct dynamically for SA [166, 167] and the potential benefits of such a correction were investigated theoretically by Booth *et al.* [30]. They found that simple aberration correction up to only third order SA is necessary to restore essentially diffraction limited imaging. The same group later reported the first adaptive aberration correction in a confocal microscope using a DMM and a modal wavefront sensor in a closed loop [33]. Demonstrations of AO have been made by several groups using a variety of techniques covering confocal microscopy [107, 168] and other imaging applications like 3D optical memory [169] and incoherent transmission microscopy [170]. In wide-field imaging techniques, AO has been successfully applied to structured light illumination [171], where a high-quality projection of a grid onto the sample is essential for the optical sectioning capability [172]. AO has also been used to extend the field of view at high resolution by addressing scan position dependent aberrations [173] and actively track and counteract sample movement [174, 175].

Chapter 4

AO in a CLSM System

Abstract In this chapter the design and implementation of a confocal laser scanning microscope (CLSM) is described. Another focus was the development of a software interface to control the beam scanning and subsequent image acquisition so that the direct integration of aberration correction was possible. Adaptive optics (AO) were incorporated in the form of a deformable membrane mirror (DMM) in double path modality, *i.e.* the DMM was passed twice, once by the illumination and once by the detected signal. The optimisations were performed with signal intensity as a merit factor using a random search algorithm (RSA). A dedicated LabVIEW program was implemented that provided an intuitive and simple, all-in-one interface to control the galvanometer movement, including parking of the beam, the mirror deformation, the RSA and the image acquisition. The program had to represent a versatile platform for system development and testing. The imaging properties of the CLSM were characterised with reflective samples in order to determine the lateral and axial resolution of the optical system and the AO system was tested by optimisations on reflective and photo-luminescent samples. Diffraction limited resolution was not restored and might require careful re-alignment of the optical system and a pinhole of different diameter. Improvements factors in signal intensity ranging from 1.2 to 8 fold could be achieved in both imaging modalities.

Acknowledgments Some of the samples used in this chapter were fabricated at the Institute of Photonics. The cylindrical micro-lenses, racetrack- and stripe waveguides and the nanocrystal composite have been kindly provided by Dr. Benoit Guilhabert and the microLED was kindly provided by Dr. David Massoubre. Dr. Simon Poland helped with the development of the scanning software.

Contents This chapter is structured as follows. In the first section the experimental conditions are covered, including the optical setup (subsection 4.1.1) which was operated in a reflection and a fluorescence modality and the galvo-based scanning system (subsection 4.1.2). The scanning system was custom built from individual components and operated with custom written software. The mapping of the DMM is described in subsection 4.1.3, and the samples under investigation in subsection 4.1.4. The section on experimental details concludes with the methodology of axial and lateral resolution measurements (subsection 4.1.5).

The original results obtained in these studies are presented in section 4.2. After discussing the calibration and characterisation of the CLSM (subsection 4.2.1), including the determination of the pixel pitch and the sampling frequency, some test trials are presented in form of images of various reflective samples (subsection 4.2.2). The resolution of the optical system is analysed for the lateral and axial direction in subsection 4.2.3 in terms of transfer function analysis. The outcome of optimisations performed on a reflective sample are detailed in subsection 4.2.4. The effect of the optimisation on signal intensity and resolution is analysed as well as repeatability of improvement by previously acquired DMM shapes. In subsection 4.2.5 optimisations performed on photoluminescence emitting quantum dots (QDs) are presented and the effects of photo-induced damage is also examined. This chapter finishes with a discussion (section 4.3) and the summary and conclusions given in section 4.4.

4.1 Experimental details

4.1.1 Optical setup

The optical setup, shown in Fig. 4.1, incorporates a custom built CLSM system and a DMM for aberration correction. A diode-pumped, solid-state laser source (Laser2000, SDL-532-500T) emitting at a wavelength of 532 nm is mounted at height on the optical bench and directed with a pair of beam-steering mirrors so as to enter a cage system (30 mm system, Thorlabs) perfectly centrally and on-axis. The cage system has been built from individual components to provide a housing for the galvo-based scanning system with a high degree of alignment accuracy. The laser beam is reflected downwards by a periscope mirror through a 4f re-imaging system (L1 & L2) that collimates the beam and expands its diameter to just fill the surface of the first galvo-mounted scan mirror.

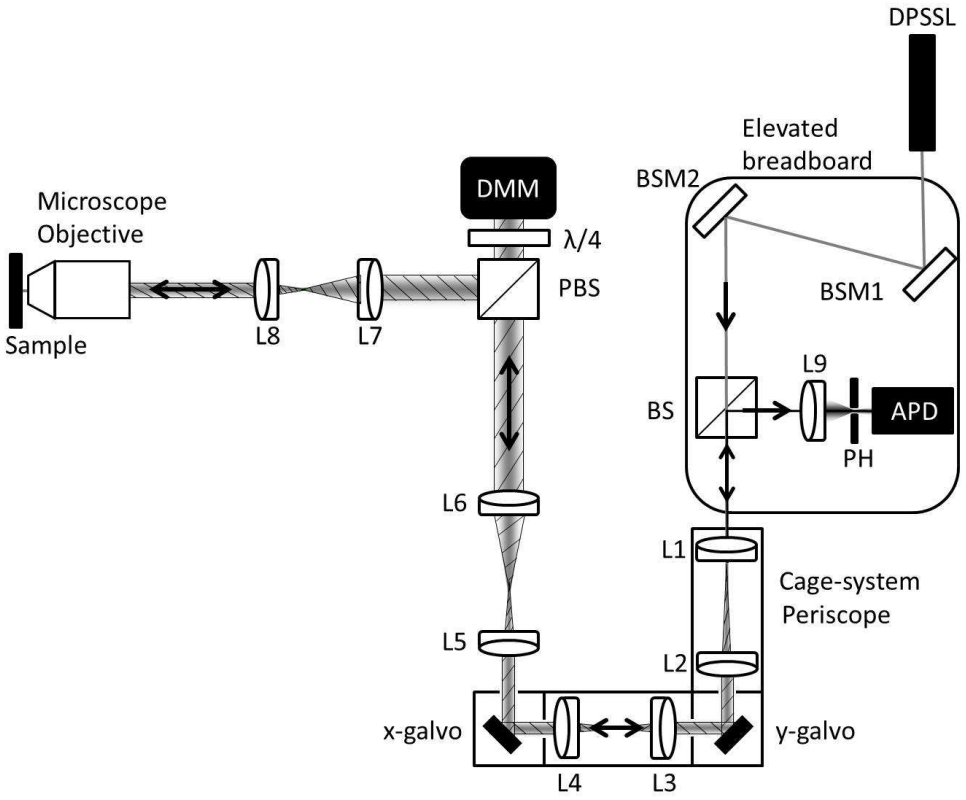

(a)

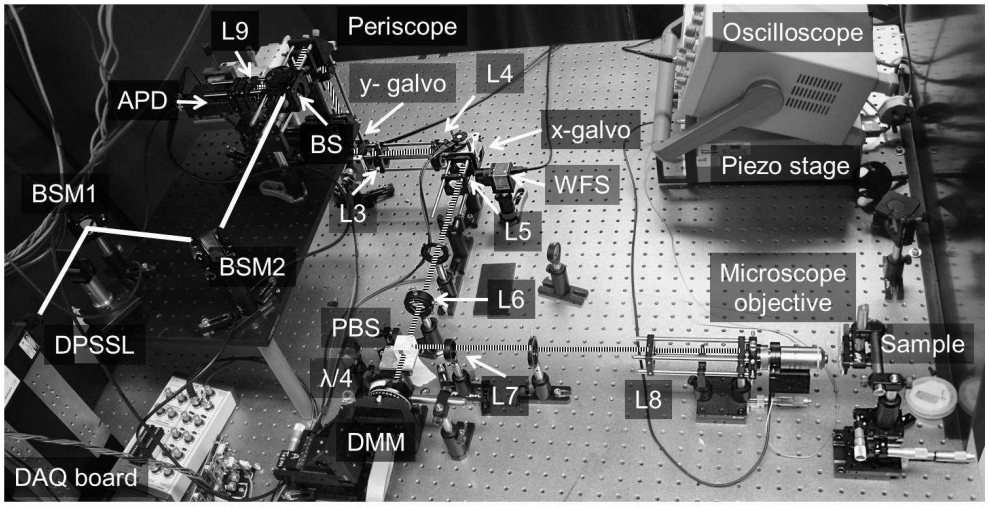

(b)

Figure 4.1: (a) Experimental setup of the confocal laser scanning microscope in a double pass configuration. DPSSL: diode-pumped, solid-state laser, BSM: beam steering mirror; BS: beam splitter; PBS: polarising beam splitter; $\lambda/4$: quarter waveplate; DMM: deformable membrane mirror. Relay lenses: L1 (f=50 mm), L2 (f=75 mm), L3 & L4 (f=50 mm), L5 (f=75 mm), L6 (f=175 mm), L7 & L8 (f=150 mm), L9 (f=30 mm). **(b)** Photograph of the optical setup.

This scan mirror deflects the beam to produce the vertical scan (y, fast scan) of the final image. A second telescope (L3 & L4) re-images the first scan mirror onto a second galvo-mounted scanning mirror located in an optically conjugate plane. The second mirror produces the horizontal scan (x, slow scan) in the final image. The telescope (L3 & L4) consists of achromatic doublets of equal focal lengths and therefore maintains beam diameter. Upon reflection of the second scan mirror, a third 4f re-imaging system (L5 & L6) expands the beam to match the active area of the DMM and also ensures that the second galvo and the DMM surface are in optically conjugate planes. According to Devaney *et al.* [74], 63 % of the actuated area of 15 mm of the OKO37 should be used as optical pupil in order to greatly enhance performance by having a ring of actuators outside the optical pupil, as this improves the correction of the pupil edge. Appropriate polarisation optics allow for an incident angle of 0° onto the DMM surface as described in more detail in the first chapter (section 8.1.1) of this thesis.

The DMM employed in this work (OKO37, Flexible Optical Technology former OKOtech) uses 37 hexagonal electrostatic actuators mounted underneath a thin silicon nitride membrane coated with a highly reflective aluminium layer. The DMM membrane can only be pulled towards the actuators therefore the DMM has to be employed in bias mode where half the driving voltage is applied to all actuators. In this way the DMM can create concave and convex shapes. The defocus which is introduce by this bias voltage is compensated by displacement of lens L7 in the 4f re-imaging system from its nominal position. More details on the DMM can be found in section 2.5.1 on p.24 of this work.

The DMM is re-imaged with a fourth 4f re-imaging telescope (L7 & L8) onto the back aperture of a microscope objective. Two plan fluor, dry microscope objectives have been employed in this work: a 20x 0.5NA lens with a working distance (WD) of 2.1 mm and a 40x 0.75NA with WD= 0.72 mm. Both objectives are infinity corrected and manufactured for use with a coverslip of thickness 0.17 mm (# 1.5) by Nikon. The objective is mounted on a piezoelectric z-translation stage (PI, E-662) and focuses the beam onto a vertically mounted sample. The translation stage is computer controlled through custom written LabVIEW software. The sample is mounted on a stage that allows for axial and lateral movement as well as tip and tilt. Two imaging modalities have been considered in this work, reflection and fluorescent mode. Both modalities are described in more detail in the next sections.

Reflection mode

In reflection mode, light is retro-reflected from the sample and collected by the microscope objective. On its return path the light passes again through the DMM and AO optics in a so-called double pass configuration. The light traces back its way to the cage system where it is descanned by both scan mirrors and eventually hits the BS which is mounted on the breadboard. The BS couples out a part of the signal by reflecting 50 % of light intensity towards a detector lens (L9) which focuses the light onto a 75 µm diameter confocal pinhole (PH). The PH effectively hinders out-of-focus light to reach the APD (Theoptics APD50) placed immediately behind it. The APD signal is displayed on an oscilloscope and read in by a data acquisition (DAQ) board (BNC-2110, National Instruments). The DAQ board is connected to a PC via a PCI card (NI PCI-6110, National Instruments). Communication with the DAQ board and signal manipulation is done with a custom written LabVIEW program.

Fluorescence mode

In fluorescence mode, a light emitting sample is used to generate signal. The wavelength separation between excitation and emission allows for a more efficient signal detection. The 50/50 BS is replaced with a dichroic mirror (565 nm short pass) that reflects the red-shifted fluorescence light while transmitting the green excitation light. Additionally, an emission filter (590 nm long pass) was placed in front of the APD to hinder any excitation light from bleeding through to the detector. The detector lens is replaced with an achromatic doublet of short focal length to ensure a tight focal spot on the confocal PH. The excitation filter is omitted due to the spectral purity of the excitation source. It should be noted that 50 % of the emitted fluorescence is lost by using the PBS as the fluorescence is randomly polarised. An alternative setup without polarising optics that employs reflection off the DMM at a slight angle instead could provide for more efficient detection of the emitted fluorescence.

4.1.2 Galvo-based scanning system

The concept of telecentricity was introduced in section 3.3.1 of this thesis. The telecentric planes and image planes in the CLSM setup are visualised in Fig. 4.2a. In a telecentric arrangement, a change in the incident angle on a lens results in

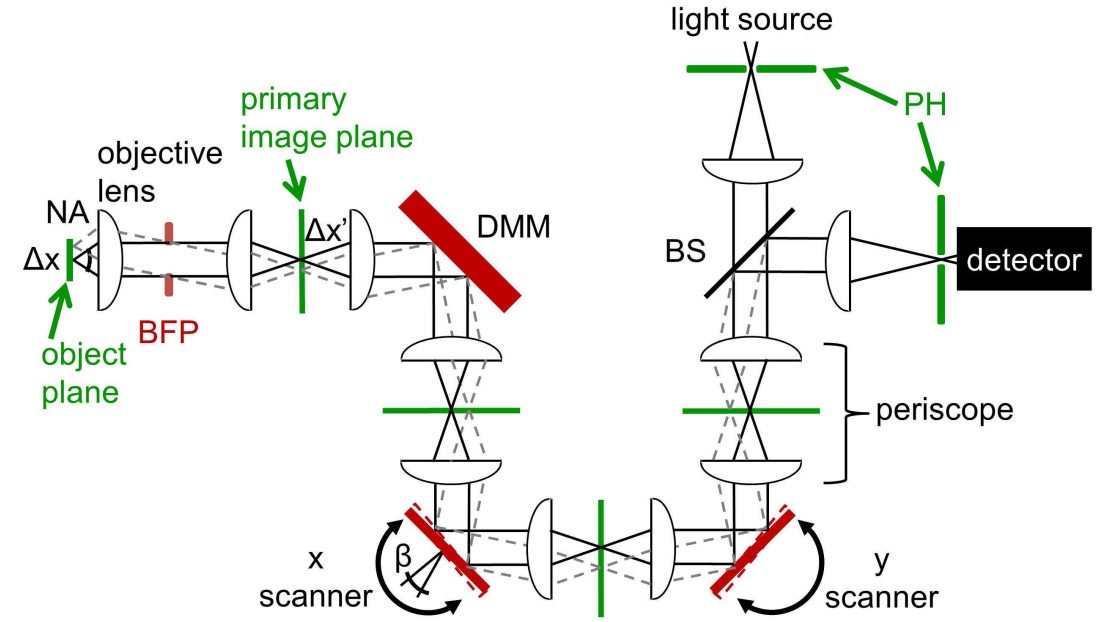

(a)

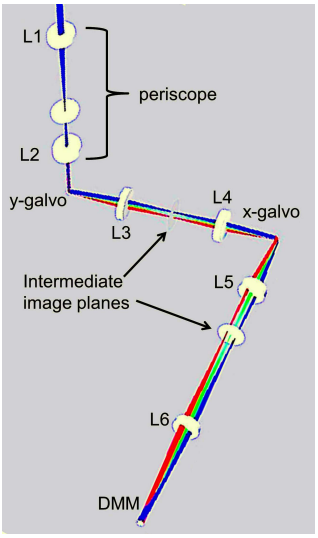

(b)

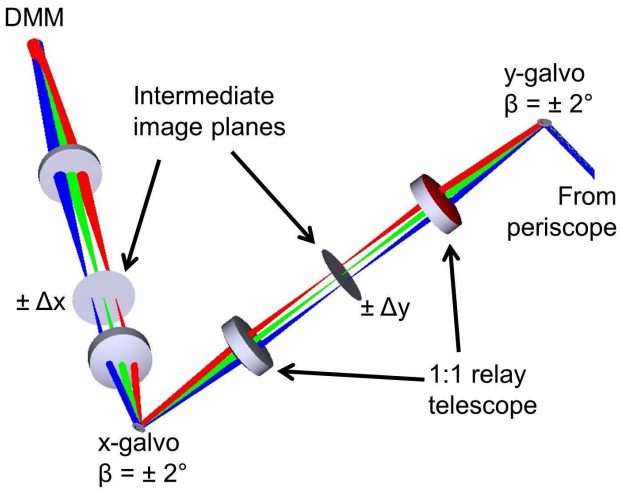

(c)

Figure 4.2: **(a)** Schematic of the telecentric and image planes in the CLSM. The distance between two adjacent image planes (green) or telecentric planes (red) was always four focal lengths. The back focal plane (BFP) of the microscope objective, the so-called primary telecentric plane, was re-imaged onto the DMM and both scan mirrors which were each positioned in conjugate telecentric planes with 4f re-imaging systems. The system is confocal because the light source, the focal point in the object plane and the detection pinhole are in conjugate image planes. **(b)** Zemax simulation of the telescope-conjugated scanning mirrors. **(c)** The scan mirrors were deflected by ±2°(red, blue) from the normal position (green).

the lateral translation of the focal spot of that lens (see Fig. 3.2a). In this way the rotation β of a scan mirror in a telecentric plane (red), sometimes also called a Fourier plane, causes a lateral displacement Δx of the focused spot in the object plane. A focal point in the object plane is re-imaged onto the primary image plane and any other conjugate image planes (green). For the system to be confocal, the point source, the focal spot in the object plane and the confocal PH placed before the detector have to been in conjugate image planes.

Relay scanner

There are two possibilities to implement a scanning system. In a close-coupled system, the scan mirrors are placed as closely together as possible in such a way that the geometric midpoint between them is in a conjugate telecentric plane. The disadvantage of this configuration is that both scan mirrors are only approximately telecentric. The alternative method, the relaying of one scan mirror onto the other with appropriate optics [176], was chosen in this work. Two achromatic doublets of equal focal length were combined in a 1:1 relaying telescope to form an image of the first mirror on the axis of the second mirror such that in an ideal arrangement both are in telecentric planes. More intermediate telescopes eventually form an image of both scan mirrors in the entrance aperture of the microscope objective where the scanning raster is generated. Figs 4.2b and 4.2c show a simulation with the ray-tracing software Zemax. The scan mirrors where rotated by $\pm 2^\circ$ creating the resulting deviations (blue and red) from the normal beam along the optical axis (green).

Galvanometers and servo boards

The scanning system consists of scan mirrors mounted on two different galvos, an analog and a digital galvo. This was due to the partner galvo of each set being broken. The digital galvo was chosen for the fast scan along the vertical (y-axis) while the analog galvo performs the slow scan (x-axis). The digital galvo (Model 6215H, Cambridge Technology) is of the moving magnet type with optical position detection for closed loop operation. It features up to 20° of mechanical rotation resulting in a deflection of the beam by up to 40°. It is addressed through a servo driver board (Position-Pro2, Cambridge Technology) that can also receive analog inputs. The scan mirror with an optical aperture of 5.8 mm is made of fused silica substrate with a high-reflective, protected silver coating.

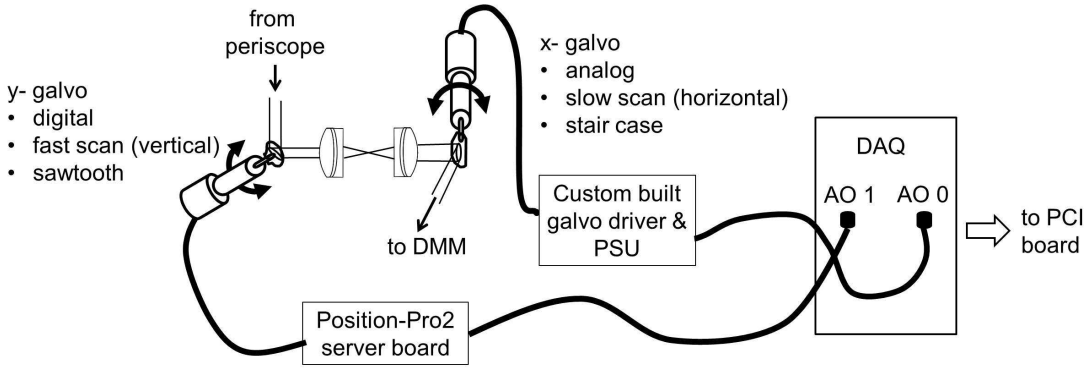

Figure 4.3: Schematic of the digital and analog galvos with associated boards. PSU: power supply unit, AO: analog output.

The analog galvo scanner (Model 6800HP, Cambridge Technology) is also of the moving magnet type with an optical position detector. The range of mirror position is quoted as 40°. The mirror is controlled by a custom built power supply unit and driver. The same DAQ board (BNC 2110, National Instruments) that is used to read in the signal intensity from the APD is also used to generate the driving signals for the galvos. Analog outputs (AO) 0 and 1 are connected through BNC cables with the custom built driver box in case of the analog galvo and with the Position-Pro2 driver board in case of the digital galvo. A schematic in Fig. 4.3 visualises the connections. A custom written LabVIEW program allows for the beam to be parked or for frames to be scanned at various digital zoom settings and is described in more detail in the following section.

Software control

A custom written LabVIEW program was developed in order to provide an intuitive interface to control the galvo movement, the mirror deformation, the RSA and the image acquisition from a single panel. The program initiates with the step generation for both galvos where the user inputs the number of fast axis points N_y, and the frequencies for the slow and the fast axis, f_x and f_y respectively. Other starting parameters include the starting position $-A$, amplitude A and DC offset O. From these inputs the program calculates the derived parameters, the number of slow axis points $N_x = {}^{f_y}/_{f_x}$, the stepping size $\delta = {}^{2A}/_{N_x}$ and the DAQ points per second $N_{DAQ} = N_x \cdot f_x$.

Table 4.1 lists the initialising and derived scanning parameters used to produce a 512 x 512 image and the typical values employed in this work. The fast scan is generated as an array of voltage values in a saw tooth pattern whereas the

Table 4.1: Scanning parameters to produce a 512 x 512 pixel image.

fast axis (y) freq.	[Hz]	f_y	128
slow axis (x) freq.	[Hz]	f_x	0.25
amplitude	[V]	A	1
starting position	[V]	$-A$	-1
DC offset	[V]	O	0
fast axis points		N_y	512
slow axis points		$N_x = {}^{f_y}/_{f_x}$	512
step size	[V]	$\delta = {}^{2A}/_{N_x}$	0.004
DAQ points/sec	[s^{-1}]	$N_{DAQ} = N_x \cdot f_x$	65,536

slow scan follows a simple staircase function. In a next step the voltage arrays are sent to the galvos and the signal intensity from the APD is read out in a synchronised manner so as to reconstruct the resulting image. Synchronisation of data acquisition and galvo scanning was achieved on the same DAQ board with pixel clock subroutines incorporated in LabVIEW. As the torque for the galvo is generally not identical in the forward and backward scan direction and, for ease of implementation, a uni-direction scan has been employed. The sawtooth pattern for the fast scan allows for a constant speed and uniform scan direction during data acquisition, and a swift backward scan at the expense of a reduced duty cycle, *i.e.* the proportion of the each full-frame scanning interval that is utilised to actually scan the specimen. Finally, the program allows for the image to be continuously displayed and saved on demand as a `.txt` file.

One of the advantages of single point galvanometric scanning is the ability to digitally zoom the image by decreasing the amplitude of the mirror deflection while maintaining the number of axis points in the scan image. The magnification provided by the confocal scanner is determined by the amplitude of the sawtooth y-scan and the staircase x-scan: for each increase in the digital zoom the amplitude of galvo oscillation and the step size was halved. In this way a smaller area on the specimen is sampled with the same amount of points resulting in an

Table 4.2: Parameters to digitally zoom while maintaining a 512 x 512 pixel image.

zoom	A [V]	$-A$ [V]	δ [V]
one	1.000	-1.000	0.0040
two	0.500	-0.500	0.0020
three	0.250	-0.250	0.0010
four	0.125	-0.125	0.0005

apparent zoom. The parameters for various digital zoom settings are given in Table 4.2. The effects of digital zooming on the sampling frequency of the CLSM according to the Nyquist criterion is discussed in more detail in section 4.2.1.

4.1.3 Mapping of the OKO37 DMM

The DMM was controlled using in-house built electronic boxes, originally developed for intracavity use in a laser system [100] and comprised of a 40-channel digital-to-analog converter linked to a 40-channel DC high voltage amplifier which were connected to a PC via a USB port. In order to map the 37 individual control channels for the 37 actuators, the maximum driving voltage, $U_c = 255\,V$ on an 8 bit scale, was individually and sequentially applied to each channel and the position of the corresponding actuator within the hexagonal pattern was determined with a volt meter on the backside of the mirror (Fig. 2.5a). Also indicated with red circles are rings of actuators that have been weighted with a Gaussian function to speed up the convergence of the optimisation algorithm. For example, the central actuator in ring 3 is selected more often than the 24 actuators in ring 0 located at the periphery of the actuated membrane (see also section 2.6.2).

4.1.4 Samples

The CLSM was tested in reflection and fluorescent modalities. In reflection mode, a test chart developed by the United States Air Force (USAF) was used as a sample with precise and known patterns to determine the resolution of the optical system. In fluorescence mode, a nanocomposite of quantum dots (QDs) was used to generate a photoluminescent signal.

USAF resolution test chart

The USAF resolution test chart is a pattern with increasing smaller features that dates back from 1951. It has since then been widely used to measure the resolving power of cameras and microscopes [178]. Each element consists of three vertical and three horizontal bars (Fig. 4.4a). The elements of each group have increasingly finer thicknesses and spacings and each group has increasingly smaller elements than the previous one. The entire pattern is self-repetitive in such a way that the groups containing the finer elements are placed in the centre of the groups containing the larger elements.

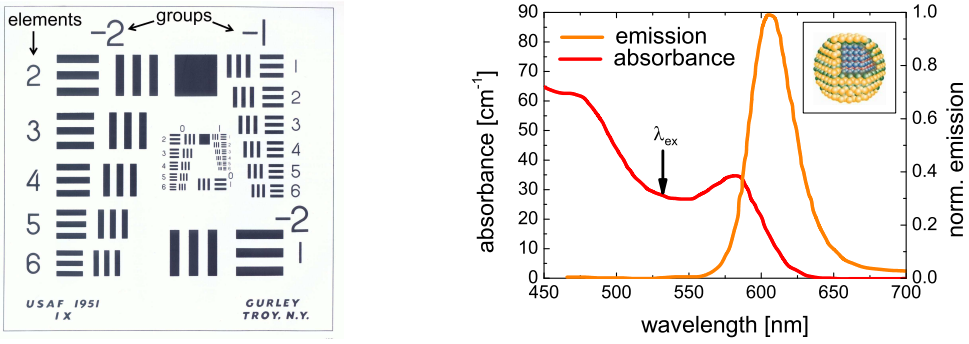

(a) **(b)**

Figure 4.4: **(a)** USAF resolution test chart pattern. Each element consists of three vertical and three horizontal bars with increasingly finer thicknesses and spacings. **(b)** Absorbance and emission spectrum of the NC nanocomposite films (taken from [177]). Inset: Schematic of a CdSe/ZnS core/shell quantum dot.

Nanocrystal composite

QDs nanocrystals (NC) have received a tremendous research interest in the past decades and now find applications in areas including selective biological labeling and optoelectronics. QDs are nanoparticles made up of a few thousand atoms and are composed of certain semiconductor crystals, here a CdSe core and a ZnS shell (Fig. 4.4b inset). In their colloidal form, they are suspended in a solvent, however, for many optoelectronic applications they are required to be in a film phase [179]. Commercially available mono-dispersed semiconductor NC color converters (Evident Technologies Inc.) were used for the formation of a nano-composite in a photocurable epoxy polymer [177]. The QDs exhibit narrow photoluminescence (emission peak at 610 ± 10 nm with a FWHM of 30 nm, Fig. 4.4b), sharp excitonic absorption and high quantum yields across the visible spectrum. A thin solid film of the host polymer containing the QDs was spin coated on a glass slide, kindly provided by Benoit Guilhabert, and used as a photoluminescent sample to test the CLSM in the fluorescent mode.

4.1.5 Methodology

Axial PSF measurements

A piezoelectric device with a range of 100 µm controls the z-position of the microscope lens. By scanning the objective in z-direction, whilst recording the intensity of the reflected beam detected by the APD, the axial point spread function (PSF)

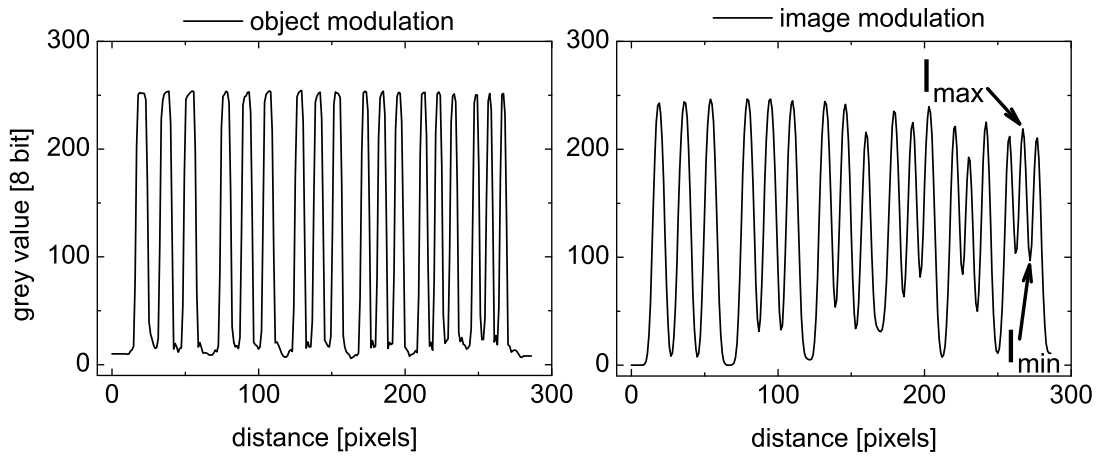

Figure 4.5: **(a)** Modulation of an object with increasingly higher spatial frequencies and **(b)** modulation of the resulting image taken with the CLSM.

was recorded. A Gaussian function was fitted to the data in OriginPro in order to determine the full-width-half-maximum (FWHM), a convenient measure for spatial resolution [163].

MTF measurements

Within a region of interest (ROI), the modulation of an image is a function of spatial frequency and can be defined as [44]:

$$m = \frac{I_{\max} - I_{\min}}{I_{\max} + I_{\min}}. \tag{4.1}$$

where, $I_{\max}$ and $I_{\min}$ are the maximum and minimum intensities in grey levels of that ROI. Assuming unity modulation in the object, the modulation in the image will decrease with increasing spatial frequency.

Fig. 4.5 shows the modulation of bars of increasingly smaller width from the USAF chart. For the object (a), modulation is only limited by the quality of fabrication of the pattern and the plot ranges from 0 to 255 even for the thinner bars. An 8 bit image of that object was taken with the CLSM and the modulation of the image is shown in (b). For the bars with smaller widths, the plot reaches neither 0 nor 255, such that the modulation in the source object is no longer faithfully reproduced in the image for higher spatial frequencies. At the cut-off frequency, modulation eventually decreases to zero and an image of that spatial frequency corresponds to a uniform grey patch. This can be graphically described by the modulation transfer function (MTF, Fig 4.6d) which states the modulation from unity at zero spatial frequency to the cut-off frequency of the

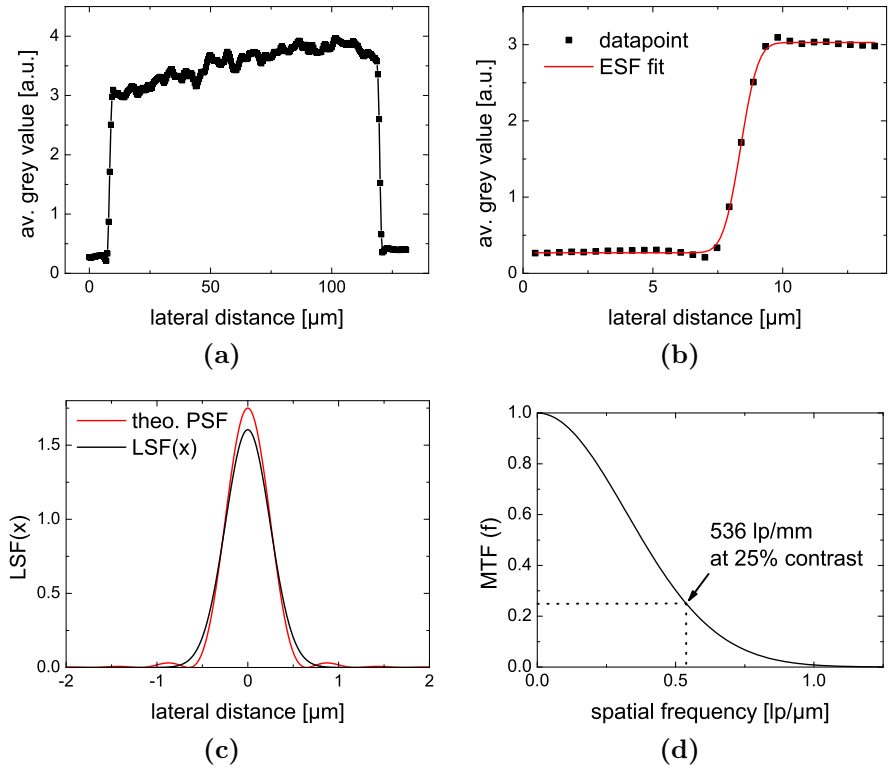

Figure 4.6: MTF measurements. **(a)** Intensity profile through a horizontal bar of the 2nd element in the 2nd group on the USAF test chart taken with the 20x objective and a digital zoom of two. **(b)** Fit of an analytical ESF function to the edge of the bar. **(c)** LSF computed with the fitting parameters for the ESF (black). Also shown is the theoretical PSF (eq. 2.7)(red). **(d)** MTF computed with the fitting parameters for the ESF. The spatial frequency at which the modulation has dropped to 25 % is used as the resolution limit.

system where the features become too small to be resolved and modulation drops to zero (eq.2.5).

In practice, the MTF is obtained by imaging a slit to obtain the line spread function (LSF) [46, 180]. The LSF is the response of the imaging system to a test device with a very narrow slit. The profile of the pixel values across the slit can be fitted by a weighted sum of Gaussian and exponential functions using a least squares fitting technique [181]. The MTF can be obtained by normalising the modulus of the Fourier transform of the analytical LSF function. The test device, however, is expensive to fabricate and difficult to align. Therefore an edge method is often employed in which a test device with a sharp, straight edge is imaged to obtain the edge spread function (ESF) (Fig 4.6). These test devices are more cost effective and less sensitive to physical imperfections. The MTF can be calculated through numerical differentiation of the ESF to obtain the

LSF [45, 182]:

$$\mathrm{LSF}_k(x) = \frac{\mathrm{ESF}_{k+1}(x) - \mathrm{ESF}_{k-1}(x)}{2\Delta x} \tag{4.2}$$

In this work, the edge method according to Boone *et al.* was employed to obtain the pre-sampled MTF [45]. The pre-sampled MTF includes the effect of aperture blurring but does not take aliasing effects due to the discrete sampling of an analogue signal into account (see also p.16 this thesis). In Fig 4.6 the image of a horizontal bar of the second element in the second group on the USAF chart was taken with the 20x objective with a digital zoom of two. The edge intensity profile was extracted with ImageJ (a) and fitted to an analytical ESF function in OriginPro (b). The analytical function and the fitting parameters that were used to fit the ESF are given in detail in appendix B.

By substituting those fitting parameters into analytical functions the LSF and MTF were computed. The corresponding LSF is plotted in (c) as well as the theoretical PSF $p(u, v) = \frac{2J_1^2(v)}{v^2}$ where J_1 denotes the first order Bessel function of the first kind and v is the normalised transverse optical unit with $v = \frac{2\pi}{\lambda} r\mathrm{NA}$. Both the LSF and the PSF are normed to give unity area. The ESF was adequately fitted by an error function and therefore the LSF is given by a Gaussian function. The MTF (d) can be used to assess the resolution of the optical system over the entire range of spatial frequencies and therefore gives a more detailed picture of system performance than just comparing a single value of spatial resolution to its diffraction limited counterpart. It is common to use the spatial frequency at which the image modulation has dropped to 25 % as the resolution limit.

4.2 Results

4.2.1 Calibration of the system

Pixel size

In order to calibrate the scanning system, a bar of known width on the USAF chart was imaged with both objectives for a range of digital magnification settings (one to three, see Table 4.2). The text image was imported into ImageJ and rotated such that the edge of the reflective bar ran vertically through the image. The images were rotated by a maximum of 2.68°. This corresponds to a cross talk of approximately 3 % between the calibration for the two lateral directions.

Table 4.3: Pixel pitch Δ [µm/pixel] for both microscope objectives for various digital zoom settings (one to three). $\divideontimes$: extrapolated value.

	20x, 0.5NA			40x, 0.75NA		
zoom	Δ_{hor}	Δ_{ver}	FOV [µm^2]	Δ_{hor}	Δ_{ver}	FOV [µm^2]
one	0.93	1.01	476 x 517	0.47	0.50	241 x 256
two	0.47	0.50	241 x 256	0.23	0.25	118 x 128
three	0.23*	0.25*	118 x 128	0.12*	0.12*	64 x 64

A ROI containing the bar along the entire height of the image was selected and the line profile imported into OriginPro. From this line profile the number of pixels needed to image the known width of the bar was determined. Table 4.3 lists the scaling ratios for both objectives for various zoom settings. Here, the $\divideontimes$ symbolises a imaging ratio that was extrapolated from the previous values rather than being experimentally measured. An experimental measurement was not possible as the width of the bar was too large to be imaged in the field of view with higher zoom settings.

For the 20x, 0.5NA objective, bars from the second element of the second group with a width of 111.36 µm were imaged (Figs. 4.7a and 4.7b). Figs 4.7e and 4.7f show the same bars imaged with a digital zoom of two. The bright circular patch indicates that the FOV is not evenly illuminated for this objective, which is possibly due to a slight change in the size of the back aperture compared to the 40x objective. More likely, the beam size is slightly too large for the

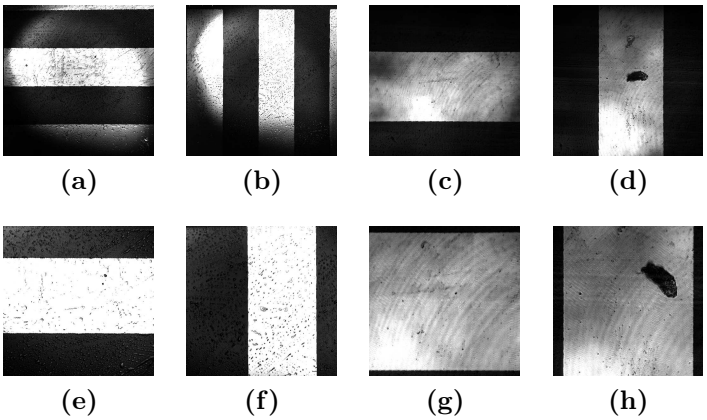

Figure 4.7: Calibration of the 20x microscope objective with a bar of 111 µm width **(a)** horizontally and **(b)** vertically with digital zoom of one, **(e)** horizontally and **(f)** vertically with zoom two. The 40x objective was calibrated with a bar of 99 µm width **(c)** horizontally and **(d)** vertically with digital zoom of one, **(g)** horizontally and **(h)** vertically with a zoom of two.

Table 4.4: Derived Nyquist frequencies f_N [μm^{-1}] for both microscope objectives at various digital zoom settings.

	20x, 0.5NA		40x, 0.75NA	
zoom	f_N^{hor} [μm^{-1}]	f_N^{ver} [μm^{-1}]	f_N^{hor} [μm^{-1}]	f_N^{ver} [μm^{-1}]
one	0.54	0.50	1.08	1.01
two	1.07	1.00	2.16	2.00
three	2.14^*	1.99^*	4.32^*	4.01^*

aperture of the scanning mirrors which leads to clipping at high angles. For the 40x, 0.75NA objective, bars from the third element of the second group (99.21 µm width) were imaged (Figs 4.7c and 4.7d). Figs 4.7g and 4.7h show the same bars imaged with a digital zoom of two. From those calibrations the field of view (FOV) for images containing 512 x 512 pixels was calculated for various digital zoom settings and is also given in Table 4.3.

Sampling frequency

The Nyquist frequency is dependent on the digital zoom setting and is given in eq. 2.14 as:

$$f_N = \frac{1}{2\Delta} \tag{4.3}$$

where Δ is the pixel pitch. In order to avoid aliasing of the analog signal the Nyquist frequency should be equal to the highest frequency expected to be present in the object. The smallest spatial distance that can be resolved in the microscope is the radius of the Airy disk associated with the PSF of a diffraction limited focal spot. The frequency corresponding to this radius, here termed Rayleigh frequency, is given by $f_R = \frac{\mathrm{NA}}{0.61\lambda}$. For the 20x objective $f_R^{20x} = 1.54\,\mu m^{-1}$ and $f_R^{40x} = 2.33\,\mu m^{-1}$ for the 40x.

Table 4.4 lists the Nyquist frequencies derived from the pixel pitch for both microscope objectives at various digital zoom settings. When comparing these values to the Rayleigh frequency for each objective it can be deduced that for the 20x objective some aliasing of higher frequency might occur for the digital zoom settings of two, whereas the digital zoom setting of three allowed for sampling well above the Rayleigh frequency. For the 40x objective, the digital zoom setting of two allowed for sampling which is very close to the Rayleigh frequency. Aliasing of high frequencies had to be expected for both objectives if a digital zoom of one was applied.

(a) **(b)** **(c)**

Figure 4.8: Visual confirmation that the scan was not distorted and reproduced accurate images. **(a)** Image of the number "2" labeling the second element (of the second group) on the USAF chart taken with the 20x objective. **(b)** Image of the number "3" labeling the third element (of the second group) taken with the 40x objective. **(c)** Image of the smallest elements of the smallest groups (6 and 7) taken with the 40x objective.

4.2.2 Trials

Fig. 4.8 shows a simple test to ascertain that the scanning did not introduce any distortions. The image of the "2" labeling the second element in the second group was taken with the 20x, 0.5NA objective and the "3" labeling the third element of the second group was taken with the 40x, 0.75NA objective. The image in (c) shows the smallest elements of the two smallest groups, 6 and 7, on the USAF chart and was taken with the 40x objective. Even the smallest bars of element 6 in group 7 could be resolved. The largest bar that cannot be resolved determines the resolution of the imaging system according to Resolution [lp/mm] $= 2^{\text{group}+\frac{\text{element}-1}{6}}$. This means the USAF test chart had not sufficiently small features to directly measure the resolution of the system and the resolution of the CLSM is at least 228 lp/mm for the 40x objective. The image of group 7 shown in (c) was the basis for the data shown in the image modulation graph in Figure 4.5.

Various other reflective test samples were imaged with the 40x objective (Fig. 4.9). Panel (a) depicts an InGaN/GaN microLED with a diameter of 160 µm. In (b) an array of cylindrical HTP2 microlenses is shown. HTP2 is an epoxy functionalised carbon based material that is transparent in the deep UV. Using self alignment methods, the polymer can be shaped into lenses [179]. The cylindrical lenses in (b) had a spacing of 24 µm. HTP materials can be used for focusing or waveguiding of UV light. The stripe and racetrack waveguides (shown in (c) and (d)) also made from HTP2 polymer had a width of 21.6 µm and 136.5 µm respectively.

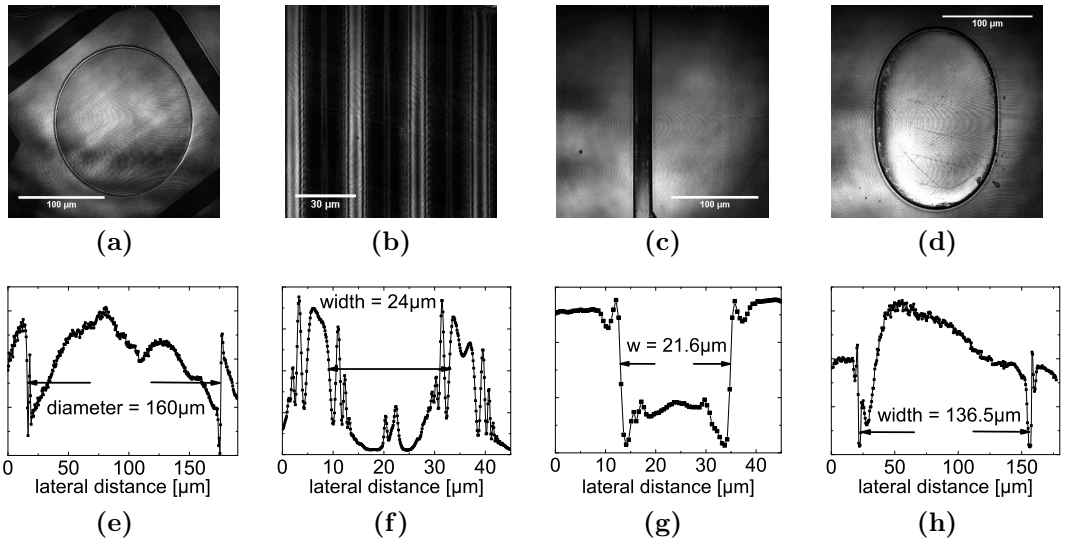

Figure 4.9: Test imaging with the 40x objective of various reflective samples. **(a)** InGaN/GaN µLED, kindly provided by Dr. Massoubre. **(b)** cylindrical HTP2 microlens array with a spacing of 24 µm, kindly provided by Dr. Guilhabert. **(c)** Stripe and **(d)** racetrack waveguide made from HTP2 polymer. **(e-h)** Lateral intensity profiles in arbitrary units across the structures above.

4.2.3 Resolution of the system

Lateral resolution

The resolution of the CLSM was assessed firstly by determining the FWHM of the LSF which was derived from ESF measurements and secondly, the MTF was computed either by parametrisation of an analytical function for the ESF or by directly calculating the modulus of the FT of the LSF/PSF and normalising the curve (see methodology section 4.1.5 for details).

For confocal microscopy, the minimum separation of two bright, resolved objects is given by eq. 3.2:

$$\Delta r_{\mathrm{conf}} = 0.72 \cdot r_{\mathrm{Airy}} = 0.44 \frac{\lambda}{\mathrm{NA}} \tag{4.4}$$

where r_{Airy} is half the diameter of the Airy disk. For the objectives used in this study, the theoretically expected values are $\Delta r_{\mathrm{conf}}(20x, 0.5\mathrm{NA}) = 0.47\,\mu\mathrm{m}$ and $\Delta r_{\mathrm{conf}}(40x, 0.75\mathrm{NA}) = 0.31\,\mu\mathrm{m}$. A convenient measure for spatial resolution is provided by the FWHM of a PSF acquired by the imaging from sub-resolution beads or straight edges. The FWHM of the PSF is related to the separation described above by

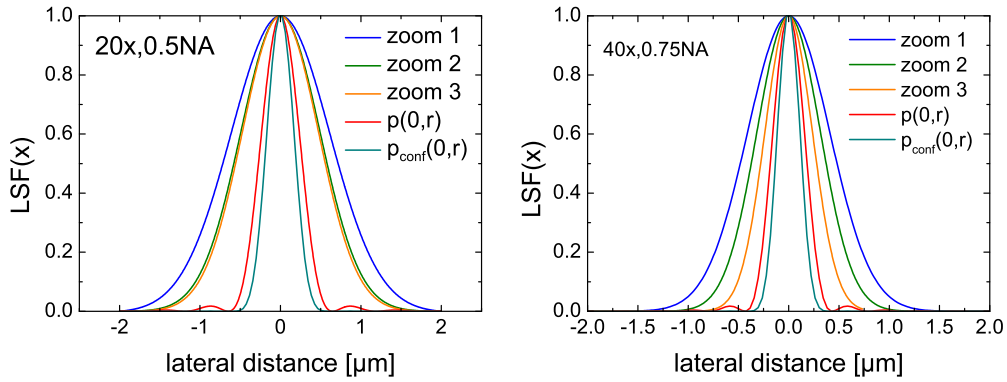

Figure 4.10: Line spread functions for the 20x **(a)** and the 40x **(b)** microscope objective for various digital zoom settings. For the 20x objective Nyquist sampling is observed with a digital zoom of 2.54 and for the 40x objective this value is 2.33. The functions $p(0,r)$ and $p_{conf}(0,r)$ are the lateral PSF in the focal plane for the single lens and the confocal case respectively.

$$\Delta r_{\text{conf}} = 0.66 \cdot \text{FWHM}. \tag{4.5}$$

Therefore the theoretically expected value for the FWHM of a diffraction limited confocal PSF is $\text{FWHM}_{\text{conf}}$ (20x, 0.5NA) = 0.71 µm and $\text{FWHM}_{\text{conf}}$ (40x, 0.75NA) = 0.47 µm.

Figure 4.10 shows the LSF for various zoom settings for the 20x objective (a) and the 40x objective (b) that were calculated from fitting the ESF to an analytical function (appendix B). Both graphs show the LSFs which were deduced from images taken with a digital magnification of one (blue), two (green) and three (orange) as well as the theoretically expected LSF for the case of a single lens (red) and confocal imaging (dark cyan). The theoretical PSFs for the case of a single lens and confocal imaging are given by eqs. 2.7 and 3.1 respectively. These functions are given only as an approximate measure of diffraction limited resolution as they are derived for a single lens only. The LSF of an entire optical system is likely to be broader.

For the 20x objective, the LSF deduced from the image of an edge taken with a digital magnification of one (blue) is reduced by doubling the sampling rate by increasing the digital magnification to two (green). Structures like edges contain high frequency components that are more faithfully reproduced when the Nyquist frequency is observed for sampling. Further increasing the digital magnification to a factor of three (orange) does not lead to a further major improvement in

Table 4.5: Lateral resolution for the 20x,0.5NA objective and the 40x,0.75NA objective in terms of the FWHM of the LSFs.

	20x		40x	
zoom	FWHM [µm]	theo. [%]	FWHM [µm]	theo. [%]
one	1.44	203	0.96	204
two	1.16	163	0.75	160
three	1.12	157	0.56	119

resolution because the Nyquist frequency is already nearly observed in the previous (green) case. The disparity between the orange LSF and the theoretically expected LSF is now purely due to the misalignment of the optical system which caused the CLSM not to be diffraction limited.

The CLSM was then re-aligned to try and bring it closer to diffraction -limited performance and then tested with an objective of higher NA with 40x magnification. The FWHM of the LSF could be improved (Fig. 4.10b) but the system was still not operating at its diffraction limit. Again increasing the sampling frequency to observe the Nyquist criterion improved spatial resolution.

The FWHM of the LSFs in the lateral directions with the 20x,0.5NA and the 40x,0.75NA microscope objectives are listed in Table 4.5 where the second and fourth column give the percentage of the theoretically expected value. For the 40x objective the diffraction limit is almost reached (119 %) for a digital zoom of three.

In Figure 4.11 the MTFs for both objectives and various digital magnification settings are shown. The MTFs were calculated by inserting the parameters from the ESF fitting into an analytical function (appendix B). In the case of the 20x objective (a) the MTF was also calculated by using the OriginPro fast Fourier transform (FFT) of the LSF and calculating the modulus for complex numbers: $|x + iy| = \sqrt{x^2 + y^2}$ of that transform. This function was then normed to unity to yield the MTF and is shown with closed symbols almost underlying each respective solid line. This confirmed the accuracy of the method using the analytical function hence this double check has been omitted for clarity for the case of the 40x microscope. Also indicated in both graphs is the frequency relating to the smallest, diffraction-limited resolvable feature in the image, termed Rayleigh frequency f_R which is the correspondent to the radius of the Airy disc in the frequency domain.

The equivalent of the Rayleigh criterion for resolution in transfer function

Table 4.6: Spatial frequencies at which image modulation dropped to 25 % for both microscope objectives and various digital magnification settings.

zoom	20x,0.5NA f [μm^{-1}]	40x,0.75NA f [μm^{-1}]
one	0.43	0.65
two	0.54	0.80
three	0.56	1.12
sgl. lens	1.20	1.81
conf.	1.62	2.44

analysis is commonly taken to be the spatial frequency at which image modulation dropped down to 25 %. These values were extracted from Fig. 4.11 and are listed in Table 4.6. Also listed are the extracted values for the single lens PSF and the confocal PSF.

Axial resolution

Two equally bright points on the optically axis separated by:

$$\Delta z_{\text{conf}} = 1.5 \frac{n\lambda}{\text{NA}^2} \tag{4.6}$$

are resolved, where n is the refractive index of the immersion medium (eq.3.3). The theoretical values for the two objectives used in this work are Δz_{conf} (20x,

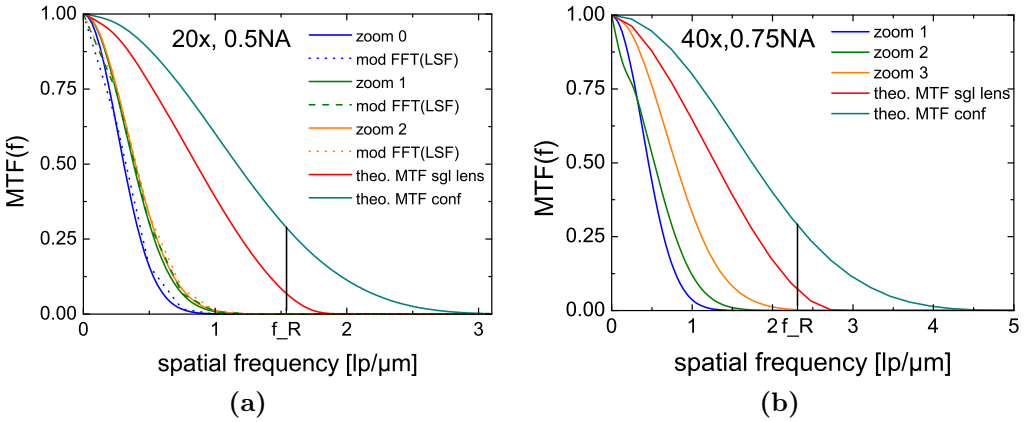

Figure 4.11: MTFs **(a)** for the 20x either from fitting to an analytical ESF (lines) or computation by taking the modulus of the fast Fourier transform (FFT) of the LSF (closed symbols) and **(b)** for the 40x microscope objective for various zoom settings. The theoretical MTF for the single lens and confocal case are also shown. The spatial frequency f_R corresponding to the radius of the Airy disk is also indicated.

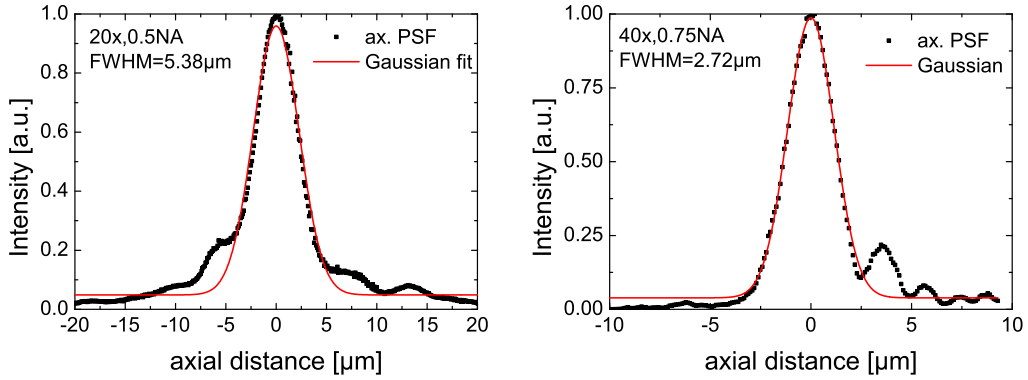

(a) **(b)**

Figure 4.12: Axial resolution in terms of the FWHM of the intensity response function for the 20x **(a)** and the 40x **(b)** microscope objective.

0.5NA) = 3.19 µm and Δz_{conf} (40x, 0.75NA) = 1.42 µm. The FWHM of a Gaussian fit is related to this distance through eq. 3.4:

$$\Delta z_{\text{conf}} = 1.19 \cdot \text{FWHM} \tag{4.7}$$

The expected theoretical values are $\text{FWHM}_{\text{conf}}$ (20x) = 3.80 µm and $\text{FWHM}_{\text{conf}}$ (40x) = 1.69 µm for the 20x and the 40x objective respectively.

Fig. 4.12 shows the axial intensity response functions for both microscope objectives (black squares). The red lines indicate the fitting of a Gaussian function to the data and the insets state the FWHM of this fit. Both functions have been normalised to unity. For the 20x objective the FWHM was measured as $\text{FWHM}_{20x} = 5.38$ µm (142 % of the theoretical value). After re-alignment the axial response function for the 40x objective was measured as $\text{FWHM}_{40x} = 2.72$ µm (161 % of the theoretical value) and showed the influence of strong aberrations in form of several side lobes on the distal side.

4.2.4 Optimisation in reflection mode

The outcome of three optimisations performed on the signal retro-reflected from the USAF test chart using the 40x microscope objective for optimisation and imaging are presented in the following. The beam was parked by sending zero voltage commands to both galvos and signal intensity from that position was used as a merit factor (MF). It is assumed that the optimisation on a reflective surface leads to a DMM shape that mainly corrects for system-induced aberrations. This hypothesis was tested by applying an optimised DMM shape from the previous

day to a different area on the USAF test chart and analysing the repeatability of improvement in signal intensity and resolution. After re-aligning the optical system another optimisation was performed.

Improvement in intensity and resolution

Figure 4.13 shows the improvement achieved with an optimisation that was performed on the reflective square on the USAF test chart. The ROI which was used to extract the lateral intensity profile in ImageJ is indicated in 4.13a. The lateral intensity profile across the edge averaged over the height of the ROI is depicted in 4.13b. An error function was fitted to the data and subsequently differentiated to obtain the associated Gaussian function. The amplitude and FWHM of this Gaussian function were taken as a mean of comparing the intensity and resolution of the images before and after optimisation. The intensity after optimisation was improved by a factor of 1.40 whereas the FWHM was reduced to 86 % (from 1.62 µm to 1.39 µm) with the optimised DMM shape.

Fig. 4.13c shows the improvement in axial resolution. The axial intensity response function was measured for both the optimised and the bias mirror shape and a Gaussian was fitted to the main peak. The insets in the graph state the FWHM of this fit. For the bias mirror shape the FWHM was 9.32 µm. This value was decreased to 83 % (7.71 µm) with the optimised DMM shape. The peak intensity was improved by a factor of 1.62 (from 1.14 a.u. to 1.85 a.u.). In both cases the axial intensity response function showed considerable aberrations in form of side lobes on the distal side.

The optimisation graph where the improvement in MF (signal intensity) is plotted against the iteration number is given in Fig. 4.13d. This particular optimisation ran for $\approx$ 3500 iterations and improved the MF from a starting value of 1.4 V to 2.2 V (improvement of 157 %) at iteration 2995. The optimised DMM shape and the underlying actuator map indicating the applied control voltages for each actuator are shown in Fig. 4.13e. An analysis of the control voltages applied to each single actuator of the optimised DMM shape showed that the DMM was not running out of stroke. The mean control voltage applied to actuators (U_c on an 8 bit scale) was $U_c^{mean} \approx 126 \pm 33$ V within a range of U_c^{min}=35 V and U_c^{max}=247 V.

On another day, the validity of this optimised DMM shape was tested for repeatability. Fig. 4.13f shows the elements of group 7 on the USAF test chart

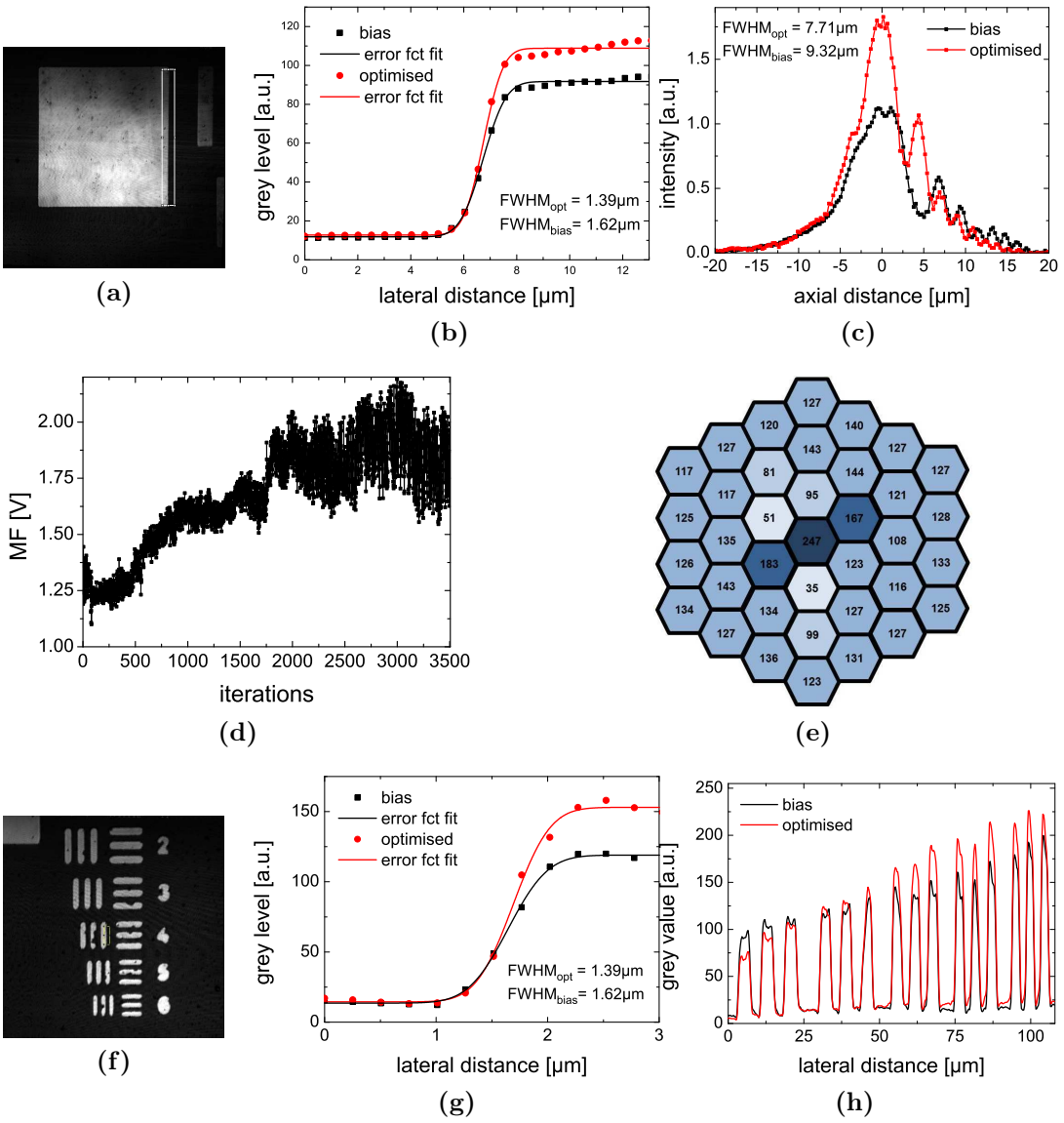

Figure 4.13: Optimisation on a reflective target. **(a)** Reflective square on the USAF test chart and the ROI considered in the lateral intensity profiles. **(b)** Lateral intensity profile through the edge before and after optimisation and fit with an error function (lines). The insets state the FWHM of the Gaussian associated with the error function. **(c)** Axial resolution in terms of the FWHM of the intensity response function before and after optimisation. Both functions show considerable aberrations in form of side lobes. **(d)** Optimisation graph giving the improvement in MF (signal intensity) with iteration number. **(e)** Voltage map of the optimised DMM shape. **(e)** Repeatability of optimised DMM shapes. Image of the elements of group 7 on the USAF test chart after optimisation and the ROI considered. **(f)** Lateral intensity profile across the edge indicated in the ROI (closed symbols) and the fit with an error function (lines). The insets state the FWHM of the Gaussian functions associated with the respective error functions. **(g)** Modulation in the image before and after optimisation across the elements 2-6 of group 7.

that have been imaged with the 40x microscope objective with a digital magnification of two. In 4.13g the FWHM was again reduced to 86 % (from 1.62 µm to 1.39 µm) and the amplitude was increased by a factor of 1.41 with the optimised DMM shape. The image modulation of the horizontal elements 2-6 in group 7 is shown before optimisation and after optimisation in 4.13h. For the higher spatial frequencies, the modulation was increased with the optimised DMM shape.

Realignment

Figure 4.14 shows the outcome of a different optimisation that was also performed on the reflective square on the USAF test chart after a re-alignment of the optical system. The ROI which was used to extract the lateral intensity profile in ImageJ is indicated in the image taken before optimisation (a, top) while the image taken with the optimised DMM shape is shown in (a, bottom). The lateral intensity profile across the edge averaged over the height of the ROI is depicted in Fig. 4.14b. Again an error function was fitted to the data and subsequently differentiated to obtain the associated Gaussian function. The intensity after optimisation was improved by a factor of 7.97 whereas the FWHM was diminished to 77 % (from 0.95 µm to 0.73 µm) with the optimised DMM shape. Fig. 4.14c shows the improvement in axial resolution. The axial intensity response function

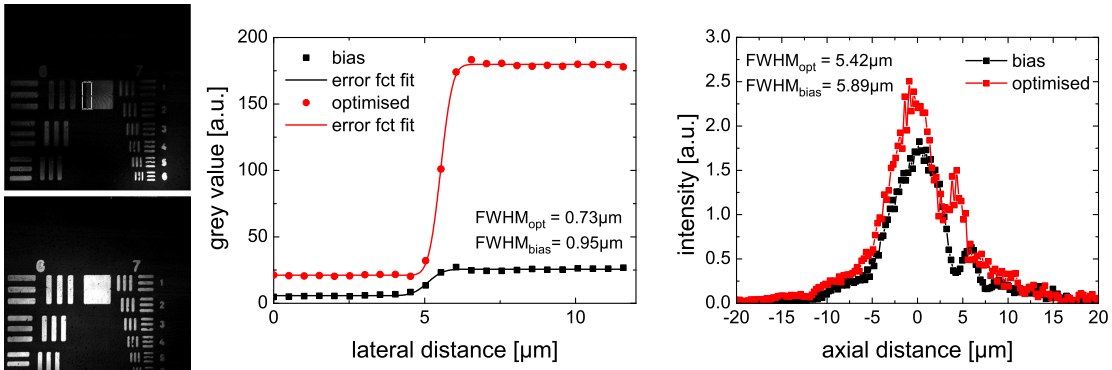

(a) **(b)** **(c)**

Figure 4.14: Optimisation on the centre of the reflective square. **(a)** The USAF test chart before (top) and after optimisation (bottom) including the ROI considered in the intensity line profiles. **(b)** Lateral intensity profile through the edge (closed symbols) and fit with an error function (lines). Insets: FWHM of the associated Gaussian functions. **(c)** Axial intensity response function. The line serves as a guide to the eye. Insets: FWHM of the Gaussian functions fitted to the main peaks before and after optimisation.

was measured for both the optimised and the bias mirror shape and a Gaussian was fitted to the main peak. The insets in the graph state the FWHM of this fit. For the bias mirror shape the FWHM was 5.89 µm. This value was decreased to 92 % (5.42 µm) with the optimised DMM shape. The peak intensity was improved by a factor of 1.37 (from 1.86 a.u. to 2.55 a.u.). In both cases the axial intensity response function showed considerable aberrations in form of side lobes on the distal side.

The signal to noise ratio (SNR) in decibels of a noisy edge image can be calculated with [183]:

$$\mathrm{SNR} = 20 \log \left(\frac{2(\mu_b - \mu_d)}{\sigma_b + \sigma_d} \right) \tag{4.8}$$

where μ_b and μ_d are the mean grey value of a ROI containing the bright and dark side respectively and σ_b and σ_d are the standard deviation of those ROIs. Using this equation the SNR was improved by a factor of 1.86 (from 12.60 dB to 23.38 dB) with the optimised DMM shape.

4.2.5 Optimisation on a fluorescent sample

In order to test the CLSM in fluorescent mode, the 50/50 beam splitter cube was replaced with a dichroic mirror and an emission filter was inserted into the setup as described earlier in section 4.1.1. All optimisations were performed with the 40x microscope objective on the nanocomposite containing the QD nanocrystals. The outcome of two optimisation on the edge of the polymer containing the QDs is shown in the following section. Optimisations were also attempted on a sample of *convallaria* (see p.97 this thesis), however, the amount of photobleaching occurring made the MF too unstable to optimise on despite the bleaching compensation algorithm. Photo-induced damage is qualitatively considered in the last section.

Improvement in intensity and resolution

Figure 4.15 outlines the outcome of two optimisation that were performed on the photoluminescence emitted from QDs as a MF. The MF was improved from a starting value of 0.14 V by a factor of 1.39. The optimisation was left running for 597 iterations, 143 of which were successful and the best DMM shape occurred at iteration 494. The image of an in-house fabricated polymer containing QDs spin

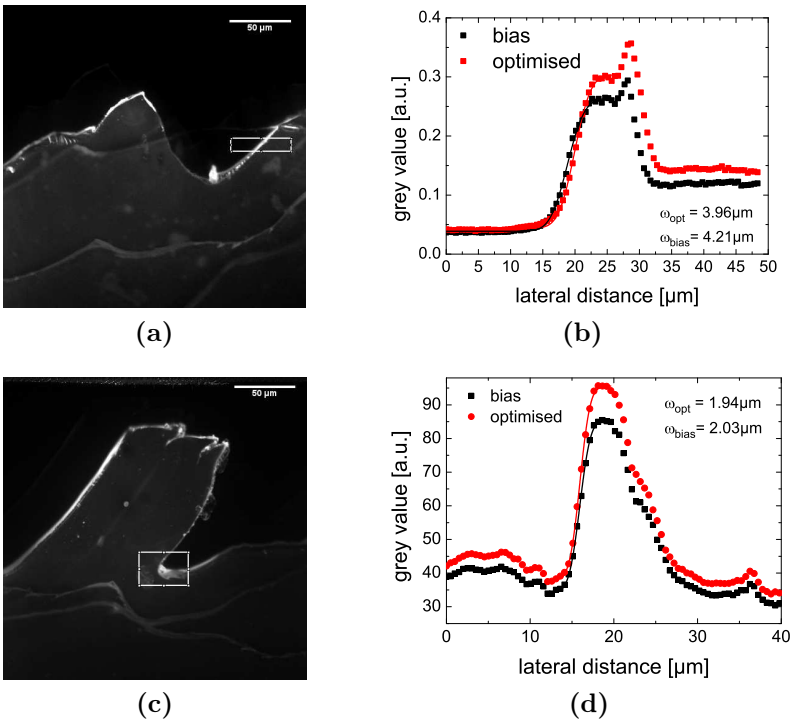

Figure 4.15: Optimisations on the photoluminescence emitted by QDs. **(a)** and **(c)** Edge of the polymer containing the QDs spin coated on a coverslip. The reflection of the host polymer off the coverslip is faintly visible. Scale bar: 50 µm. **(b)** and **(d)** Lateral intensity profiles through the edge within the indicated ROIs with the bias shape and the optimised shape. Lines: error function fit; insets: width of error function.

coated on a cover glass is shown in (a) and (c), both taken with the respective optimised DMM shape. The reflection of the polymer layer off the coverslip on which it has been spin-coated can be faintly seen. The lateral intensity profiles through the edge within the indicated ROIs are shown in (b) and (d) where the lines represent the fitting of error functions to the edge data (closed symbols) for the bias shape and the optimised error shape. Even though it can not be assumed that the edge is perfectly straight and therefore should be corresponding to a step function, fitting the same edge with an error function for both cases allows for a relative comparison of the width ω of the error function (stated in the insets for the bias and optimised DMM shapes). In (a,b), the amplitude was increased by a factor of 1.15 and the width was reduced to 94 % by the optimised DMM shape. In (c,d) the amplitude was increased by a factor of 1.13 and the width was reduced to 96 % by the optimised DMM shape.

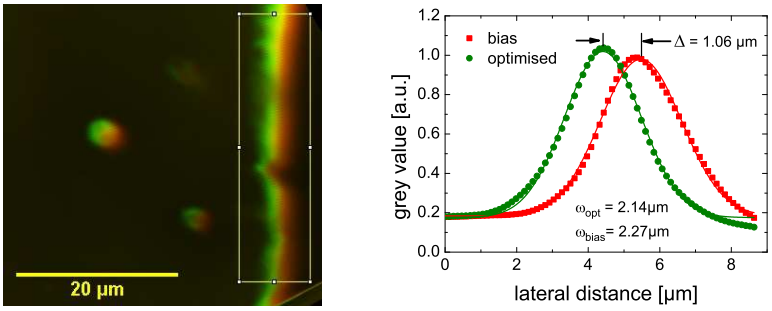

(a) **(b)**

Figure 4.16: Lateral shift. (a) Colour merging of the image taken with the bias shape (red) and the optimised DMM shape (green) (b) Lateral intensity profiles through the edge with the ROI and fits with Gaussian functions (lines). Insets: widths ω of the Gaussian functions and shift Δ between the peaks.

Lateral shift

In order to determine the lateral shift due to an optimised DMM shape, the images taken with the bias (red) and the optimised DMM shape (green) were merged as different colour channels in ImageJ. Fig. 4.16 shows the edge of the polymer containing the QDs and the ROI that has been considered in the lateral intensity profiles. The optimised DMM shape caused a shift of 1.06 µm which was determined by the shift between the peaks of the Gaussian functions fitted to the edge for the optimised and bias case. The width of the Gaussian functions was reduced to 94 % (from 2.27 µm to 2.14 µm) and the intensity was improved by a moderate factor of 1.06 fold.

Photodamage

Photodamage also played a role in the CLSM setup. Fig. 4.17 shows an image for the two photoluminescent samples used. Optimisations could not be performed on *convallaria* because the fluorescence signal picked up by the APD was either too low or too unstable even when running the bleaching compensation routine described in section 6.2.2. The likely cause for this was the inefficient collection of fluorescence emission due to the polarising optics. Approximately 50 % of fluorescence is lost at the PBS. As a consequence, signal levels were low and the noise in the images was very high (a). In (b) the same QD sample that was used in the previous section is shown. Even though the QDs can not be photobleached, the host polymer can be destroyed by high photon intensities. The arrows mark the spots were the laser beam was focused to perform optimisations.

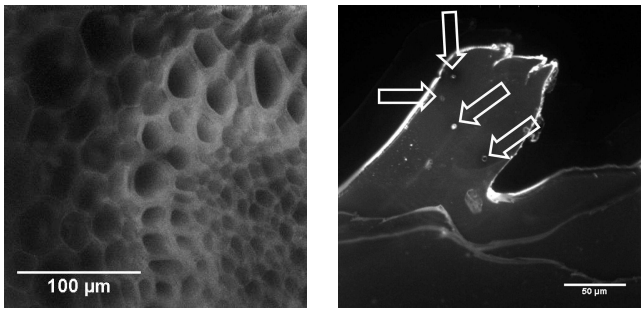

(a) **(b)**

Figure 4.17: Photo-induced damage in fluorescent samples. **(a)** *Convallaria* was prone to strong bleaching, hence image acquisition was only possibly with low power resulting in a noisy image. **(b)** QDs do not photobleach, yet the polymer can be damaged with high photon intensities. Arrows mark the spots were previous optimisations have been performed.

4.3 Discussion

4.3.1 Spatial resolution

The resolution of the CLSM was not diffraction limited and the possible reasons for this are discussed for the case of the 40x,0.75NA microscope objective.

The first reason for not achieving diffraction limited resolution is that the microscope objective was corrected for use with 0.17 mm cover glasses (# 1.5). For high NA (>0.5) dry immersion objectives the thickness of the coverslip is particularly important and tolerances of $\pm 10\,\mu m$ for top quality coverslips, can affect the FWHM by more than 2 fold [53]. No coverslips were used in this work because it was believed that omitting them would introduce spherical aberrations into the optical system that could be compensated for with AO.

The second reason is that Nyquist sampling was not always strictly observed. For the 40x, a zoom factor of 2.33 would be necessary to image the diffraction limited Airy disc with at least 4 pixels, however, the images taken before and after optimisations in order to assess the optimisation outcome were always taken with a digital zoom of one. Therefore finer structures might be obscured by this undersampling.

The size of the pinhole (PH) is another factor that could have lead to non-ideal imaging. The diameter of the PH is strictly only correct for a certain magnification, wavelength and NA [39]. Changes in these settings require adaptation of PH size, however the PH diameter remained the same throughout the experiments,

regardless of the change in wavelength due to fluorescence or the interchange in microscope objectives. The optimal diameter of a PH is approximately expressed as

$$D_{PH} = \frac{0.5\lambda M}{\mathrm{NA}} \tag{4.9}$$

where M and NA are the magnification and numerical aperture of the microscope objective and λ is the wavelength [128]. This equation sets the PH diameter at the FWHM of the Airy disc and therefore lets through only about 75 % of the light in the central maximum. In biology applications, the PH is often set at the first dark fringe of the Airy disc, about twice as big. According to this equation, the ideal PH diameter should be about 28 µm in diameter. The smallest PH available and the one used in this work had a diameter of 75 µm. This larger PH diameter might be accountable for the degraded resolution, especially in the axial direction.

Finally, the electromechanical properties of the galvos, for example mass, spring constant, frequency response, overshoot, resonant frequency, tolerance, rigidity etc, produce positioning errors. In a CLSM imperfect scanning precision can introduce distortions that will affect the resolution of the imaging system.

Table 4.7 lists the spatial resolution before and after optimisations on either a reflective (refl.) or a photoluminescent (ph.) target. The fifth column lists the percentage of the post optimisation value in relation to the value measured preoptimisation and indicates the improvement the optimisation has achieved in absolute terms. The optical system was re-aligned after each first trial in each

Table 4.7: Comparison of results. Resolution obtained with the 40x,0.75NA microscope objective and signal improvement factors in signal intensity f for various optimisations. Theoretical resolution: laterally 0.47 µm, axially 1.69 µm.

		Resolution FWHM [µm]		% pre	% theo.	Intensity f
	mode	pre opt.	post opt.			
lat.	refl. 1	1.62	1.39	86	296	1.40
	refl. 2	0.95	0.73	77	155	7.97
	ph. 1	4.21	3.96	94	-	1.15
	ph. 2	2.03	1.94	96	-	1.37
ax.	refl.1	9.32	7.71	83	456	1.62
	refl.2	5.89	5.42	92	321	1.37

modality. This is the reason why the second optimisation of each modality is closer to the diffraction limit. The sixth column gives the FWHM after optimisation as a percentage of the theoretically calculated diffraction limited case. For example, in the second optimisation on reflection mode, the lateral and axial resolution were 155 % and 321 % of the theoretical diffraction limit respectively. Resolution measurements were not possible in the fluorescence mode because the sample lacked structure with sharp edges.

4.3.2 Optimisations

In terms of optimisation performance signal intensity was improved on average by 1.4 fold with the exception of one optimisation that increased signal by a factor of almost 8. The resolution was on average improved to 88 % of the pre-optimisation value where optimisations on reflectance performed better than those on photoluminescence (reduction to 85 % vs 95 %).

4.4 Summary and conclusions

This chapter describes design and implementation of a CLSM system that was custom built from individual components so as to provide a cheap and versatile platform for the test and development of adaptive aberration correction. The software was written using the LabVIEW programming language and represented an intuitive, all-in-one user interface that allowed for galvo movement, image acquisition, algorithm development and DMM deformation to be controlled from the same front panel.

The basic components that were necessary for the construction and control of the galvo-based scanning system were covered and the basic alignment and calibration procedures of the final optical system were presented. AO was incorporated in form of a DMM that simultaneously corrected for the aberrations in the excitation and emission path. The DMM shape for aberration correction was determined with a RSA algorithm optimising either on a retro-reflected signal or on the photoluminescence generated by quantum dots. To this end, emission filters and dichroic mirrors were substituted into the system.

The imaging properties of the CLSM were characterised including the examination of spatial resolution by transfer function analysis and the necessary digital

zoom factors for sampling observing the Nyquist frequency. Various fluorescent and reflective samples were used to test the CLSM in both imaging modalities.

The AO system was tested with optimisations performed on a USAF resolution test chart and a sample containing quantum dots. The effect of the optimisation was analysed in terms of improvement of resolution and signal intensity as well as repeatability of improvement by previously acquired DMM shapes. Some improvement in signal intensity could be achieved in both imaging modalities with improvement factors ranging from 1.2 to 8 fold. However, diffraction limited resolution was not restored and might require careful re-alignment of the entire optical system and investment in a PH of different size. Ideally a system with more magnification in the detection arm would allow for the use of an iris instead of a PH with the added benefit of variable aperture sizes which can be adapted to the microscope objective currently in use.

Chapter 5

Nonlinear Microscopy

The field of optical microscopy is often divided into two categories: conventional (linear) microscopy and nonlinear microscopy. In conventional microscopy, including confocal microscopy, contrast is generated from light-matter interactions, in which the elementary process, absorption, scattering etc, only involves a single photon and which therefore depends only linearly on the incident light intensity. Nonlinear microscopy methods on the other side, rely on higher-order light matter interactions involving two or more photons for contrast generation. This fundamental difference is the origin of numerous qualitatively new imaging properties. Nonlinear optical microscopy (NLOM) techniques are especially suited for deep tissue imaging as they have special features that make them less sensitive to scattering that obligatorily occurs in most biological tissues. NLOM is capable of imaging biological tissue noninvasively with sub-micrometer resolution at depth in three dimensions and is the method of choice for investigating cells and cellular functions in a variety of fields including neuroscience, immunology and cancer research [52, 184].

NLOM methods can be further divided into coherent processes, which include harmonic generation, and non-coherent processes, like the non-linear excitation of fluorescence with two or more photons, generally termed multiphoton microscopy (MPM). Since its first demonstration over two decades ago, MPM has become the technique of choice for high-resolution fluorescence imaging of physiology, morphology and cell-cell interactions in intact tissues and live animals.

5.1 TPEF

By far the most employed non-linear imaging modality is two photon excitation fluorescence microscopy (TPEFM). With this technique, biological specimens can be studied noninvasively in three dimensions with submicrometer resolution [185]. Moreover, due to the excitation process, which results from the simultaneous absorption of two photons, there are a number of unique advantages, such as reduced specimen photodamage and enhanced penetration depth, that contribute to the increasing popularity of TPEFM applications in biology and medicine.

The potential of highly intense light to trigger nonlinear processes has been perceived as early as 1931 when Maria Göppert-Mayer predicted multiphoton excitation processes in her doctoral dissertation on the theory of two-photon quantum transitions in atoms [6]. Göppert-Mayer's theory was finally verified 30 years after its formulation, when the invention of pulsed ruby lasers made an experimental realisation possible. Kaiser and Garret published the first report on two photon excitation of CaF_2:Eu^2 fluorescence in 1961 and later demonstrated that two photons can also excite the fluorescence of organic dyes [186]. In extension of two photon processes, three photon excitation processes were also soon reported [187, 188]. However, the full potential of imaging two-photon excited fluorescence in a scanning microscope was not realised until the seminal work of Denk et al. in 1990 [5], now cited over 4000 times, after major improvements in the technology of short-pulsed, tunable laser sources had been made.

Even though TPEFM is by now a quite mature technique, recent research pushes its technology further in terms of imaging speed, resolution, chronic imaging, miniaturisation and mobilisation. Along with improvements in new fluorescent proteins, these advances have extended the range of applications available to TPEFM from in-vivo tissues to behaving animals [189]. Tissues as diverse as lymphatic organs, kidney, heart, skin and brain have been investigated in detail at depths of up to one millimeter and TPEFM has also found applications in the diagnosis and potential treatment of pathological conditions such as tumors and Alzheimer's disease [52]. The following reviews provide information beyond this introductory chapter [184, 185, 190].

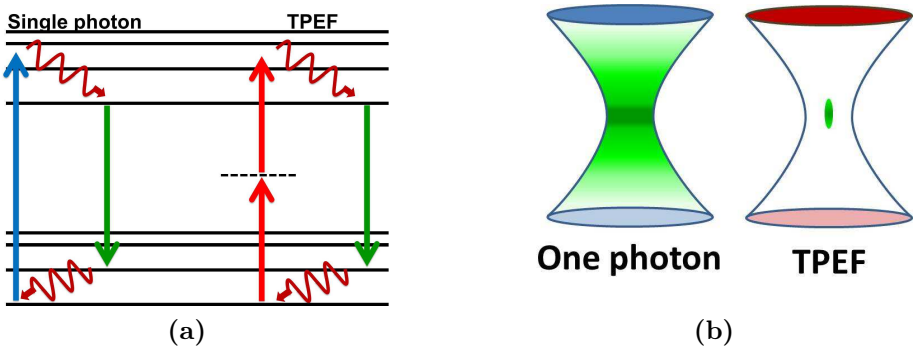

(a) (b)

Figure 5.1: (a) Jablonski diagram: Excitation occurs between the ground state and the vibrational levels of the first electronic excited state via absorption of one photon (left) and via absorption of two lower-energy photons through a short-lived intermediate state (right). After either excitation, the fluorophore relaxes through vibrational process to the lowest energy level of the first excited electronic states. The subsequent fluorescence emission is identical in both processes. **(b)** Single vs. two photon excitation volume. Left: visible (blue) light is used for single photon excitation which is only localised in lateral directions and generates fluorescence (green) all along the optical axis. Right: two photon excitation with near infrared (red) allows for localisation of the lateral directions as well as selectivity of the axial plane.

5.1.1 Physical background

Three-dimensionally localised excitation

In conventional fluorescence spectroscopy, a fluorescent molecule is excited by absorption of one photon whose energy corresponds to the energy gap between the ground state and the excited state. However, the same excitation is also possible by the simultaneous absorption, *i.e.* within $1 \cdot 10^{-16}$ s, of two photons of approximately double the wavelength via a short-lived, virtual intermediate state [191] (Fig. 5.1a). The two photons interacting with the molecule produce an excitation equivalent to the absorption of a single photon possessing twice the energy and the combined energy is therefore sufficient to promote the electron into the excited level. The emitted fluorescence generated by the simultaneous absorption of two photons is identical to the single photon excitation fluorescence emission.

The basic physical principle of fluorescence excitation is the interaction between the fluorophore and the electromagnetic field that is providing the excitation. This interaction is described by a time-dependent Schrödinger equation, in which the Hamiltonian contains an electric dipole interaction term $\vec{E} \cdot \vec{r}$, where $\vec{E}$

is the electric field vector and $\vec{r}$ is the position operator [185]. Using perturbation theory, the first-order solution corresponds to the one-photon excitation, and the multiphoton transitions are represented by higher order solutions.

The simultaneous absorption of two photons is the origin of the quadratic dependence on the light intensity rather than the linear dependency of conventional fluorescence generation. In TPEFM, doubling the intensity produces four times the fluorescence. This nonlinear dependence is the basis of the intrinsic localisation of fluorescence generation and therefore the optical sectioning capability of TPEFM. Like most nonlinear processes, the transition probability in TPEF is extremely low but can be optimised with two approaches to generate enough signal: the excitation light has to be concentrated in space and time. Spatial compression is achieved by a tight focal spot which is produced by the use of high NA objective lenses. This increases the local intensity at the focal point and with it the probability for TPEF. Away from the three dimensional focal spot the probability for simultaneous absorption drops off drastically so that virtually no fluorescence is generated outside the focal volume and intrinsic three dimensional resolution is achieved (Fig. 5.1b) [184]. Scattered excitation light is too dilute to excite by two photon absorption and too long in wavelength to be absorbed otherwise [192]. It hence just bounces around harmlessly in the tissue which lacks chromophores that are able to absorb at this wavelength.

However, focusing with a high NA objective alone is not enough to produce enough fluorescence signal to make TPEFM practical. In order to generate the necessary photon density to allow for the simultaneous absorption of two photons, pulsed femtosecond lasers are used to compress excitation intensity in the time domain. These lasers concentrate photons into very short (pulse width τ), high peak intensity pulses separated by $\approx 10^{-8}$ intervals (repetition rate f_r), keeping the average power relatively low. This increases the signal by a factor of $1/(\tau f_r)^{n-1}$ compared to continuous-wave illumination where n is the number of photons involved in the elementary process [52]. At present, the most commonly used lasers in multiphoton microscopy setups are mode-locked titanium sapphire (Ti:Sa) which typically generate pulses with $\tau = (100 - 150)\,\mathrm{fs}$ at $f_r = (80 - 100)\,\mathrm{MHz}$. They are tunable from $(680 - 1050)\,\mathrm{nm}$ and can simultaneously be used as a pump source for optical parametric oscillators (OPO) as well as fluorescence excitation (see section 5.3.2).

In TPEFM, a laser is focused onto the sample and this focused beam is scanned through the specimen in a raster like fashion by a non-resonant, point scanner with an adjustable scan speed. The image is reconstructed from digitising the point measurements of the fluorescence intensity at each position in the sample (see also chapter 3 on confocal laser scanning microscopy). Emission collection can be efficient and simple because all photons generated are signal and there is virtually no background. Even multiply scattered signal photons can be assigned to their origin due to the localised nature of signal generation. Although confocal detection has been shown to increase resolution under certain conditions [193, 194] it is counter productive in most application as a confocal pinhole will reject scattered fluorescence even though it originated from the focal volume.

To increase efficiency of fluorescence collection, non-descanned detectors are employed, most commonly large area photomultiplier tubes (PMTs) close to the back aperture of the microscope objective. PMTs allow for the detection of multiply scattered fluorescence photons that may leave the objective lens at randomly divergent angles [195] and are also favoured for their high gain and low readout noise. Because of their 'whole field' detection, PMTs are very sensitive to ambient light and require operation in a light tight microscope enclosure as even light emitted from computer screens can affect their read out.

Optical resolution of MPM

The optical resolution in MPM is defined by the square of the illumination point spread function (p_{ill}).

$$p_{\text{TPEF}}(u,v) = p_{\text{ill}}^2(\frac{u}{2},\frac{v}{2}) = p^2(\frac{u}{2},\frac{v}{2}) \tag{5.1}$$

with $\frac{u}{2}, \frac{v}{2}$ indicating an illumination wavelength about twice as high as in the confocal case. Fig. 5.2 shows a comparison of the PSF for one photon and TPEF microscopy, where v and u are the lateral and axial normalised optical coordinates, defined on p.13 of this thesis. Assuming an oil-immersion objective of 1.3 NA in both cases, TPEFM has a wider PSF owing to the longer wavelength used (here: 425 nm and 850 nm respectively). The true strength of TPEFM is its ability to discriminate against out of focus fluorescence: the total two-photon fluorescence falls off rapidly away from the focal plane in contrast to the one-photon case where the total fluorescence generated is constant for each axial plane (Fig. 5.1b).

Based on the work of Richards [40], p_{ill} can be calculated and fits of the

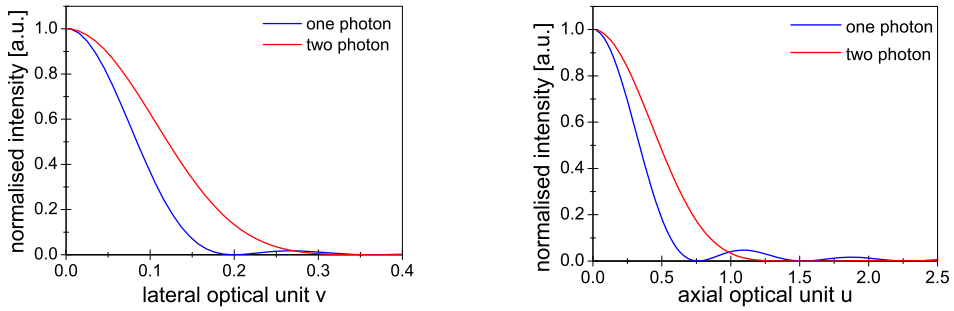

(a) **(b)**

Figure 5.2: **(a)** Lateral PSF for one- and two photon excitation . **(b)** Axial PSF for one- and two photon excitation. In these figures, v and u are the normalised optical coordinates (calculated for an 1.3 NA oil-immersion objective and wavelengths of 425 nm and 850 nm respectively and assuming the paraxial approximation).

intensity squared profiles to a Gaussian function yield expressions for estimating the diffraction-limited lateral (ω_{xy}) and axial (ω_z) $1/e$ radii [184]:

$$\omega_{xy} = \begin{cases} \frac{0.320\lambda}{\sqrt{2}\,\mathrm{NA}} & \text{for NA} \leq 0.7 \\ \frac{0.325\lambda}{\sqrt{2}\,\mathrm{NA}^{0.91}} & \text{for NA} > 0.7 \end{cases} \tag{5.2}$$

$$\omega_z = \frac{0.532\lambda}{\sqrt{2}} \left[\frac{1}{n - \sqrt{n^2 - \mathrm{NA}^2}} \right]. \tag{5.3}$$

From these values the full width half maximum (FWHM) can be obtained:

$$\mathrm{FWHM} = 2\sqrt{ln2} \cdot \omega. \tag{5.4}$$

The TPE focal volume can be approximated by fitting the illumination PSF with a three dimensional Gaussian volume and analytical integration over the whole space [184]:

$$V_{\mathrm{TPE}} = \pi^{3/2} \omega_{xy}^2 \omega_z. \tag{5.5}$$

This approximation yields 68 % of the value obtained with a full vectorial approach. For example, with this correction, the effective TPE volume for an oil-immersion, 1.3-NA lens at 1090 nm is $(5.57)(0.199\,\mu\mathrm{m})^2(0.550\,\mu\mathrm{m})/0.68 = 0.178\,\mu\mathrm{m}^3$ or ≈ 100 aL. This localised excitation volume offers greatly improved axial discrimination and improvement in image contrast, compared with conventional microscopy.

5.1.2 Properties

Viability, photobleaching and photodamage

MPM limits fluorophore excitation to the focal volume and virtually eliminates the risk of photobleaching and photodamage everywhere else in the sample. Photo-induced damage is also decreased by use of near infrared (NIR) excitation rather than ultra violet (UV) or visible radiation. However, within the focal volume, the possibility of bleaching, damage and reduced viability remains [196,197]. Three major mechanisms of two-photon induced photodamage have been recognised [185]. Firstly, photo-oxidative damage of fluorophores with pathways similar to that of UV irradiation results in the formation of reactive oxygen species that trigger subsequent biochemical damage cascades in cells [198–200]. Secondly, thermal damage produced by one- and two photon absorption of high-power IR radiation can be quite significant in presence of strong IR absorber like melanin but is generally believed to be of no concern at moderate excitation powers [201]. Thirdly, mechanisms which are triggered by the high peak power of fs laser pulses for example dielectric breakdown occasionally occur [198]. It is generally believed that single- and three- photon excitation damage is usually negligible, and photodamage in the focal plane is primarily due to two photon processes [202]. The advantages and disadvantages of NLM are summarised in Table 5.1 at the end of this section.

Reduced scattering and absorption

Other advantages of TPEFM is the reduced attenuation in biological specimens due to the reduced scattering and absorption of NIR light in biological sample when compared to UV and visible light. Even though Rayleigh scattering is just an approximation in biological imaging, the inverse relationship ($\propto \lambda^{-2}$) between scattering and excitation wavelength remains valid [203]. This results in deeper penetration of the TPEF source into scattering sample compared to conventional microscopy. Also, the 'optical window', placed at $(700 - 1000)\,\mathrm{nm}$ where tissue absorbance is orders of magnitude less than the absorption in the UV or visible region falls conveniently into the spectral excitation window of TPEFM (Fig. 5.3). Lower photon absorption in the tissue additionally means lower levels of phototoxicity and sample heating.

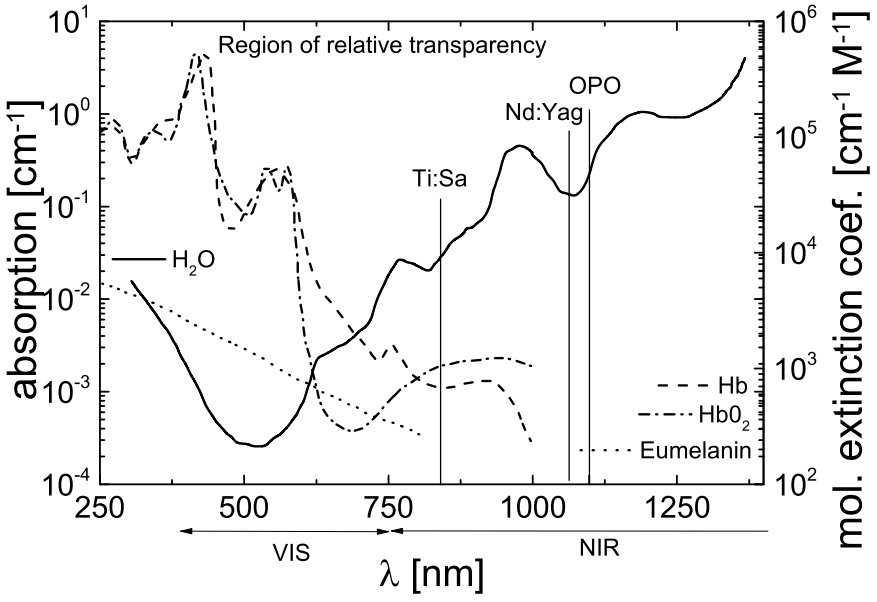

Figure 5.3: Optical window in biological tissue. The relative transparency of biological tissue in the NIR is a consequence of lack of absorption by water (H_2O) and common intrinsic chromophores (here Oxyhemoglobin HbO_2, Deoxyhaemonglobin Hb and Melanin given as the molar extinction coefficient). Also indicated is a common emission laser line of a Ti:Sa laser at 840 nm, Nd:Yag emission at 1064 nm and the OPO emission wavelength used in this work at 1098 nm.

High SNR

In conventional fluorescence microscopy the emission spectrum and excitation spectrum usually overlap and band pass filters are employed to eliminate the leak-through of excitation light into the detection channel. These filters often have to cut off a part of the emission band. Due to the larger spectral gap between excitation and emission in TPEFM the elimination of leak-through is possible with only minimal attenuation of the signal leading to higher signal to noise ratios (SNR). Also, unlike confocal microscopy, detection pinholes and descanning optics are not necessary to achieve depth discrimination. As TPEF is already localised to the focal volume, there is no appreciable out-of focus fluorescence to reject.

5.1.3 Advances and applications

The optimisation of TPE properties in fluorophores promises a reduction of laser excitation intensity and thus the risk of photo-induced damage to the sample and has therefore gained a lot of interest in the last decade [204]. Additionally, multi-colour TPEF offers the possibility of simultaneously exciting different fluorophores whose emission spectra vary by hundreds of nanometers [184, 205].

Single molecule applications of TPEF include single molecule detection and imaging in the far- and near field modality [206,207], fluorescence correlation spectroscopy for the determination of molecular dynamics in the cytoplasm of living cells [208,209] and the monitoring of drug delivery efficiency [210,211]. Functional imaging with TPEF on a cellular level was realised with the three dimensional, localised uncaging of signal molecules through photolysis for receptor mapping and the study of signaling pathways [212, 213] and recovery after photobleaching experiments [214]. *In vivo* cellular imaging with TPEF was also explored in calcium signaling studies [215] and in the case of three-photon absorption for the distribution of the neural transmitter serotonin which was important in the way that MPM was used to access new far-UV chromophores that were virtually inaccessible otherwise [216]. The precise ablation and cutting on subcellular level obtained through plasma-induced lesion generated by energy deposition due to multiphoton ionization in the focal volume has also been investigated [217, 218]. Uncaging experiments allowing photo-controlled gene expression in cells or living organisms include studies in a live zebrafish embryo [219].

On tissue level, TPEFM shows advantages in the imaging of thick, highly scattering specimens [220] and has been successfully applied to study tissue physiology including the cornea [221], retina [222], skin [223], kidney [224] and heart [225] and in neurobiological studies [226, 227]. In the field of embryology, TPEFM has been employed to image hamster embryos repeatedly and over hours without observable damage and those embryos eventually developed into normal, healthy animals after re-implantation [228]. Applications of TPEF for clinical diagnosis in the form of optical biopsy with a two-photon endoscope [229, 230], the monitoring of Alzheimer's disease [231] and treatment in the form of photodynamic therapy [232] have been reported.

Table 5.1: Advantages and disadvantages of nonlinear optical microscopy.

Advantages	Disadvantages
Intrinsic optical sectioning	High photodamage in focus
Cellular resolution	Decreased resolution with higher λ_{exc}
Imaging in optical window	Necessity for IR corrected optics
High SNR	Expensive laser sources
Large penetration depth	Low TPE efficiency of fluorophores
Reduced photodamage outside focus	
Localised photo-uncaging, -ablation	

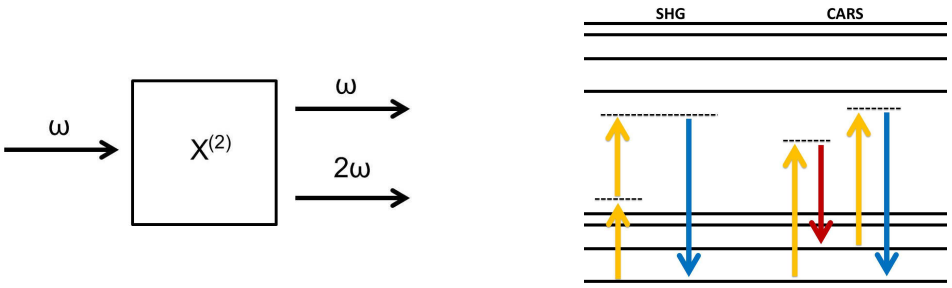

Figure 5.4: **(a)** Process of SHG. **(b)** Jablonski diagram for SHG (left) and CARS (right). In SHG two photons are simultaneously scattered, generating a single photon of exactly twice the energy. Both the intermediate levels are virtual states. In CARS a pump beam ω_p (yellow) and a Stokes beam ω_s (red) interact to generate a signal at the anti-Stokes frequency $\omega_{AS} = 2\omega_p - \omega_s$ (blue).

5.2 Second-harmonic generation

Second harmonic generation (SHG) is a nonlinear, energy conserving process in which two incident photons scatter simultaneously with molecules without being absorbed, producing light of exactly half the wavelength (Fig. 5.4). No actual electronic excitation takes place, instead an intense laser field induces a nonlinear, second-order, polarisation in the assembly of molecules, resulting in the production of a coherent wave at exactly twice the incident frequency. Second harmonics are generated in noncentrosymmetric, organized structures found in many biological specimen [233], such as type-1 collagen fibrils, myosin thick filaments or microtubules when these noncentrosymmetric structures allow optical field oscillation at twice the frequency of the incident field.

5.2.1 Physical background

The nonlinear polarisation P (dipole moment per unit volume) for a material is given by:

$$\vec{P} = \chi^{(1)} \otimes \vec{E} + \chi^{(2)} \otimes \vec{E} \otimes \vec{E} + \chi^{(3)} \otimes \vec{E} \otimes \vec{E} \otimes \vec{E} + ... \tag{5.6}$$

where $\vec{E}$ represents the electric field vector, $\chi^{(i)}$ is the i^{th} order susceptibility tensor and $\otimes$ represents a combined tensor product and integral over frequencies. The first order term describes processes like absorption and reflection whereas the second order process relates to SHG and sum frequency generation. The third order term describes multiphoton absorption, third harmonic generation (THG)

and coherent anti-Stokes Raman scattering (CARS) [234]. The necessity for the environment lacking a centre of symmetry is seen in $\chi^{(2)}$ which is a bulk property and related to the molecular hyperpolarisability γ by:

$$\chi^{(2)} = N_s \langle \gamma \rangle \tag{5.7}$$

where N_s is the density of molecules and the brackets denote an orientational average. The SHG intensity in such a medium scales as:

$$S_{\text{SHG}} \propto \left(\frac{p}{a\tau}\right)^2 \tau a (\chi^{(2)})^2 \tag{5.8}$$

where p and τ are the laser pulse energy and pulse width, respectively and a is the area of the focused spot.

5.2.2 Properties

SHG and THG are coherent and polarisation sensitive processes and the scattered photons maintain phase information. The scattered beam must therefore satisfy phase matching conditions producing highly directed radiation rather than isotropic emission (Fig. 5.5) [235, 236]. In contrast to fluorescence, where the emission properties are only dependent on the molecular properties and are independent of the characteristics of the excitation laser both the spectral and temporal characteristics of SHG are derived from the laser source. The bandwidth scales with the bandwidth of the excitation laser, and the SHG pulse is temporally synchronised with the excitation pulse [237].

THG is sensitive to local differences in refractive index and dispersion, that is, the contrast arises from interfaces and optical heterogeneities of size comparable

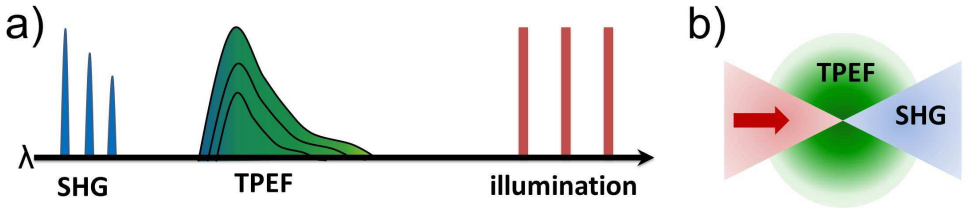

Figure 5.5: **(a)** SHG occurs at exactly half the excitation wavelength and tunes with the laser. In contrast, fluorescence emission spectrally remains unchanged but diminishes in magnitude as the laser tunes through the absorption peak. **(b)** SHG is highly directional and either emitted in forward or backward direction whereas fluorescence is emitted isotropically.

to the beam focus, such as cell membranes, lipid bodies or axon myelin. SHG and THG generate contrast with intrinsic structures and do not require exogenous labeling. Unlike fluorescence, generation of higher harmonics involves only virtual state transitions. Consequently the signal does not bleach over time and stays stable without generation of toxic reactive oxygen species. As the instrumentation for generating and observing SHG is similar to that used for TPEFM, data collection can occur simultaneously to TPEF providing complementary information in multi modal MPM [238].

5.2.3 Applications

Franken *et al.* begun the work on SHG of light in quartz crystals in 1961 [239], leading up to the first exploration of all nonlinear microscopy methods in 1974 when Hellwarth *et al.* used second harmonic imaging microscopy (SHIM) to analyse the polycrystalline structure of ZnSe [240]. The combination of harmonic generation and scanning microscopy was suggested by a group in Oxford, which realised the benefits of the non-linear process for the investigation of thick biological specimens [241, 242].

SHIM has been explored for a few decades and has come to several applications [234, 243]. The first biological experiments were performed by Freund *et al.* in 1986 to study the endogenous collagen structure in rat tail tendon [243]. Guo and co-workers used stage scanning laser excitation to image SHG within muscle and connective tissue [244]. SHIM is highly sensitive to the electric field in the cell membrane [245,246], and hence is able to measure neuronal membrane potential [236]. It has also been used for the visualisation of microtubule polarity [237, 247] and unstained collagen structures [248, 249]. SHIM has also proven to be a valuable tool for the probing of *in vivo* molecular and supramolecular conformation [250] and may provide new insights into the processes of wound healing and scar formation. There is a great need to synthesise contrast agents that respond to SHG and THG. Exogenous sources has been investigated with SHRIMPs 'Second Harmonic Radiation IMaging Probes'. The SHG active nanoparticles of metallic, semiconductor, organic or hybrid origin have been used as labels for bioimaging applications including studies with human HeLa cells and zebrafish embryos [251–253].

Application of THG include microscopy with living, dynamical specimens [254–257] for example to visualize the cell lineage of unstained *C. elegans* embryos [258].

5.3 Other nonlinear effects

5.3.1 CARS

Coherent anti-Stokes Raman scattering (CARS) microscopy requires two synchronised pulsed lasers, the pump- and the Stokes beam, to generate contrast which derives directly from Raman-active vibrational modes within molecules (Fig. 5.4) [259, 260]. If the beat frequency (the difference between the pump- and the Stokes frequencies) coincides with the Raman vibrational frequency of a molecule, the vibrations are driven coherently and a strong anti-Stokes signal is obtained at twice the pump frequency minus the Stokes frequency [261]. CARS probes intramolecular vibrations and can thus detect specific chemical bonds [262, 263], for example to image biomolecules such as lipids and water in cells and cell membranes. Much like TPEF, CARS was proposed and demonstrated decades ago but lay dormant until the improvement of pulsed, tunable lasers in the IR wavelength range. CARS microscopy has been applied to the 3D imaging of neuronal myelin under physiological conditions [264] and further applications are detailed elsewhere [265].

5.3.2 Parametric oscillation

Optical parametric oscillators (OPOs) are commonly used to extend the wavelength range further into the IR region [266]. Their working principle is based on a birefringent, non-linear crystal which is pumped by a laser of frequency ω_p (usually a Ti:Sa tuned between $800 - 850\,\mathrm{nm}$). The output wavelength of lesser energy is generated through parametric down conversion in the crystal, a process which splits the pump photon into a lower energy s-signal and an i-idler photon, where $\omega_s > \omega_i$ and $\omega_p = \omega_s + \omega_i$ [267]. Crystals used include potassium tytanyl phosphate (KTP), beta baryum borate (BBO) and lithium triborate (LBO). Tuning the OPO output wavelength is achieved by modifying the temperature or the angle of incident light on the crystal [268].

5.4 Deep imaging

TPEFM allows cellular imaging hundreds of microns deep into various tissues of living animals. Several directions have been proposed to attempt and image even deeper into biological samples.

5.4.1 Advances

Given advances in laser technology, the power that current lasers can provide is less likely to be a limit to the total imaging depth, rather the light levels that the specimens can sustain provide a fundamental limit [47]. The maximum imaging depth for a given average power $\bar{P}$ is given by [269]:

$$z_{max} = \iota \ln \left[\bar{P} \kappa \sqrt{\frac{1}{f_r \tau}} \right], \qquad \kappa = \sqrt{\frac{\eta_{2P} \phi(z_m ax)}{\bar{P}(z_{max})}} \tag{5.9}$$

where ι is the scattering mean free path length, f_r is the repetition rate, τ the pulse width, η_{2P} is the fluorescence quantum efficiency, $\phi(z_{max})$ and $\bar{P}(z_{max})$ are the collection efficiency and the required average excitation power at the focal plane, respectively. This equation illustrates which parameters can be optimised to increase the yield of nonlinear processes.

Collection efficiency In MPM all generated fluorescence contributes to the signal and discrimination of signal photons from background occurs according to their colour not where they exit the sample. Strongly dependent on tissue constitution, signal photons can have been scattered on multiple occasions and exit the tissue from an area that is wider than the focus is deep [51]. For this reason the detection field of view needs to be as large as possible to allow efficient signal collection with increasing depth. Special objectives that combine a high NA with low magnification have particularly high collection efficiencies due to their large spatioangular acceptance range [48].

Reduction in the duty cycle $(f_r \tau)$ The reduction of the repetition rate f_r of the excitation source increases the single pulse energy [270]. For instance, with the use of a 200 kHz Ti:S regenerative amplifier, imaging depths as large as 1 mm were reached in cortex [269]. A limitation of this approach is given by the lowest usable repetition rate which is given by the pixel rate since at least one laser pulse must be delivered per image pixel. The reduction of the pulse width τ also leads to increased TPEF signal but requires accurate dispersion correction in the optical train as the spectral width of the pulse rises as the pulse width falls. A hard limit to the benefits of shorter pulses is reached, however, when the spectral width of the laser excitation approaches or exceeds the width of the excitation spectrum of the dye ($\approx (30 - 40)$ nm FWHM) [271].

Increasing the scattering mean free path length The maximum imaging depth in TPM depends on the ability of ballistic excitation and of emitted fluorescence to reach the detector. Recent advances in fs lasers and OPOs have opened doors for imaging at unprecedented wavelengths centered in the optical window and have led to IR MPM which enables the use of red fluorophores and proteins, doubles imaging depth and strongly reduces phototoxicity and photobleaching compared with conventional MPM [272, 273]. Effort has also been dedicated to the engineering of new fluorophores whose absorption and emission spectra are shifted towards the IR [274, 275] with the development of red fluorescent protein (RFP) [276], fruit red proteins [277] and mRuby [278] being recent milestones.

Due to lesser distortions of the focal spot by reduced photon scattering in the tissue, IR increases by 40 - 80 % the maximal light penetration and the spatial resolution at 70 µm depth is improved by a factor of 1.7 in heavily scattering samples such as brain slices, compared to conventional Ti:Sa excitation [203]. Additional beneficial effects are the longer emission wavelength of redder fluorophores which also reduce scattering and allow for better collection of fluorescence from deeper tissue layers. These effects were found to outweigh the fundamental decrease in resolution that comes with the use of longer excitation wavelength (see p.76) [279].

5.4.2 Optical aberrations

For scattering-absorbing samples, ultimately, out-of-focus fluorescence generated near the surface of the sample by ballistic and scattered photons limits the imaging depth [51]. Whereas scattering and absorption are inevitable characteristics of the tissue, the amount of aberrations introduced by the sample can be manipulated in various ways. The distortion of the beam profile through aberrations introduced by refractive index mismatch (RIM) have been shown to severely degrade NLM (see also p. 37) [47, 280, 281]. For efficient MP signal generation, it is necessary to focus high power, ultra-fast laser pulses into a volume of femtoliters as the size of the focal spot is critical for achieving the necessary photon densities required for this imaging modality. Aberrations introduced either by the system's optical setup or the sample under investigation distort the wavefront and cause a broadening of the diffraction limited focal spot. In NLM this does not only result in reduction of image quality due to a decrease in resolution but also to a considerable loss of fluorescence, as signal scales with the square of the laser power [282].

NLM is routinely done with a high NA objective in order to produce the required high photon density. High NA objectives are designed to be used in conjunction with an immersion oil to minimise a discontinuity in refractive index when imaging through a coverslip, therefore RIM is unavoidable when imaging into a aqueous solution. The mismatch between the refractive index of oil/ glass and of water has been shown to be the origin of spherical aberrations (SA) [149, 152, 283–288] (see also Fig. 7.3 on p.149). The magnitude of aberrations, especially higher orders, have been shown to increase with NA [286, 289] and imaging depth [282]. Additionally, rays that travel at larger angles through the sample are more likely to be scattered than paraxial rays simply because they travel a longer distance to the focus, which leads to a reduction of the effective NA with increasing imaging depth in scattering tissue [52, 269]. When using IR excitation, the performance of the objective degrades even more [290] as most objectives have not been designed to be used in this regime. The consequences are chromatic aberrations and decreased light transmission.

Naturally, the tissue under investigation will introduce itself intrinsic optical aberrations due to the inhomogeneous distribution of refractive indices caused by subcellular structures like cell membranes and fat deposits and these aberrations will become more dominant the deeper one tries to image. This results in inefficient fluorophore excitation and, consequently, in a smaller number of emitted photons making longer acquisition times necessary. These are often in the order of seconds and therefore limit observations of dynamic processes in living samples with high temporal resolution. A common reaction to this problem is to increase the laser power above the non-toxic level to generate more fluorescence. However, once a certain power level is crossed the nonlinear photodamage rises faster with increasing laser power than the number of excited molecules [197, 217] and thus strongly increases phototoxic damage to sensitive cell and tissue functions [291].

5.4.3 Spherical aberration compensation

Several techniques have been suggested and implemented to specifically compensate for SA. Tung *et al.* reported that low NA objectives can outperform high NA objectives of the same immersion medium for MPM of test samples and biological tissues at depth and should be chosen if obtainable imaging depths rather than image resolution is of primary consideration [292].

A different approach involves the compensation of SA by adjustment of the

correction collar of water immersion objectives leading to an increase in signal by up to 50 % [293, 294]. Additional methods for manipulating SA include tuning the immersion medium, using coverslips of different thicknesses and adaptive lens systems. Tsai *et al.* used a transparent deformable membrane mounted infront of a vacuum to correct specifically for negative SA that arise when water immersion objective is used to image into sample of higher refractive index [68].

The drawback of all these techniques, however, is that the correction is essentially static and not readily altered during imaging. The dynamic correction of aberrations is possible with means of adaptive optics (AO).

5.4.4 Adaptive optics

Two approaches have been mainly used to implement closed-loop AO into NLM, feedback via fluorescence/higher harmonic light and feedback via reflected excitation light. When reflected excitation light is used as a feedback, a wavefront sensor is usually employed. Closed-loop adaptive wavefront correction based on sensing the wavefront of coherence gated backscattered light was used to restore the focal spot to nearly diffraction limit even in living biological samples [295]. In this approach the reflected light signal from the focal plane is selected with a modified Michelson interferometer, and the wavefront distortion is quantified using a shearing interferometer. The confocal principle for depth selection was chosen by Cha *et al* to detect reflected light from the focal region and measure its wavefront distortion with a Shack-Hartmann sensor [296].

The first implementation of adaptive aberration correction in TPEFM by measuring the specimen-induced aberrations and preshaping the wavefronts in the input beam was reported by Neil *et al.* [34]. They used a liquid crystal spatial light modulator (SLM) to measure the specimen induced aberrations and apply the phase conjugate of these aberrations to the imaging laser beam. They reported the restoration of resolution 28 µm into a watery sample when using an 1.25NA oil-immersion lens. A drawback of their method was the significant loss of power due to both the continuous monitoring of the wavefront and the SLM.

When fluorescence light is used as a feedback, signal strength is often optimised by varying the shape of the incoming light via genetic algorithms [37, 98, 99, 289], or image-based algorithms [36, 297, 298], although other feedback parameters like brightness, contrast and resolution have also been investigated [106]. In Marsh *et al* a deformable membrane mirror (DMM) was placed post scan and a

look-up-table approach was implemented that used preoptimised DMM shapes at specific depths as intelligent starting points for subsequent optimisations using a Hill climbing algorithm [35]. For higher generation harmonics, sharpness rather than intensity provides an appropriate feedback [299]. Alternatively a differential aberration imaging technique has been demonstrated that rejects out-of-focus fluorescence background signals by using a defocus image [300]. In a new development, fluorescent light emitted by artificial guide stars has been used to measure the aberrations directly with a wavefront sensor in order to apply the optically conjugate aberrations with a DMM in a closed-loop configuration. The reference sources employed were either injected fluorescent microspheres or non-linear guide stars created by TPEF [301–303].

In the next chapter, PSF engineering by means of a 32 actuator MEMS DMM in an adaptive NLM was employed. The aberration correction was determined in a wavefront sensorless approach by rapidly altering the DMM shape with a random search algorithm (RSA) (section 2.6.2) until the TPEF or SHG signal intensity was satisfactorily improved. Using a RSA in conjunction with a merit factor (MF) has two distinctive advantages in this microscopy application. First, it eliminates the need for re-imaging and wavefront sensing, thereby reducing complexity and cost of the optical setup. Second, this approach uses the specific signal that is to be improved as a MF such that every increase in MF directly leads to an enhancement of fluorescence excitation at the depth of optimisation. The RSA used in this work has previously been successfully applied to AO in CARS, confocal imaging microscopy and optical trapping [38, 102, 104].

The benefits of wavefront compensation for system- and sample induced aberrations is demonstrated in a variety of samples. For example, the imaging of fluorescent beads, *convallaria* and urea crystals are compared with and without aberration correction. Additionally intermediate tissue culture systems in form of organotypic collagen I assays are investigated. These tissues allow for the possibility of optimising on an intrinsic SHG signal providing an optimisation procedure which is not limited by photobleaching therefore allowing many algorithm iterations. This optimised mirror shape can then be stored in a look-up-table and called upon for multiphoton imaging at a specific depth.

High quality beam profiles and stable focusing at depth are important not only in high-resolution microscopy but are also central to other applications in optical and photonic engineering, for example, in the fields of laser micro/ nanofabrication [8–10].

Chapter 6

AO in a Nonlinear Microscopy System

Abstract This chapter describes the implementation and characterisation of a multiphoton and second harmonic microscope system with incorporated deformable membrane mirror (DMM). Its use, capabilities and limitations for compensating system- and sample induced aberrations are demonstrated. The optimum shape of the DMM was determined with a random search algorithm (RSA) optimising on either two photon excited fluorescence (TPEF) or second harmonic generation (SHG) signals. A variety of samples were investigated, including fluorescent beads for spatial resolution analysis and *convallaria*, an easy to use test sample, typically employed in microscopy due to yielding large amounts of fluorescent signal. Organotypics, tissue-like samples comprised of red fibroblast cells embedded in collagen, can produce TPEF as well as SHG signals. This chapter investigates using these and other samples to optimise on an intrinsic SHG signal to determine the aberration correction required, an approach which is not limited by photobleaching and to then determine the usefulness of this DMM shape in imaging fluorescent structures. Additionally, z-stacks, series of images along the z-axis with a fixed lateral position, were recorded. This allows the quality of the image to be analysed with depth. Some significant improvement in signal intensity was achieved in TPEF and SHG imaging modalities with improvement factors ranging from 1.2 to 8.5 fold. However, diffraction limited resolution was not restored and might require careful re-consideration of the merit factor. Even if the penetration depth is ultimately limited by scattering in many biological specimens, it was demonstrated that adaptive optics (AO) can improve the quality of images at depths at which imaging would not have been possible without aberration correction.

Acknowledgments All laboratory related measurements presented in this chapter were conducted in collaboration with Dr. Ewan McGhee in the Advanced Imaging Resource within the Beatson Institute of Cancer Research in Glasgow under the direction of Prof. Kurt Anderson. The organotypics, samples routinely cultured and investigated at the Beatson institute, were kindly provided by Dr. Paul Timpson and Max Nobis.

Contents In the first section of this chapter the experimental conditions are detailed, including the optical setup (subsection 6.1.1), the alignment procedure (subsection 6.1.2), and the samples under investigation (subsection 6.1.3). The original results obtained in these studies are presented in section 6.2. After giving more information on the calibration and characterisation of the optical setup (subsection 6.2.1), the necessary adaptations of the RSA to the application are detailed. This includes a routine for the compensation of photobleaching (subsection 6.2.2) and the acquisition of the merit factor through either parking of the beam or scanning of a small region of interest (subsection 6.2.2). The problem of imaging at depth and the resulting degradation of signal strength and resolution is discussed in subsection 6.2.3. The outcome of optimisations performed on fluorescent beads of two different sizes are detailed in subsection 6.2.4. The effect of the optimisation on signal intensity and resolution is analysed as well as displacements and distortions introduced by the optimised DMM shape. In subsection 6.2.5 optimisations performed on SHG signal producing urea crystals are presented and it is also discussed how such a DMM shape performed in the imaging of fluorescent beads. The imaging of organotypic samples with DMM shapes that have been previously optimised on either fluorescent beads, urea crystals or the fibroblast cells within the organotypic sample is compared in section 6.2.6. This chapter concludes with a discussion (section 6.3) and the summary and conclusions given in section 6.4.

6.1 Experimental details

6.1.1 Optical setup

The experimental setup combines nonlinear imaging within an inverted microscope (Nikon Eclipse TE2000-U) and an AO system for aberration correction (Fig. 6.1). A fs pulsed Ti:Sapphire laser (Chameleon, Coherent UK), lasing at a

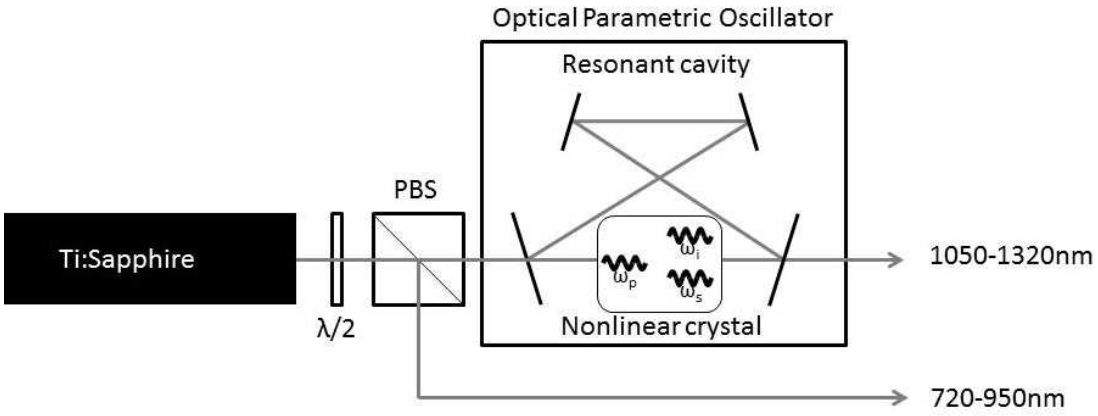

(a)

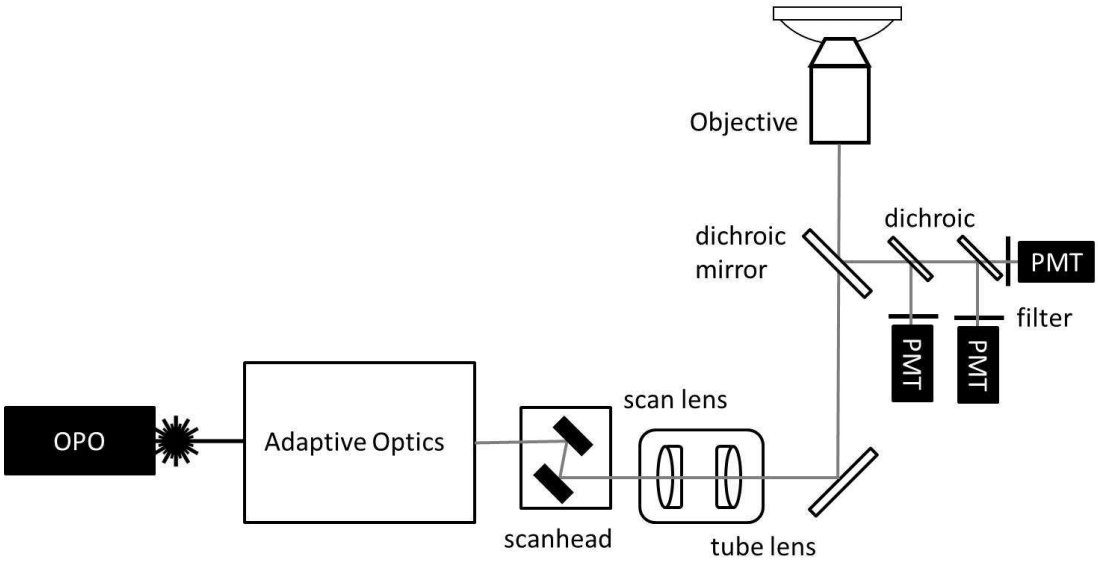

(b)

Figure 6.1: Simplified nonlinear microscope setup. **(a)** Light sources: the Ti:Sapphire is split into two components through polarisation optics. The first one can be used directly as an excitation source, the other one is used as a pump source for the OPO (optical parametric oscillator). $\lambda/2$: half-wave plate, PBS: polarising beam splitter. **(b)** The light from the OPO first passes through the AO system (shown in Fig. 6.2) and is then directed toward the scanhead. From there it is re-imaged onto the back aperture of the microscope objective within an inverted microscope through a telescope made up from the scan lens and the tube lens. Fluorescence light is collected by the same objective and re-directed with a dichroic mirror towards the photomultiplier tubes (PMTs) in epi-configuration for detection in a non-descanned mode.

repetition rate of 80 MHz and tuned to a wavelength of 840 nm is used to pump an optical parametric oscillator (OPO) (MIRA, Coherent Ape). Optical parametric oscillation is a nonlinear process based on non-critical phase-matched interaction within a periodically poled crystal. In this process, a short wavelength pump beam is converted into two tunable beams (the signal and idler beam) of longer wavelength [304]. The OPO allows automated, software-controlled wavelength tuning and stabilization with a feedback loop based on a miniature spectrometer in combination with motorised cavity length tuning integrated inside the OPO head enclosure. The OPO is tuned to emit at the wavelength of 1098 nm and the output power is kept below 15 mW at the back aperture of the microscope objective throughout the experiments. All optical elements in the pathway are coated and corrected for the extended wavelength to optimise efficiency.

The AO components are detailed in Fig. 6.2. The OPO output beam passes a 994 nm long pass filter cutting out any visible wavelengths and is then directed towards the active region (1.5 mm ⌀) of the DMM. Appropriate polarisation optics allow for an incident angle of 0° onto the DMM surface as described in more detail in the previous chapter (section 8.1.1) of this thesis.

The DMM employed in this work (Mini-DM, Boston Micromachines Corporation) uses 32 independent electrostatic actuators to control the shape of the highly reflective, gold coated membrane which is placed beneath a protective window with $400 - 1100$ nm AR coating. By applying control voltages U_c of up to 255 V (8 bit scale) to underlying actuators the membrane can be deformed. More details on the DMM can be found in section 2.5.1 on page 25 of this work. The DMM is re-imaged onto a conjugate point between the close-coupled, galvanometer-based scan mirrors inside a commercial scan head specifically designed for multiphoton excitation (Trim-scope, LaVision BioTec, Germany). This is done with a 4f re-imaging system that ensures that the DMM and the closed coupled scanner are in conjugate planes and also that the beam is expanded to a size that allows maximum transmission through the scan head. A pair of flipper mirrors was inserted into the setup such that imaging with the system including AO optics could be easily compared to the original system. They also ensured that the imaging routine of other users of the Beatson imaging facilities would not be disrupted by the experiments presented in this work.

The light is imaged from the scanner onto the back aperture of the microscope objective via a combination of an inbuilt scan lens- tube lens telescope and a dichroic mirror within the microscope turret which reflects the IR light to-

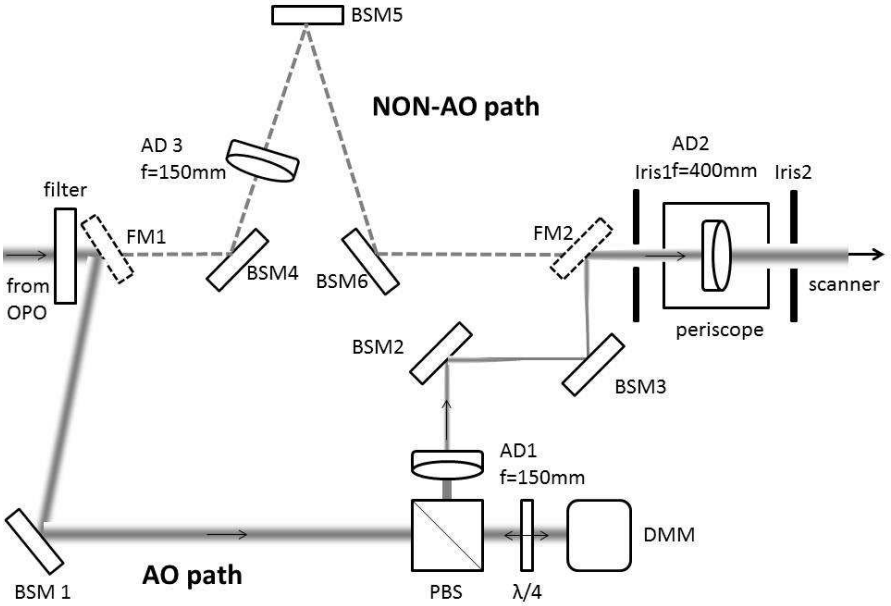

(a)

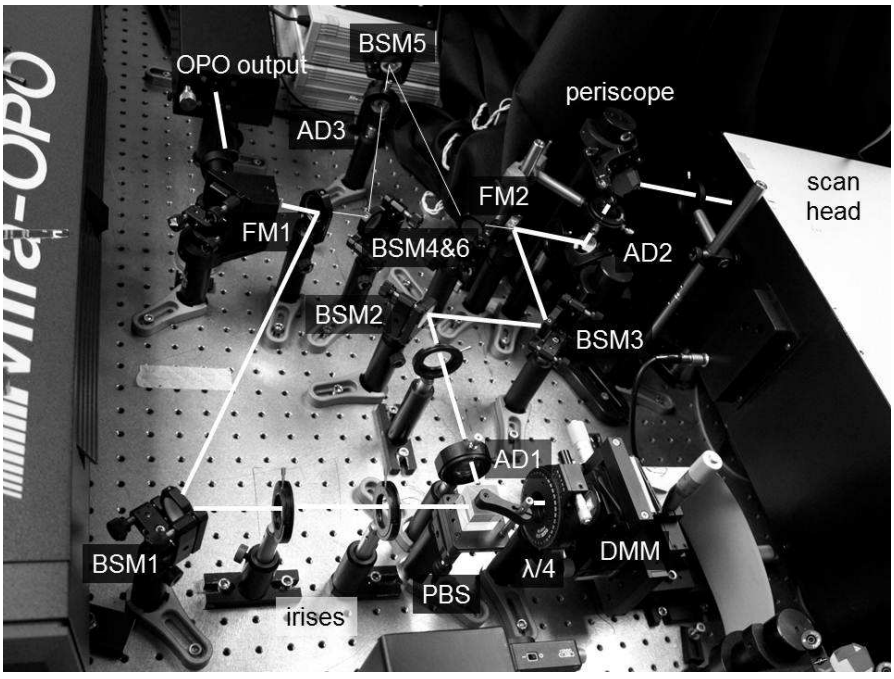

(b)

Figure 6.2: AO components in the nonlinear setup. **(a)** OPO: optical parametric oscillator, FM1, FM2: flipping mirrors, BSM1-6: beam steering mirrors, AD1-3: achromatic doublets, PBS: polarising beam splitter cube, $\lambda/4$: quarter-wave plate, DMM: deformable membrane mirror. **(b)** Photograph of the AO components in the nonlinear microscope setup.

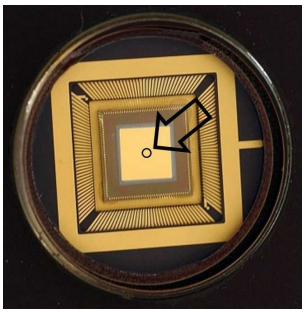

Figure 6.3: Active region of the BMC DMM of 1.5 mm^2 within a large, visually identical reflective area of roughly 1 cm^2 (source: [305]).

wards the microscope objective. Care has been taken to only slightly overfill the 6 mm back aperture of the objective in order to make use of its full NA while not losing significant modulation power of the DMM in the periphery. All imaging was done with a high NA, oil immersion objective (100x 1.3NA, Nikon) which focuses the light into a sample mounted on an xyz translation stage. The galvanometer scanner in combination with the motorised microscope stage allows for three-dimensional rastering of objects. Scanning and image acquisition was done with the commercial software of LaVision BioTec. The blue-shifted fluorescence is collected by the same objective, transmitted by the dichroic mirror and finally detected by non-descanned detector photomultiplier tubes (PMTs) (Hamamatsu H6780-20-LV 1M for >500 nm detection) located at the back focal plane of the objective (epi-configuration). A combination of a dichroic mirror (Semrock, DIO-R594 LP) and two emission filters (SHG: Semrock 549/15 BP, TPEF: Semrock 630/60 BP) allow for the simultaneous detection of SHG and TPEF in two detection channels and keep the IR light from saturating the detectors.

The modal content of the DMM shape was determined by Zernike mode decomposition measured by replacing the microscope objective with a Shack-Hartmann wavefront sensor (WFS, Thorlabs WFS150C) in such a way that the DMM surface was re-imaged onto the sensor array.

6.1.2 Alignment

When aligning the AO setup it is essential to hit the DMM exactly in the centre of its active region. This can prove to be extremely difficult because of multiple reasons. An invisible laser wavelength, a small active region of only 1.5 mm^2 in the centre of a large reflecting area (roughly 1 cm^2) that visually looks the same (Fig. 6.3), and a window with AR coating which is mounted at an angle over the

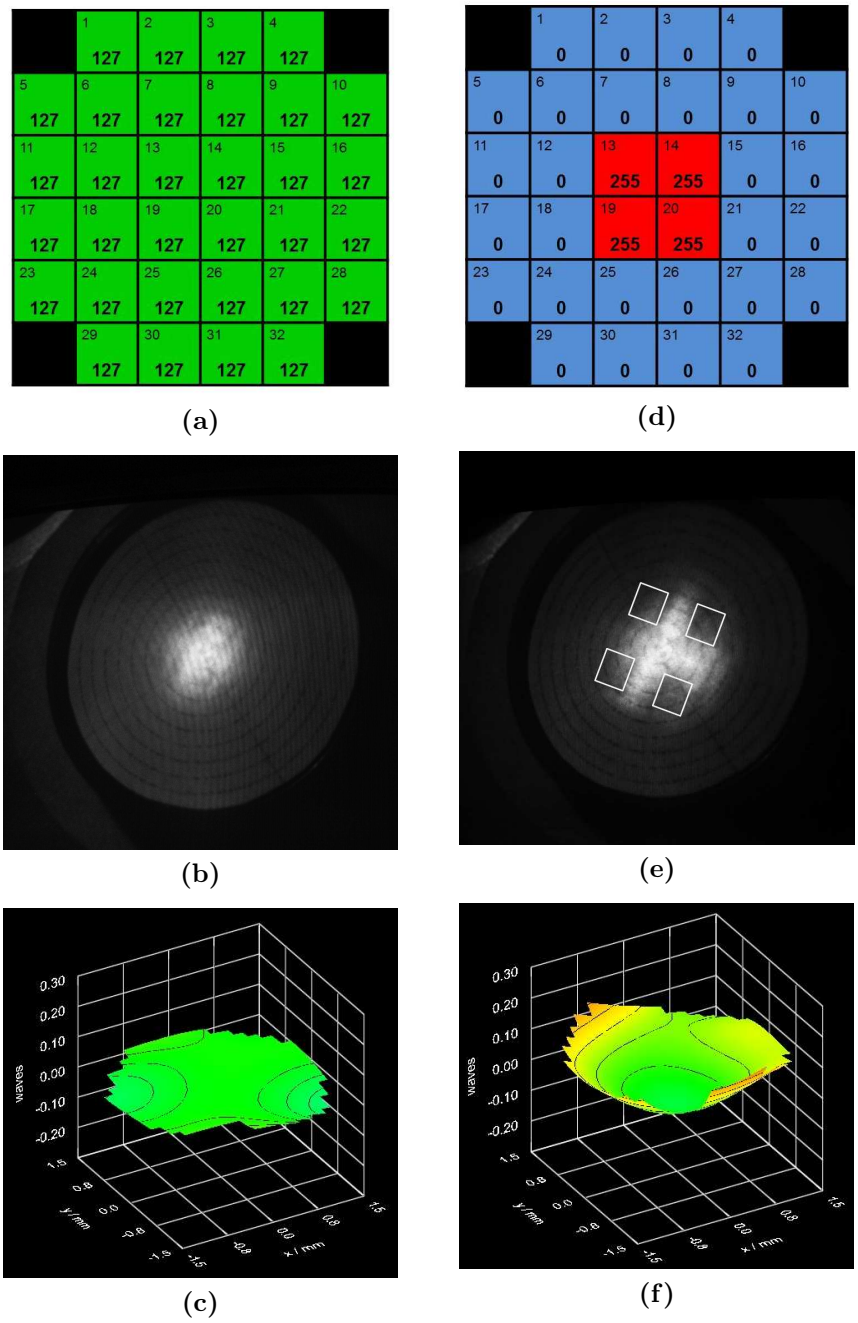

Figure 6.4: DMM shapes imaged onto a target mounted on the turret for microscope objectives viewed by an IR camera. **(a)** Bias shape: all actuators are set to a control voltage of $U_c = 127\,\mathrm{V}$. **(b)** Image of the bias shape on the target. The pattern produced by the regular matrix of actuators can be used to find the centre of the active region on the DMM. **(c)** Reconstruction of the DMM shape with the WFS. **(d)** DMM shape with the central four actuators set to maximum control voltage ($U_c = 255\,\mathrm{V}$) while all other actuators are set to $0\,\mathrm{V}$. **(e)** Image of the DMM shape schematically shown in 6.4d on the target. The white squares indicate the position of the central four actuators set to maximum voltage. This shape and image has been used to perfectly align the DMM in the lateral directions with the optical axis coinciding with the cross hair of the target. **(f)** Reconstruction of the DMM shape with the WFS.

DMM membrane all contribute to the problem. We have developed a simple and effective way to align the active region with high accuracy on the optical axis of the system by imaging the actuator pattern of the DMM onto a target which can be screwed onto the turret of the microscope. The image is taken with an IR camera mounted on a laboratory clamp that allows it to be easily positioned vertically above the microscope turret.

When the bias DMM shape (Fig. 6.4a, is applied, the symmetric matrix of the actuator array is imaged onto the target (Fig. 6.4b). For rough alignment it is then possible to adjust the lateral position of the DMM along x with the translation stage of the mount such that, by counting the squares in the actuator matrix from one edge of the chip to the other, the DMM can be brought back to mid position. This is repeated in y-direction until the centre of the active region is found. The next step provides an even finer adjustment by applying a DMM shape which will put the maximum permissible control voltage of $U_c = 255\,\mathrm{V}$ on the central four actuators while keeping all remaining actuators at 0 V (Fig. 6.4d). When this DMM shape is applied a clearly distinguishable, cross-shaped pattern is produced on the target (Fig. 6.4e) whose centre can then precisely be aligned with the cross hairs on the target, again by using the translation stages on the DMM mount. The reconstructions of the wavefronts corresponding to the bias DMM shape and the DMM shape which has the central four actuators on maximum voltage are depicted in Figures 6.4c and 6.4f respectively.

6.1.3 Samples

In MPM fluorescence is excited by the simultaneous absorption of $n \geq 2$ photons that together provide the necessary energy for excitation which predicts optimum excitation wavelengths at roughly twice the corresponding single photon wavelength. The excitation wavelength of 1098 nm was selected so as to simultaneously excite TPEF and SHG emitted from the same tissue structure (organotypic samples, described below) while remaining inside the anti-reflection coating window on the DMM. The emission wavelength of SHG is always exactly half the excitation wavelength which is not the case for TPEF (Fig. 5.5) and affects the choice of filters in the detection channels of the microscope. In this section a brief introduction of the samples used in the experiments is given.

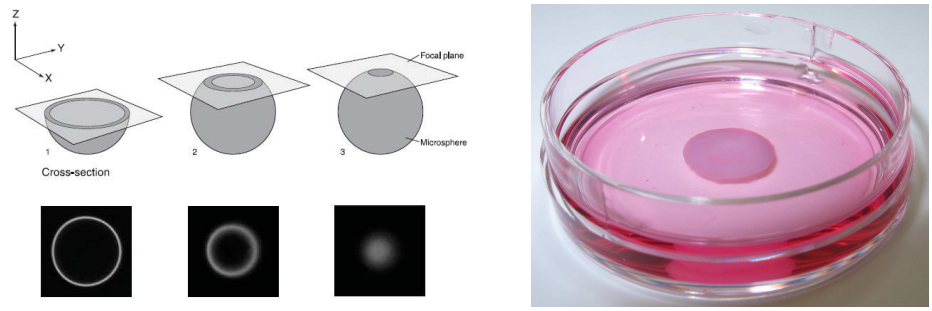

(a) **(b)**

Figure 6.5: **(a)** Calibration of a laser-scanning microscope with ring stained microspheres. The diameter of the fluorescent ring (or disc) is dependent on the depth of the focal plane (source: Invitrogen [306]). **(b)** Photograph of the contracted organotypic collagen assay.

Fluorescent beads Fluorescent microspheres, mounted on the surface of a test slide (F36909 FocalCheck^{TM} fluorescence microscope test slide #1, invitrogen, molecular probes), were available in various sizes. This test slide is commonly used for the calibration of fluorescence microscope systems and to evaluate their performance. The spheres are mounted in optical cement of refractive index n=1.515 to maximise stability and minimise the introduction of spherical aberrations when imaging with an oil immersion microscope objective. A bead of 15 µm diameter was used as a target to calibrate the microscope objective in its typical magnification settings and also to assess the spatial resolution by using the sphere's stained walls as structures below the resolution limit. Imaging these walls provides a line spread function (LSF) whose fitting parameters are used to plot the modulation transfer function (MTF) of the system. Fig. 6.5a depicts a ring stained fluorescent bead and the dependency of the fluorescent ring (or disc) on the depth of the focal plane (Source: Invitrogen [306]).

A fluorescent microsphere (PS-Speck^{TM} Microscope Point Source Kit, Molecular Probes, Invitrogen) with a diameter of (175 ± 5) nm was used as a uniform, sub-resolution fluorescent point source for the determination of lateral and axial resolution through fitting of a Gaussian function to the resulting point spread function. The full width half maximum of this fit is a common way to quantify spatial resolution. These bright, mono-dispersed microspheres exhibit a single photon excitation/emission wavelength of 540 nm/560 nm.

Convallaria *Convallaria majalis*, commonly known as lily-of-the-valley, is a test sample often used in fluorescence microscopy [307, 308]. A *convallaria* rhi-

zome cross-section specimen (Johannes Lieder GmbH & Co. KG, Ludwigsburg, Germany) which is stained with acridine orange and mounted beneath a glass coverslip was used to test the system in the TPEF modality. This sample provides ample TPEF signal throughout a broad range of wavelengths and exhibits sub-cellular features such as nuclei and cell membranes.

Urea crystals Urea (Carbamide, Carbonyldiamide, $(NH_2)_2CO$, refractive index n = 1.49) in the form of white powder (U7378, Sigma Aldrich) was diluted in distilled water and left for crystalisation. The urea crystals have nonlinear properties that can generate second harmonics [309,310]. The dried crystals were placed on a petri dish and imaged to test the system in the SHG modality.

Basement membrane The basement membrane is a thin sheet of fibers fusing two types of lamina each made up of different types of collagen. The basement membrane underlies the epithelium and the endothelium, tissues lining the interior surface of organs or blood vessels. The specimen used in this work was excised from a freshly killed mouse and immediately imaged through the SHG signal exhibited by the collagen.

Organotypic collagen I assay These intermediate tissue culture systems, shown in Fig. 6.5b, are important experimental mediates often replacing naturally occurring living animal samples. These cultures approximate certain aspects of *in vivo* environments but are more easily accessible for experimental manipulation such as the use of stably transfected cell lines, drug treatment regimes, long term and high-resolution imaging [312]. The cultures are comprised of fibroblast

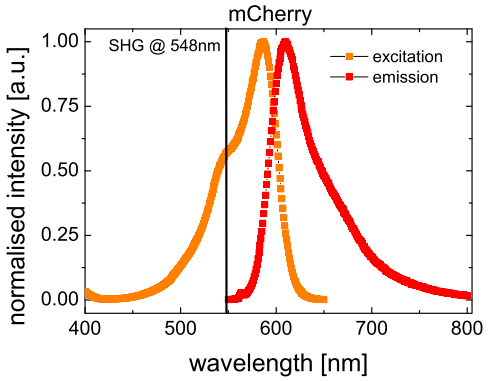

Figure 6.6: Excitation and emission spectra of mCherry. Also shown is the SHG emission for excitation with $\lambda = 1098\,\mathrm{nm}$ (source of spectral data: [311]).

cells, acquired from a human forearm, and type I collagen, extracted from the tendons of rat tails. The organotypic cultures used in this work have all been grown in house at the Beatson Institute of Cancer Research and a detailed protocol for their production can be found in Timpson *et al.* [312]. The fibroblast cells contract the gel-like collagen so that it assumes fibrillar form. This fibrillar collagen exhibits narrow band SHG from a broad input wavelength range with maxima at 1100 nm [272] whereas the living fibroblast cells are transfected with mCherry. This bright, monomeric, red fluorescent protein has been re-evolved by extensive mutagenesis from mRFP1 which in turn has been derived by cloning and expression of a fluorescent protein known as DsRed from *Discosoma* coral [313]. The excitation and emission spectra of mCherry are shown in Fig. 6.6 as well as the SHG emission line when an excitation wavelength of 1098 nm is selected.

6.2 Results

The following section details the original work carried out by the author at the Beatson Institute labs.

6.2.1 Calibration and characterisation

Magnification

In order to calibrate the microscope system an image of the largest fluorescent bead on the test slide was taken with the typical magnification settings of the full field of view being imaged by 503 x 503 pixels. The bead diameter of 15 µm ((Fig. 6.7)) was imaged with 74 pixels giving an imaging ratio of 4.93 pixel/µm

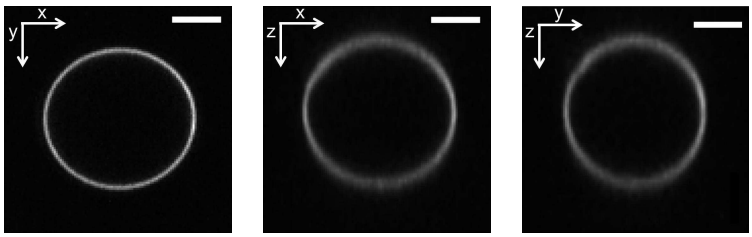

(a) **(b)** **(c)**

Figure 6.7: Calibration with a ring stained bead of 15 µm diameter. The bead was imaged with a z stack and orthogonal views were reconstructed with ImageJ. Equatorial plane **(a)** in the xy plane, **(b)** the xz plane, **(c)** and the yz plane. Scale bar is 5 µm.

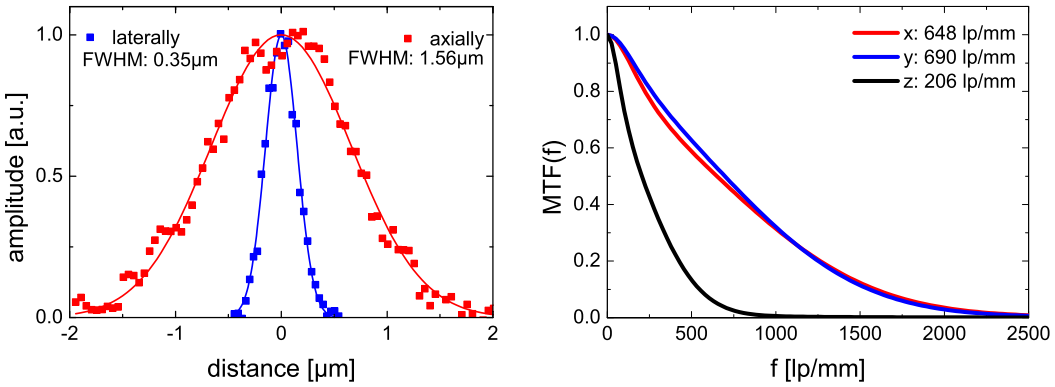

(a) (b)

Figure 6.8: **(a)** Spatial resolution in terms of the FWHM of a Gaussian fit (line) to the lateral and axial line profiles of a subresolution sized bead (∅ = 175 nm) (closed symbols). **(b)** Spatial resolution in terms of the MTF vs. spatial frequency.

(1 pixel equals 0.203 µm in the lateral directions). In the axial direction the step size of the image stack gives the pixel to micron ratio and is therefore dependent on the individual stack.

Spatial resolution

FWHM The most common way of quantifying spatial resolution is by imaging a subresolution sized microsphere and fitting a Gaussian function to the one dimensional line profile. The full width half maximum (FWHM) of that fit gives a value for the spatial resolution in that dimension. Fig. 6.8a shows the lateral (blue) and axial (red) line profile taken from a stack imaging a bead of 175 nm diameter. The insets quote the FWHM of the fits to Gaussian functions (lines): $\mathrm{FWHM}_{\mathrm{lat}}^{\mathrm{exp}} = 0.35 \pm 0.01\,\mu\mathrm{m}$ in the lateral direction and $\mathrm{FWHM}_{\mathrm{ax}}^{\mathrm{exp}} = 1.56 \pm 0.03\,\mu\mathrm{m}$ in the axial direction. With the equations 5.2 and 5.3 for the width of the lateral and axial Gaussian functions (page 76), the theoretical values can be calculated. For $n = 1.515$, NA=1.3 and $\lambda = 1098\,\mathrm{nm}$, $\mathrm{FWHM}_{\mathrm{lat}}^{\mathrm{theo}} = 0.33\,\mu\mathrm{m}$ and $\mathrm{FWHM}_{\mathrm{ax}}^{\mathrm{theo}} = 0.93\,\mu\mathrm{m}$. Whereas the resolution in lateral directions is in good agreement with the theoretical resolution limit, the axial resolution is slightly above the expected theoretical value. These measurements, however, were made with the DMM in place and operated with bias voltage which could explain slightly degraded resolution.

MTF Another way of quantifying spatial resolution is by means of the modulation transfer function (MTF). The MTF plots the loss in contrast when imaging increasingly finer structures. Mathematically, the MTF is the discrete Fourier transform of the line spread function MTF = $\mathscr{F}$(LSF) (see also p. 11 and section 4.1.5), which in turn is acquired from an image of a thin line. The fluorescent hull of the ring stained bead of 15 µm diameter spanning roughly over 2 pixels ($\approx$ 0.4 µm) was used, which is marginally above the theoretical lateral resolution limit. To obtain the MTF, the sample points of the LSF, corresponding to the grey values of the pixels illuminated by the hull, were first fitted to an analytical model function taken from [181] (Fig. 6.9a). This function is comprised of a Gaussian function, corresponding to the narrow central component, and an exponential function, corresponding to the broad tail component of the LSF:

$$\mathrm{LSF(x)} = a_2 \exp\left(-\frac{(x-a_1)^2}{2a_3^2}\right) + a_4 \exp\left(-\frac{|x-a_1|}{a_5}\right) \tag{6.1}$$

where the parameter a_1 represents the center of the fitted LSF, a_2 and a_3 are the amplitude and standard deviation (STD) of the Gaussian function respectively and a_4 and a_5 are the weighting and the slope of the exponential function respectively. The fitting was performed with OriginPro and required a set of well chosen initial values for all parameters. The MTF is obtained from the modulus of the Fourier transformation of Eq. 6.1 and is given by [181]:

$$\mathrm{MTF(u)} = \frac{1}{\sqrt{2\pi}\,a_2a_3 + 2a_4a_5}\left(\sqrt{2\pi}\,a_2a_3 \exp\left(-2(\pi a_3 u)^2\right) + \frac{2a_4a_5}{1+4(\pi a_5 u)^2}\right) \tag{6.2}$$

where u is the spatial frequency. The MTF was plotted by substituting the parameters $a_2 - a_5$ which were obtained from the fitting of the LSF into equation 6.2. The resulting MTF, shown in Fig. 6.9b, allows for a simple quantification of spatial resolution by determining the number of line pairs per mm (lp/mm) that can be imaged at 25 % contrast.

The spatial resolution of a scanning laser system is dependent on the scanning direction, due to the galvanometer for each scanning direction operating at a different scanning frequency (fast scan vs slow scan). Fig. 6.8b shows the three MTFs corresponding to the three dimensions. Each MTF has been plotted by averaging the parameters obtained from the fits of four different LSFs on the same bead. In our system, similar resolutions were found along the horizontal- and vertical-

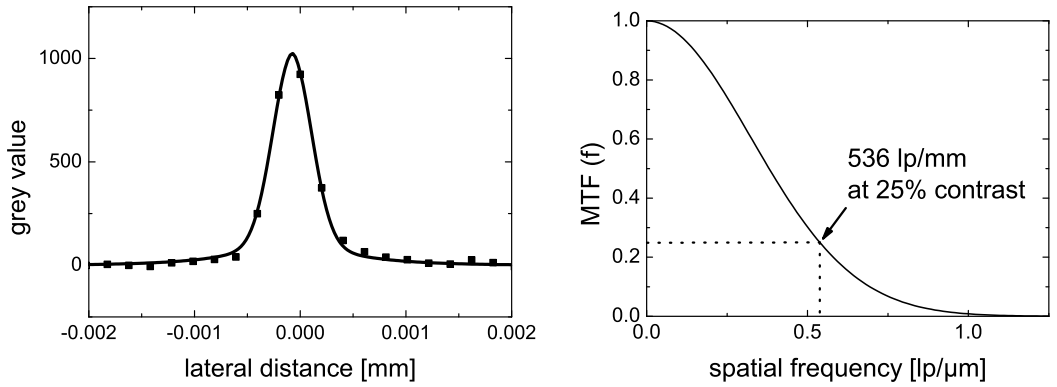

(a) **(b)**

Figure 6.9: Calculating the MTF. **(a)** The LSF obtained from imaging the fluorescent hull of a 15 µm diameter bead (closed symbols) and the fit to the data according to the model function (eq. 6.1, line). The parameters obtained from this fit are used to plot the MTF. **(b)** Normalised MTF generated by Fourier transform of the fitted LSF function (eq. 6.2). The line indicates the spatial resolution in linepairs/µm where contrast has dropped to 25 %.

scanning direction. The resolution of the optical system is $r_x = 648\,\mathrm{lp/mm}$ for the horizontal and $r_y = 690\,\mathrm{lp/mm}$ for the vertical scanning direction. Along the z axis, resolution was worse by a factor of 3.2 ($r_z = 206\,\mathrm{lp/mm}$) where the theoretically predicted factor is 2.82 fold.

6.2.2 Adaptation of the algorithm

The following sections are giving details about necessary adaptations to the general RSA described in section 2.6.2 on page 29 in order to make it suitable for this specific application.

Proof of concept

As an initial proof of concept image quality was intentionally degraded by applying a highly distorting DMM shape in order to test whether the optimisation routine was able to restore signal strength. The starting shape (Fig. 6.4d), results from applying the maximum control voltages ($U_c = 255\,\mathrm{V}$) to the central four actuators while setting the remaining actuators to zero and introduces a considerable amount of distortions, predominantly defocus. The effect on the image was an immediate degradation of signal intensity (Fig. 6.10a). An optimisation was run with the aim of restoring signal intensity and the resulting image is shown in Fig. 6.10b. A strong improvement in signal and contrast is noticeable especially

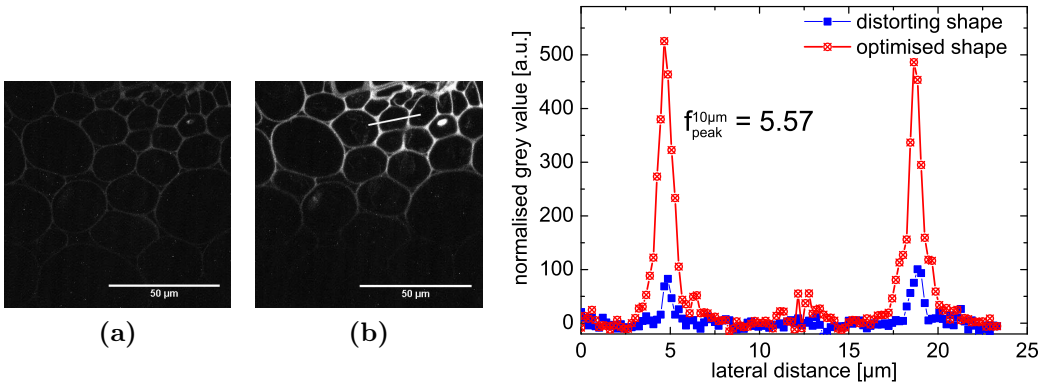

(a) **(b)** **(c)**

Figure 6.10: *Convallaria* **(a)** imaged with the highly distorting DMM shape(Fig. 6.4d) and **(b)** after optimisation. The loss in signal intensity introduced by the highly distorting starting shape was recovered through the optimisation process. **(c)** Intensity profiles along the line marked in (b) before and after optimisation. The signal intensity improvement factor for the peaks was $f_{\text{peak}} = 5.57 \pm 1.23$. The lines serve as a guide to the eye.

in the upper right corner of the image. Fig. 6.10c quantifies the improvement by depicting the grey value along the line profile shown in (b). After subtraction of the background for both images, the grey values have been scaled to give 100 % for the intensity peak before optimisation. This gives an improvement factor at the peaks in the line profiles of $f_{\text{peak}} = 5.57 \pm 1.23$.

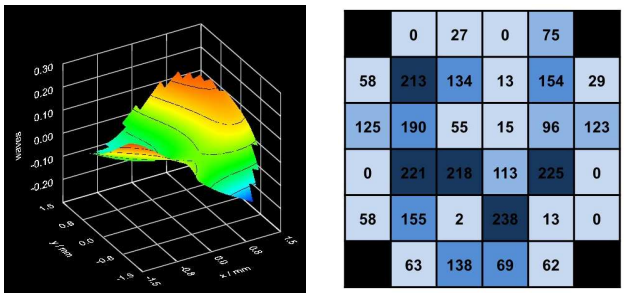

(a) **(b)**

Figure 6.11: DMM shape after optimisation. **(a)** Reconstruction of the DMM shape. **(b)** Actuator map of the control voltages applied. The mean applied control voltage was $U_c^{\text{mean}} \approx 90 \pm 78\,\text{V}$ within a range of $U_c^{\text{min}} = 0\,\text{V}$ and $U_c^{\text{max}} = 238\,\text{V}$.

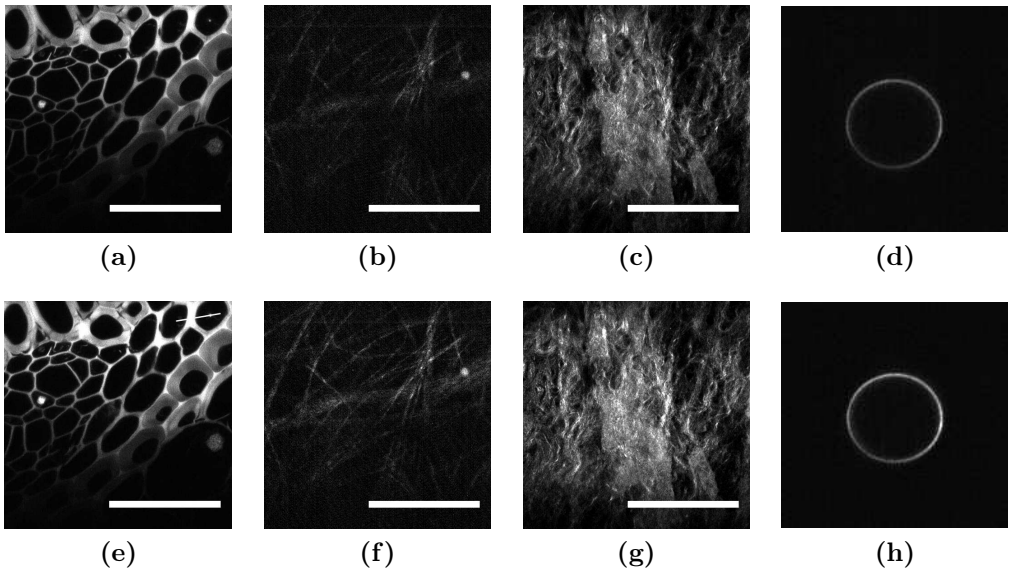

Figure 6.12: Samples qualitatively tested for their suitability for optimisations in terms of SNR and bleaching. **(a,e)**: *convallaria* (TPEF), **(b,f)**: basement membrane (SHG), **(c,g)** basement membrane (SHG), **(d,h)** ring-stained fluorescent microsphere (TPEF) ($\varnothing = 15\,\mu m$). The first row shows the sample imaged with the bias shape whereas the second row shows the same sample after optimisation. The scale bar is $50\,\mu m$.

DMM stroke

This test run confirmed various important points. First, that the DMM was well aligned, meaning that the active area was well illuminated and properly reimaged onto the back aperture of the microscope objective. Second, the stroke of the DMM was sufficient to induce changes in the wavefront that were large enough to considerably affect imaging. The optimised DMM shape and the underlying actuator map indicating the applied control voltages for each actuator are shown in Fig. 6.11. An analysis of the control voltages applied to each single actuator of the optimised shape showed that the DMM was not running out of stroke. The mean control voltage (U_c on an 8 bit scale) applied to actuators was $U_c^{mean} \approx 90 \pm 78\,V$ within a range of U_c^{min}=0 V and U_c^{max}=238 V.

In a next step, optimisations on different samples, starting from the bias shape, were performed to test the signal to noise ratios and bleaching levels produced by different imaging modalities (TPEF *vs.* SHG) and different tissues.

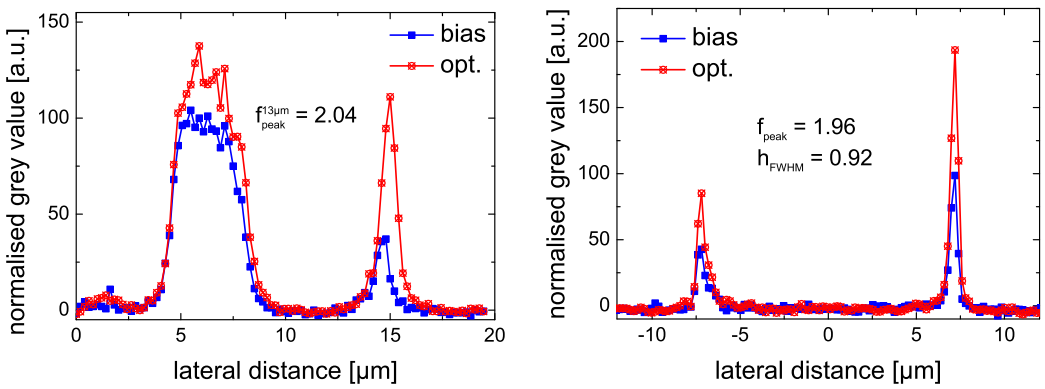

Figure 6.13: Signal improvement in TPEF. **(a)** Normalised grey value along the line profile depicted in Fig. 6.12e from an optimisation on *convallaria*. Fluorescent signal improvement factor $f_{\text{peak}}^{\text{conv}} = 2.04 \pm 1.16$. **(b)** Normalised grey value across the diameter of a ring-stained fluorescent microsphere shown in Fig. 6.12h. Fluorescent signal improvement factor $f_{\text{peak}}^{\text{bead}} = 1.96 \pm 0.03$. The lines are displayed to guide the eye.

Signal to Noise

Fig. 6.12 shows images acquired with the bias shape (a-d) and an optimised DMM shape (e-h) of various samples such as *convallaria* (signal: TPEF) (a,e), basement membrane (signal: SHG) (b,c,f,g) and a ring-stained fluorescent microsphere of 15 µm diameter (signal: TPEF) (d,h). It was possible to run successful optimisations for all of the tested samples, however, SHG signals produced much higher SNR and can not be photobleached making them an easier merit factor (MF) to optimise on.

Fig. 6.13 exemplarily shows the improvement in the fluorescence signal generated by *convallaria* (Fig. 6.13a) and the fluorescent bead of 15 µm diameter (Fig. 6.13b). Both optimisations started from the bias DMM shape. In the case of *convallaria*, a signal improvement factor of $f_{\text{peak}}^{\text{conv}} = 2.04 \pm 1.16$ was achieved. This factor was calculated by subtracting the same background for both images and normalising the peak before optimisation to 100 %. For the fluorescent bead, the same procedure yielded an improvement factor in fluorescence signal intensity at the peak of $f_{\text{peak}}^{\text{bead}} = 1.96 \pm 0.03$. In addition, the improvement in resolution was quantified by fitting a Gaussian function to the wall profile. Before optimisation, resolution was $\text{FWHM}_{\text{bias}} = (0.59 \pm 0.14)$ µm. After optimisation this value became $\text{FWHM}_{\text{AO}} = (0.54 \pm 0.06)$ µm. This means the FHWM was reduced to 91.5 % of its original value but did not reach the theoretical diffraction limit.

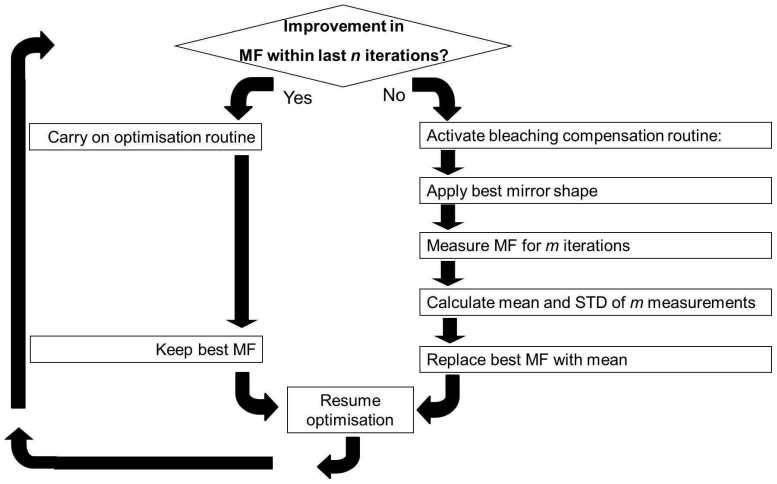

Figure 6.14: Schematic of the bleaching compensation routine. This loop is executed within the general random search algorithm described in section 2.6.2 and provides a regular re-normalisation of the MF.

A third important point, the ability of the algorithm to converge towards an improvement of the MF (signal intensity), proved to be strongly dependent on the implementation of a bleaching compensation, which will be described in the next subsection.

Bleaching compensation

In order to be able to optimise on a signal that will intrinsically decline with time due to photobleaching, a dedicated bleaching compensation routine was programmed into the general RSA.

Algorithm The compensation loop is schematically visualised in Fig. 6.14. If the optimisation algorithm did not achieve a successful iteration within a user-defined number of steps n, this routine applies the DMM shape that is currently saved as the best DMM shape so far (*i.e.* the shape producing the highest MF). The MF is then consequently measured for a user-defined number of iterations m without any changes to the DMM shape. The routine then automatically calculates the mean and standard deviation (STD) of these measurements. The mean is set as the new best MF, therefore taking into account that the old best value for the MF might no longer be achievable due to permanent photobleaching of fluorophores. The STD is used as a measure of the noise in the system by requiring that the MF associated with a new potential best DMM shape is at least one STD higher than the MF associated with the current best DMM shape.

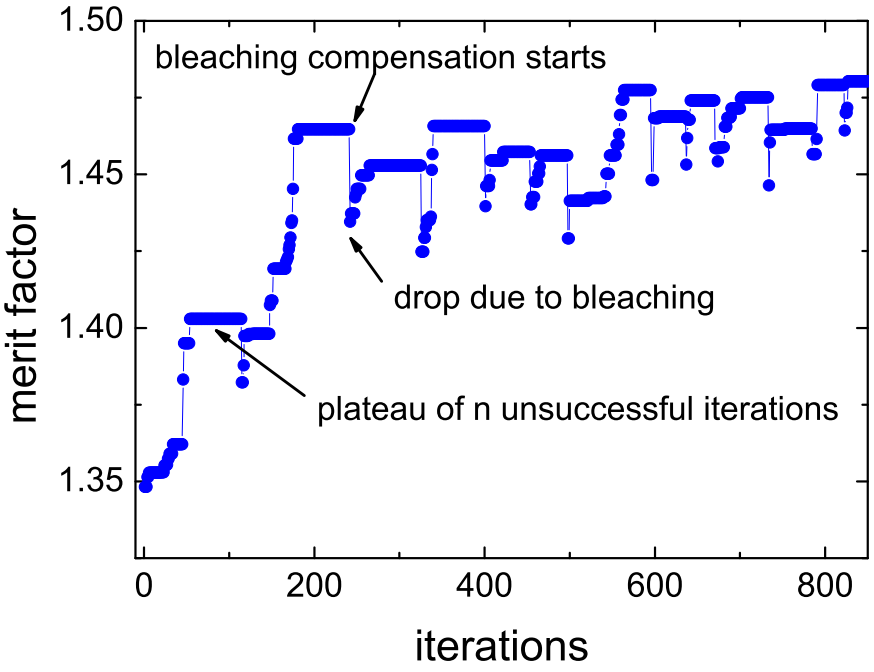

Figure 6.15: Optimisation graph showing the improvement of the MF (signal intensity) with each iteration. The arrows indicate the activation of the bleaching compensation (plateau in the optimisation graph). The subsequent drop in signal intensity is due to photobleaching.

In other words, in order to be accepted as the new best DMM shape, the currently measured MF will have to be one STD higher than the average calculated the last time the bleaching compensation routine was executed. In that way any decrease in signal strength due to photobleaching is taken into account in regular intervals. Depending on the noise in the signal $n = 10 - 20$ and $m = 7 - 15$ was chosen.

Optimisation graph Fig. 6.15 shows a typical optimisation graph displaying the improvement of the MF (signal intensity) with each iteration step. The arrows indicate a characteristic cycle of the bleaching compensation where the steep drop in the MF after each plateau is a measure of the photobleaching that has occurred since the last time the bleaching compensation routine has been called and is caused by the re-setting of the currently best MF to a revised, lower value. This particular optimisation was left running for almost 1000 iterations, roughly 100 of which were successful. This amount of successful iterations was a useful rule of thumb to determine when to stop the optimisation algorithm implying that, on average, each actuator was changed in value roughly three times. Here, the MF was improved from 1.35 to 1.46 which is an improvement of 8 %. We found, however, that an improvement of usually 10 % in the value of

the MF leads to a more pronounced improvement in signal intensity in terms of pixel grey value in the final image.

MF acquisition

The signal used as input for the MF had to be carefully chosen. Two possibilities for the signal source were identified each with its own benefits and disadvantages.

Parking In the first method, the galvo based scanning system was parked on one pixel in the full field image. The motionlessness of the scanning mirrors were confirmed to be stationary by clamping the driving voltages from within the scan head and displaying this signal on an oscilloscope. Accordingly, the signal read out by the PMT was the TPEF/SHG signal generated within this one pixel. The advantage of this method was that no detrimental driving signals associated with the frame rate of the scanner bled back into the PMT signal detection, distorting the MF. The disadvantage of this method, however, was that during the optimisation process the shape of the DMM is changed in a way that leads to considerable movement of the focal spot on the sample. Therefore a different region on the sample might be illuminated, corresponding to a different pixel on the image. If that area was not previously subjected to photobleaching, the signal suddenly jumped up simply because fresh, unbleached material generated the signal and not because the DMM shape had actually achieved an improvement in the illumination pattern.

Selecting a ROI The second method applied in this work, was to use the scanning software to manually select a small region of interest (ROI) encompassing a structure in its entirety in such a way that it included some black background pixels in the periphery. In this way, if the illuminated area on the sample under went a major jump caused by the change in DMM shape no fresh material within the sample was illuminated. The disadvantage of this method was the previously mentioned spikes caused by the driving signals for the galvo mirrors bleeding back into the PMT signal. In the following, parking of the galvos was used for optimisations performed on SHG signals because any improvement in signal intensity automatically was a consequence of an improvement in wavefront engineering. In the case of optimisation with TPEF, a ROI including an isolated structure surrounded by black background pixels was selected to generate the MF

so as to guarantee that only one fluorescent object would be imaged. Additionally, the scan frequency was reduced to 50 Hz to minimise the effect of spikes due to driving signals.

6.2.3 Degradation of image quality with depth

A detailed understanding of the ways images are degraded in quality and how this degradation can be quantitatively expressed is necessary for the further discussion. Equally, this knowledge will also allow a sensible treatment of images so as to extract the information needed to assess the success or failure of an optimisation. The decrease in signal intensity and resolution with increasing imaging depth has been evaluated qualitatively and quantitatively in *convallaria* (Fig. 6.16).

Degradation in resolution The first row highlights the decrease in resolution and image quality when the imaging depth was increased by 47 µm from an imaging depth of 13 µm (6.16a) to 34 µm (6.16b) and 60 µm (6.16c). This is best seen when all images are displayed in individual 8 bit scales which ensures that the tonal range of each image makes use of the full dynamic range of the 8 bit scale. As a consequence the images appear to be of equal brightness. Qualitatively, the image taken at a depth of 60 µm is considerably noisier and grainier compared to that taken at a depth of 13 µm and has lost all the details in structure.

For a quantitative analysis, the image histograms, displaying the distribution of each grey value, have to be compared. The histograms of images (a-c) are split into two components for clarity: the main bulk of the tonal range is given in Fig. 6.16g while 6.16h zooms into the information in the highlights of the image at the upper end of the 8 bit scale. From Fig. 6.16h it can be seen that all three images make use of the full dynamic range, *i.e.* all three are reaching grey values close to 255 which is explained by the fact that each image was displayed on its own optimum grey scale so as to appear of equal brightness.

The degradation in contrast, however, can be deduced by the spread and steepness of the slope of the main bulk of tonal values in Fig. 6.16g (on page 16 contrast was defined as the slope between dark and bright areas). The steeper the angle, the more contrast the image has. The histogram for the image taken at depth (blue) is spread out flat over a wide range while the histogram for the image taken closest to the surface (green) has a sharp peak in the shadow end of the scale. This can be quantified by the modal grey value, the most frequently

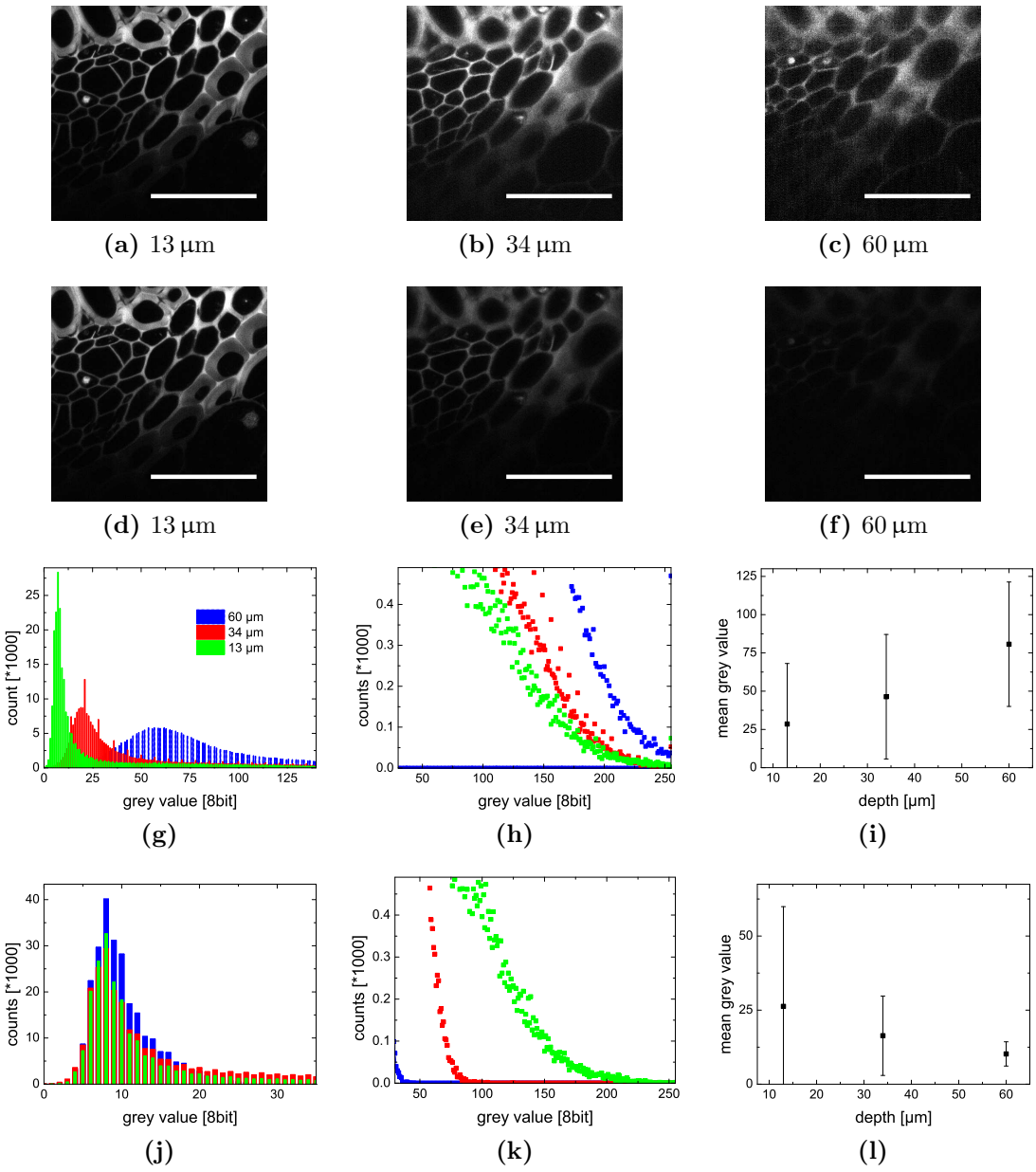

Figure 6.16: Degradation of signal intensity and resolution with imaging depth. All images were taken of the same *convallaria* sample (scale bar: 50 µm) with increasing imaging depth of **(a,d)** 13 µm, **(b,e)** 34 µm and **(c,f)** 60 µm. **(a-c)** show the images with equal brightnesses so as to highlight the degradation in resolution and image quality. **(d-f)** show the same images normalised to the grey scale of the image taken at a depth of 13 µm in (d) so as to highlight the decrease in signal intensity. **(g,h)** Histograms of (a-c). **(j,k)** Histograms of (d-f). **(i,l)** Mean grey value over the entire image as a function of imaging depth. The error bars are one STD.

occurring gray value corresponding to the highest peak in the histogram and the count of pixels with this grey value. These values are 7 (count 28,235), 21 (count 12,810), and 57 (count 5.796) for the image taken at a depth of 13 µm, 47 µm, and 60 µm respectively. This is illustrated by an increase in the mean grey value with depth according to the spreading out of the bulk tonal range (Fig. 6.16i). The STD remains the same for all three images as a consequence of displaying them on individual grey scales. This becomes sensible when recalling that roughly 7 times the STD has to contain 100 % of the population per definition and the population is equal in all three cases (255 values in the 8 bit grey scale).

Degradation in signal intensity An additional aspect of image degradation becomes more apparent in the second row where the same three images are displayed in an 8 bit grey scale which was normalised to the image taken at 13 µm (Figs. 6.16d, 6.16e, and 6.16f). Qualitatively, signal intensity drops drastically with imaging depth until in the last image, signal intensity is down to almost background level, covering up any degradation of resolution. The respective histograms for this case are shown in Figs. 6.16j and 6.16k again first for the bulk of the tonal range and then zoomed in for the situation at the highlights.

Here only the image at 13 µm makes use of the full 8 bit dynamic range (min-max: 0 - 255) whereas the images at 34 µm and 60 µm only use half (min-max: 0 - 125) and one sixth (min-max: 1 - 45) of the dynamic range respectively. The mean grey value averaged over the entire image is given as a function of imaging depth in Fig. 6.16l. The mean grey value, now a comparable measure for signal intensity, has decreased to less than 40 % by imaging 47 µm deeper into the sample. The error bars represent one STD and now decrease with imaging depth mirroring the loss in tonal range with imaging depth.

This reasoning is now used to justify the procedure of image comparison in the following discussion. Whenever signal intensity is compared before and after an optimisation, both images were first scaled to be displayed on the same grey scale as the image taken after optimisation. In this way the pixel (or mean) grey value becomes a comparable measure for signal intensity.

6.2.4 Optimisation on fluorescent beads

The outcome of optimisations performed on surface-mounted, fluorescent beads with diameters of 1 µm and 175 nm are presented in the following. In both cases

the optimisation was performed on a ROI containing the entire bead. In order to take account of apparent axial displacements due to distortions introduced by the optimised DMM shape, z stacks, series of images along the z-axis with fixed lateral position, of several times the bead diameter in depth were taken with the bias DMM shape and with the optimised DMM shape. This ensured the acquisition of a complete data set to accurately describe the effects of the optimised DMM shape on the image. For the 1 µm bead, the z stack had a total depth of 5 µm with 0.1 µm steps. For the 175 nm bead, the stack comprised a total depth of 4 µm in 50 nm steps.

Improvement in signal, not resolution

Fig. 6.17 shows the fluorescent beads before (a,c) and after optimisation (b,d) for a diameter of 1 µm (a,b) and 175 nm (c,d). For each bead size, first the axial profile (mean intensity over the entire bead with depth) is plotted (Figs. 6.18a and 6.18c). From this data the axial position featuring the highest mean intensity can be calculated by fitting of a Gaussian to the data and extracting the position of the peak. The stack slice closest to this peak position was deemed to be the slice closest to the equator of the bead and then used to compare the lateral profiles before and after optimisation. For example, in the case of the 1 µm bead, slice 33 in the bias stack was compared with slice 26 in the optimised stack. For the 175 nm bead, slice 40 in the bias stack was compared with slice 36 in the optimised stack.

The profiles through the diameter of the bead are plotted in Fig. 6.18 for the lateral direction (b,d) and axial direction (a,c) before and after optimisation for the 1 µm bead (a,b) and the 175 nm diameter bead (c,d). The dimensions of the PSF are calculated by applying one-dimensional Gaussian fits to the respective

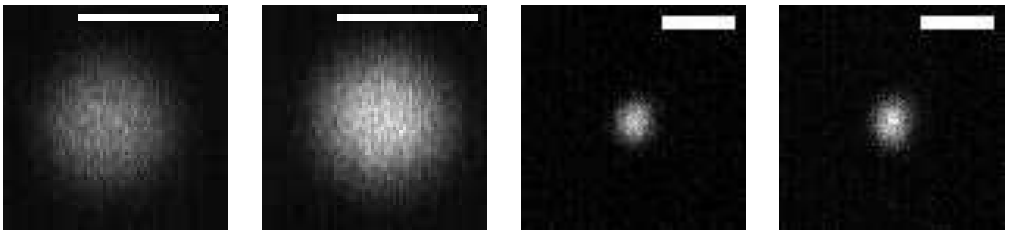

(a) **(b)** **(c)** **(d)**

Figure 6.17: Fluorescent bead of 1 µm **(a,b)** and 175 nm diameter **(c,d)** before optimisation **(a,c)** and after optimisation **(b,d)**. Scale bar is 1 µm.

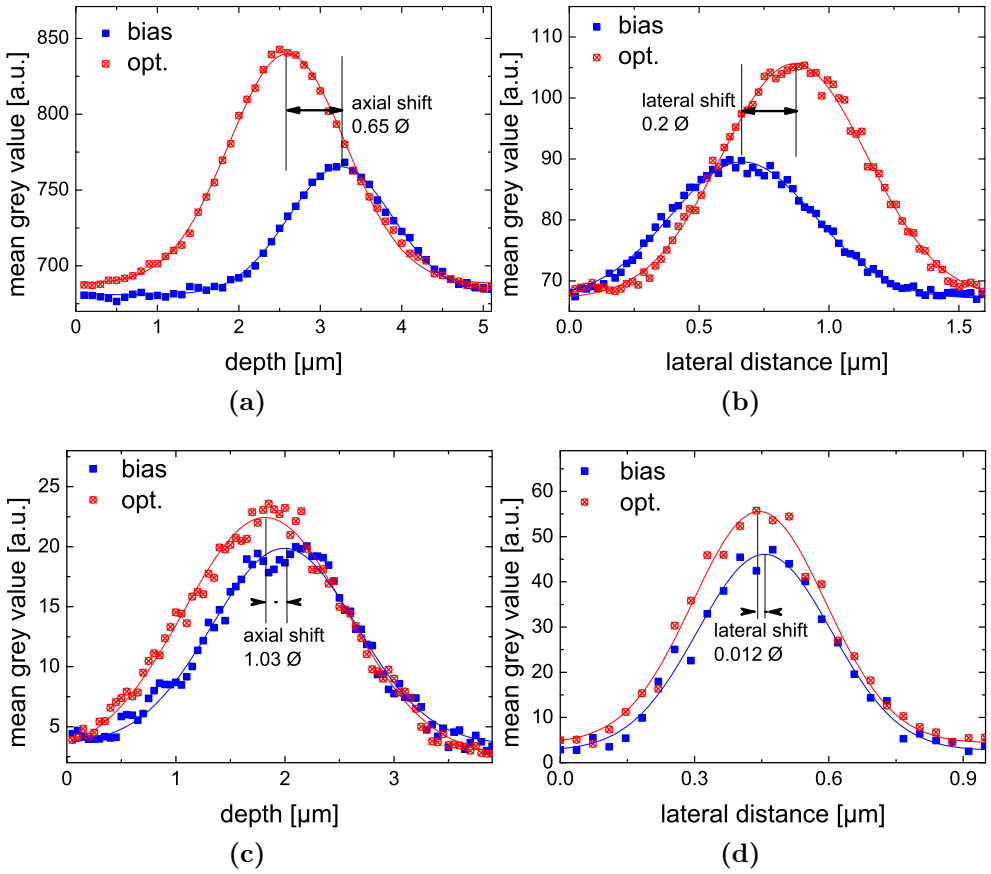

Figure 6.18: Line profiles through the diameter of the beads before and after optimisation for the 1 µm bead **(a,b)** and the 175 nm diameter bead **(c,d)** in axial direction **(a,c)** and lateral direction **(b,d)**. The lines indicate the Gaussian fit to the data (values in Table 6.1). The insets state the displacement in bead diameters in the lateral and axial directions respectively.

lateral and axial intensity profiles and taking the FWHM values. The insets state the displacement in bead diameters and are further discussed in the next section.

The FWHM of lateral and axial line profiles through the diameter of the bead fitted to a Gaussian are given in Table 6.1. The improvement factors are calculated by dividing the values for the optimised case by the according values for the unoptimised case. This means that, for a successful optimisation, the improvement factor f for signal intensity would therefore be greater than one whereas the improvement factor h for resolution would be smaller than one. For the 1 µm bead signal intensity was improved by a factor of $f_{\mathrm{av}}^{1\mu\mathrm{m}} = 1.76 \pm 0.05$ where the averaging was done over the improvement from the axial and the lateral measurement. The resolution was not improved, however, was not dramatically degraded either (factor $h_{\mathrm{av}}^{1\mu\mathrm{m}} = 1.07 \pm 0.08$ worse). For the 175 nm diameter bead,

Table 6.1: FWHM (in µm) of Gaussian fits to the line profiles in axial and lateral directions for the optimised and unoptimised case. Improvement factor in signal intensity f and resolution h. av.: average.

diam. [µm]				f_{lat}	f_{ax}	f_{av}
1				1.72	1.79	1.76
0.175				1.18	1.22	1.20

diam. [µm]	dir.	$\mathrm{FWHM_{bias}}$	$\mathrm{FWHM_{AO}}$	h	h_{av}
1	lat.	0.65	0.66	1.01	1.07
	ax.	1.51	1.69	1.12	
0.175	lat.	0.35	0.35	0.99	1.06
	ax.	1.56	1.77	1.13	

signal intensity was improved by a factor of $f_{\mathrm{av}}^{0.17\mu\mathrm{m}} = 1.20 \pm 0.03$ and resolution degraded by a factor of $h_{\mathrm{av}}^{0.17\mu\mathrm{m}} = 1.06 \pm 0.10$.

The improvement in signal throughout the stack is visualised representatively for the bead of 1 µm diameter in Fig. 6.19 which is a montage of each slice of the stack (a) before optimisation and (b) after optimisation. Two observations became apparent from this montage. First, after optimisation the images were noticeably brighter than before optimisation and also, it visually confirmed that the optimisation had seemingly displaced the bead closer to the surface (as indicated in Fig. 6.18a). This displacement is further analysed in the next section.

Displacement towards the surface

The insets in Fig. 6.18 state the displacements in peak positions for both bead sizes in the lateral and axial directions. Whereas the lateral shifts were quite moderate in both cases ($\Delta_{\mathrm{lat}}^{1\mu\mathrm{m}} = 0.2\,\varnothing$ and $\Delta_{\mathrm{lat}}^{175\mathrm{nm}} = 0.01\,\varnothing$) the axial shift was much more pronounced for both bead sizes and has been calculated by the shift of the Gaussian fit to the z profiles. The difference in peak position for the optimised and unoptimised case respectively was $\Delta_{\mathrm{ax}}^{1\mu\mathrm{m}}$=0.65 ⌀ for the 1 µm bead and $\Delta_{\mathrm{ax}}^{0.175\mu\mathrm{m}}$=1.03 ⌀. These shifts are visualised for the case of the 1 µm diameter bead in Fig. 6.19. The montage shown in (c) displays both stacks as different colour channels (red: optimised stack, green: unoptimised stack). The red bead appeared further up in the stack while the green bead was more pronounced in the deeper slices. Note that both colour channels have been adjusted to appear of similar brightness. The projection of this colour merged stack along z is shown in (d) which allows a visualisation of the lateral displacement caused by the optimised DMM shape.

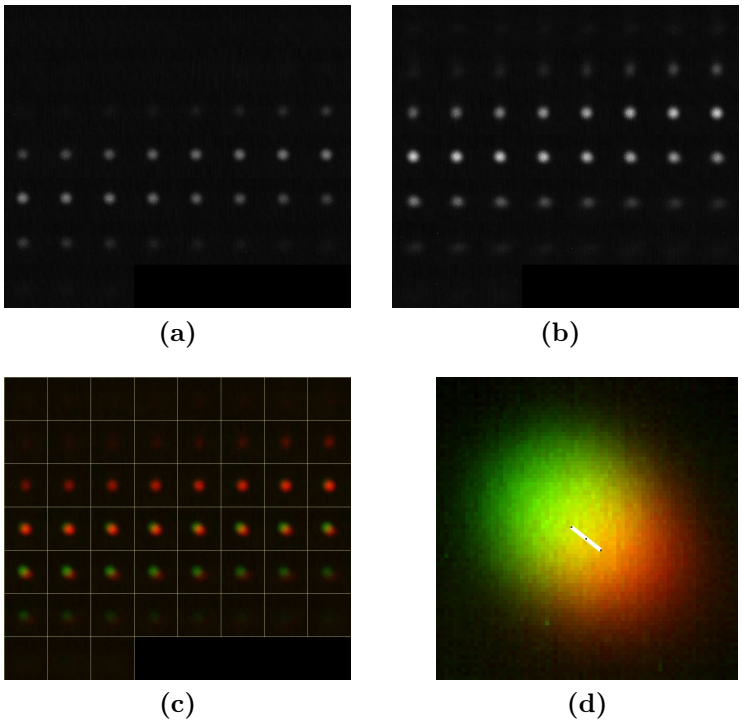

Figure 6.19: Montage of the z stack of the fluorescent bead of 1 µm diameter **(a)** before optimisation and **(b)** after optimisation. Signal intensity is improved in the optimised case. Display of the two stacks shown in (a,b) in different colour channels before optimisation **(green)** and after optimisation **(red)** to highlight the shift in position **(c)** axially and **(d)** laterally. Scale bar is 0.2 µm.

Distortions by the DMM shape

The stack imaging of the 175 nm sized bead allowed a more detailed analysis of distortions introduced on a perfectly spherical shape by the optimised DMM shape. Fig. 6.20 shows the nm-sized bead imaged with the bias DMM shape (a) and the optimised DMM shape (b) by projection of the mean grey value within the entire stack along the z axis. The optimised DMM shape aggravates the presence of halos surrounding the bead especially along one of the lateral directions. Two line profiles along perpendicular lateral directions and their Gaussian fits are given in Figs. 6.20c and 6.20d. The insets state the values for the adjusted R-square, a measure for the goodness of the fit. In (c) both bead profiles provided a close fit to a Gaussian; the adjusted R square deviation from unity is 0.29 % for the bias DMM shape and 0.12 % for the optimised miror shape. In the perpendicular direction (d), however, stronger deviations from a Gaussian occured, especially for the optimised DMM shape. Here, the deviation of the adjusted R square value from unity was 0.90 % for the bias shape and more than twice as much for

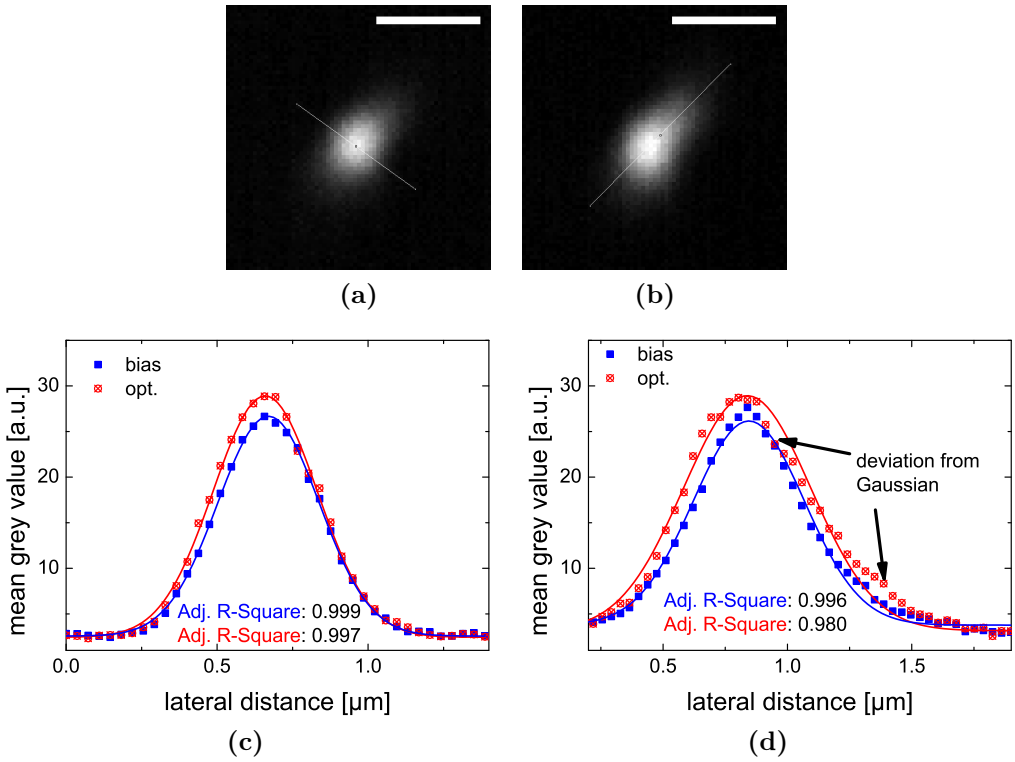

Figure 6.20: Distortions of the image of a spherical bead of 175 nm diameter introduced by **(a)** the bias shape and **(b)** the optimised DMM shape. The optimised DMM shape aggravated the appearance of halos surrounding the bead. Scale bar 1 µm. The line profiles and the Gaussian fits (lines) are given for two orthogonal directions in **(c,d)**. The arrows indicate the areas with strong departure from the Gaussian profile. The insets state the adjusted R-square values for the fit.

the optimised DMM shape (1.97 %). It should be noted that even the bias DMM shape exhibited halos that are likely due to comatic aberrations introduced into the optical system by light rays not entering the objective on axis.

Bleaching

During any optimisation on a fluorescent signal a considerable amount of bleaching can occur. The inset of Fig. 6.21 shows two fluorescent beads of 1 µm diameter. The bleached bead in the bottom right corner was used as a MF source for the optimisation routine while the unbleached bead in the upper left corner was used after completion of the optimisation routine to take two image stacks with the bias shape and the optimised DMM shape respectively. In order to quantify the amount of bleaching, the graph in Fig. 6.21 shows line profiles through the intact bead (closed symbols) and the bleached bead (open symbols) with the bias

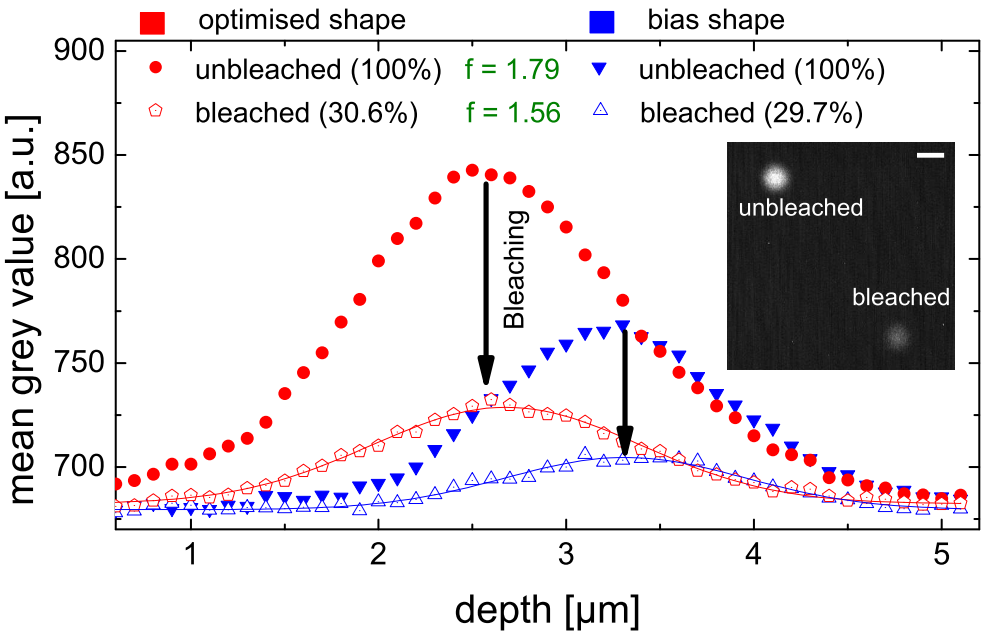

Figure 6.21: Bleaching of TPEF. The line profiles through the intact (closed symbol) and bleached (open symbol) bead imaged with the bias shape (blue) and the optimised shape (red). Bleaching (arrows) during the duration of the optimisation routine reduced the fluorescence signal to 30 %. Inset: bleached and unbleached bead. Scale bar is 1 µm.

shape (blue) and the optimised DMM shape (red). When using the bias shape for imaging, the optimisation routine reduced the signal of the bead to 29.7 % through photobleaching. The amount of bleaching was slightly less when the optimised DMM shape was used for imaging (reduction to 30.6 %). Most of the signal, however, was permanently lost. By applying the optimised DMM shape to image a fresh, unbleached bead, the signal was improved by a factor of 1.79 while the signal of the bleached bead was only improved by a factor of 1.56.

6.2.5 Optimisation on urea crystals

Various samples and materials exhibiting SHG were tested, however, urea proved to be easiest and quickest to use. The crystals can simply be placed on a dish requiring no further sample preparation. The following optimisations were all run on urea crystals in order to assess system performance in the SHG modality. SHG does not suffer from photobleaching and generally produced a much stronger SNR than TPEF therefore facilitating the optimisation routine. An image stack was acquired in order to assess the effects of the optimised DMM shape in the lateral directions as well as the axial direction. The image stack had a total depth of

50 µm with steps of 1.852 µm and consisted of 28 slices. The optimisation was run on a single pixel with parked galvos for roughly 2000 iterations, 104 of which were successful. The bleaching compensation routine was used, as it was expected that it potentially could have a beneficial effect by compensating for laser output power instabilities and other low frequency drifts while no negative side effects were anticipated. The MF is plotted versus iteration number in Fig. 6.22a. It is not known why this cyclic drop in signal intensity occurred. After over 2000 iterations none of the actuator control voltages was saturated. The average control voltage applied was $U_c^{\text{mean}} = (151.94 \pm 60.24)\,\text{V}$ with values reaching from $U_c^{\text{min}} = 1\,\text{V}$ to $U_c^{\text{max}} = 230\,\text{V}$ (Fig. 6.22b).

Improvement in signal

The improvement in signal intensity on the plane of optimisation can be seen in Fig. 6.23 which depicts urea crystals before (a) and after optimisation (b). The arrow in 6.23a indicates the bright region which contained the pixel on which the optimisation was performed. Qualitatively, signal and contrast was considerably improved after the optimisation, revealing more details in the crystal structure. Figs. 6.23c and 6.23d compare montages of the z-stacks of urea crystals taken before optimisation (a) and after optimisation (b). The signal intensity was considerably increased in the optimised case throughout the depth of the stack.

In order to quantify the improvement, three slices throughout the stacks imaged with the optimised and the bias DMM shape were compared. Fig. 6.24

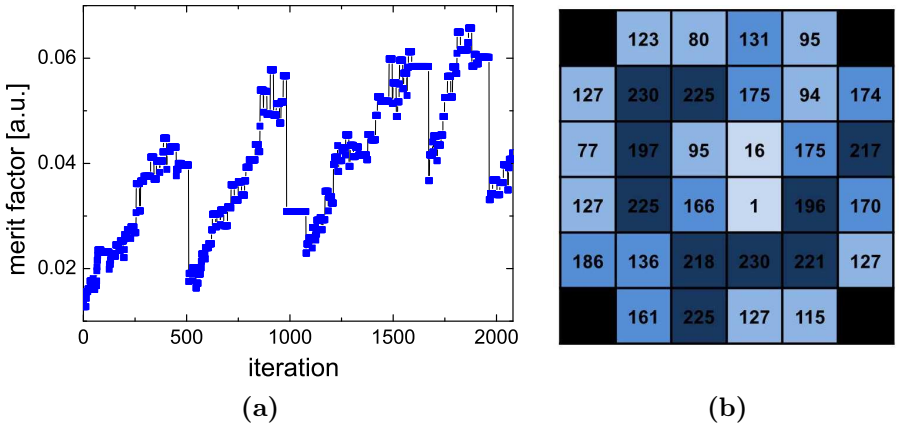

(a) **(b)**

Figure 6.22: Optimisation on SHG signal emitted by urea crystals. **(a)** Optimisation graph showing the improvement of MF with iteration number. **(b)** Voltage map, the DMM stroke was not saturated after over 2000 iterations.

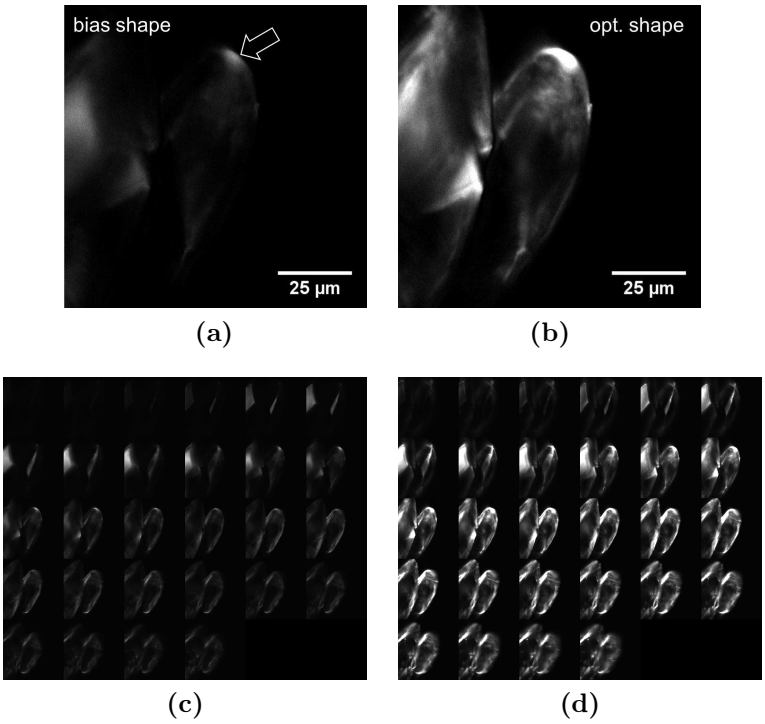

Figure 6.23: Plane of optimisation for the urea crystal roughly 18.5 µm from the surface **(a)** before optimisation and **(b)** after optimisation. The arrow indicates the bright region containing the pixel used as MF source. Montages of z stack imaging urea crystals **(c)** before optimisation and **(d)** after optimisation. Signal intensity was substantially improved throughout depth in the optimised case.

shows slices 5, 8 and 28, at the depths of 7.4 µm, 13.0 µm, and 50 µm respectively, of the stack imaged with the optimised DMM shape along with the ROI that was considered in the graphs underneath the respective image. The grey values in the images were normalised to give a peak at 100 a.u. for the bias shape after subtraction of the background. In the lateral direction (Figs. 6.24a, 6.24d), an improvement at the peak of $f_{\text{peak}}^{7\mu\text{m}} = 5.73$ was achieved. When averaging all grey values within the ROI for the optimised and unoptimised case and taking the quotient thereof, the improvement factor was $f_{\text{av}}^{7\mu\text{m}} = 7.60$. The improvement in axial direction is demonstrated in Figs. 6.24b and 6.24e, where the signal was increased at the peak by a factor of $f_{\text{peak}}^{13\mu\text{m}} = 3.74$ and in average by $f_{\text{av}}^{13\mu\text{m}} = 5.92$. Figs. 6.24c and 6.24f show the situation at the deepest slice of the stack (slice 28) at 50 µm deep into the crystal. Here, the signal was improved by $f_{\text{peak}}^{50\mu\text{m}} = 3.96$. When averaging the grey values within the ROI along z, the improvement factor was $f_{\text{av}}^{50\mu\text{m}} = 8.52$. Table 6.2 summarises those values.

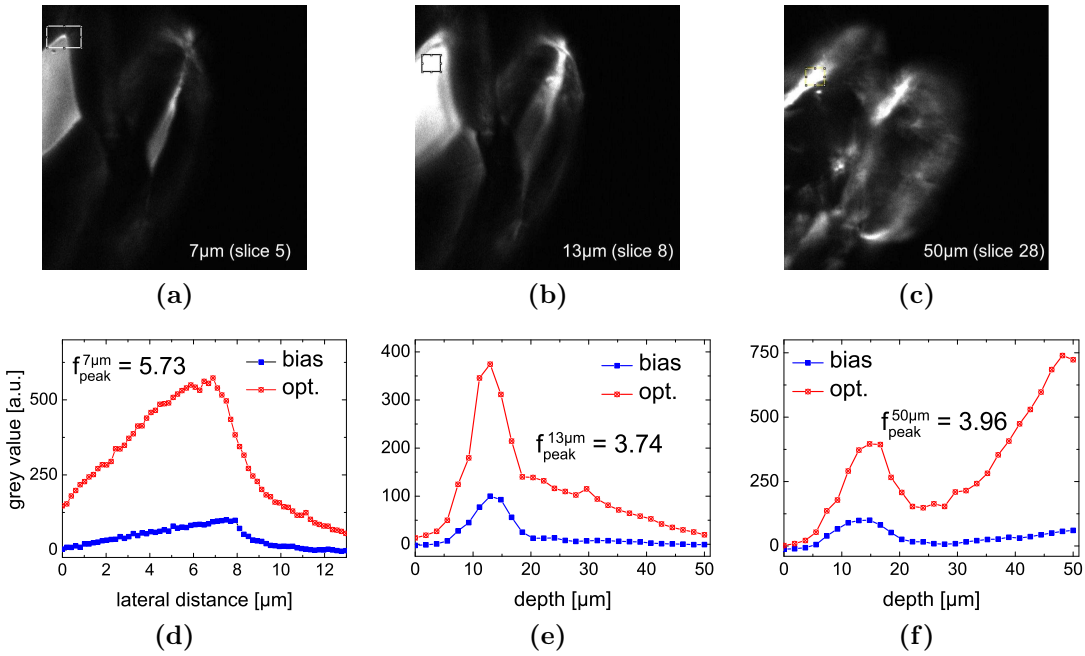

Figure 6.24: Slice 5 **(a)**, slice 8 **(b)**, and slice 28 **(c)** from the optimised stack. The ROI in each image indicate where the line profiles in the graph underneath the image have been taken. The plots in **(d,e,f)** compare the line profiles before and after optimisation. Improvement in signal intensity in lateral direction **(a,d)**, in axial direction **(b,e)** and at depth on the last slide of the stack **(c,f)** is shown.

Changes in depth of focus

A different aspect of the optimisation became apparent when the projection of the STD of each stack along z were compared (Fig. 6.25). Each pixel in this projection is the STD of all pixel values within the stack at the same lateral coordinate expressed as an 8 bit grey value. That means the brighter the pixel the higher the variation in brightness at this specific coordinate throughout the stack. The STD projection of the unoptimised stack corresponds well with the information contained in a few neighbouring slices in the stack which is taken as an indication that the focal spot had a shallow depth of field. SHG signal was

Table 6.2: Improvement factor f_{peak} of the peaks (Fig. 6.24) along with the improvement factor f_{av} calculated as the quotient of the averaged grey level within the ROI for the optimised and the bias shape.

slice	depth [µm]	dir.	f_{peak}	f_{av}
5	7.4	lat.	5.73	7.60
8	13.0	ax.	3.74	5.92
28	50.0	ax.	3.96	8.52

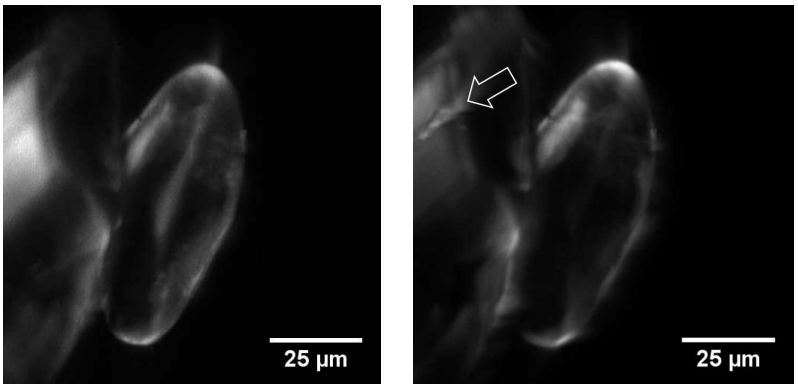

(a) **(b)**

Figure 6.25: Projection along z of the STD for the stack imaged with the bias shape **(a)** and the optimised shape **(b)**. The arrow indicates a region where signal from a slice much deeper into the stack is strong enough to permeate the signal predominantly produced in a slice roughly in the centre of the stack.

only generated within a thin region of the stack while keeping the slices above and below dark.

For the projection of the optimised stack, however, information from various slices throughout the stack bled through. The arrow indicates an area, where signal from a slice deeper into the sample is strong enough to permeate through a region created mainly from the SHG of a slice in the middle of the stack. This region was visible in the optimised stack but not in the unoptimised stack. This was taken to indicate that the depth of focus created with the optimised shape is broader possibly as a consequence of optimising on purely increasing signal intensity. Note that both projections have been adjusted so as to appear of equal brightness.

Fig. 6.26 shows both stacks merged as different colour channels to facilitate detection of any shift in lateral or axial direction. The optimised stack is displayed in red whereas the unoptimised stack is displayed in green. The irregular shape of the crystals made it harder to discern any lateral or axial shifts, however, no considerable shifts were found in either the lateral or the axial direction.

Applied to the imaging of fluorescent beads

For live cell microscopy, repeated exposure to laser light leads to photobleaching of fluorophores associated with *de novo* formation of reactive oxygen intermediates, ultimately compromising imaging sensitivity as well as cell viability and function [196]. SHG does not suffer from photobleaching and therefore provides

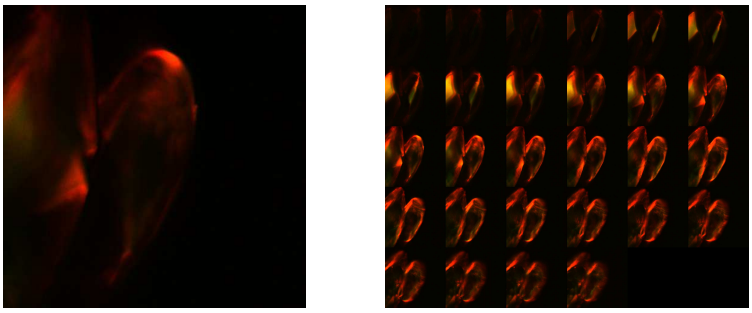

(a) **(b)**

Figure 6.26: Merging of both stacks as colour channels before optimisation (green) and after optimisation (red) to investigate shifts in position **(a)** laterally (slice 12) and **(b)** axially through a montage of the entire stack. No shift in lateral or axial direction was perceived.

a superior signal to optimise on in algorithm based AO. The collagen within the organotypic samples is co-located with fluorescent structures, making the following approach interesting: can the DMM shape obtained from an optimisation performed on SHG be usefully applied to the imaging of fluorescent structures?

In order to test this approach the DMM shape that was acquired while optimising on urea crystals (Fig. 6.22b) was used to image fluorescent beads. Even though the sample under investigation was very different from the sample used to find the optimised DMM shape, the aberrations introduced by the imaging system were expected to be similar in both cases. Imaging with a preoptimised DMM shape was therefore expected to be potentially beneficial even if the shape could possibly not correct for sample induced aberrations. The advantage of using fluorescent beads is that, in addition to determining any improvement in signal, changes in resolution and distortions in the imaging could be assessed due to their perfectly geometrical shape. Ideally, the optimisation would be performed on a sample that exhibits both, TPEF and SHG, such that the system- and sample induced aberrations would be similar. This will be discussed in more detail in the next section.

In the following section, image stacks of surface-mounted, fluorescent beads of two different sizes, each acquired with the bias shape and with a shape that was previously optimised on urea, are compared (Fig. 6.27). The stack imaging a bead of 1 µm diameter had a total depth of 4.5 µm containing 46 slices with a step size of 0.1 µm. The stack imaging a bead of 4 µm had a depth of 9.25 µm in steps of 0.25 µm containing 38 slices. For the 1 µm bead, the optimised DMM shape reduced signal intensity on the brightest respective slides by a factor of

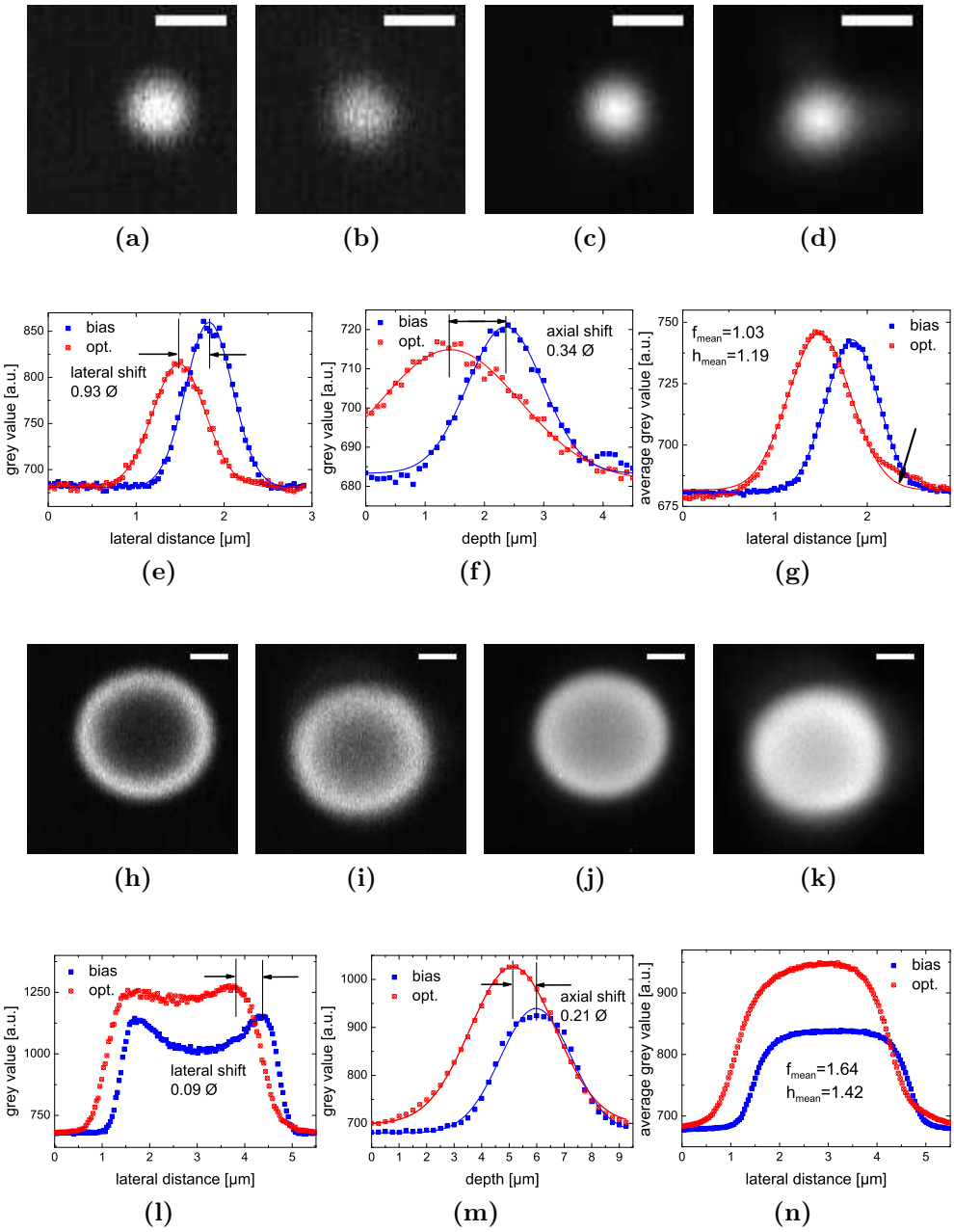

Figure 6.27: Imaging of a fluorescent bead of 1 µm **(a-d)** and 4 µm diameter **(h-k)**. The slices shown are those of brightest intensity within their respective stacks imaged with the bias shape **(a,h)** and the DMM shape previously optimised on urea crystals (Fig. 6.22b) **(b,i)**. Scale bar is 1 µm. Projection along the z axis of the average intensity for the bias shape **(c,j)** and the optimised shape **(d,k)**. Line profiles for the 1 µm **(e,f,g)** and 4 µm diameter **(l,m,n)** in the lateral direction **(e,l)**, the axial direction **(f,m)** and for the average projection **(g,n)** comparing the optimised shape (opt.) with the bias shape (bias). Lines indicate Gaussian fits. Arrow indicates region where line profile strongly deviates from Gaussian. Insets give shifts in lateral and axial directions respectively in units of bead diameter.

Table 6.3: FWHM (in µm) of Gaussian fits to the line profiles in axial and lateral directions for the optimised and unoptimised case. Improvement factor in signal intensity f and resolution h. av.: average of lateral and axial.

diam. [µm]				f_{lat}	f_{ax}	f_{av}	f_{mean}
1				0.75	0.89	0.82	1.03
4				1.27	1.26	1.27	1.64

diam. [µm]	dir.	$\mathrm{FWHM_{bias}}$	$\mathrm{FWHM_{AO}}$	h	h_{av}	h_{mean}
1	lat.	0.63	0.70	1.11	1.48	1.19
	ax.	1.50	2.77	1.85		
4	lat.	1.06	0.66	0.62	0.91	1.42
	ax.	3.04	3.65	1.20		

$f_{\mathrm{lat}}^{1\mu m} = 0.75$ in the lateral direction (Fig. 6.27e) and by a factor of $f_{\mathrm{ax}}^{1\mu m} = 0.89$ in the axial direction (Fig. 6.27f). For the 4 µm bead, the optimised DMM shape improved signal intensity by a factor of $f_{\mathrm{lat}}^{4\mu m} = 1.27$ in the lateral direction and $f_{\mathrm{ax}}^{4\mu m} = 1.26$ in the axial direction (Figs. 6.27l and 6.27m). The DMM shape optimised on urea improved signal intensity for the larger bead and decreased it for the smaller bead.

The apparent shift in position induced by the optimised DMM shape in the lateral and axial directions was estimated by the differences Δ, in the peak positions of the Gaussian fits. For the 1 µm bead, there was a pronounced shift in lateral direction of $\Delta_{lat}^{1\mu m} = 0.93\,\varnothing$ and in the axial direction of $\Delta_{ax}^{1\mu m} = 0.34\,\varnothing$. The shifts in absolute distance were comparable but less apparent for the larger bead because of its bigger size ($\Delta_{lat}^{4\mu m} = 0.09\,\varnothing$ and $\Delta_{ax}^{4\mu m} = 0.21\,\varnothing$).

The changes in resolution were calculated as the quotient of the FWHM for the bias shape and the optimised shape. The resolution degraded in both directions for both bead sizes. For the 1 µm bead the factors were $h_{\mathrm{lat}}^{1\mu m} = 1.11$ and $h_{\mathrm{ax}}^{1\mu m} = 1.85$ in the lateral and axial directions respectively ($h_{\mathrm{lat}}^{4\mu m} = 0.62$ and $h_{\mathrm{ax}}^{4\mu m} = 1.20$ respectively for the larger bead). The values obtained through fitting of a Gaussian to the data are summarised in Table 6.3.

Finally the effect of the optimised DMM shape was analysed with the projection of the average pixel grey value along z (Fig. 6.27g). This was done to see whether the bead as a whole got brighter when imaged with the optimised DMM shape and whether any distortions had been introduced. For the 1 µm bead, the signal intensity was improved by a factor of $f_{\mathrm{mean}}^{1\mu m} = 1.03$ whereas resolution was degraded by a factor of $h_{\mathrm{mean}}^{1\mu m} = 1.19$. The arrow highlights a region with a strong deviation from the Gaussian indicating a distortion of the image. For the 4 µm

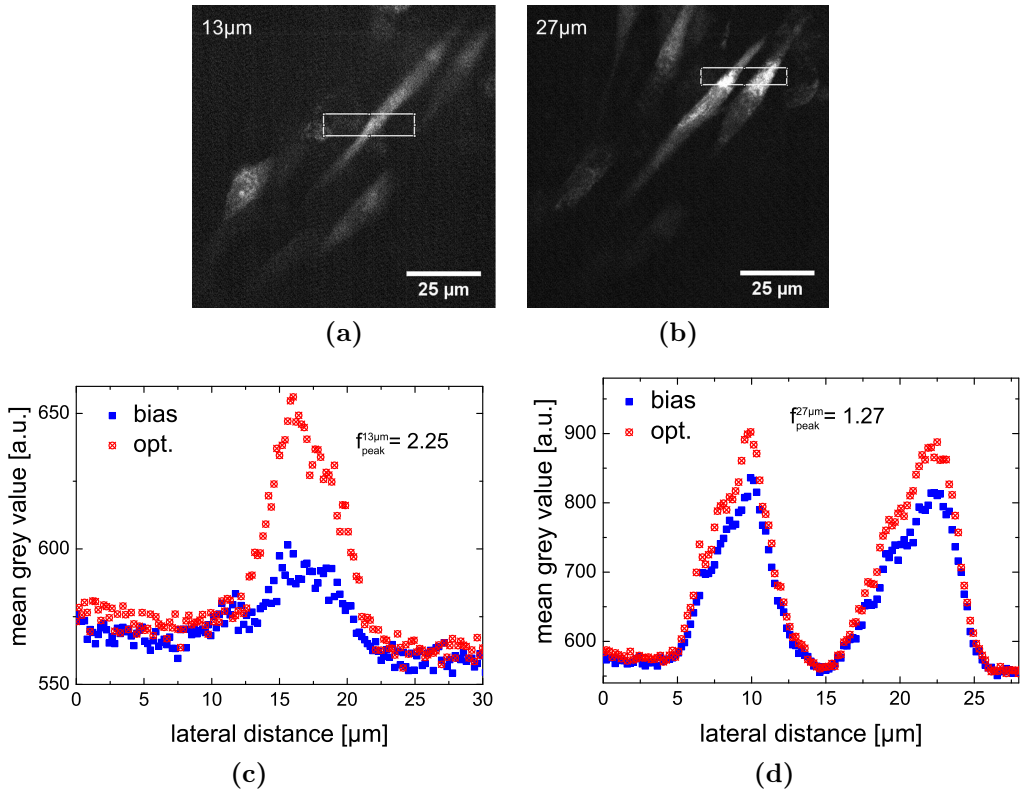

Figure 6.28: Organotypic sample showing red fibroblast cells at a depth of **(a)** 13 µm and **(b)** 27 µm. **(c,d)** Lateral line profiles within the indicated ROIs for the images taken with the bias shape and the shape that had previously been optimised on urea crystals at a depth of 18.5 µm.

bead, shown in Fig. 6.27n, these values were $f^{4\mu m}_{mean} = 1.64$ and $h^{4\mu m}_{mean} = 1.42$, which means the optimised DMM shape did improve the overall signal strength but also degrade resolution.

6.2.6 Imaging of organotypic samples

Optimisation on urea and fluorescent beads

The same DMM shape, previously optimised on urea at a depth of 18.5 µm (Fig. 6.22b), was tested on an organotypic sample, shown in Fig. 6.28 where (a) shows red fibroblast cells at a depth of 13 µm and (b) cells at a depth of 27 µm. Also indicated are the respective ROIs that were considered in the lateral line profiles in (c) and (d). The peaks in the line profiles showed an improvement in signal intensity of $f^{13\mu m}_{peak} = 2.25$ at a depth of 13 µm (Fig. 6.28c) and a more moderate improvement of $f^{27\mu m}_{peak} = 1.27$ at a depth of 27 µm (Fig. 6.28d).

The experiment was repeated with a different organotypic sample, imaged

again with the DMM shape previously optimised on urea and also with a DMM shapes resulting from a previous optimisations on a fluorescent bead. The stacks imaged with those two shapes were compared to a stack obtained with the bias DMM shape. The imaging was done with two PMTs in two different detection channels, one set up for SHG imaging and the other for the detection of TPEF. Therefore two image stacks of 100 µm depth in 2.5 µm steps, one containing the fluorescent signal and the other containing the SHG signal, were acquired with three different DMM shapes.

TPEF channel For the fluorescent detection channel, the DMM shape from the optimisation on the fluorescent bead performed best. Fig. 6.29 shows a projection along z of the average pixel intensity for the bias shape (a), the DMM shape from the urea optimisation (b) and the optimisation on the fluorescent bead (c). Qualitatively the image in (c) is brighter than either (a) or (b) especially in the region of the cell nucleus (arrow). In order to quantify the improvements for each DMM shape a ROI on three different slices, the first (surface), one in the middle (30 µm), and the last slice (100 µm) in each of the stacks were compared.

Fig. 6.29d shows the surface of the sample which had been imaged with the DMM shape previously optimised on a fluorescent bead and the ROI which was considered in the line profiles shown in Figs. 6.29e and 6.29f for the axial and lateral direction respectively. The signal intensity of the image stack taken with the DMM shape optimised on the fluorescent bead was highest, followed by the image taken with the DMM shape optimised on urea, for both the axial and the lateral direction. After subtraction of the background in all three images, signal intensity in the peak was improved along z by a factor of $f_{\text{urea}}^{0\mu\text{m}} = 1.70$ for the image taken with the DMM shape optimised on urea and a factor of $f_{\text{bead}}^{0\mu\text{m}} = 2.45$ for the image taken with the DMM shape optimised on a fluorescent bead.

At a depth of 30 µm further into the stack (slice 13), depicted in Fig. 6.29g, the rectangular ROI was used to determine the signal intensity along the axial direction (Fig. 6.29h) and the line was used to determine the signal intensity along the lateral direction (Fig. 6.29i). Again the image was brightest when taken with the DMM shape optimised on the fluorescent bead in both directions, however, the DMM shape optimised on urea performed less well than the bias shape and also a lateral shift became apparent. After subtraction of the background for all three images, signal intensity in the peak was decreased along z by a factor of $f_{\text{urea}}^{30\mu\text{m}} = 0.85$ for the image taken with the DMM shape optimised on urea and

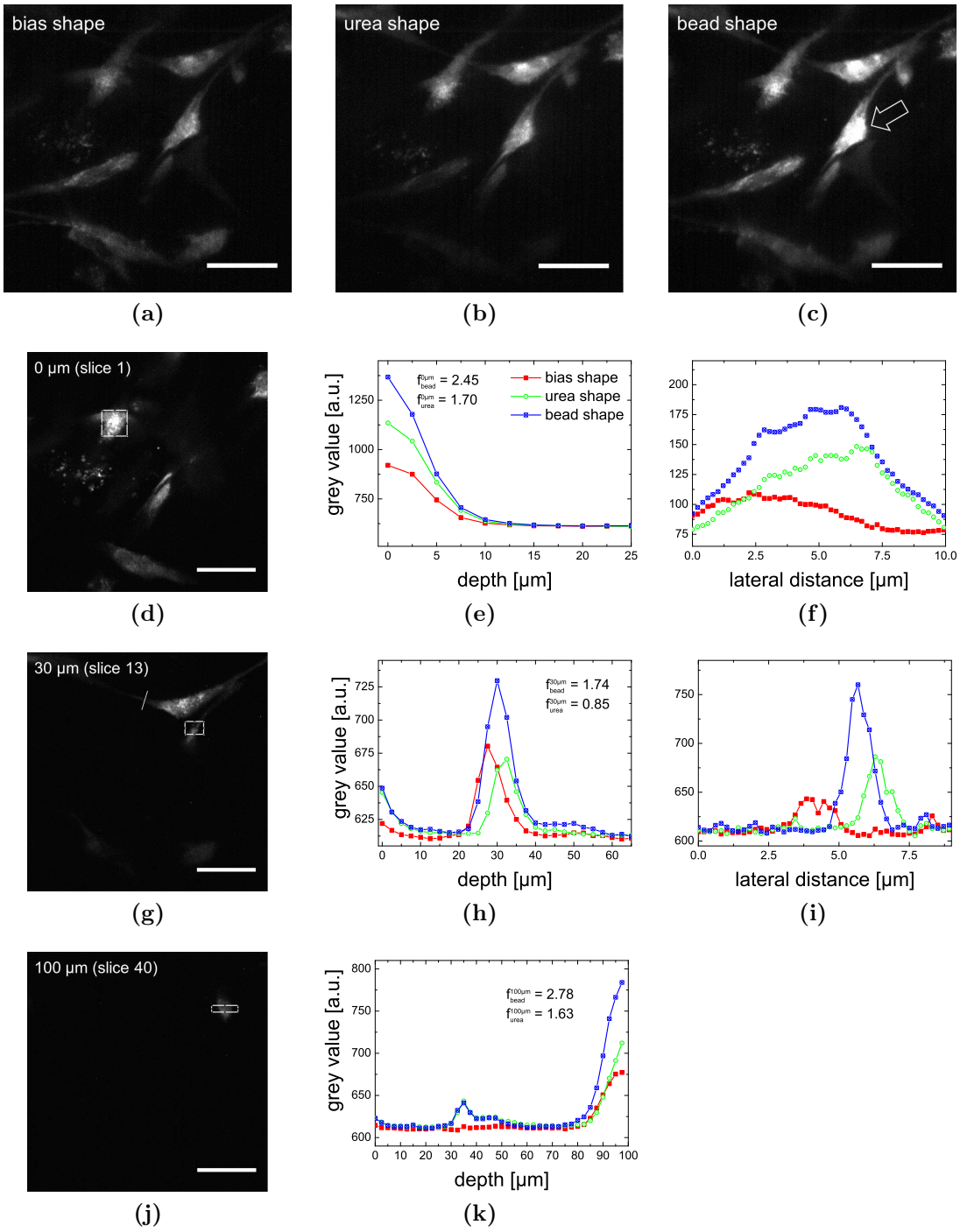

Figure 6.29: Image stack of organotypic sample. Projection of average pixel value along z imaged with the bias DMM shape **(a)**, the DMM shape of the optimisation performed on urea **(b)**, and the DMM shape of the optimisation performed on fluorescent beads **(c)**. Especially in the region of the cell nucleus (arrow) the signal is improved by imaging with the optimised DMM shapes. First **(d)**, 13th **(g)** and last slice **(j)** of the stack and line profiles within the indicated ROIs in the axial **(e,h,k)** and lateral direction **(f,i)**. Scale bar is 25 µm.

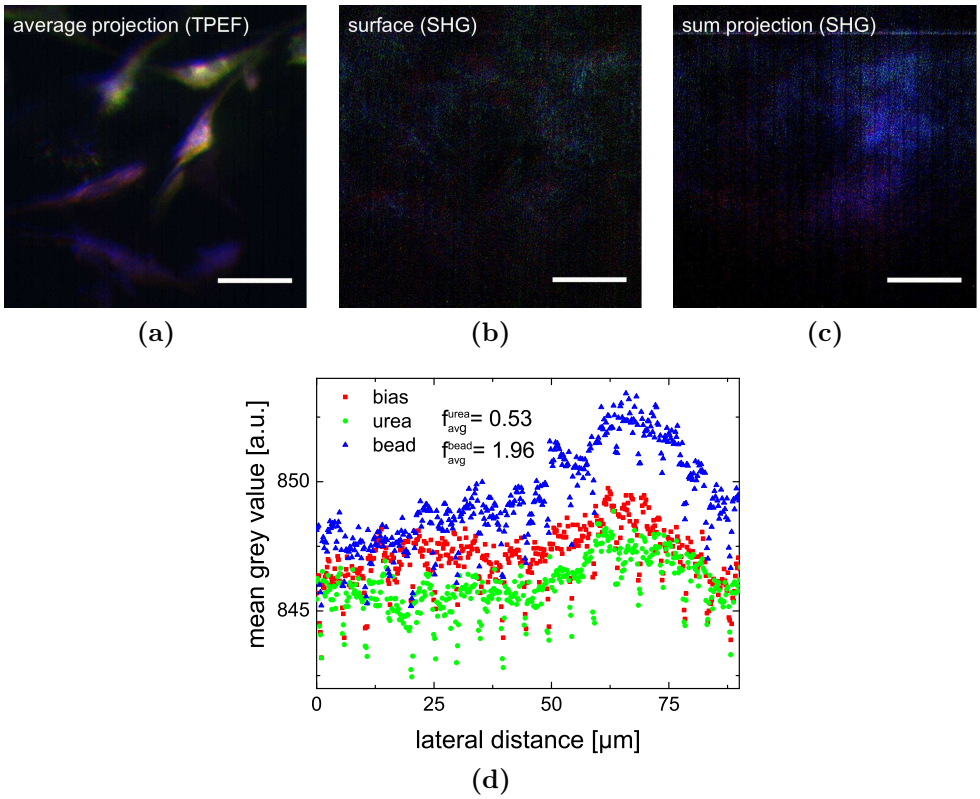

Figure 6.30: Projection of the pixel average along z as a colour merge for the fluorescent detection channel **(a)** with fibroblast cells imaged with the bias shape (red), the urea shape (green) and the bead shape (blue). The same colour coding is used in the image of the surface of a colour merged stack containing the SHG signal **(b)**. Projection of the sum of all pixels along z for the colour merged SHG stack **(c)**. Intensity profile of a ROI containing the entire image displayed in (c) **(d)**. SHG signal was highest for the stack imaged with the DMM shape previously optimised on a bead (blue).

improved by a factor of $f_{\text{bead}}^{30\,\mu\text{m}} = 1.74$ for the image taken with the DMM shape optimised on a fluorescent bead.

The improvement of signal at a depth of 100 µm is shown in the last slice of the stack (Fig. 6.29j) along with the projection of the indicated ROI with depth (Fig. 6.29k). Signal intensity was here improved by a factor of $f_{\text{urea}}^{100\,\mu\text{m}} = 1.63$ for the image taken with the DMM shape optimised on urea and a factor of $f_{\text{bead}}^{100\,\mu\text{m}} = 2.78$ for the image taken with the DMM shape optimised on a fluorescent bead.

SHG channel The signal that can ideally be collected with organotypic samples varies greatly from batch to batch and was particularly weak for this specific organotypic sample making it unsuitable for direct optimisation on SHG. The in-

formation from the three stacks obtained with different DMM shapes was colour coded and merge to a single stack. Here, red represents the stack obtained with the bias shape, green the stack obtained with the urea shape and blue the stack obtained with the DMM shape previously optimised on the fluorescent bead.

Fig. 6.30a shows the projection of the average pixel value along z for the fluorescent detection channel to illustrate this. Fig. 6.30b shows the surface of a colour merged stack containing the SHG signal. The signal was very weak but predominantly blue, which means it originated from the stack imaged with the DMM shape optimised on the fluorescent bead. Fig. 6.30c shows the projection of the sum of all pixels along z for the colour merged SHG stack and the intensity profile within a ROI encompassing the entire image is depicted in Fig. 6.30d. In order to quantify the signal improvement the average of all pixels within the image was calculated in the three cases and the same background count was subtracted. This yielded an improvement factor in signal strength throughout the entire stack of $f_{\mathrm{av}}^{\mathrm{bead}} = 1.96$ for the image stack acquired with the DMM shape that was optimised on the fluorescent bead whereas the DMM shape optimised on urea decreased the signal intensity by more than half ($f_{\mathrm{av}}^{\mathrm{urea}} = 0.53$) when compared to the signal intensity of the stack imaged with the bias shape.

Optimisation on organotypics

The optimisation routine was tested on TPEF signal produced by red fibroblast cells on the surface of an organotypic sample. Fig. 6.31 shows the cells on the surface of the organotypic imaged with the bias shape (a) and imaged with the optimised DMM shape (c). After optimisation, the signal intensity of the red fluorescent cells was considerably improved. Fig. 6.31e shows the lateral line profile along the selection shown in the image. Using the grey values at various peaks the improvement factor was $f_{\mathrm{peak}}^{0\mu\mathrm{m}} = 5.24 \pm 0.91$. The same DMM shape was then used to image 92 µm deeper into the tissue. The image obtained with the optimised DMM shape made features visible that were barely distinguishable from the background in the image obtained with the bias shape. From the line profile shown in Fig. 6.31f an average signal improvement factor of $f_{\mathrm{av}}^{92\mu\mathrm{m}} = 7.74$ was calculated.

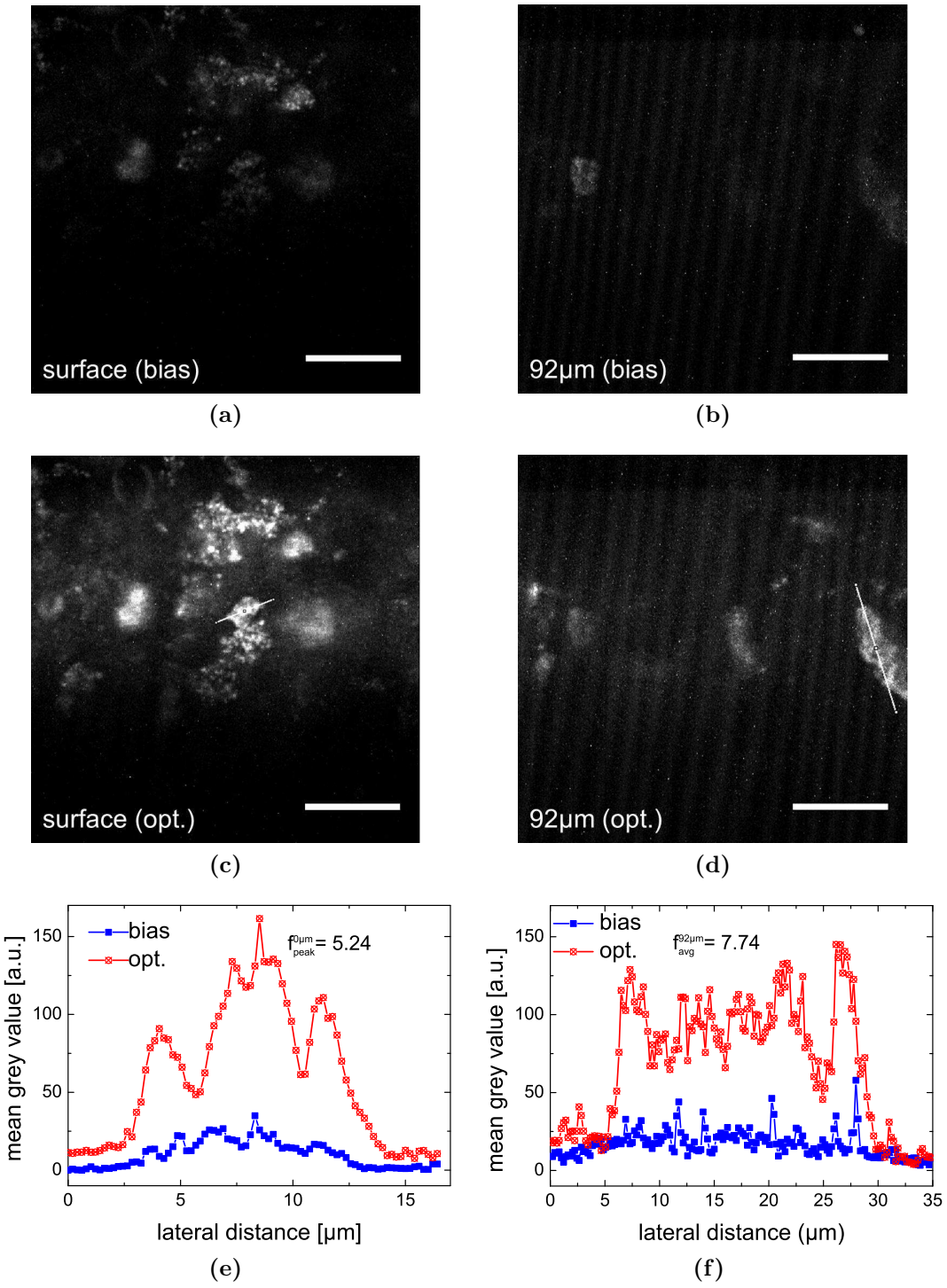

Figure 6.31: Red fibroblast cells imaged **(a,c)** on the surface and **(b,d)** at a depth of 92 µm **(a,b)** before optimisation and **(c,d)** after optimisation. The optimisation was performed on the surface. Lateral line profiles comparing the images obtained with the bias shape and the optimised DMM shape **(e)** on the surface and **(f)** 92 µm into the sample. Scale bar is 25 µm.

Table 6.4: Improvement factors in signal intensity f and resolution h for beads of various sizes. Successful optimisation has $f > 1$ and $h < 1$. Imaging of all beads in TPEF modality, optimisation on MF according to table.

dia. [µm]	MF	dir.	f	$\text{FWHM}_{\text{bias}}$ [µm]	FWHM_{AO} [µm]	h
0.175	TPEF	lat.	1.18	0.35	0.35	1
	TPEF	ax.	1.22	1.56	1.77	1.13
1	TPEF	lat.	1.72	0.65	0.66	1.01
	TPEF	ax.	1.79	1.51	1.69	1.12
	SHG (urea)	lat.	0.75	0.63	0.70	1.11
	SHG (urea)	ax.	0.89	1.50	2.77	1.85
4	SHG (urea)	lat.	1.27	1.14	0.67	1.70
	SHG (urea)	ax.	1.26	3.04	3.65	1.20
15	TPEF	lat.	1.96	0.59	0.54	0.92

6.3 Discussion

6.3.1 Theoretical resolution

The theoretical diffraction limited resolution is given by eqs. 5.2 and 5.3 for the lateral and axial direction respectively. Using $\lambda = 1098\,\text{nm}$, $n = 1.5$ and NA $= 1.3$, the FWHM in lateral direction is $\text{FWHM}_{lat}^{theo} = 0.33\,\mu\text{m}$ and for the axial direction $\text{FWHM}_{ax}^{theo} = 0.93\,\mu\text{m}$. Imaging of a sub-resolution sized bead of 175 nm diameter yielded near diffraction limited values of $\text{FWHM}_{lat}^{exp} = 0.35\,\mu\text{m}$ (106 % of the theoretical value) and $\text{FWHM}_{ax}^{exp} = 1.56\,\mu\text{m}$ (167 % of the theoretical value). The discrepancies are simliar to those reported by others [272] and probably due to a non-perfect correction of the objective lens at long excitation wavelengths and a slighly non-collimated beam entering the back aperture of the microscope objective. Resolution measurements with the LSF methods yielded a lateral resolution of $\approx 670\,\text{lp/mm}$ and an axial resolution of $200\,\text{lp/mm}$. The factor between lateral and axial resolution of 3.35 measured with this method is closer to the theoretically expected value of 2.82 compared to the factor of 4.46 obtained with the FWHM values.

6.3.2 Aberration correction

For the following discussion, aberration correction has been divided into surface mounted samples (*i.e.* fluorescent beads) and samples that allow for imaging at depth.

Surface mounted samples The outcome of optimisations performed on surface mounted fluorescent beads of various diameter is summarised in Table 6.4. The MF column states the signal used as a feedback signal which was intrinsic if not quoted otherwise, else the mirror shape was pre-optimised on the sample quoted in brackets. The optimisations did in general not improve the resolution as most of the factors $h = \frac{\mathrm{FWHM_{AO}}}{\mathrm{FWHM_{bias}}} > 1$. Optimisations with the TPEF emitted by the beads as a MF maintained resolution whereas applying a DMM shape that had previously been optimised on the SHG emitted by urea crystals degraded resolution by a factor 1.5 on average. The likely reason for this is the ill-chosen signal intensity as a MF for optimisation on higher harmonics because an extended PSF can result in a higher signal level. Instead, the MF needs to be chosen such that it reaches its maximum only in absence of aberrations. It has been pointed out previously that metrics reflecting the information content like sharpness are a more suitable as feedback signals for third harmonic generation [299].

In terms of improvement in signal intensity most optimisations were successful. On average, intensity was improved by a factor of 1.8 in beads larger than resolution limit when TPEF was chosen as a MF. When SHG was used as MF, optimisations successfully increased signal intensity for larger beads (average improvement factor of 1.3) but not for 1 µm beads where intensity was reduced to 82 %. The level of improvement in signal intensity achieved in this study compares well with previously published data. Using surface mounted lily pollen grains as a sample that emit both TPEF and THG, a 25 % increase in TPEF and a 171 % increase in THG signal was reported with image based aberration correction using THG sharpness as a MF [299].

Signal improvement at depth The optimisations performed on samples at various depths are summarised in Table 6.5 whereas Fig. 6.32 visualises some of the results. Resolution measurements were not possible in these samples due to the lack of sub-resolution sized structures. In terms of increase in signal intensity the improvement factors for peak values f_{peak} and for all pixels within the respective ROI f_{av} are listed.

First the case is considered where the MF is of the same kind as the imaging modality, that is, imaging of TPEF emitting structures with DMM shapes that have been optimised on TPEF signal are compared to imaging of SHG emitting samples with DMM shapes that have been optimised on SHG signal. Generally,

[1] not from bias, but a pre-distorted DMM shape

Table 6.5: Improvement factors in peak signal intensity f_{peak} and average signal intensity f_{av} for various samples. Conv.: *convallaria*, RFB: red fibroblast cells, Coll.: collagen.

sample	MF	depth [µm]	dir.	f_{peak}	f_{av}
Conv.[1]	TPEF	10.0	lat.	5.57	-
Conv.	TPEF	13.0	lat.	2.04	-
Urea	SHG	7.4	lat.	5.73	7.60
Urea	SHG	13.0	ax.	3.74	5.92
Urea	SHG	50.0	ax.	3.96	8.52
RFB.	SHG (urea)	13.0	lat.	2.25	-
RFB.	SHG (urea)	27.0	lat.	1.27	-
RFB.	SHG (urea)	0	ax.	1.70	-
RFB.	SHG (bead)	0	ax.	2.45	-
RFB.	SHG (urea)	30.0	ax.	0.85	-
RFB.	TPEF (bead)	30.0	ax.	1.74	-
RFB.	SHG (urea)	100.0	ax.	1.63	-
RFB.	TPEF (bead)	100.0	ax.	2.78	-
Coll.	SHG (urea)	-	-	-	0.53
Coll.	TPEF (bead)	-	-	-	1.96
RFB	TPEF	0	lat.	5.24	-
RFB	TPEF	92.0	lat.	-	7.74

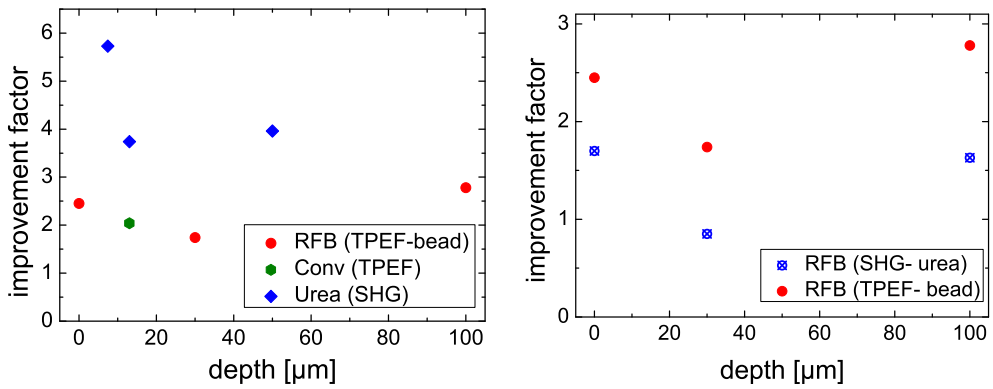

(a) (b)

Figure 6.32: **(a)** Improvement factors of optimisations on MFs that match the imaging modality. Optimisations on the intrinsic SHG signal in urea crystals imaged with SHG are compared to optimisation on intrinsic TPEF to image *convallaria* and an optimisation on the TPEF of a bead to image RFB in TPEF modality. **(b)** Improvement factors achieved with DMM shapes that have been pre-optimised on either SHG emitted from urea or TPEF emitted from a bead to image RFP in TPEF mode.

it can be observed from Fig. 6.32a that the improvement factors obtained with optimisations on intrinsic SHG in urea are greater (factor 4.5 increase on average over depth) than those achieved with TPEF as a MF either intrinsically in *convallaria* or as a preoptimisation on beads applied to the imaging of RFB in TPEF modality (factor 2.2 increase on average). This has been reported previously and is likely due to the coherent nature of higher harmonic generation for which field summation is affected in complex ways by the excitation phase distribution [299].

Secondly, the imaging of RFB cells in TPEF modality with pre-optimised DMM shapes is compared (Fig. 6.32b). The preoptimisation was either performed on the SHG signal of urea crystals or the TPEF signal of fluorescent beads. The DMM shapes obtained from optimisations performed on a fluorescent bead lead to higher improvement factors (2.3 on average through depths) than those performed on urea (1.4 on average through depths) when applied to the imaging of RFB in TPEF modality.

Comparison to literature Schwertner *et al.* used a Mach-Zehnder stepping interferometer to measure the aberrations introduced by biological specimens. The measured wavefronts were decomposed into Zernike modes in order to classify and quantify the aberrations. For the six specimens examined, they found that the average signal improvement was between 2 and 10 fold for a correction of the Zernike modes 5-22 [289]. Jesacher *et al.* implemented wavefront sensorless AO in harmonics generation microscopy optimising on total image intensity with a DMM and reported increases in peak intensity of up to 50 % [36]. The same level of signal increase has also been achieved in Débarre *et al.* where imaged-based AO in TPEFM is reported [298]. Bueno *et al.* implemented closed-loop AO comprised of a WFS and DMM to compensate for the aberrations of the illuminating beam. In conclusion of all the samples under investigation they reported an increase in both TPEF and SHG in the range between 20 - 200 % [314]. In Cha *et al.* improvement in terms of signal strength is on the order of 20 - 70 % [296] for a closed-loop system that utilises the confocal principle for depth selection of back-scattered light whose aberrations are then measured and corrected for by a DMM. Table 6.6 on p.139 summarises published literature concerned with aberration correction in nonlinear microscopy.

6.3.3 Theoretical imaging depth

The depth at which the SNR ratio of the parafocal fluorescence S to the out-of-focus background fluorescence B reaches unity can be used to define the maximum imaging depth [269]:

$$\frac{S}{B} = \frac{2\pi \mathrm{NA}^2}{\lambda n \iota} z^2 \exp\left(\frac{-2z}{\iota}\right) \tag{6.3}$$

where λ is the excitation wavelength, n is the refractive index of the medium and ι is the scattering mean free path length. Using $\lambda = 1098\,\mathrm{nm}$, NA = 1.3, n=1.33, and interpolating $\iota = 300\,\mu\mathrm{m}$ for a bioengineered connective tissue model at our wavelength from these references [315,316], the theoretical maximum imaging depth in the organotypics used in this work can be roughly estimated as $\approx z_{max} = 1500\,\mu\mathrm{m}$. In this work an optimisation was performed on the TPEF signal emitted by living fibroblast cells at the surface of an organotypic sample. The DMM shape from this optimisation allowed imaging 92 µm into the sample which was barely possible without the AO and resulted in a 7.7 fold signal intensity improvement. This imaging depth could be extended if optimisation were to be performed at the respective depth rather than on the surface of the sample. The full potential of AO to extend imaging depth in NLM has not yet been reached in this study but the results so far look promising and compare well with penetration depth improvement previously published.

Marsh *et al.* reported on a TPEFM with incorporated AO for the correction of specimen induced aberrations [35]. They used GA driven aberration correction with feedback from multi-photon fluorescence within a ROI and reported the extension of imaging depth attainable from 3.4 µm to 46.2 µm defined by an axial resolution of 1.25 µm FWHM. In Aviles-Espinosa *et al.* the intensity improvement with a closed-loop AO setup was 5.32 fold for the TPEF imaging of *C. Elegans* through a layer of scattering agar at a depth of 115 µm and 3.91 fold at a depth of 40 µm into mouse brain slices expressing green fluorescent protein [301].

6.3.4 Absorption and heat generation

The effect of absorption is negligible compared to scattering but should be taken into consideration in terms of sample heating. Water absorption increases for excitation wavelength above 900 nm thus posing a potential limitation of IR MPM for biomedical applications in live, hydrated tissues. It has been found that due

to rapid heat diffusion in biological tissue and beam scanning the temperature increase at the focal point of a laser scanning microscope is negligible [201, 279, 317]. For example it has been estimated that the temperature increase in the focal spot of a system comparable to ours is of the order of tenths of a Kelvin [318].

6.3.5 Wavefront quality and stability

High-power lasers are dynamic optical systems and the wavefront aberration of the emergent beam might suffer fluctuations at different temporal rates [319]. The output quality of femtosecond, high-power lasers is limited by lower-order, long-temporal (static) aberrations (mainly defocus and astigmatism) that arise from imperfections and misalignments of optical elements within the cavity and thermo-optical, dynamic aberrations that are caused during the strong heat generation during optical pumping [320]. Bueno *et al* measured the wavefront aberrations of a 130 fs Ti:Sa laser with 1 kHz repetition rate at two different temporal rates before and after cavity alignment with a real-time Shack-Hartmann sensor outside the cavity and found that the laser wavefront aberrations were stable over time and temporal variations never exceeded 1 % RMS [320]. They found defocus and astigmatism as the dominant aberration terms. Higher quality output beams that benefit from correction of also higher order aberrations can be achieved with intra-cavity AO [100, 321, 322], however, for this study temporal stability is sufficient as higher order aberrations can be compensated for with extra-cavity AO.

6.3.6 Chromatic aberrations

When interchanging SHG and TPEF modality, chromatic aberrations have to be considered. Chromatic effects have been shown to be negligible over a significant wavelength separation [302, 303]. For example, in the extremest case, Aviles-Espinosa *et al.* have measured the sample induced aberrations at the TPEF wavelength to apply the conjugate aberrations to the excitation beam of roughly twice the wavelength [301]. This shift in wavelength did not affect their method, allowing them impressive improvements in signal intensity and contrast. It should be noted that they employed a microscope objective, which was corrected for chromatic aberrations from UV to IR, however the wavelength shift between SHG and TPEF signals considered in this work is on the scale of a few tens of nanometers.

6.4 Summary and conclusions

This chapter presents the design and implementation of an AO system in a non-linear microscope and details the basic alignment and calibration procedures as well as specific adaptations to the RSA using the LabVIEW programming language. Image degradation due to optical aberrations that are increasing with depth was analysed qualitatively and quantitatively in terms of signal intensity and contrast.

The aberrations created by the optical system and the sample under investigation were compensated with a DMM in a way that does not require actual knowledge of the wavefront distortions. The aberration correction required by the DMM shape was determined with a RSA optimising on either TPEF or SHG signal intensity in a pixel or small ROI in the image. As expected, the optimisation on a single pixel/small ROI was sufficient to improve the image in the entire field of view [107, 142]. This approach allows for the dynamic correction of a wide variety of aberrations, generated throughout the optical train including the sample, rather than the static correction of only one specific kind of aberration, like for example spherical aberration.

Optimisations were performed on a variety of samples, including fluorescent beads for spatial resolution analysis, *convallaria* and urea crystals, as test samples in the TPEF and SHG modality respectively, and organotypics, intermediate tissue culture systems which are comprised of red fibroblast cells embedded in collagen. The latter can produce SHG signals as well as TPEF signals and have been employed to investigate the optimisation on SHG signal to determine the aberration correction required, an approach which is not limited by photobleaching and to then determine the usefulness of this DMM shape in imaging fluorescent structures.

Some significant improvement in signal intensity was achieved in TPEF and SHG imaging modalities with improvement factors ranging from 1.2 to 8.5 fold. However, diffraction limited resolution was not restored and might require careful re-consideration of the merit factor. Additionally, z-stacks, series of images along the z-axis with a fixed lateral position, were recorded. This allowed for the quality of the image to be analysed with depth. Even if the penetration depth is ultimately limited by scattering in many biological specimens, AO can improve the quality of images at depths at which imaging would not have been possible without aberration correction.

Future work on this project might include imaging in transparent samples with low scattering coefficients like, for example, Zebrafish, where it is expected that AO will have a higher impact on signal intensity and resolution. In transparent samples, imaging is less depth-restricted by scattering and therefore more optical aberrations can accumulate at a greater depth. Alternatively tissues that induce large amounts of aberrations even at shallow depths will potentially benefit from AO. For example skin tissue exhibits stratified layers with vastly different indices of refraction and hence could provide a sample where the benefits of AO outweigh the signal degradation of scattering. Another possibility is optical clearing, a procedure in which tissues have been processed in a way that reversibly decreases scattering for example by dehydration and adding of index matching medium [323].

Table 6.6: Overview of selected published literature on aberration correction in NLM. ZM: Zernike modes, HGM: harmonics generation microscopy, OPEF: one photon excitation fluorescence, SA: spherical aberrations. WF: wavefront, GA: genetic algorithm, Imp: improvement factor.

Mode	MF	Imp.	Relevance	Ref.
OPEF,TPEF	Strehl ratio	2-10	Interferometrical measurements of aberrations in biol. specimen.	[289]
TPEF	Tot. signal int.	1.5	Correction of SA with correction collar of water imm. objectives.	[294]
TPEF	Axial resolution	2	SA correction with transparent deformable membrane mounted before vacuum.	[68]
TPEF	Mean image int.	1.5	Image-based AO in TPEF, aberrations most significant in astigm., coma and SA.	[298]
THG,TPEF	Image sharpness	1.25-2.7	Image-based AO in HGM, an extended PSF can result in a higher signal level.	[238]
TPEF	-	-	Closed-loop AO with SLM, first demonstration of AO in NLM.	[92]
TPEF,SHG	Tot. signal int.	1.25-2	Closed-loop AO to compensate for aberrations of illumination beam.	[314]
TPEF	Tot. signal int.	1.2-1.7	Closed-loop AO with confocal detection of back-scattered light.	[296]
TPEF	Tot. signal int.	1.3-9.1	Closed-loop AO by creating a nonlinear guide star.	[301]
TPEF	Tot. signal int.	2	Closed-loop AO with coherence-gated WF sensing of the back-scattered light.	[295]
OPEF	Strehl ratio	2-10	Closed-loop AO with fluorescent beads as reference beacon in wide-field microscope, analysis of chromatic aberrations.	[168]
SHG,THG	Tot. image int.	1.5	WFS-less AO in HGM by sequential correction of ZM with DMM, maximum signal not necessarily corresponding to minimum aberrations.	[36]
TPEF	Pixel int.	1.3-1.5	GA based AO, using a single aberration correction per depth.	[142]
SHG	Spectral int.	6	GA based AO to compensate for aberrations of illumination beam.	[37]
SHG,TPEF	Total signal int.	-	GA based AO for correction of off-axis aberr. introduced by parabola scanning.	[99]
TPEF	Tot. signal int.	13.5	GA based AO, concept of look-up tables.	[35]
TPEF	Tot. signal int.	4	GA based AO, extension of axial scanning range.	[98]
TPEF	-	-	Rejection of out-of-focus fluores. by subtraction of highly aberrated images.	[300]

Chapter 7

Optical Trapping

7.1 Introduction

Optical trapping is the confinement in three dimensions of microscopic particles through the forces exerted by the intensity gradients of a strongly focused laser beam [324, 325]. The trapping is ascribed to the transfer of photon momentum to a transparent particle with a refractive index slightly higher than that of the surrounding medium. The net force is directed toward the highest intensity region near the beam focus.

In 1971 Ashkin *et al.* published a paper on optical levitation of a particle in air [326]. In his experiments a weakly focused laser beam was shone from below on a particle and propelled it upwards until it eventually reached an stable height, where the force due to radiation pressure was equal to the force due to gravity. Later, an arrangement of two counter-propagating beams allowed objects to be trapped in three dimensions [327]. Still working in the Bell Labs, Ashkin *et al.* published a paper that would be the first report of stable 3D confinement of dielectric particles in 1986 [328]. This seminal paper has now been cited over 2300 times and the technique, termed optical trapping or optical tweezers (OT), is now used in a wide and ever growing field of applications and has truly become a mainstream tool in a variety of research fields. Complete optical tweezers kits (OTKB from Thorlabs, £12k; HOTKit from Arryx/Bolder Nonlinear Systems) are now commercially available. Given that OT and high-magnification microscopes have many components in common, a research grade microscope, mostly of the inverted type, is normally used as the starting point for a custom built instrument adding the advantages of a sturdy frame, sample

stage, beam steering, additional ports for cameras, white light illumination and focusing optics.

Light is easily manipulated and relatively noninvasive which makes mechanical measurements with OT an especially suited tool in studies of biological systems. Single molecule mechanical measurements using OT, including biological motor motility, protein-protein unbinding, and protein unfolding, have attracted a tremendous interest in recent years [329, 330]. Recently, OT through a turbid medium was demonstrated [331]. In a multi-modal approach OT is easily combined with microscopy and Raman spectroscopy (named Micro-Raman tweezers) making it a powerful analytical tool in biotechnology [332]. Further applications of OT include nanosurgery with optical scalpels [333], nanofabrication [334, 335], particle sorting [336] and microrheology studies [337]. Not only applied research fields but also our fundamental understanding of light fields, angular momentum and Brownian dynamics has profited from recent advances in OT and the shaping of light [338]. Excellent reviews on OT provide references for further reading [339–341].

7.2 Physical background

The general theory describing OT is the interaction between an optical field and dielectric particles. The electro-magnetic energy density stored in a dielectric particle is minimised when the particle with a high dielectric constant is placed at the point of greatest intensity and a restoring force arises when the particle is removed from this equilibrium position [342]. However, the strong focusing with high NA lenses that is necessary in OT makes the field calculations in the beam waist region non-trivial as the paraxial approximation no longer holds true (see page 19). Theories for OT have therefore been developed in approximations that are dependent on a comparison between the particle radius a and the wavelength λ.

7.2.1 Geometrical optics regime

When the particle of radius a is much larger than the wavelength used for trapping, *i.e.* $a \gg \lambda$, the trapped object acts as a lens and OT can be understood in a much simplified approach: the conservation of linear momentum. An overview of the trapping forces acting on a transparent dielectric particle is given in Fig. 7.1a.

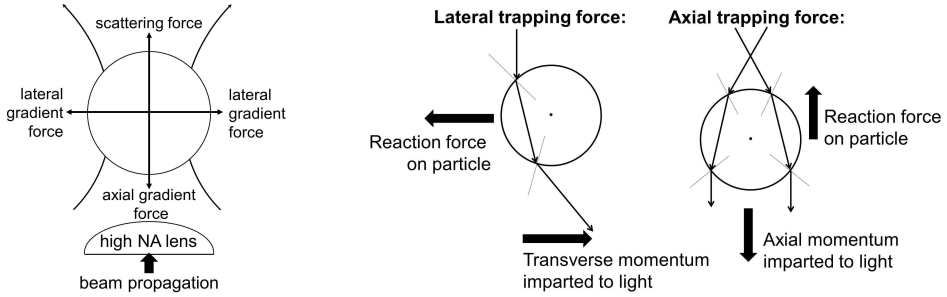

(a) **(b)**

Figure 7.1: (a) Overview of the forces acting on a transparent dielectric particle in an OT. **(b)** Origin of the lateral and axial trapping forces in the geometrical approach.

The scattering force is proportional to light intensity and acts perpendicular to the incident wavefronts pushing the object in the direction of light propagation. The lateral and axial gradient forces that are necessary for stable trapping arise because of the refraction of light rays at the surface of the transparent dielectric particle and the resulting reacting forces (Fig. 7.1b).

The gradient force is proportional to the spatial gradient of the light intensity and is directed towards the region of highest intensity. The gradient force is a consequence of the refraction of light rays and can be understood in the following way. A light beam carries a linear momentum p of $\frac{h}{\lambda}$ per photon. From special relativity theory, the relativistic energy E of a particle without mass traveling with the speed of light c is $E = pc$. The photon momentum can therefore be expressed as $\vec{p} = \frac{E}{c}\vec{n}$ where $\vec{n}$ is a unit vector pointing in the direction of the light beam. The refraction of a light beam of power $\mathcal{P}$ by a transparent object results in a change in photon momentum and the refracting object experiences a corresponding reaction force:

$$\vec{F} = -\frac{d\vec{p}}{dt} = -\frac{Ed\vec{n}}{cdt} = -\frac{\mathcal{P}}{c}\Delta\vec{n} \tag{7.1}$$

where the minus sign indicates that the Force is opposite to the change in direction the light experiences.

The intensity profile of a Gaussian beam cross-section of a TEM_{00} mode is shown in Fig. 7.2. Two rays of different intensity are diffracted by the spherical dielectric of higher refractive index than its surrounding medium. The inset of the schematic shows the net change in momentum that those two light rays experience due to their refraction. The conservation of momentum dictates that the particle

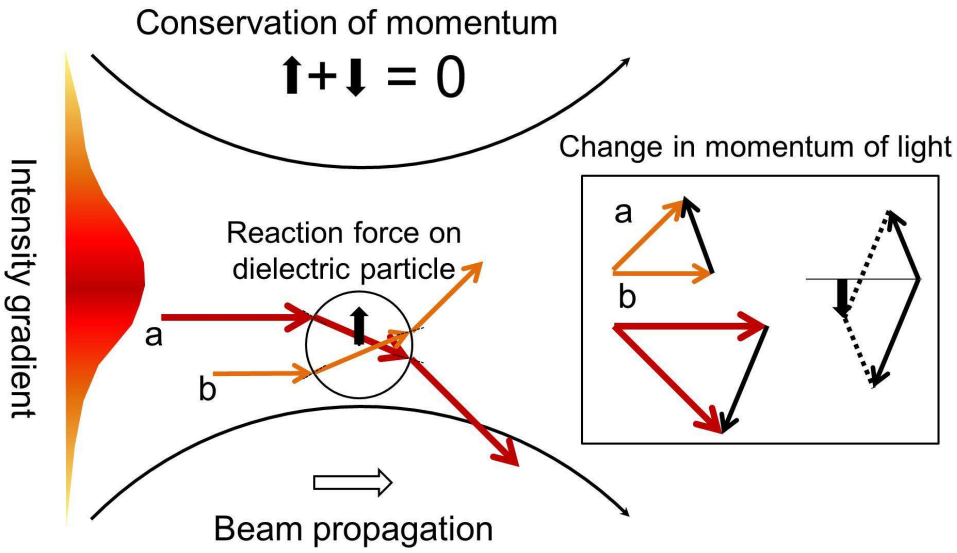

Figure 7.2: The gradient force in optical trapping.

therefore experiences a change in momentum that is equal in magnitude but opposite in direction. Due to the intensity distribution of the trapping laser beam the net force acting on the trapped particle is directed towards the region of highest intensity. The momentum transferred from a light beam of power $\mathcal{P}$ leads to a reaction force on the particle given by:

$$F_i = Q_i \frac{n_\mathrm{m} \mathcal{P}}{c} \tag{7.2}$$

with $i = (z, r)$, n_m the refractive index of the medium and Q_i a dimensionless quantity smaller than unity denoting trapping efficiency. Q represents the fraction of momentum $\frac{n_\mathrm{m} P}{c}$ carried by the laser beam that is converted to the trapping force. A similar approach also holds true for the reflection and scattering of light from the interface; however, as the trapped object is usually suspended in a fluid of similar refractive index, the resulting Fresnel reflections and corresponding recoil forces are negligible [340].

Since the scattering force acts in the beam propagation direction whereas the gradient force acts in the direction of positive intensity gradient, normally the beam focus, the stable trapping position lies just downstream of the focus point. Stable trapping occurs when the conservative gradient force is larger than the dissipative scattering force and when the thermal energy of the Brownian motion of the particle is smaller than the optical potential $U = \frac{1}{2} k r^2$ associated with the trap:

$$\exp \frac{-U}{k_B T} \ll 1 \tag{7.3}$$

where k_B is the Boltzmann constant, T the absolute temperature and k is the spring constant associated with the OT.

The gradient and the scattering force both scale linearly with light intensity, therefore it is paramount for OT to create maximal intensity gradients in the beam which is achieved with extremely tight focusing. Rays with a large incident angle contribute more to the trapping force than rays with small angle of incidents and the maximum trapping force occurs for rays of 70° angle of incidence to the particle surface [343]. For that reason, OT is always achieved with beams that are brought to a strong focus with high NA lenses, where the maximum angle of incidence is given by $\alpha = \arcsin(\frac{\mathrm{NA}}{n})$. It is worth pointing out that above considerations hold true for a particle of higher refractive index than the surrounding medium. Conversely when trapping an air bubble or hollow sphere, the gradient force is reversed and the particle is repulsed from the region of highest intensity. Trapping of such particles requires specially engineered Laguerre-Gaussian modes, which have annular intensity profiles and carry orbital angular momentum.

7.2.2 Rayleigh regime

Particles that are smaller than the beam waist of diffraction limited beams, *i.e.* $a \ll \lambda$, are treated as an induced small electric dipole moment that is immersed in an optical field which is oscillating at a frequency ν. The forces acting on this dipole generally speaking, draw the particle up intensity gradients in the electric field towards the focus.

Scattering force

Originating from the changes in momentum that light experiences by scattering, *i.e.* absorption and reradiation of light by the dipole, this force is proportional to laser intensity and pushes the particle along the laser beam propagation [340]:

$$\vec{F}_{scat}(\vec{r}) = \frac{n_2}{c}\sigma I(\vec{r}) = \hat{z}\frac{n_2}{c}\frac{128\pi^5 a^6}{3\lambda^4}\left(\frac{N^2-1}{N^2+2}\right)^2 I(\vec{r}) \tag{7.4}$$

where σ is the scattering cross section of the particle, $\hat{z}$ is the unit vector along the optical axis, r is the position vector referred to from the beam centre at the beam waist ω_0 and $N := {}^{n_1}/_{n_2}$ the ratio of refractive index of the particle (n_1) and

the surrounding medium (n_2). Here $\hat{z}I(\vec{r}) = \left\langle \vec{S}(\vec{r},t) \right\rangle_T$ denotes the time average of the Poynting vector $\vec{S}(\vec{r},t)$.

Gradient force

The gradient force is caused by the Lorentz force acting on the induced dipole moving it along the gradient of optical intensity [344]. If the refractive index of the particle is greater than that of the suspension medium, this force will pull the particle towards the more intense regions of the beam. The gradient force is proportional to the polarisability α of the sphere and the intensity gradient of the electric field:

$$\vec{F}_{grad}(\vec{r}) = \frac{2\pi\alpha}{cn_2^2}\nabla\left|\vec{E}^2(\vec{r})\right| = \frac{2\pi_0 a^3}{c}\left(\frac{N^2-1}{N^2+2}\right)\nabla\left|\vec{E}^2(\vec{r})\right| \tag{7.5}$$

Due to the resonant frequency of the induced dipole ν_0, the force acts either attractive for $\nu < \nu_0$ or repulsive for $\nu > \nu_0$ [342].

7.2.3 Calibration methods

The gradient force is a linear function of displacement over distances up to several hundred nanometers [325], this means the restoring gradient force is proportional to the offset from equilibrium position and the OT acts like a Hookian spring. The equation of motion governing the behaviour of a trapped object of mass m, in a medium with viscous damping β is a sum of inertial, viscous and elastic forces:

$$m\frac{\partial^2 x}{\partial t} + \beta\frac{\partial x}{\partial t} + kx = 0 \tag{7.6}$$

where $\beta = 6\pi a\eta$ is the viscous drag according to Stokes, η is the viscosity of the fluid and k is the spring constant. Using the resonant frequency of the object without viscous damping:

$$\omega_0 = \sqrt{\frac{k}{m}}, \tag{7.7}$$

and the viscous damping factor:

$$\xi = \frac{\beta}{2m\omega_0}, \tag{7.8}$$

eq. 7.6 can be re-written:

$$\ddot{x} + 2\xi\omega_0\dot{x} + \omega_0^2 x = 0. \tag{7.9}$$

The frequency of oscillation depends on the damping factor ξ. For typical biological applications, the motion is very over-damped [345] ($\xi > 1$) and the inertial and gravitational forces can be neglected [340]. The particle experiences an exponential decay back to equilibrium without oscillation and the solution of above differential equation is then given by:

$$x(t) = x_0 \exp\left(-\frac{kt}{\beta}\right) \tag{7.10}$$

Due to the viscous damping and the spring-like stiffness of the OT the system can be described as a low pass filter [346] with a $-3\,\mathrm{dB}$ roll-off frequency f_{3dB} given by

$$f_{3dB} = \frac{1}{2\pi}\frac{k}{\beta} \tag{7.11}$$

The trap stiffness can therefore be calculated from power spectrum analysis after determining the roll-off frequency.

Equipartition of Energy

The surrounding medium, in most cases water, does not only give rise to damping, it also provides for efficient cooling minimising the effects of laser induced heating. However, the motion of the water molecules also gives rise to a thermal energy $E_{th} = k_B T$, given as the product of the Boltzmann constant k_B and the absolute temperature T. This energy causes a random fluctuation of the particle around the equilibrium position, that can be calculated from the equipartition theorem and expressed as the mean-squared deviation in position along one axis:

$$\frac{1}{2}k_B T = \frac{1}{2}k\left\langle x^2\right\rangle. \tag{7.12}$$

This theorem dictates that the thermal energy per degree of freedom must equal the potential energy of the trapped particle. By tracking the variance $\langle x^2\rangle$ of the fluctuation, the spring stiffness k can be found through computation.

Viscous drag force method

The Reynolds number gives a measure of the ratio of inertial forces to viscous forces and consequently quantifies the relative importance of these two types of forces for given flow conditions. When considering micron length scales in aqueous media, the Reynolds number is smaller than unity, meaning that viscous forces are dominant and the flow is laminar and characterised by smooth constant fluid motion [347]. Under these circumstances, the maximum radial trapping force can be derived from the critical velocity v_c at which the particle escapes from the potential well associated with the trap [348,349]. To this end a viscous drag force F_D is exerted on the bead by fluid flow according to Stoke's law:

$$\vec{F}_{D,c} = \beta\zeta\vec{v}_i = -6\pi\eta\zeta a\vec{v}_c \tag{7.13}$$

where η is the viscosity of the medium and ζ is a factor considering surface effects (see also Faxén's law p. 170). The fluid flow can be exerted by either moving the sample stage or by scanning the trapping beam through a stationary medium.

7.3 Advances in trapping

7.3.1 Multiplexing

With a concept called time-sharing OT of multiple particles with one light beam has been realised by rapidly scanning the laser focus between two or more trap positions [350,351]. The trapping beam must revisit each trap position often enough such that the particle has not diffused a significant distance. Various techniques have been developed over the past decade including mechanical scanners [352,353] and acousto-optical modulators [345]. Alternatively, the beam is split earlier in the optical pathway and then recombined before entering the microscope objective to create two separate traps, however, computer-generated diffraction patterns, or holograms, displayed on programmable diffractive elements, like spatial light modulators (SLMs) are now the easiest and most common way of producing multiple traps simultaneously [84, 354–356]. The diffractive element in SLMs is commonly comprised of liquid crystals and allows for real time generation of a diffraction pattern such that for example TEM_{01} 'doughnut' modes can be produced [357]. These modes have an annular intensity distribution with a zero

on-axis intensity, called an optical vortex, and find application in the trapping of particles that have a lower refractive index than the surrounding medium making them experience a force that repels them from the area of highest intensity [358].

7.3.2 Novel beams

Moving away from the standard Gaussian single-beam trap, the shaping of the phase and amplitude of a light field provides unusual light patterns that add a major new dimension to research into particle manipulation [359]. The fundamental Gaussian mode emitted from most commercial lasers can now be easily converted into a beam with a different intensity and phase structure by the means of computer-generated holograms [360,361]. Novel beams like Laguerre-Gaussian beams have an annular intensity structure and carry angular momentum [362]. These beams provide means to apply torque as optical spanners [363] thereby making particles spin or orbit when applied to OT [364,365] and can furthermore create micro-pumps [366]. Undoubtedly all these advances could not have taken place if SLM technology had not equally been driven forwards. A further development is the use of 'diffraction free' Bessel beams in OT [367,368]. These beams propagate over a limited range, typically several millimeters, without diverging or changing shape and create an axial intensity distribution without gradient that allows for the lateral trapping and guiding of objects along the optical axis [369].

7.4 Applications of trapping

Optical tweezers have been used in combination with confocal microscopy [370], for scanning force microscopy [371], to excite two photon excitation fluorescence with continuous waves [372] and optical scissors [373]. By measuring the compliance of bacterial flagella [374], Block *et al.* paved the way for the use of calibrated OTs as force transducers [375]. A vast number of applications in biological science followed including studies on the forces exerted by a single motor protein [376,377] and the stretching of single deoxyribonucleic acid (DNA) molecules [378]. Often polystyrene beads are attached as handles to biological structure that are too small to be manipulated on their own. The reader is referred to recent reviews on the vast range of biological studies utilising OT [332, 359, 379, 380].

7.5 Trapping at depth

The OT can be described as a potential energy well associated with the intensity distribution at the laser focus and is therefore dependent on the shape of the incoming wavefronts. Perfectly spherical wavefronts will form a diffraction limited focal spot with the highest intensity gradients whereas any deviation from that geometry, due to the presence of optical aberrations, will cause the focal spot to broaden and elongate and the trap to weaken [381]. More specifically, truncating the tails of the Gaussian beam by finite apertures and inducing spherical aberrations (SA) that are caused by the introduction of a refractive index mismatched interface (see Fig. 7.3 and section 3.4.1) result in non-ideal trapping conditions due to distorted foci [13,152,382,383]. A theoretical approach to the depth dependency of trapping stiffness due to SA is given in Rohrbach and Stelzer based on the propagation of electromagnetic waves for sub-wavelength sized particles [384] and in Fällman and Axner in the ray-optics approximation for micrometer sized particles [385].

It should be noted that water-immersion lenses do not suffer from spherical aberration when trapping in aqueous media [282] and therefore no depth dependence degradation of trapping efficiency can be observed in those cases. [101,386]. A lot of attention has been recently paid to aberration correction in micromanipulation [331, 351], and several methods have been suggested to compensate

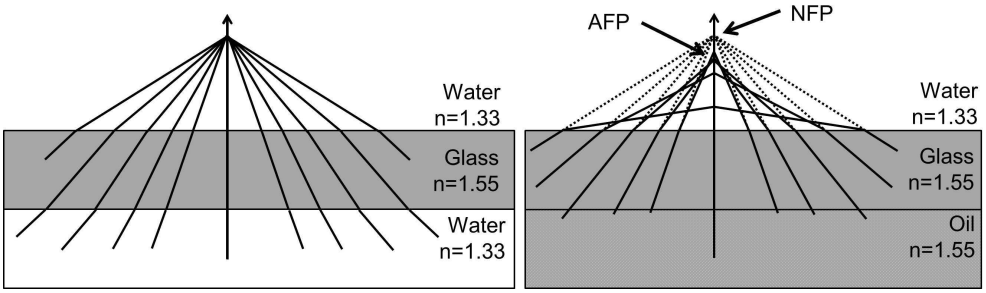

Figure 7.3: Spherical wavefront impinging on a plane dielectric interface. **(a)** Using a water-immersion objective. The rays are refracted at the water-glass and at the glass-water interface resulting in an unaberrated focus. **(b)** Using an oil-immersion objective. Spherical aberrations are introduced due to the phase difference between rays of different convergence angles. The actual focal spot (AFP) is elongated with paraxial rays focusing deeper into the sample than marginal rays. Rays at critical angle for total internal reflection remain at the surface. The dotted line indicates the position where the focus would have been without refractive index mismatch, (nominal focus position, NFP).

for aberration induced deterioration of trap performance. Theofanidou *et al.* extended the trapping depth by using a DMM to optimise on the two-photon fluorescence signal generated by a trapped, dye-stained polystyrene bead [101]. Ota *et al.* improve the axial trapping force by also specifically correcting for SA by the use of a DMM [387]. The presence of SA was also addressed by tuning the refractive index of the immersion oil [388] as well as changing the collimation of the beam by adjusting the effective tube length of the objective to enhance transverse trapping efficiency [389] and axial trapping strength [390].

In chapter 8 of this thesis, the use of an optimisation algorithm is described that rapidly alters the shape of a DMM until a specifically chosen merit factor is satisfactorily improved. The random search algorithm (RSA) used in this work has previously been successfully applied to adaptive optics in multiphoton and CARS imaging microscopy [38, 104].

Using a RSA in conjunction with a merit factor has several distinctive advantages in the application of micromanipulation described in this work. First, it eliminates the need for re-imaging and wavefront sensing since an *a priori* knowledge of the aberrations introduced is not necessary for their correction, thereby reducing complexity and cost of the optical setup. Second, this approach allows for the dynamic correction of a wide variety of aberrations rather than the static correction of only one specific kind of aberration, for example SA. Third, the merit factor used in the optimisation routine can be chosen such that it is directly proportional to the specific quantity that is to be improved. The aim of the AO system is to enhance the lateral trapping strength at depth. Our choice of lateral bead displacement from equilibrium due to a viscous drag force as a merit factor is a straightforward approach to that aim. By minimising this displacement, the spring constant is directly proportionally increased and the trapping strength improved.

Achieving a stronger trapping force at depth without having to increase incident laser power is especially beneficial when working with cells where prolonged exposure to high power laser radiation can affect their viability [11]. Uniformly distributed trapping strength throughout depth is also a critical issue when the OT is used as a force transducer investigating mechanical properties such as elasticity, stiffness, rigidity and torque of cells, intracellular structures, single molecules and their suspending fluids [12, 13]. The trapping of small nanoparticles is another application where a perfectly aberration-free system is crucial to the success of the experiment [391, 392].

Chapter 8

AO in an Optical Trapping System

Abstract In essence, optical trapping (OT) is the confinement in three dimensions of microscopic, dielectric particles through the forces exerted by the high intensity gradients in the electric field near the beam waist of a strongly focused laser beam. The trapping is ascribed to the transfer of photon momentum to a transparent particle with a refractive index slightly higher than that of the surrounding medium. The net force is directed toward the highest intensity region of the beam. In an OT performance often deteriorates with depth due to aberrations arising mainly from the refractive index mismatch when an oil immersion objective is used to trap deep within an aqueous solution.

This chapter describes the implementation of sensorless adaptive optics (AO) technology based on a deformable membrane mirror (DMM) and the modifications made to the optimisation algorithm in order to correct for these and residual aberrations in an OT setup. The optimum shape of the DMM was determined with a random search algorithm (RSA) optimising on a merit factor (MF) that was chosen to be directly proportional to the lateral trapping force. By minimising the lateral bead displacement from equilibrium due to a viscous drag force which was applied through controlled motion of the sample stage the spring constant of the trap is directly increased. The improvement in the trapping force of a 1 µm diameter silica bead was quantified with a study of spring constants with and without aberration correction at increasing depths. The stiffness of the trap could be improved throughout the trapping range of the conventional trap and beyond. At a depth of 131 µm the trapping stiffness was improved by a factor of 4.37 and 3.31 for the x- and y- axis respectively, demonstrating the pronounced power of optimisation algorithm based AO for micromanipulation.

Contents This chapter is structured as follows. In the first section the experimental conditions are introduced, including the optical setup (subsection 8.1.1), the sample preparation (subsection 8.1.2), and the experimental methodology (subsection 8.1.3). The results obtained in these studies are presented in section 8.2. After noting the measured magnification of the optical setup (subsection 8.2.1), the necessary adaptations of the RSA to this specific application are covered in subsection 8.2.2. This includes details on the calculation of the MF which was chosen specifically to be directly proportional to the lateral trapping strength, and a sequence of code for the tracking of the bead's centroid. The problem of trap strength degradation at depth is discussed for the trapping of 3 µm beads in subsection 8.2.3. The outcome of optimisations performed on the lateral trapping strength for a 1 µm bead is detailed in the following subsections. The effect of the optimised DMM shape on residual Brownian motion is analysed (subsection 8.2.4) as well as the evolution of spring constants with depth for the optimised and unoptimised case (subsection 8.2.5). In subsection 8.2.6 the modal content of the optimised DMM shapes is compared in terms of the higher order Zernike coefficients. This chapter concludes with a discussion (section 8.3) and the summary and conclusions given in section 8.4.

8.1 Experimental details

8.1.1 Optical setup

The experimental setup, combines particle trapping within a commercial, inverted microscope (Nikon, Eclipse) and an AO system for aberration correction (Fig. 8.1). A laser beam from a diode-pumped, solid-state laser (Laser2000, SDL-532-500T) emitting at 532 nm with a linear polarisation is expanded to match the active area (15 mm ∅) of the DMM. Appropriate polarisation optics allow for an incident angle of 0° onto the DMM surface. A half-wave plate first p-polarises the light which is then transmitted by the polarising beam splitter (PBS) cube. The quarter-wave plate produces circularly polarised light which changes its handedness upon reflection off the DMM and is therefore reflected from the PBS. The DMM employed in this work (Mirao52e, Imagine Optic) uses 52 independent magnetic actuators to control the shape of the highly reflective, silver coated membrane. The actuators can be either pushed or pulled with an individual stroke of $10 - 15\,\mu m$ by applying control voltages of up to $\pm 1\,V$ to underlying

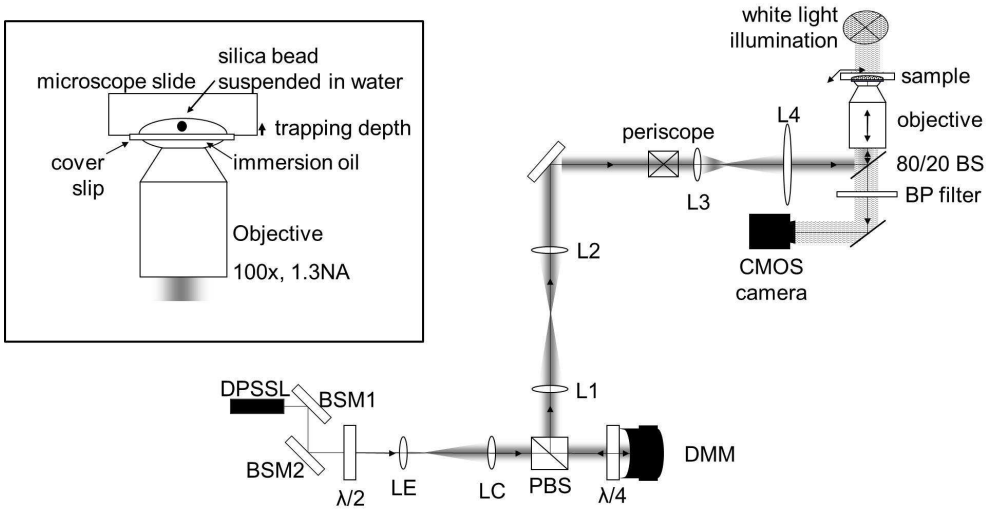

(a)

Figure 8.1: Optical trapping setup. DPSSL: diode-pumped, solid-state laser, BSM: beam steering mirror, LE: expanding lens (f=100 mm), LC: collimating lens (f=750 mm), $\lambda/2$: half-wave plate, $\lambda/4$: quarter-wave plate, PBS: polarising beam splitter, BS: beam splitter, BP: band pass. Relay lenses: L1 (f=630 mm), L2 (f=90 mm), L3 (f=70 mm), L4 (f=250 mm). Inset: oil immersion objective trapping a bead suspended in water within a cavity slide.

coils. More details on the DMM can be found in section 2.5.1 on page 26 of this thesis.

The DMM is re-imaged onto the back aperture of the microscope objective via two 4f re-imaging systems ensuring that both the DMM and the back aperture of the objective are in conjugate planes. The two 4f-systems allow for the creation of a plane conjugate to the back aperture of the microscope objective on one of the periscope mirrors. In this way the lateral trapping position within the field of view can be changed by using the adjustment screws of the mirror mount. The trapping beam is coupled into the microscope housing which allows taking advantage of its sample stage, microscope objective turret, white light illumination and output ports. Care has been taken to only slightly overfill the 6 mm back aperture in order to increase the power in the marginal rays at the edge of the illumination while not losing significant modulation power of the DMM in the periphery. The power was measured at the back aperture of the objective and kept at 5 mW throughout the experiments. The high NA objective (Nikon, 100x, 1.3 NA, oil immersion) with a working distance of 0.2 mm is infinity corrected and manufactured for use with a coverslip of thickness 0.17 mm (# 1.5). It is mounted on a piezoelectric z-translation stage (Physik Instrumente, PI E-665.CR) and focuses

the light into a sample mounted on the xy-translation stage (ASI, MS-2000) of the microscope. Both translation stages are computer controlled through custom written LabVIEW software.

White light is used to trans-illuminate the trapped particle from the top and is collected by the same microscope objective that is used for trapping. The objective lens images the bead onto a CMOS camera (Dalsa Genie HM640) which is connected to a desktop PC with a GigE ethernet interface (IEEE 1394). The camera features a resolution of 640 x 480 pixels and a frame rate of 300 Hz at full resolution. The functionality of region of interest (ROI) readout, however, allows for partial scan and hence a substantial increase in the frame rate when a smaller ROI is imaged. A band pass filter prevents the camera from being saturated by the trapping laser.

In another, similar setup, an alternative illumination source is used in combination with a pathway including an SLM instead of the DMM. The beam from a 3 W infrared 1064 nm Laser (Ventus, Laser Quantum) is expanded to just overfill the active area of an SLM (XY series, Boulder Nonlinear Systems). The SLM consists of 512 x 512 individually addressable pixels which alter the phase of the light (see also section 2.5.2). The SLM displays a hologram which is relayed onto the back aperture of the microscope objective. The power was measured at the back of the microscope objective in previous work by our group [11], and by assuming 40 % loses in the objective [325], the power at the sample was calculated to be $\approx$ 200 mW. This setup was used to much lesser extend and contributed only to few data shown in this thesis (Fig. 8.7).

8.1.2 Sample preparation

Silica beads of 1 µm or 3 µm diameter (MicroSil Microspheres, Bangs Laboratories Inc, 2.00 g/cm^3 density, 1.46 refractive index) were diluted in distilled water to a final concentration of a few particles/µl. A droplet of this solution was placed into a cavity slide, secured with a coverslip and sealed to avoid evaporation and contamination. The depth of the cavity is approximately 350 µm. The refractive index of the oil and coverslip are matched, so the first optical interface encountered by the laser beam is between the coverslip and the suspension water. Samples were prepared freshly for each set of experiments.

It has been shown that radial trap stiffness is maximised when the radius of the trapped particle and the beam waist of the trapping beam are nearly

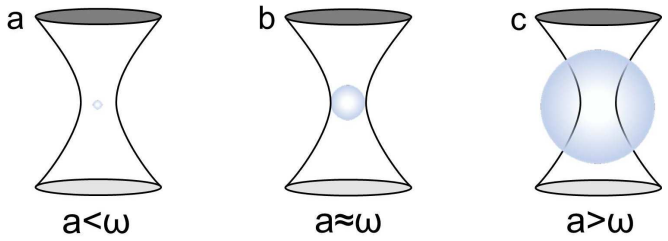

Figure 8.2: Schematic for the trapping of different sized beads. **(a)** The bead radius a is much smaller than the beam waist ω making trapping harder because of the smaller overlap of scatter volume and focal volume. **(b)** The radius is roughly equal to the beam waist. **(c)** The bead diameter is much larger than the beam waist which makes any shaping of the focal region less relevant due to the larger beads' decreased sensitivity to spot shape.

equal [382]. In Fig. 8.2 (a), the bead diameter $2a$ is much smaller than the beam waist 2ω making trapping harder because of the small overlap of scatter volume of the bead and the focal volume of the laser beam which creates the trapping forces. In (b), the bead diameter is roughly equal to the beam waist. This case is optimal for trapping stability [344] and also for the effectiveness of the optimisation routine [393]. In (c), the bead diameter is much larger than the beam waist which makes any shaping of the focal region less relevant due to the larger beads' decreased sensitivity to spot shape. On the other hand, it has been observed that smaller beads are more susceptible to aberration induced changes in trapping strength [394]. With a beam waist of $\omega_o \approx 0.4\,\mu$m, obtained with an 100x 1.3NA objective [348], a sphere diameter of 1 µm was chosen as a compromise between sensitivity for induced aberrations and overlap of scatter volume and beam waist for stable trapping. Stable trapping was important to ensure that the bead was not lost during the optimisation routine. A bead diameter of 3 µm was chosen for trapping with the SLM due to difficulties of stably trapping smaller particles.

8.1.3 Methodology

Trapping depth

A bead was trapped close to the coverslip surface and then dragged deep into the sample with the z translation stage in order to avoid surface effects. Optimisations were performed at various depths by moving the microscope objective 50 µm, 75 µm, 100 µm, 125 µm, 150 µm, and 175 µm into the sample resulting in optical trapping at the depths of 44 µm, 66 µm, 88 µm, 109 µm, 131 µm, and 153 µm.

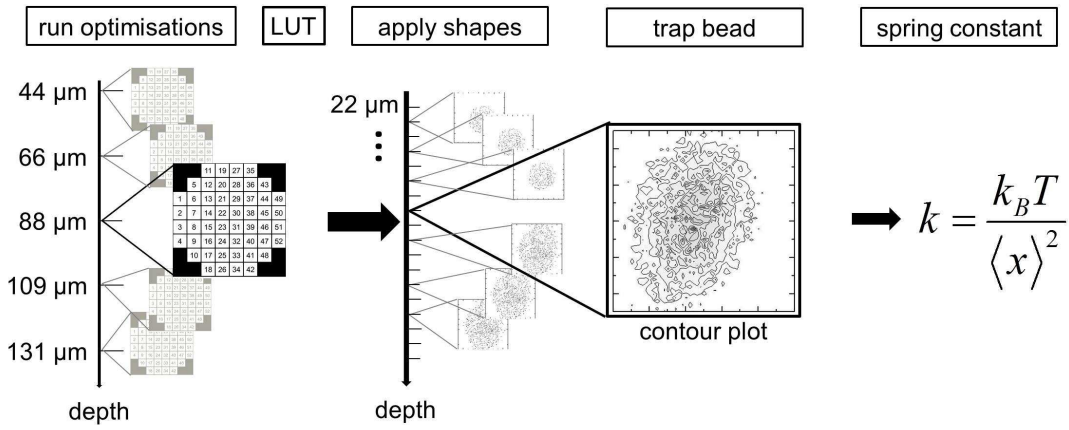

Figure 8.3: Schematic work flow. Optimisations were performed at specific depths. The best DMM shape from each optimisation was saved in a look-up table (LUT). Each DMM shape in the LUT was used to acquire contour plots containing 20,000 coordinates of the residual Brownian motion of a trapped bead. This was repeated from a depth of 22 µm in roughly 4 µm steps until the bead got lost from the trap.

This discrepancy is due to the axial trap location being controlled solely by the mechanical displacement of the focusing objective with respect to the glass/water interface. The actual trapping position is shifted closer towards this interface (see also Fig. 7.3, p. 149) [13]. Moving the objective over a distance Δ_{lens} with respect to the interface causes a shift in the position of the peak intensity Δ_{peak}. According to Wiersma *et al.*, this shift can be predicted in a paraxial geometrical approximation with $\Delta_{\text{lens}}/\Delta_{\text{peak}} \approx n_{\text{oil}}/n_{\text{water}} = 0.875$ [283]. All trapping depths given in this work were calculated by multiplying the distance the objective was moved according to the stage display with this factor. Using this factor and the working distance of 200 µm of the microscope lens, the absolute limit that the focus plane can be below the top surface of the coverslip is at 175 µm.

Look-up table

After each optimisation the DMM shape resulting in the lowest MF was saved into a look-up table (LUT). All shapes saved in the LUT were subsequently individually applied to the DMM and the residual Brownian motion of a trapped bead was rapidly tracked for various trapping depths, starting at 22 µm and in roughly 4 µm intervals until the bead was ultimately lost from the trap. The work flow is visualised in Figure 8.3. In this way, each LUT shape produced a dataset containing 20,000 coordinates for each trapping depth. From these

datasets the variance $\langle x^2 \rangle$ of the residual Brownian motion was determined and used to calculate the lateral trap stiffnesses k_x and k_y associated with this specific LUT shape and trapping depth through the equipartition of energy (section 7.2.3):

$$\frac{1}{2}k_B T = \frac{1}{2}k \left\langle x^2 \right\rangle \tag{8.1}$$

where k_B is the Boltzmann constant and T=298 K is the room temperature. Each data set was binned and converted into a matrix for further analysis with a bin size of approximately 10 nm. Comparison between the optimised case and the unoptimised case could be drawn because all scatter plots were binned with the same parameters. Analysis on the matrices included the generation of contour plots and the fitting of Gaussian functions to the data.

Zernike mode decomposition

The modal content of the DMM shape was determined by Zernike mode decomposition measured by replacing the microscope objective with a Shack-Hartmann wavefront sensor (Thorlabs WFS150C). The WFS could be conveniently screwed onto the microscope turret such that the CCD array was approximately positioned at the back aperture of the microscope objective. Amplitude modulation, however, was not of concern as the wavefront sensor did not need to measure absolute values for closed-loop aberration correction but instead was used to get information on the relative changes between DMM shapes optimised at various depths. Each shape in the LUT was therefore sequentially applied to the DMM and the Zernike coefficients up to $k = 15$ were measured (see appendix A). The measured coefficients with the flat shape on the DMM were subtracted from the coefficients of each shape of the LUT. The square root σ_ϕ of the variance of the residual wavefront, commonly referred to as the root mean square (RMS) was calculated with:

$$\mathrm{RMS} = \sqrt{\sum_n \sum_m \left(c_n^m\right)^2} \tag{8.2}$$

while the norm for each radial order n is given by:

$$N_n = \sqrt{\sum_m \left(c_n^m\right)^2}. \tag{8.3}$$

The effect of a small aberration in an imaging system is to decrease the am-

plitude of the intensity of the PSF and redistribute the energy towards the side lobes, in particular, filling in the zero nodes. The Strehl ratio S is defined as the ratio of the aberrated PSF intensity maximum of a point source to the diffraction limited PSF intensity maximum. Strehl proposed a value of 0.8 as a suitable criterion for the quality of an imaging system. If $S > 0.8$ the system is effectively diffraction limited, for values smaller than that degradation of system performance due to aberrations is significant [395]. For small aberrations ($\sigma_\phi \ll 1$), the Strehl ratio can be approximated by the Maréchal equation:

$$S \approx e^{-\sigma_\phi^2} \approx 1 - \sigma_\phi^2 = 1 - \left(\frac{2\pi}{\lambda}\right)^2 (\mathrm{RMS})^2. \tag{8.4}$$

8.2 Results

The following section details the original work carried out by the author at the Institute of Photonics labs.

8.2.1 Magnification of the optical system

The magnification of the system was measured with a target slide exhibiting a grid pattern. One square in that pattern measured 50 µm on all sides and imaged with the 100x objective combined with a x1.5 fold magnification on the microscope output port, was used to calculate the magnification of the imaging system. The 50 µm sized square spanned over 412x412 pixels^2 giving an imaging ratio of 8.24 pixels/µm (1 pixel corresponds to 121 nm on the sample).

8.2.2 Adaptation of the algorithm

The following sections are giving details about necessary adaptations to the general RSA described in section 2.6.2 of this thesis in order to adapt it to this specific OT application. This involved the calculation of a MF appropriately chosen to directly enhance lateral trapping strength and a sequence of code for the tracking of the centre of mass of the trapped particle.

Merit factor

The aim of the AO system was to enhance the lateral trapping strength at depth. The MF was therefore chosen to be directly proportional to the specific quantity

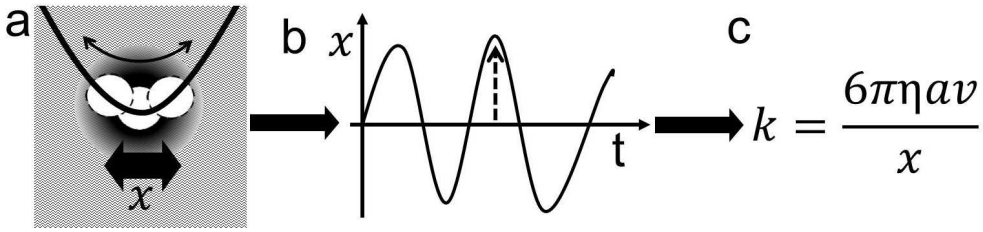

Figure 8.4: Calculation of the merit factor. **(a)** Viscous drag force imparted on the trapped bead causes it to oscillate (thin arrow) in the harmonic potential well of the trap. The drag force was imparted by the dispersion water through motion of the sample stage (thick arrow). **(b)** The amplitude of this oscillation (dashed arrow) is directly proportional to the spring constant k via Stokes' law **(c)**.

that was to be improved (Fig. 8.4) and was calculated from the displacement of a trapped bead from its equilibrium position at the centre of the trap by moving the xy- translation stage onto which the sample was mounted with a constant speed. The stage was moved diagonally with respect to its intrinsic x- and y-directions and repeatedly back and forth for the entire duration of the optimisation procedure. This stage motion caused a viscous drag force (thick arrow in (a)) exerted by fluid flow of the dispersion water according to Stoke's law on the trapped bead:

$$\vec{F_D} = -6\pi\eta a\vec{v} \tag{8.5}$$

where η is the dynamic viscosity of water, a is the radius of the sphere and v is the settling velocity of the fluid. As a consequence, the bead oscillated in its position within the harmonic trapping well (b). The amplitude (dashed arrow) of the oscillation was determined by tracking this movement with a camera. The RSA was set to minimise the lateral bead displacement from equilibrium which directly leads to an increase in the spring constant k of the trap using Hooke's law $F = -kx$:

$$k = \frac{6\pi\eta av}{x} \tag{8.6}$$

where x is the displacement of the bead within the trap. The speed of the stage movement was chosen to allow stable trapping but maximise bead displacement from the trap centre. The speed was therefore slightly less than the critical speed required for the bead to escape from the trap and typically $10 - 30\,\mu\text{m/s}$ depending on trapping depth. These speeds lead to a displacement of roughly

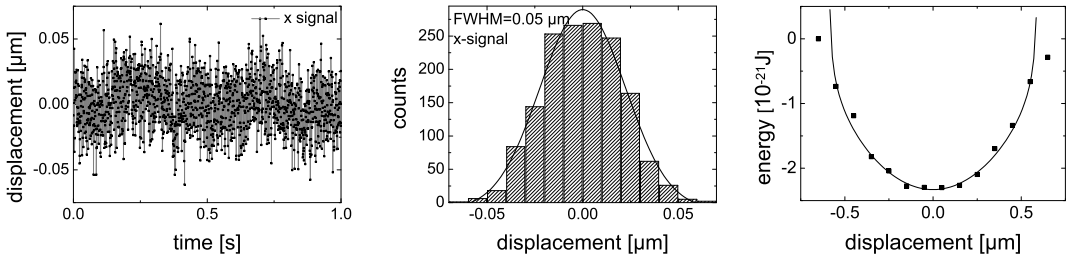

(a) **(b)** **(c)**

Figure 8.5: (a) Typical trace of the measured position of a 3 µm diameter bead thermally fluctuating inside an OT as a function of time. **(b)** Position histogram of (a). The line indicates a Gaussian fit to the data. **(c)** Energy profile for the trapped bead along the x-axis using Boltzmann statistics. The solid line shows a parabolic fit assuming a harmonically trapped Brownian particle.

50 nm from the equilibrium position and a spring constant k of $\approx 2\,\mathrm{pN/\mu m}$ (beam waist $\omega = 0.4\,\mu\mathrm{m}$, bead diameter $2a = 1\,\mu\mathrm{m}$). Great care was taken to leave the system enough time to restore dynamic equilibrium after each change in the DMM shape by allowing the stage to move back and forth a set number of times (usually three to five) before the MF was calculated again and sent to the RSA.

Centroid tracking

A custom written centroid tracking algorithm was implemented in LabVIEW to track the motion of the trapped particle. This was done by using a subVI which calculates the centre of mass of an inputted ROI according to:

$$x_c = \frac{\sum_{i=0}^{w}\sum_{j=0}^{h} x_{ij} I(x_{ij}, y_{ij})}{\sum_{i=0}^{w}\sum_{j=0}^{h} I(x_{ij}, y_{ij})} \tag{8.7}$$

where the summation is done over the width (w) and height (h) of the ROI and a similar formula applies for the other lateral coordinate. Fig. 8.5a shows exemplarily the measured bead position along the x-axis of a 3 µm diameter bead which fluctuates due to Brownian motion inside the trap. The position histogram shown in Fig. 8.5b is generated by binning the displacements and counting the frequency. The fit of a Gaussian to the data is also shown. In Fig. 8.5c the harmonic potential $E(x)$ along the x-axis is determined with Boltzmann statistics by calculating the logarithm of the frequency distribution $p(x)$ in (b) and

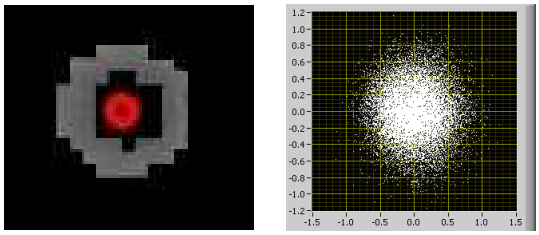

(a) **(b)**

Figure 8.6: (a) ROI with a threshold setting that allowed for the display of a bright bead on a completely black background. The red circle marks the position of the centroid. **(b)** Scatter plot of 20,000 coordinates of the centroid which is thermally fluctuating due to Brownian motion inside the trap. Each data point represents a displacement from the centre of the trap in units of pixels.

multiplying by the thermal energy k_BT according to [396]:

$$E(x) = -k_BT \ln p(x) + C = \frac{1}{2}kx^2 + C \tag{8.8}$$

The line indicates a numerical fit to a harmonic potential with a force constant k of $1.14 \cdot 10^{-5}\,\mathrm{N/m}$.

For these measurements the frame rate of the camera was increased by selecting a region of interest (ROI) (Fig. 8.6a) such that the field of view of the camera was restricted to the area surrounding the trapped bead. The ROI was reduced to approximately 40 by 40 pixels corresponding to a square of a little less than $5\,\mu\mathrm{m}$ in size. The frame rate was thus increased to $1.5\,\mathrm{kHz}$ with an exposure time of $650\,\mu\mathrm{s}$ making this camera suitable for tracking a bead which fluctuates thermally within the trap due to Brownian motion [397].

Thresholding To avoid a strong bias towards the geometrical centre of the ROI it is vital to exclude as much of the image background as possible [398]. This was done by setting a threshold value that every pixel intensity had to exceed in order to be included into the calculation. Values below the threshold were set to zero so as to create a completely black background. With the applied threshold values, the bead appeared as a bright disc or ring on a black background. The red circle marks the position of the centroid (Fig. 8.6a). The threshold setting was highly user dependent and could affect the absolute value which is obtained for the trap stiffness. However, once a threshold value was found for a specific depth it was kept the same for the flat DMM shape and the optimised shape so as to allow direct comparison.

In future applications this thresholding process could be automated very easily if the centroid algorithm was re-written to use a Gaussian fitting technique. The peak of an intensity distribution of a point source, is well approximated by a Gaussian. Thus, directly fitting the equation for a two dimensional Gaussian to images of spherical particles has become a common method of particle tracking [399].

Accuracy Fig. 8.6b shows a representative plot of 20,000 centroid coordinates where each point is a displacement from the mean value (the centre of the trap) in units of pixels. Sub-pixel resolution can routinely be achieved in centroid tracking through an averaging and interpolation process. Whereas all bright pixels within the bead contribute to the calculation of the position of the centroid only the pixels on the periphery define the accuracy with which the centroid can be determined. The maximum x1.5 fold magnification on the microscope output port was chosen such that the bead within the ROI was re-imaged onto the camera with the highest number of pixels possible.

The accuracy of the centroid position is estimated in the following. The position of peripheral pixels is known with the accuracy of one pixel. This means each periphery pixel position is an estimate of the true edge position with an uniform error distribution within $\pm 0.5\,\text{pixels}$. In other words, the probability of finding the true edge is equally probable within a range of one pixel width of the periphery pixel position and zero outside this range. The variance of a continuous uniform distribution is given by $s^2 = \frac{1}{12}w^2$ where w is the width of the distribution. For $w = 1\,\text{pixel}$, the variance is $s^2 = 0.083\,\text{pixel}^2$. The standard deviation u for the centroid position is given by:

$$u^2 = \frac{s^2}{\sqrt{N}}. \tag{8.9}$$

The accuracy of the centroid position is determined by the square root of the number of pixels $N = \pi 2a$ illuminated by the edge of the bead where $2a$ is the bead diameter. When projecting the edge pixels for each lateral direction the number determining the accuracy becomes $N = 4a$. Therefore, for the 1 µm (=8.24 pixels) bead, $\frac{1}{\sqrt{N}} \approx 0.25$ and it follows $u \approx 0.14\,\text{pixels} \approx 30\,\text{nm}$.

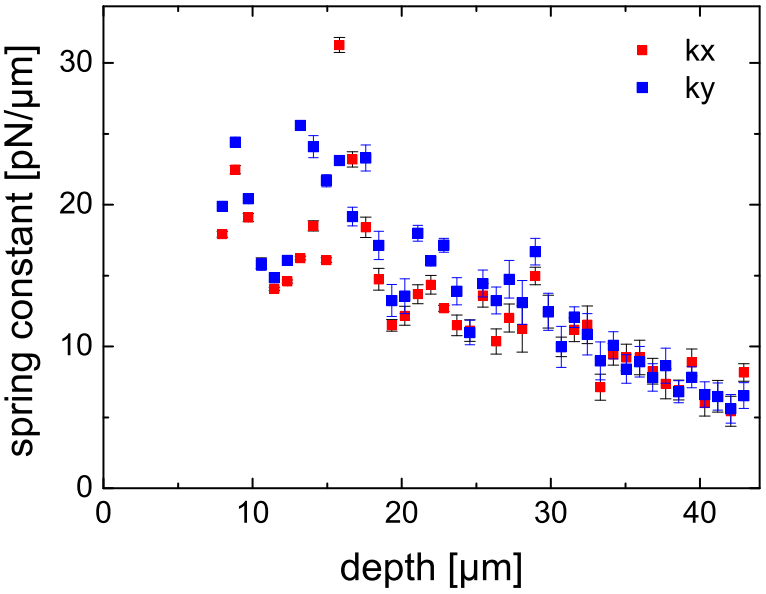

Figure 8.7: The residual motion of a 3 µm bead, trapped with the SLM, was used to determine the degradation of lateral trapping strength (k_x, k_y) with depth. The errors indicate the error of the mean.

8.2.3 Degradation of lateral trapping strength with depth

The problem of trapping at depth lies with a loss of diffraction limited focusing due to an increased amount of wavefront aberrations which are distorting the focal spot. The motion of the trapped particle corresponds to that of a thermally excited, overdamped oscillator in a harmonic potential characterised according to Hooke's law with the spring stiffness k. The trap can be described as a potential energy well associated with the intensity distribution at the laser focus and is therefore dependent on the shape of the incoming wavefronts. Perfectly spherical wavefronts will form a diffraction limited focal spot with the highest intensity gradients whereas any deviation from that geometry, due to the presence of optical aberrations, will cause the focal spot to broaden and elongate and the trap to weaken. More specifically, truncating the tails of the Gaussian beam by a finite aperture and inducing spherical aberrations, caused by the introduction of a refractive index mismatched interface, result in non-ideal trapping conditions.

The continuing decrease in lateral trap stiffness with increasing trapping depth was measured for a silica bead of 3 µm trapped with an SLM. Fig. 8.7 shows the decrease in lateral trapping stiffness, given as the spring constant $k_{x,y}$ for the x- and y-direction respectively, over a trapping range of 35 µm. The errors given are the standard deviation of a repeated series of measurements divided by the number of experiments and therefore represent the error on the mean. Whereas

the errors are fairly small at the shallow trapping regions due to a stable trapping regime which allowed for a multitude of repeated measurements of k, the errors increase at larger trapping depth where the bead often got lost from the trap and fewer successful measurements of k were possible. At a trapping distance of three bead diameters away from the coverslip surface the spring constant was measured as $(22.5 \pm 0.3)\,\mathrm{pN/\mu m}$ and $(24.4 \pm 0.3)\,\mathrm{pN/\mu m}$ for the x- and y-directions respectively. At a depth of 42 µm these values were reduced to 24 % ($(5.4 \pm 1.0)\,\mathrm{pN/\mu m}$) and 23 % ($(5.6 \pm 1.0)\,\mathrm{pN\mu m}$).

8.2.4 Brownian motion

Contour plots The coordinates of 20,000 centroid positions of a trapped bead of 1 µm diameter were plotted in contour plots to visualise the improvement achieved for the lateral trapping strength. The first row in Fig. 8.8 shows the

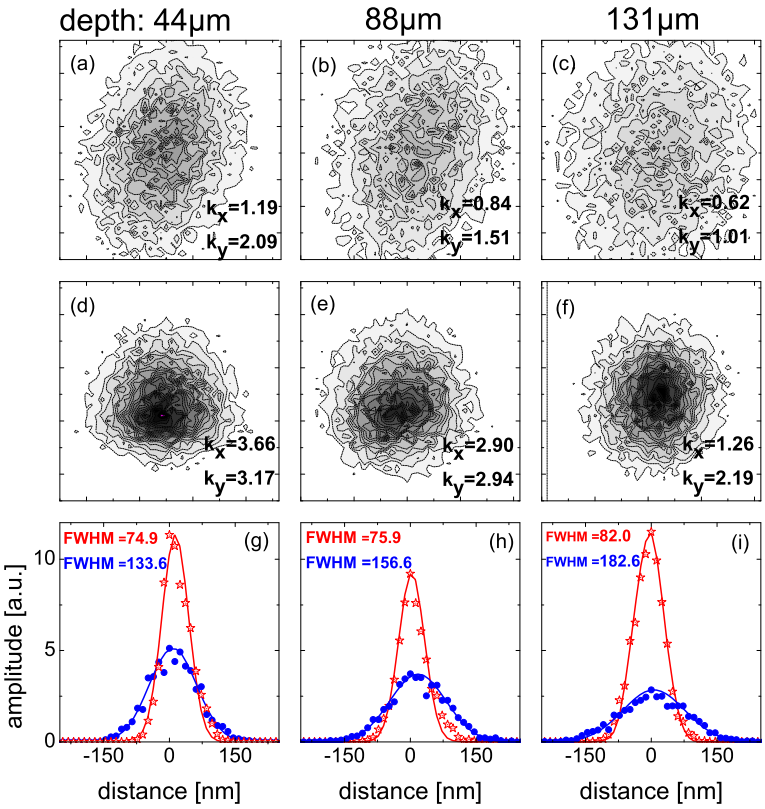

Figure 8.8: Contour plots of the Brownian motion of a trapped bead of 1 µm diameter before aberration correction **(a-c)** and after aberration correction **(d-f)**. Size of box: 250 nm x 250 nm. Insets: spring constants in x- and y- directions in pN/µm. Gaussian fits to the scatter plots at $x = x_{max}$ before aberration correction (blue circles) and after aberration correction (red stars) at a depth of **(g)** 44 µm, **(h)** 88 µm and **(i)** 131 µm. Insets state FWHM in nm.

spread of the residual Brownian motion of the bead which was trapped with the flat DMM shape at the depths of 44 µm, 88 µm and 131 µm respectively while the second row shows the extent of the respective residual Brownian motion when the bead was trapped with a previously optimised DMM for each respective depth. From the reduced spread of the scatter it can qualitatively be seen that each optimisation successfully increased the lateral stiffness of the trap. The insets state the spring constants for the x- and y- directions in pN/µm.

It is also noticeable that the optimisation succeeded in making the trap strength more uniform in both lateral directions. Before aberration correction the scatter plot took on an elongated, elliptical shape which was attributed to the linear polarisation of the laser beam [344] along with circularly asymmetric aberrations like coma and astigmatism. After aberration correction the scatter plot showed a more circular distribution (see also section 8.2.5).

Position histograms The third row in Fig. 8.8 shows the Gaussian fits to the same data plotted at fixed $x = x_{max}$ position. The insets state the full width half maximum (FWHM) in nm. For the flat DMM shape the Gaussian bell broadened and flattened by 137 % of its FWHM over the 87 µm increase in depth. After optimisation the width was reduced on average by 50 % and also kept on an almost stable level over depth (109 % increase in the FWHM over an 87 µm increase in depth). The random errors on the data points are determined by the count N of coordinates in each bin through $1/\sqrt{N}$ and are too small to be displayed.

8.2.5 Trap stiffness and uniformity

The evolution of spring constants with increasing trapping depth is depicted for a 1 µm diameter silica bead trapped with the flat DMM shape in Fig. 8.9. Trapping stiffness deteriorated as the trap was moved deeper into the sample. While the spring constant amounted to $k_x = (1.72 \pm 0.02)$ pN/µm and $k_y = (2.72 \pm 0.03)$ pN/µm at 17.5 µm, these spring constants decreased to 36 % ($k_x = (0.62 \pm 0.01)$ pN/µm and $k_y = (1.01 \pm 0.01)$ pN/µm) at a depth of 131 µm where the bead ultimately escaped from the trap. The evolution of spring constants with trapping depth for three optimised DMM shapes is shown in Fig. 8.10. The error bars have been omitted for clarity. The DMM shapes were obtained from three optimisations previously performed at depths of 44 µm, 88 µm, and

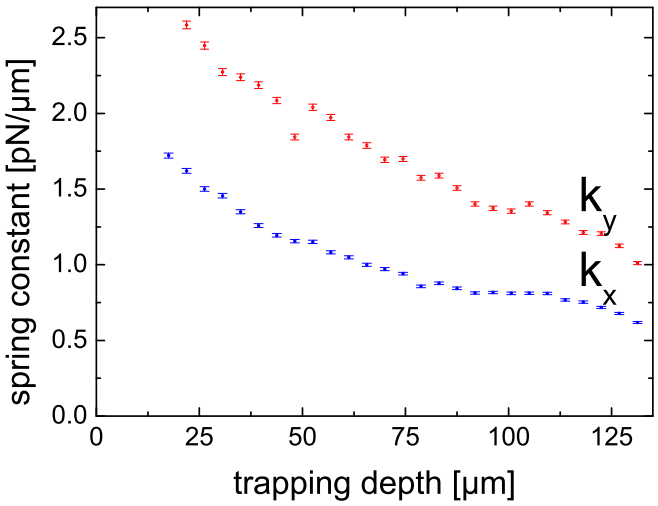

Figure 8.9: Evolution of spring constants with trapping depth for a 1 µm bead trapped with the flat DMM shape. The fractional error is 1 % (see p.167).

131 µm respectively. The arrows mark the depth at which the optimisation had been run, whereas the other data points indicate how the corresponding DMM shape performed at a depth for which it had not been optimised. The stiffness of the trap obtained with the flat DMM shape (blue data points) is identical to the data shown in Fig. 8.9 and is displayed as a visual scale for improvement. Table 8.1 lists the spring constants before and after aberration corrections as well as the improvement factors for the x- and y- directions with increasing depth. On an average through depth, the optimisation routine improved the lateral trapping strength by a factor of 3.46±0.78 and 2.12±0.90 for the x- and y-axis respectively. The maximum trapping depth was increased from 131 µm for the flat DMM shape to 166 µm for the DMM shape optimised at 131 µm. This constitutes an improvement of 127 %.

Eccentricity Trapping force uniformity was quantified by calculating the eccentricity of the OT given by:

$$\epsilon = \sqrt{\frac{{k_i}^2 - {k_j}^2}{{k_i}^2}} \tag{8.10}$$

for $k_i, k_j = k_x, k_y$ and $k_i \geq k_j$. In this notation k_x and k_y represent the one-half of the ellipse's major and minor axes respectively. A perfect circle has an eccentricity of zero while an ellipse has an eccentricity greater than zero but less than one. Table 8.1 also states the eccentricities calculated for trapping with the flat DMM shape and the optimised DMM shapes. Typically the trap was

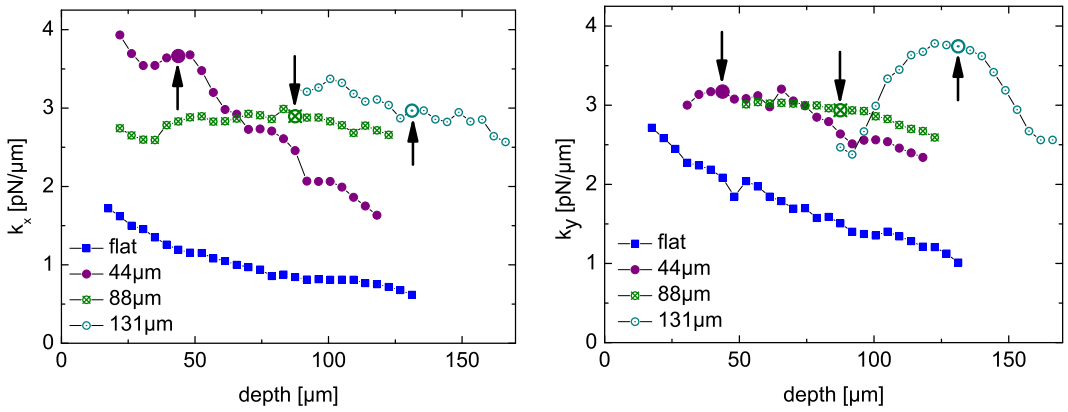

Figure 8.10: Evolution of spring constants with depth for the x-axis **(a)** and y-axis **(b)**. The arrows mark the specific depth at which the respective optimisation was run. The lines have been displayed as a guide to the eye. The error bars have been omitted for clarity.

found to be weaker along the x axis. The eccentricity before optimisation was 0.84±0.02 on average through depth. This value was reduced by half by optimised DMM shapes (0.41 ± 0.17). The elliptical shape of the trap before optimisation was attributed to the linear polarisation of the laser beam along x as well as circularly asymmetric aberrations like coma and astigmatism.

Errors The spring constant k was calculated with:

$$k = \frac{k_B T}{\sigma^2} = c\sigma^{-2} \tag{8.11}$$

where $c = k_B T$ and σ^2 denotes the variance of the distribution representing

Table 8.1: Spring constants k_x, k_y (in pN/µm) before and after aberration correction and their derived eccentricities through depth. The fractional error of k is 1 % (see p.167 for error analysis). The last columns give the improvement ratios. Bead diameter: 1 µm, power: 5 mW at back aperture.

depth	unopt.			opt.			ratio		
[µm]	k_x	k_y	ϵ	k_x	k_y	ϵ	k_x	k_y	ϵ
44	1.19	2.09	0.82	3.66	3.17	0.50	3.08	1.52	0.61
66	1.00	1.79	0.83	3.17	2.87	0.42	3.17	1.60	0.51
88	0.84	1.51	0.83	2.90	2.94	0.16	3.45	1.95	0.19
109	0.81	1.34	0.80	2.28	2.46	0.38	2.81	1.84	0.48
131	0.62	1.01	0.79	2.97	3.74	0.61	4.79	3.70	0.77

the position of the trapped bead. The error δ_k on the spring constant k is given by

$$\frac{\delta_k}{k} = 2 \cdot \frac{\delta_\sigma}{\sigma} \tag{8.12}$$

where $\frac{\delta\sigma}{\sigma}$ is the fractional error on the standard deviation σ of the distribution:

$$\frac{\delta\sigma}{\sigma} = \frac{1}{\sqrt{2N-2}} \tag{8.13}$$

With $N = 20,000$ data points used to calculate the variance of the residual motion of a trapped bead the fractional error on the standard deviation of the distribution is 0.5 %. The fractional error of a spring constant was therefore calculated as: $\frac{\delta_k}{k} = 1\,\%$.

Applicability The depth interval over which DMM shapes could be usefully applied was arbitrarily defined as the range within which the spring constant remained within 5 % of its optimised value. Individual optimisations showed different behaviour; whereas the DMM shapes which had been optimised at depths of 44 µm and 131 µm showed similar ranges of applicability of ≈ 35 µm and ≈ 33 µm respectively, the shape obtained at 88 µm showed twice that range of applicability (≈ 68 µm).

8.2.6 Zernike coefficients

Fig. 8.11 compares the modal content of each DMM shape of the LUT in terms of their higher order Zernike coefficients c_n^m. The coefficients that were measured with the flat shape on the DMM were subtracted to obtain changes due to depth dependent optimisation. The dominant higher order aberrations were astigmatism,trefoil and spherical aberration. Whereas some aberrations like coma in y-direction and secondary astigmatism remained fairly constant over the entire depth range which might imply that they were predominantly system induced other aberrations like astigmatism along ± 45 °, trefoil along y direction and spherical aberration showed a distinct trend with depth. This was taken as an indication that their origin was due to the sample and specifically due to the refractive index mismatch between the oil/glass- water interface.

It has been previously noted that uncorrected astigmatism leads to a corresponding elliptical symmetry in the motion of the trapped particle [393]. The

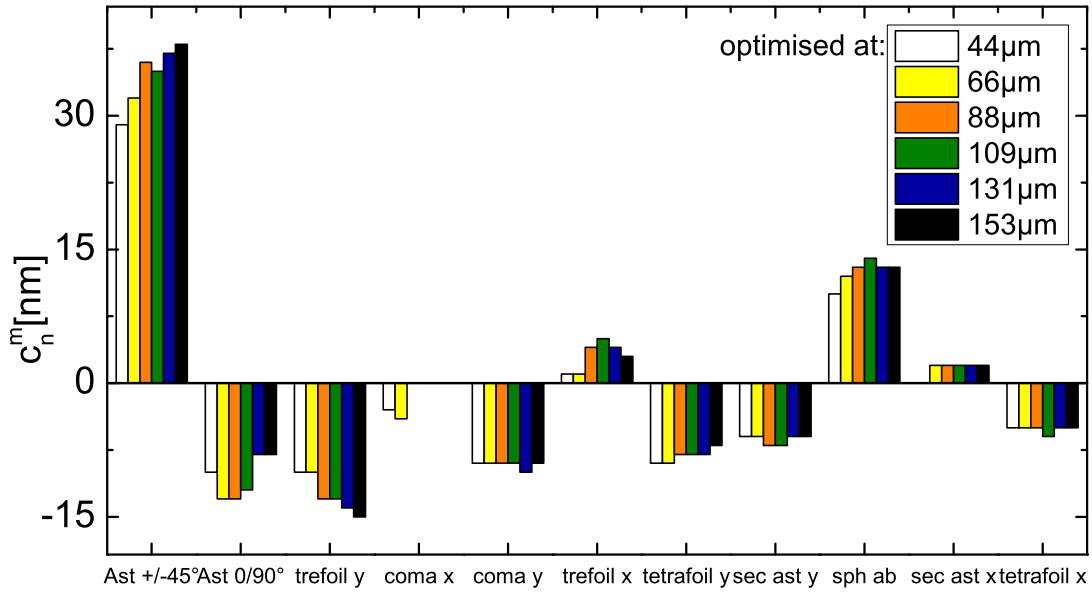

Figure 8.11: Modal content of the DMM shapes of the LUT in terms of higher order Zernike aberrations, n: radial order, m: azimuthal frequency.

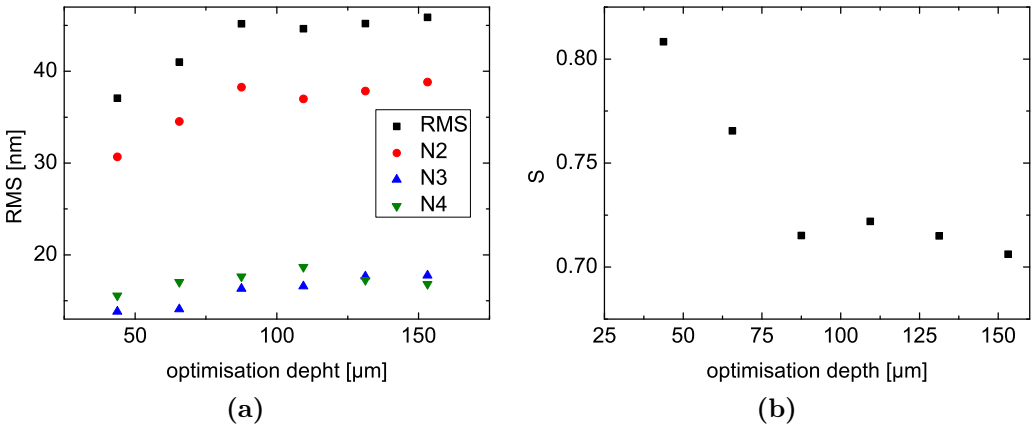

Figure 8.12: **(a)** Root mean square (RMS) and norm N_n for each Zernike radial order $n = 2, 3, 4$ of each DMM shape in the LUT. **(b)** Depth dependent degradation of the Strehl ratio.

large amount in both astigmatism modes applied in the optimised DMM shapes explains the improvement in eccentricity observed in this work.

In Fig. 8.12a the root mean square (RMS, eq.8.2) and norm N_n (eq.8.3) for each Zernike radial order $n = 2, 3, 4$ of each DMM shape in the LUT is shown. As expected, the RMS steadily increases with optimisation depths because increasingly larger deformations of the membrane are necessary to compensate for the increasingly higher accumulation of aberrations. At a optimisation depth of 88 µm the RMS levels out into a plateau. The norm N_n shows the weighted relevance of each order towards the total amount of aberrations. N_2 emphasizes the strong influence of astigmatism (note that N_2 does not include defocus but solely both astigmatism terms). N_3 contains both terms of each coma and trefoil, whereas N_4 includes two terms of each tetrafoil and secondary astigmatism as well as spherical aberration. The Strehl ratio S (eq.8.4) is plotted for each DMM shape of the LUT in Fig. 8.12b. The flat DMM shape was subtracted from each DMM shape in the LUT and the residual wavefront was used to calculated the Strehl ratio. Therefore the degradation in S represents the depth dependent decrease in resolution that the optimisation routine was able to compensate.

8.3 Discussion

8.3.1 Surface effects- Faxén's law

Applying a speed of up to 30 µm/s to the sample stage, the viscous drag force imparted on the 1 µm bead in this work was in the order of magnitude of 0.3 pN leading to a displacement of $\approx$ 0.05 µm which is in excellent agreement with previous findings [382].

In microfluidic devices, the fluid flow and drag forces on moving objects are strongly influenced by boundary walls [400]. The Stokes drag force (see p.147) acting on a sphere translating in fluid holds true for a particle that is far from any boundary walls, however, it is increased by the presence of a neighboring wall by a factor given by Faxén's correction [401]:

$$F_D = \frac{6\pi\eta a v}{1 - \frac{9}{16}\left(\frac{a}{l}\right) + \frac{1}{8}\left(\frac{a}{l}\right)^3 - \frac{45}{256}\left(\frac{a}{l}\right)^4 - \frac{1}{16}\left(\frac{a}{l}\right)^5}. \tag{8.14}$$

Faxén's correction is expressed as a power series in the ratio of particle radius a to the distance from the surface l. Leach *et al.* found that for a 2 µm bead a

10 % increase in drag coefficient $\beta = 6\pi\eta a$ occurs at a distance of five radii [400].

For small Reynolds numbers the drag coefficient is simply the inverse of particle motility μ. The spring constants in Fig 8.7 have been measured by tracking the Brownian motion of the bead which is affected by the same change in the drag coefficient according to the Stokes-Einstein equation which relates the diffusion constant D to the viscosity η of the medium [347]:

$$D = \mu k_B T = \frac{k_B T}{6\pi\eta a} \tag{8.15}$$

$$\left\langle x^2 \right\rangle = 2Dt. \tag{8.16}$$

The fluctuations in spring constant at trapping depths below 15 µm (five bead radii) in Fig. 8.7 are most likely due to surface effects influencing the measurements. Additionally the possibility exists that a second (and third) bead fell into the trap at shallow trapping depth, which would effectively constitute an increased bead diameter and therefore lead to decreased trap stiffness. At larger trapping depth, however, the bead concentration is more diluted and the probability of such simultaneous trapping of more than one bead is decreased.

8.3.2 Spring constants

The following section compares the spring stiffnesses measured in this study with previously published data, however, it is difficult to find published data of measured spring constants that fits exactly in all relevant parameters so that comparisons can be made. Table 8.2 on p.178 provides an overview on the published literature concerned with the trapping of beads. Vermeulen *et al.* published data for the lateral and axial trap stiffness in the presence of spherical aberrations as a function of focusing depth for polystyrene and silica beads of a diameter of 2 µm [386]. Using a 100x, 1.3NA oil immersion objective to trap beads suspended in water, they found a strong depth dependency of trap stiffness similar to the one presented in this work. Fig. 8.13 compares the data from their study with the data measured in this work. As their trapping was done with a power of 200 mW and trapping strength scales linearly with power [345], the trapping stiffnesses presented in their work were scaled down to 5 mW for ease of comparison. The same was done with the data from the SLM based trapping presented in Fig. 8.7 of this work. Consistent with their findings, a monotonic decrease in trapping

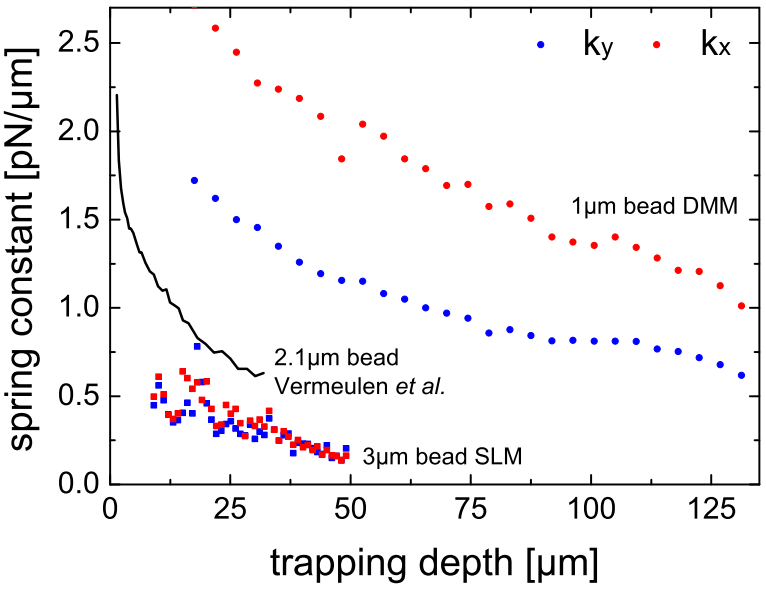

Figure 8.13: Discussion. The lateral spring constants measured in this work were determined with the Brownian motion technique. Data from trapping with the DMM: $\lambda = 532\,\text{nm}$, silica bead $\varnothing = 1\,\mu\text{m}$, power at sample: $\approx 5\,\text{mW}$. Data from the trapping with the SLM: $\lambda = 1064\,\text{nm}$, silica bead $\varnothing = 3\,\mu\text{m}$, values scaled down from a power at sample of 200 mW for ease of comparison. Also shown is the data published by Vermeulen *et al.* [386]: $\lambda = 1064\,\text{nm}$, silica bead $\varnothing = 2.1\,\mu\text{m}$, values scaled down from a power at sample of 200 mW for ease of comparison. They determined trap stiffness with the corner-frequency method. All beads were trapped with an immersion oil objective (100x, 1.3NA).

stiffness was observed. This is attributed to marginal rays increasingly lagging behind the main focus when focusing deeper into the lower-index medium and therefore no longer contributing to the gradient force which is essential for stable trapping. The decrease of trap stiffness with increasing bead diameter is also expected [342, 345].

Ghislain *et al.* used a 63x, 1.25NA oil immersion objective and light of 1064 nm wavelength to trap a 1 µm diameter silica bead at a distance of 8 µm under the coverslip with an incident power of 60 mW and measured a lateral spring constant of $k_{r,exp}$=60 pN/µm [382]. In Rohrbach *et al.* [384] an experimental model is presented that can calculate the spring constants for trapping experiments with sphere diameters smaller than or equal to the wavelength. For the same parameters as in [382] they predict a lateral spring constant of $k_{r,theory} = 102\,\text{pN}/\mu\text{m}$. Considering the reduced power ($\approx 5\,\text{mW}$ at the sample) and greater trapping depth ($25 - 125\,\mu\text{m}$) in the experiments presented in this work, our spring constants ($\approx 2\,\text{pN}/\mu\text{m}$) are in good qualitative agreement. Also, Polin *et al.* reported the trapping of a silica bead (1.53 µm diameter) with a lateral spring

constant of k= 0.5 pN/μm with an incident power of 5 mW at an unspecified depth using an 100X, 1.4 NA oil immersion objective and light of 532 nm wavelength [402]. In Malagnino *et al.* [342] the lateral trapping stiffness of a 15 μm diameter polystyrene bead (n=1.57) was ≈ 0.5 pN/μm (trapping depth not quoted) using a 40x, 0.65NA objective and a laser power of 5 mW. These findings are difficult to compare directly to the results from this work but confirm the order of magnitude of the trapping stiffnesses measured.

8.3.3 Spherical aberration

When using an oil-immersion objective for trapping the refractive indices of the immersion oil and the cover glass are matched such that the first optical interface the beam experiences when it exits the objective is the mismatch between the coverslip (n=1.52) and the immersion water (n=1.33) and this interface causes spherical aberrations to be introduced into the system [149, 152]. The phase delay of a ray increases with the angle to the optical axis and therefore leads to a distorted focus, especially in the axial direction.

Several papers have reported a decrease in trapping efficiency with increasing trapping depth due to spherical aberrations [339,383,389]. The decrease of lateral spring stiffness in the presence of spherical aberrations with trapping depth in Ghislain *et al.* was quoted as 12 % over a depth of 25 μm [382]. The decrease measured in this work under similar experimental conditions (*i.e.* the DMM trapping setup) is comparable but slightly higher: $17 - 23$ % for the an increase in trapping depth of 25 μm (from ≈ 25 μm to 50 μm). In Florin *et al.* the trapping of a 600 nm diameter latex bead with a 100x, 1.3NA objective and light of 1064 nm is reported and the decrease in lateral spring constant up to a distance of 10 μm shows a qualitative similar behaviour as the one observed in this work, however, as they did not report the power of the trapping beam a quantitative comparison is not possible [396].

Other groups have reported efforts in compensating for aberration induced trapping degradation. Ota *et al.* used a DMM to specifically apply a shape which introduces spherical aberrations of opposite sign as the sample into the optical system [387]. By iteratively stepping through the amount of spherical aberrations introduced by the DMM they were able to find an optimum compensation for their system which lead to an improvement factor in the axial trapping efficiency of 1.35 fold at a depth of 5 μm and 1.83 fold at a depth of 10 μm.

In Theofanidou *et al.* a similar approach is used. Spherical aberrations are compensated by optimising on the TPEF signal emitted by the dye-stained, trapped beads with a DMM by iteratively changing electrode voltages in small increments [101]. They report that for any given fluorescence intensity (and therefore trapping potential) the trap can be moved about 1.7 times deeper into the sample. A draw back of this method however, is that the DMM had to be restricted in such a way that it would only apply spherical aberrations. The use of total fluorescence intensity as a MF meant that the mirror would otherwise apply defocus which would move the trap closer to the surface and therefore increase the fluorescence signal. The method of addressing the DMM in such a way that only its spherical aberration Zernike mode is varied without changing the defocus component requires careful characterisation and calibration of the DMM and correction is limited to this one single aberration.

The effects of 1^{st} order spherical aberration and defocus on axial trapping stiffness are also investigated in Dinerowitz *et al.* [403] where the improvement of axial stiffness by a factor of 3 fold and trapping of 1 µm polystyrene beads up to 50 µm into the sample is reported. They found that it is not possible to maintain the optimum trap stiffness over a range of depths by optimising 1st order spherical aberration alone. A combination of spherical, defocus and objective position is used to optimise axial trapping stiffness.

In Ke *et al.* the improvement by 20 % in tansverse trapping efficiency through change in tube length is reported [389]. Nader *et al.* published a paper using the same technique but this time to enhance axial trapping. They reported stable trapping of a 1 µm silica bead up to a depth of 100 µm (λ= 1064 nm, P=23.6 mW at the back focal plane) [390]. In a different publication, the same group proposed the compensation of spherical aberration by changing the refractive index of the immersion medium, which allowed for an increase of 3 µm in trapping depth per change of 0.01 in the refractive index of the immersion medium using oils with refractive index ranging from 1.51-1.57 [388].

8.3.4 Zernike aberrations

The predominant aberrations found in our setup occur commonly in imaging. Astigmatism originates in light rays lying in meridional and equatorial planes being refracted into different focal planes. Astigmatic aberrations are often found in multi element systems comparable to our setup. This is due to the meridional

plane being usually coherent throughout the setup whereas the equatorial plane usually changes in the incident angle with each optical element. Spherical aberrations are mainly encountered when light waves passing through the periphery of an uncorrected lens are not brought into focus with those passing through the centre and therefore generate multiple focal points along the optical axis. Comatic aberrations are most pronounced when a microscope is out of alignment and components are hit by off-axis beams. Also optics under tension or stress within their holders, defects of surfaces and imperfections of optical elements can all lead to higher order aberrations. It has been previously noted that astigmatism and coma bear the greatest effect on lateral trapping efficiency [381]. Despite our expectations of mainly correcting for spherical aberrations we actually corrected for various aberrations of presumably different origin, highlighting the benefits of a multi-modal approach in aberration correction.

8.3.5 Applicability

The search space of DMM shapes is, in theory, of infinite dimensions. However, as the shape of the DMM is controlled via its 52 actuators, the search space of possible DMM shapes is in practice reduced to 52 dimensions. Within this search space there is no certainty that a unique solution exists to a given problem as several different DMM shapes could well lead to the same improvement in MF. Inversely, each optimisation could end in a different DMM shape if it were to be repeated under the exact same conditions, giving a possible explanation for the different ranges of applicability of DMM shapes in this work. The relatively large range of applicability observed in this work for some optimised DMM shapes could potentially mean that the optimisation did not reach its global maximum and that the trap had therefore not quite reached its diffraction limited performance. Given the combination of high NA and refractive index mismatch used in this work, it would be expected that each mirror shape was applicable for a shorter depth interval only where the spherical aberrations introduced by the DMM perfectly match the spherical aberrations introduced by the slab of water through which trapping is attempted. A possible improvement in optimisation performance could be achieved by giving the DMM an intelligent starting point which could be based around the shape obtained from a shallower depths at which the mirror had been previously optimised.

8.4 Summary and conclusion

This chapter details the design and implementation of an optical trapping system based on an inverted microscope and illustrates the basic components required to trap a micron sized particle. The system was designed to be as versatile and easy to use as possible and to be computer controlled using the LabVIEW programming language. The effect of spherical aberration on an OT formed in water suspension with an oil immersion objective has been mapped qualitatively and quantitatively for silica beads of 1 µm and 3 µm diameter.

This chapter demonstrated the use of a DMM to increase the lateral trapping force in an OT setup. The optimum shape of the DMM was determined with a random search algorithm (RSA) using lateral bead displacement from equilibrium due to a viscous drag force applied through motion of the sample stage as a MF. The viscous drag approach was chosen over the Brownian approach because it takes less time to produce a MF and therefore the time necessary to complete an optimisation is reduced. For example, Brownian motion was tracked for approximately a minute in order to determine a reliable k value with our camera, whereas with the viscous drag method the MF could be updated roughly every 10 seconds. The displacement from equilibrium position is directly proportional to the spring constant of the OT. By minimising this displacement, the spring constant is directly proportionally increased and the trapping strength improved. This approach allows for the dynamic correction of a wide variety of aberrations rather than the static correction of only one specific kind of aberration, like for example, spherical aberration.

The success of the optimisation routine was quantified by a study of spring constants with and without aberration correction at varying depths. The stiffness of the trap could be improved throughout the trapping range of a conventional OT and beyond. At a depth of 131 µm the trapping stiffness was improved by a factor of 4.37 and 3.31 for the x- and y- axis respectively, demonstrating the pronounced power of optimisation algorithm based AO for micromanipulation. Furthermore, the same DMM shape obtained from an optimisation at one depth lead to an improvement of trap stiffness throughout a wide range of trap depths. The optimisation routine also had the beneficial effect of making the trapping forces in the lateral directions more uniform. This technique might prove useful in applications of OTs as force transducers where a constant and uniform lateral trapping force with increasing depth is paramount.

Future work in this field could include aberration correction in the periphery, that is off-axis particle trapping. There have been only few studies investigating image degradation resulting from off-axis imaging [404] and so far only aberrations produced along the optical axis have been corrected for. By using the adjustment screws on the periscope mirror which was placed in a telecentric plane the position of the OT can be laterally translated within the plane of focus of the microscope objective. In this way optimisations could be performed on aberrations that arise in an OT when it is used off-axis in the periphery of the field of view.

Taking the work with the SLM one step further it would be possible to correct for optical aberrations using the SLM in conjunction with an RSA that is based on the decomposition of Zernike modes rather than actuators. It would also be interesting to see if direct optimisations on the spring constant could be performed maybe in conjunction with a fast quadrant photodiode, making use of its kHz bandwidth to measure k directly with the Brownian motion approach. The advantage of using SLMs to investigate trapping efficiency is the possibility to produce to neighbouring traps, one with the aberration correction and one without, such that same sized particle could be compared simultaneously in identical environments [393].

Table 8.2: Overview of selected published literature on the trapping of beads. PS: polystyrene, Si: silica, HOT: holographic optical tweezers, SA: spherical aberrations.

Diam. [μm]	Mat.	Obj. (oil)	Power [mW]	λ [nm]	k $\left[\frac{\text{pN}}{\mu\text{m}}\right]$	Depth [μm]	Imp. fold	Relevance	Ref.
2.1	Si	100x,1.30	200	1064	50.0	8	-	k measurements with frequency method	[386]
1.0	Si	63x,1.25	60	1064	60.0	8	-	Degradation of k with depth	[382]
1.0	Si	63x,1.25	60	1064	102.0	8	-	Exp. model for predicting k values	[384]
1.5	Si	100x,1.40	5	532	0.5	-	-	Trapping with holographic tweezers	[402]
15.0	PS	40x,0.65	73	830	5.6	-	-	k measurements with viscous drag method	[342]
0.6	Si	100x,1.30	-	1064	12	8	-	Decrease in lateral trapping strength with depth	[396]
1.0	PS	60x,1.40	30	1064	0.7	10	1.8	Enhancement of ax. trapping by compensating for SA with DMM	[387]
1.0	PS	100x,1.30	-	1064	-	-	1.7	Optimisation on TPEF of trapped bead to improve trapping depth by compensating for SA	[101]
1.0	PS	100x,1.30	-	830	-	50	3	Improvement of ax. trapping, by combination of SA, defocus and objective position in HOT	[403]
1.9	PS	100x,1.25	17	633	-	-	1.2	Changes in effective tube length to improve lat. trapping	[389]
1.1	Si	100x,1.25	24	1064	-	100	-	Changes in effective tube length to improve ax. trapping	[390]
1.0	PS	63x,1.32	37	1064	37	14	2	Tuning of refractive index of immersion medium	[388]
0.8	Si	100x,1.30	-	515	-	-	1.3	Impact of optimisation in HOT is function of bead diameter	[393]

Chapter 9

Conclusions and Future Work

The work presented in this thesis has been concerned with the implementation of sensorless adaptive optics (AO) in optical microscopy and micromanipulation setups, with a focus on optical trapping and nonlinear microscopy. The performance of these systems degrade with penetration depth due to increasing optical aberrations and this work demonstrated the improvement of the degraded performance through aberration correction by means of a deformable membrane mirror (DMM) without prior knowledge of the wavefront.

9.1 Summary

The aim of this work was tackling some of the major issues of the application of sensorless AO techniques to the correction of optical aberrations at depth. Several issues have been identified.

9.1.1 Choice of merit factor

The optimum shape of the DMM was determined with a random search algorithm (RSA) optimising on application specific merit factors (MF). The MF needs to be carefully chosen such that it is only maximised in the absence of optical aberrations.

The strength of this technique is that it makes the need for wavefront sensing and reconstruction redundant, since an *a priori* knowledge of the aberrations introduced is not necessary for their correction, thereby reducing complexity and cost of the optical setup. Additionally, this approach allows for the dynamic correction of a wide variety of aberrations rather than the static correction of only one

specific aberration, like for example spherical aberration. Other benefits of this method are the efficient use of the signal as no light has to be coupled out toward a wavefront sensor for aberration measurements and correction of aberrations along the entire image path up to the detector in contrast to a wavefront sensor which can only partially correct for the optics system, excluding non-common path aberrations. If the MF can be chosen such that it is directly proportional to the specific quality that is to be improved, this 'blind' optimisation approach becomes straight forward and can show considerable improvements in the chosen quality, as this work has demonstrated.

However, the choice of MF is not always easy and requires careful consideration. The MF needs to be chosen according to the specific sample and application, the quality that needs to be improved, the level of improvement the user requires, and the temporal dynamics of the processes involved. For example, a MF that is deduced from signal intensity alone can considerably improve intensity in the resulting image yet do very little to improve resolution, for which image sharpness might be a better choice of MF. Similarly, a MF that has been chosen to specifically improve lateral trapping strength might not affect axial trapping strength at all. Methods that are based on the excitation of fluorescence light and, thus, are interrelated to tissue damage through photobleaching and phototoxicity bear the risk of a temporally varying MF and complications in the optimisation routine.

This research concentrated on aberrations that are static in time and no attempt has been made to correct for temporally dynamic aberrations.

9.1.2 Look-up tables

The choice of MF also affects the speed of optimisation convergence. If signal intensity is used as MF only one measurement from the detector is required for each DMM shape which means that less time is needed per iteration to compute the MF. For the optical trapping application, the MF was chosen to be directly proportional to the quality that was to be improved but that came at the expense of relatively long acquisition times to compute the MF in each iteration. In those cases optimisations can take up a considerable amount of time (up to 40 minutes) and therefore make *in situ* optimisations for each given depth impractical. Instead, it has been proposed to use look-up tables (LUT) which consist of preoptimised DMM shapes that can be called upon for certain depths [38]. This approach, however, is only valid for relatively homogeneous samples exhibiting

dominating depth-specific aberrations that do not vary over time.

When an heterogeneous sample is imaged an incremental approach could be employed to reduce optimisation convergence time. This approach would make use of a previously optimised DMM shape from a shallower depth or the system aberrations only as an intelligent starting point for the optimisation at hand. Alternatively a LUT from a material with similar optical properties to the tissue could be used as a starting point.

9.1.3 Contributions

The main conclusions from each individual application are listed below:

Confocal laser scanning microscopy

Chapter 4 described the design and implementation of a CLSM system that was custom built from individual components so as to provide a cheap and versatile platform for the testing and development of adaptive aberration correction. The software was written using the LabVIEW programming language and represented an intuitive, all-in-one user interface that allowed for galvo movement, image acquisition, algorithm development and DMM deformation to be controlled from the same front panel. This integrated interface opens up the possibility for diversity and flexibility in the design and test of different MFs, LUTs and aberration compensation, for example it would be feasible to apply a different DMM shape to the centre as opposed to the edges of the image or to use contrast between two distinct regions in the image as a MF by rapidly switching the position of the beam with the galvos whilst optimising.

The imaging properties of the CLSM were characterised including the examination of spatial resolution by transfer function analysis and the necessary digital zoom factors for sampling observing the Nyquist frequency. Various fluorescent and reflective samples were used to test the CLSM in both imaging modalities. The DMM shape for aberration correction was determined with a RSA algorithm optimising either on a retro-reflected signal using a resolution test chart or on the photoluminescence generated by quantum dots.

The effect of the optimisation was analysed in terms of improvement of resolution and signal intensity as well as repeatability of improvement by previously acquired DMM shapes. Some improvement in signal intensity could be achieved in both imaging modalities with improvement factors ranging from 1.2 to 8 fold.

However, diffraction limited resolution was not restored and might require careful re-alignment of the entire optical system and a different sized pinhole.

Nonlinear microscopy

Chapter 6 presented the design and implementation of an AO system in a nonlinear microscope for two photon excitation fluorescence (TPEF) and second harmonic generation (SHG) imaging. The aberrations created by the optical system and the sample under investigation were compensated with a DMM whose shape was determined with a RSA optimising on either TPEF or SHG signal intensity in a pixel or small ROI in the image. The optimisation on a single pixel/small ROI is sufficient to improve the image in the entire field of view [107, 142], as was demonstrated in this work. Signal intensity was chosen as a MF because it provided for a fast feedback on the randomly chosen DMM shape, however, a different MF should be chosen for the optimisation on SHG if resolution improvement is paramount.

Optimisations were performed on a variety of samples including organotypics, intermediate tissue culture systems which are comprised of red fibroblast cells embedded in collagen such that SHG signals as well as TPEF signals can be produced. These samples have been employed to investigate the optimisation on SHG signal to determine the aberration correction required, an approach which is not limited by photobleaching and to then determine the usefulness of this DMM shape in imaging fluorescent structures.

Some significant improvement in signal intensity was achieved in TPEF and SHG imaging modalities with improvement factors ranging from 1.2 to 8.5 fold. However, diffraction limited resolution was not restored and might require careful re-consideration of the merit factor. Even if the penetration depth is ultimately limited by scattering in many biological specimens, AO can improve the quality of images at depths at which imaging would not have been possible without aberration correction.

Optical trapping

In chapter 8 the design and implementation of an optical trapping system with adaptive optics for aberration correction at depth was presented. The effect of spherical aberration on an optical trap formed in water suspension with an oil

immersion objective was mapped qualitatively and quantitatively for silica beads of 1 µm and 3 µm diameter.

The use of a DMM to increase the lateral trapping force at depth was demonstrated. By correcting the aberrations that arise because of the refractive index mismatch between the cover glass and the water, the enhancement of the lateral spring constant was successfully performed. Lateral bead displacement from equilibrium due to a viscous drag force applied through motion of the sample stage was chosen as a merit factor that is directly proportional to the spring constant of the trap. By minimising this displacement, the spring constant was directly proportionally increased and the trapping strength improved. No attempt was made to analyse or improve the axial spring constant of the trap in this work.

The success of the optimisation routine was quantified by a study of spring constants with and without aberration correction at varying depths. The stiffness of the trap could be improved throughout the trapping range of the conventional trap and beyond. At a depth of 131 µm the trapping stiffness was improved by a factor of 4.37 and 3.31 for the x- and y- axis respectively, demonstrating the pronounced power of optimisation algorithm based AO for micromanipulation. This technique will prove useful in applications of optical traps as force transducers where a constant and uniform lateral trapping force with increasing depth is paramount.

9.2 Outlook

Several routes could be explored to extend the research presented in this thesis and the following sections point into directions for future improvements.

9.2.1 Modal decomposition

The optimisation algorithm employed in this work alters the mirror shape by randomly changing the control voltages of actuators. This zonal approach modulates areas on the DMM surface according to the MF. Alternatively, the wavefront correction applied could be decomposed in a modal approach using Zernike polynomials. This could be easily achieved with the spatial light modulator or else with a DMM if the influence functions were measured (see also section 2.5.1). This would allow for a closer conjugation between the optical aberrations and the wavefront corrector and therefore the affect of specific aberrations on the MF

could be investigated, for example by monitoring the MF as a function of varying magnitude of the aberration. Possibly some insights on the complexity of the search space could also be gained from such experiments.

The search space has a large number of degrees of freedom and a systematic search is hence not practical. A random search was employed in this work which has the advantage of locating the global maximum of the system if left running long enough. The downside of this random search, however, is that the search routine is not tailored to specific aberrations present in the system or the specific MF chosen for optimisation. A comprehensive analysis of the dependency of the search space on modal aberrations and the exploration of alternative algorithms like the genetic algorithm, hill climbing algorithm or simulated annealing algorithms are worth investigating and might well provide better solutions depending on the application and the sample.

9.2.2 Aberration correction in the periphery

Another challenge with potentially high beneficial outcome is the extension of the field of correction. There have been only few studies investigating image degradation resulting from off-axis imaging [60, 404] and also in this work only aberrations produced along the optical axis have been corrected. In optical trapping SLMs can be used for simultaneous generation of several dozen traps which are also necessarily affected by off axis aberrations. In confocal scanning the light mostly traverses the optical setup off-axis and therefore aberrations produced at the periphery have a profound effect on image quality. Recently the challenge of combining high resolution, wide field-of-view, and a flat image field has resulted in a novel microscope design, called the Adaptive Scanning Optical Microscope (ASOM) which utilises a DMM to expand the field-of-view without sacrificing resolution [405, 406].

9.2.3 Imaging at depth

Imaging at depth is mostly hampered by the scattering properties of the tissue. Highly transparent samples with low scattering coefficients like for example Zebrafish, would allow for imaging at depths where optical aberrations accumulate and eventually prevail over the scattering. The study of optical aberrations and their compensation would be aided with those tissues and it is expected that AO will have a particularly high impact on signal intensity and resolution. Another

possibility is optical clearing, a procedure in which tissues have been processed in a way that reversibly decreases scattering for example by dehydration and adding of index matching medium [323].

9.2.4 Future trends

The afore mentioned ideas are just a small sample of the broad range of topics in the fundamental implementation of wavefront sensorless AO that could be explored in order to complement the presented research. The next few sections briefly mention other trends that have been reported.

Dual correction

A better quality of correction might be required in certain applications, either if the magnitude of lower order aberrations is especially high or else if the correction of increasingly higher order aberrations is necessary. Next generation AO systems will be required for both high-amplitude correction of low-order aberrations and low-amplitude correction for high-order aberrations. For such applications a combination of two correctors, commonly named woofer and tweeter, has been reported. The woofer, typically the corrector with the larger stroke and lower spatial resolution, compensates for lower order aberrations like astigmatism and coma and can also axially vary the focus of the system whereas the full dynamic range of the low-stroke, high-resolution tweeter remains for the correction of residual higher order aberrations [407]. These systems are especially of interest in retinal imaging with ophthalmoscopes where the large individual differences in defocus (accommodation) and astigmatism in the human eye need to be compensated [408].

Super-resolution microscopy

After having shown its potential in conventional high-resolution microscopy techniques like two-photon and confocal microscopy, an important area of application might be novel super-resolution techniques such as stimulated emission depletion (STED) fluorescence [409] and structured illumination [171] microscopy. In optical coherence tomography (OCT) [410] the lateral resolution might be improved with AO to complement the high-resolution axial sectioning capability [411].

9.3 Conclusion

While sensorless AO may not be able to compete with direct wavefront sensing methods in terms of speed and guaranteed success in the correction, its simplicity might well make it a tool of choice in applications only requiring correction of static aberrations. In conclusion, wavefront sensorless AO is a very sensitive technique that still requires lot of attention to detailed implementation followed by the regular control and adjustments from an experienced user. It is therefore far from having found a form that is universally applicable to a broad range of applications with a guaranteed good performance. The robust implementation of sensorless AO for imaging and microscopy needs to be further studied and thoroughly investigated through a collaboration involving physicists and biologists.

Bibliography

[1] Abbe, E. Beiträge zur theorie des mikroskops und der mikroskopischen wahrnehmung. *Arch. Mikrosk. Anat.* **9**, 413 (1873). 1

[2] Abbe, E. Note on the proper definition of the amplifying power of a lens or lens-system. *J. Roy. Microsc. Soc.* **4**, 348 (1884). 1

[3] Minsky, M. Microscopy apparatus (1961). US Patent 3,013,467. 1, 31

[4] Minsky, M. Memoir on inventing the confocal scanning microscope. *Scanning* **10**, 128 (1988). 1, 31

[5] Denk, W., Strickler, J. & Webb, W. Two-photon laser scanning fluorescence microscopy. *Science* **248**, 73 (1990). 2, 72

[6] Göppert-Mayer, M. Über elementarakte mit zwei quantensprüngen. *Ann. Phys.* **9**, 274 (1931). 2, 72

[7] Hargrove, L., Fork, R. & Pollack, M. Locking of he-ne laser modes induced by synchronous intracavity modulation. *Appl. Phys. Lett.* **5**, 4 (1964). 2

[8] Zhou, G. & Gu, M. Direct optical fabrication of three-dimensional photonic crystals in a high refractive index linbo3 crystal. *Opt. Lett.* **31**, 2783 (2006). 5, 88

[9] Serbin, J. *et al.* Femtosecond laser-induced two-photon polymerization of inorganic organic hybrid materials for applications in photonics. *Opt. Lett.* **28**, 301 (2003). 5, 88

[10] Sun, H. & Kawata, S. Two-photon photopolymerization and 3d lithographic microfabrication. *Adv. Polym. Sci.* 169 (2004). 5, 88

[11] McAlinden, N., Glass, D., Millington, O. & Wright, A. Viability studies of optically trapped t-cells. *Proc. SPIE* **8097**, 80970J (2011). 5, 150, 154

[12] Watts, F. *et al.* The viscoelastic properties of the vitreous humor measured using an optically trapped local probe. In *Proc. SPIE*, vol. 8097, 80970H (2011). 5, 150

[13] Dogariu, A. & Rajagopalan, R. Optical traps as force transducers: the effects of focusing the trapping beam through a dielectric interface. *Langmuir* **16**, 2770 (2000). 5, 149, 150, 156

[14] Love, G. *Adaptive Optics for Industry and Medicine* (World Scientific, 2000). 8

[15] Tyson, R. *Principles of adaptive optics* (CRC Press, 2010). 8

[16] Newton, I. *Opticks, Or a Treatise of the Reflections, Refractions, Inflections and Colours of Light* (William Innys, 1730). 8

[17] Babcock, H. The possibility of compensating astronomical seeing. *Publ. Astron. Soc. Pac.* **65**, 229 (1953). 8

[18] Buffington, A., Crawford, F., Muller, R., Schwemin, A. & Smits, R. Active image restoration with a flexible mirror. In *Society of Photo-Optical Instrumentation Engineers (SPIE) Conference Series*, vol. 75, 90–96 (1976). 8

[19] Hardy, J. Active optics: a new technology for the control of light. *Proc. IEEE* **66**, 651 (1978). 8

[20] Hardy, J. *Adaptive optics for astronomical telescopes* (Oxford University Press, USA, 1998). 8

[21] Wizinowich, P. *et al.* First light adaptive optics images from the keck ii telescope: a new era of high angular resolution imagery. *Publ. Astron. Soc. Pac.* **112**, 315 (2000). 8

[22] Roorda, A. & Williams, D. *Retinal Imaging Using Adaptive Optics*, vol. 53 (Slack Incorporated, 2004). 9

[23] Bille, J., Jahn, M. & Fieben, M. Modal wavefront reconstruction and adaptive optics. advanced technology, optical telescopes (SPIE, 1982). 9

[24] Bille, J., Dreher, A. & Zinser, G. Scanning laser tomography of the living human eye. *Noninvasive Diagnostic Techniques in Ophthalmology. New York: Springer-Verlag* 528 (1990). 9

[25] Liang, J., Grimm, B., Goelz, S. & Bille, J. Objective measurement of wave aberrations of the human eye with use of a hartmann-shack wave-front sensor. *J. Opt. Soc. Am. A* **11**, 11 (1994). 9

[26] Liang, J. & Williams, D. Aberrations and retinal image quality of the normal human eye. *J. Opt. Soc. Am. A* **14**, 2873 (1997). 9

[27] Roorda, A. & Williams, D. The arrangement of the three cone classes in the living human eye. *Nature* **15**, 16 (1998). 10

[28] Bigelow, C. *et al.* Compact multimodal adaptive-optics spectral-domain optical coherence tomography instrument for retinal imaging. *J. Opt. Soc. Am. A* **24**, 1327 (2007). 10

[29] Zawadzki, R. *et al.* Adaptive-optics optical coherence tomography for high-resolution and high-speed 3d retinal in vivo imaging. *Opt. Express* **13**, 8532 (2005). 10

[30] Booth, M., Neil, M. & Wilson, T. Aberration correction for confocal imaging in refractive-index-mismatched media. *J. Microsc.* **192**, 90 (1998). 10, 19, 38

[31] Girkin, J., Poland, S. & Wright, A. Adaptive optics for deeper imaging of biological samples. *Curr. Opin. Biotech.* **20**, 106 (2009). 10

[32] Booth, M. Adaptive optics in microscopy. *Philos. T. Roy. Soc. A* **365**, 2829 (2007). 10, 19, 22

[33] Booth, M., Neil, M., Juskaitis, R. & Wilson, T. Adaptive aberration correction in a confocal microscope. *P. Natl. Acad. Sci.* 82544799 (2002). 10, 29, 38

[34] Neil, M. *et al.* Adaptive aberration correction in a two-photon microscope. *J. Microsc.* **200**, 105 (2000). 10, 87

[35] Marsh, P., Burns, D. & Girkin, J. Practical implementation of adaptive optics in multi-photon microscopy. *Opt. Express* **11**, 1123 (2003). 10, 29, 88, 135, 139

[36] Jesacher, A. *et al.* Adaptive harmonic generation microscopy of mammalian embryos. *Opt. Lett.* **34**, 3154 (2009). 10, 87, 134, 139

[37] Villoresi, P. *et al.* Optimization of high-order harmonic generation by adaptive control of a sub-10-fs pulse wave front. *Opt. Lett.* **29**, 207 (2004). 10, 87, 139

[38] Wright, A. *et al.* Adaptive optics for enhanced signal in cars microscopy. *Opt. Express* **15**, 18209 (2007). 10, 29, 88, 150, 180

[39] Pawley, J. B. *Handbook of Biological Confocal Microscopy*, chap. Fundamental Limits in Confocal Microscopy, 20–42 (Springer, 2006), 3rd edn. 13, 17, 67

[40] Richards, B. & Wolf, E. Electromagnetic diffraction in optical systems. ii. structure of the image field in an aplanatic system. *Proc. R. Soc. Lon. Ser.- A* **253**, 358 (1959). 14, 75

[41] Webb, R. Confocal optical microscopy. *Rep. Prog. Phys.* **59**, 427 (1996). 14, 16, 32, 33, 36

[42] Inoué, S. *Handbook of Biological Confocal Microscopy*, chap. Foundations of Confocal Scanned Imaging in Light Microscopy, 1–19 (Springer, 2006), 3rd edn. 14, 15, 19

[43] Rose, A. Television pickup tubes and the problem of vision. *Adv. Electron. El. Phys.* **1**, 131 (1948). 15

[44] Brüllmann, D. & d'Hoedt, B. The modulation transfer function and signal-to-noise ratio of different digital filters: a technical approach. *Dentomaxillofac. Rad.* **40**, 222 (2011). 15, 50

[45] Boone, J. & Seibert, J. An analytical edge spread function model for computer fitting and subsequent calculation of the lsf and mtf. *Med. Phys.* **21**, 1541 (1994). 16, 52, 210, 211

[46] Giger, M. & Doi, K. Investigation of basic imaging properties in digital radiography. i. modulation transfer function. *Med. Phys.* **11**, 287 (1984). 17, 51

[47] Niesner, R., Andresen, V., Neumann, J., Spiecker, H. & Gunzer, M. The power of single and multibeam two-photon microscopy for high-resolution and high-speed deep tissue and intravital imaging. *Biophys. J.* **93**, 2519 (2007). 17, 84, 85

[48] Oheim, M., Beaurepaire, E., Chaigneau, E., Mertz, J. & Charpak, S. Two-photon microscopy in brain tissue: parameters influencing the imaging depth. *J. Neurosci. Meth.* **111**, 29 (2001). 18, 84

[49] Cheng, P.-C. *Handbook of Biological Confocal Microscopy*, chap. 21: Interaction of Light with Botanical Specimens, 414–441 (Springer, 2006). 18

[50] Cheng, P.-C. *Handbook of Biological Confocal Mircoscopy*, chap. 8: The Contrast Formation in Optical Microscopy, 162–206 (Springer, 2006). 18

[51] Theer, P. & Denk, W. On the fundamental imaging-depth limit in two-photon microscopy. *J. Opt. Soc. Am. A* **23**, 3139 (2006). 18, 19, 84, 85

[52] Helmchen, F. & Denk, F. Deep tissue two-photon microscopy. *Nat. Methods* **2**, 932 (2005). 18, 71, 72, 74, 86

[53] Keller, H. E. *Handbook of Biological Confocal Mircoscopy*, chap. Objective Lenses for Confocal Microscopy, 145–161 (Springer, 2006), 3rd edn. 19, 67

[54] Kashima, S. & Kashima, A. Cover slip for use in microscope (1995). US Patent 5,406,421. 19

[55] Egener, A. & Hell, S. W. *Handbook of Biological Confocal Microscopy*, chap. 20: Aberrations in Confocal and Multi-Photon Fluorescence Microscopy induced by Refractive Index Mismatch, 404 (Springer New York, 2006), 3rd edn. 19

[56] Zernike, F. Beugungstheorie des schneidenverfahrens und seiner verbesserten form, der phasenkontrastmethode. *Physica* **1**, 689 (1934). 21

[57] Noll, R. Zernike polynomials and atmospheric turbulence. *J. Opt. Soc. Am* **66**, 207 (1976). 21

[58] Wang, J. & Silva, D. Wave-front interpretation with zernike polynomials. *Appl. Optics* **19**, 1510 (1980). 21

[59] Born, M., Wolf, E. & Bhatia, A. *Principles of optics: electromagnetic theory of propagation, interference and diffraction of light* (Cambridge Univ Pr, 1999). 21

[60] Schwertner, M., Booth, M. & Wilson, T. Specimen-induced distortions in light microscopy. *J. Microsc.* **228**, 97 (2007). 22, 37, 184

[61] Grosso, R. & Yellin, M. The membrane mirror as an adaptive optical element. *J. Opt. Soc. Am.* **67**, 399 (1977). 22

[62] Vdovin, G., Sarro, P. & Middelhoek, S. Technology and applications of micromachined adaptive mirrors. *J. Micromech. Microeng.* **9**, R8 (1999). 22, 24

[63] Bifano, T., Perreault, J., Krishnamoorthy Mali, R. & Horenstein, M. Microelectromechanical deformable mirrors. *IEEE J. Sel. Top. Quant.* **5**, 83 (1999). 22, 25

[64] Fernandez, E. *et al.* Adaptive optics with a magnetic deformable mirror: applications in the human eye. *Opt. Express* **14**, 8900 (2006). 22, 23, 26

[65] Simonov, A., Hong, S. & Vdovin, G. Piezoelectric deformable mirror with adaptive multiplexing control. *Opt. Eng.* **45**, 070501 (2006). 22

[66] Dainty, J., Koryabin, A. & Kudryashov, A. Low-order adaptive deformable mirror. *Appl. Optics* **37**, 4663 (1998). 22

[67] Vdovin, G. & Loktev, M. Deformable mirror with thermal actuators. *Opt. Lett.* **27**, 677 (2002). 22

[68] Tsai, P. *et al.* Spherical aberration correction in nonlinear microscopy and optical ablation using a transparent deformable membrane. *Appl. Phys. Lett.* **91**, 191102 (2007). 22, 87, 139

[69] Vuelban, E., Bhattacharya, N. & Braat, J. Liquid deformable mirror for high-order wavefront correction. *Opt. Lett.* **31**, 1717 (2006). 22

[70] Laird, P., Caron, N., Rioux, M., Borra, E. & Ritcey, A. Ferrofluidic adaptive mirrors. *Appl. Optics* **45**, 3495 (2006). 22

[71] Paterson, C., Munro, I. & Dainty, J. A low cost adaptive optics system using a membrane mirror. *Opt. Express* **6**, 175 (2000). 22

[72] Fernandez, E. & Artal, P. Membrane deformable mirror for adaptive optics: performance limits in visual optics. *Opt. Express* **11**, 1056 (2003). 22

[73] Booth, M., Wilson, T., Sun, H., Ota, T. & Kawata, S. Methods for the characterization of deformable membrane mirrors. *Appl. Optics* **44**, 5131 (2005). 22

[74] Devaney, N. *et al.* Correction of ocular and atmospheric wavefronts: a comparison of the performance of various deformable mirrors. *Appl. Optics* **47**, 6550 (2008). 23, 24, 42

[75] Farrell, T., Daly, E., Dalimier, E. & Dainty, C. Task-based assessment of deformable mirrors. *P. SPIE* **6467**, 64670F (2007). 23

[76] FlexibleOptical. Adaptive optics product guide. http://www.okotech.com, Röntgenweg1, 2624 BD, Delft, The Netherlands (2008). 24

[77] Vdovin, G. & Sarro, P. Flexible mirror micromachined in silicon. *Applied Optics* **34**, 2968 (1995). 24

[78] Zhu, L., Sun, P., Bartsch, D., Freeman, W. & Fainman, Y. Adaptive control of a micromachined continuous-membrane deformable mirror for aberration compensation. *Appl. Optics* **38**, 168 (1999). 24

[79] Vdovin, G., Soloviev, O., Samokhin, A. & Loktev, M. Correction of low order aberrations using continuous deformable mirrors. *Opt. Express* **16**, 2859 (2008). 24

[80] Doble, N. *et al.* Use of a microelectromechanical mirror for adaptive optics in the human eye. *Opt. Lett.* **27**, 1537 (2002). 25

[81] Vargas-Martín, F., Prieto, P. & Artal, P. Correction of the aberrations in the human eye with a liquid-crystal spatial light modulator: limits to performance. *J. Opt. Soc. Am. A* **15**, 2552 (1998). 27

[82] Mu, Q., Cao, Z., Hu, L., Li, D. & Xuan, L. An adaptive optics imaging system based on a high-resolution liquid crystal on silicon device. *Opt. Express* **14**, 8013 (2006). 27

[83] Schmidt, J., Goda, M. & Duncan, B. Aberration production using a high-resolution liquid-crystal spatial light modulator. *Appl. Optics* **46**, 2423 (2007). 27

[84] Padgett, M. & Di Leonardo, R. Holographic optical tweezers and their relevance to lab on chip devices. *Lab Chip* **11**, 1196 (2011). 27, 147

[85] Bowman, R. *et al.* itweezers: optical micromanipulation controlled by an apple ipad. *J. Opt.* **13**, 044002 (2011). 27

[86] Koliopoulos, C. Radial grating lateral shear heterodyne interferometer. *Appl. Optics* **19**, 1523 (1980). 27

[87] Ragazzoni, R. Pupil plane wavefront sensing with an oscillating prism. *J. Mod. Optic.* **43**, 289 (1996). 27

[88] Shack, R. & Platt, B. Production and use of a lenticular hartmann screen. *J. Opt. Soc. Am* **61**, 1971 (1971). 27

[89] Roddier, F. Wavefront sensing and the irradiance transport equation. *Appl. Optics* **29**, 1402 (1990). 27

[90] Gonsalves, R. Phase retrieval and diversity in adaptive optics. *Opt. Eng.* **21**, 829 (1982). 27

[91] Neil, M., Booth, M. & Wilson, T. New modal wave-front sensor: a theoretical analysis. *J. Opt. Soc. Am. A* **17**, 1098 (2000). 27

[92] Neil, M., Booth, M. & Wilson, T. Closed-loop aberration correction by use of a modal zernike wave-front sensor. *Opt. Lett.* **25**, 1083 (2000). 27, 139

[93] Booth, M., Neil, M. & Wilson, T. New modal wave-front sensor: application to adaptive confocal fluorescence microscopy and two-photon excitation fluorescence microscopy. *J. Opt. Soc. Am. A* **19**, 2112 (2002). 27

[94] Angel, J. Ground-based imaging of extrasolar planets using adaptive optics. *Nature* **368**, 203 (1994). 27

[95] Shack, R. & Platt, B. Production and use of a lenticular hartmann screen. *J. Opt. Soc. Am* **61**, 656 (1971). 27

[96] Platt, B. History and principles of shack-hartmann wavefront sensing. *J. Refract. Surg.* **17**, 573 (2001). 27

[97] Cubalchini, R. Modal wave-front estimation from phase derivative measurements. *J. Opt. Soc. Am.* **69**, 972 (1979). 28

[98] Sherman, L., Ye, J., Albert, O. & Norris, T. Adaptive correction of depth-induced aberrations in multiphoton scanning microscopy using a deformable mirror. *J. Microsc.* **206**, 65 (2002). 29, 87, 139

[99] Albert, O., Sherman, L., Mourou, G., Norris, T. & Vdovin, G. Smart microscope: an adaptive optics learning system for aberration correction in multiphoton confocal microscopy. *Opt. Lett.* **25**, 52 (2000). 29, 87, 139

[100] Lubeigt, W., Valentine, G., Girkin, J., Bente, E. & Burns, D. Active transverse mode control and optimization of an all-solid-state laser using an intracavity adaptive-optic mirror. *Opt. Express* **10**, 550 (2002). 29, 48, 136

[101] Theofanidou, E., Wilson, L., Hossack, W. & Arlt, J. Spherical aberration correction for optical tweezers. *Opt. Commun.* **236**, 145 (2004). 29, 149, 150, 174, 178

[102] Muellenbroich, C., McAlinden, N. & Wright, A. Aberration correction in an optical trapping system using a deformable membrane mirror. In *Frontiers in Optics* (Optical Society of America, 2011). 29, 88

[103] Gonté, F., Courteville, A. & Dändliker, R. Optimization of single-mode fiber coupling efficiency with an adaptive membrane mirror. *Opt. Eng.* **41**, 1073 (2002). 29

[104] Wright, A. *et al.* Exploration of the optimisation algorithms used in the implementation of adaptive optics in confocal and multiphoton microscopy. *Microsc. Res. Techniq.* **67**, 36 (2005). 29, 88, 150

[105] Booth, M. Wave front sensor-less adaptive optics: a model-based approach using sphere packings. *Opt. Express* **14**, 1339 (2006). 29

[106] Poland, S., Wright, A. & Girkin, J. Evaluation of fitness parameters used in an iterative approach to aberration correction in optical sectioning microscopy. *Appl. Optics* **47**, 731 (2008). 29, 87

[107] Poland, S., Wright, A., Cobb, S., Vijverberg, J. & Girkin, J. A demonstration of the effectiveness of a single aberration correction per optical slice in beam scanned optically sectioning microscopes. *Micron* **42**, 318 (2011). 29, 35, 38, 137, 182

[108] Gu, M. *Advanced optical imaging theory*, vol. 75 (Springer Verlag, 2000). 31, 32

[109] Sheppard, C., Gannaway, J., Kompfner, R. & Walsh, D. The scanning harmonic optical microscope. *IEEE J. Quantum Elect.* **13**, 912 (1977). 31

[110] Sheppard, C., Gannaway, J., Walsh, D. & Wilson, T. Scanning optical microscope for the inspection of electronic devices. *J. Microsc.* **118**, 309 (1978). 31

[111] Wilson, T., Gannaway, J. & Johnson, P. A scanning optical microscope for the inspection of semiconductor materials and devices. *J. Microsc.* **118**, 309 (1980). 31

[112] Wilson, T. & Sheppard, C. Theory and practice of scanning optical microscopy. *Academic Press, London* **1** (1984). 31

[113] Wilson, T. Scanning optical microscopy. *Scanning* **7**, 79 (1985). 31

[114] Cremer, C. & Cremer, T. Considerations on a laser-scanning-microscope with high resolution and depth of field. *Microsc. acta* **2**, 19 (1978). 31

[115] Brakenhoff, G., Blom, P. & Barends, P. Confocal scanning light microscopy with high aperture immersion lenses. *J. Microsc.* **117**, 219 (1979). 31

[116] Carlsson, K. *et al.* Three-dimensional microscopy using a confocal laser scanning microscope. *Opt. Lett.* **10**, 53 (1985). 31

[117] Resandt, R. *et al.* Optical fluorescence microscopy in three dimensions: microtomoscopy. *J. Microsc.* **138**, 29 (1985). 31

[118] Brakenhoff, G., Voort, H., Spronsen, E. & Nanninga, N. Three-dimensional imaging by confocal scanning fluorescence microscopya. *Ann. NY Acad. Sci.* **483**, 405 (1986). 31

[119] White, J. An evaluation of confocal versus conventional imaging of biological structures by fluorescence light microscopy. *J. Cell. Biol.* **105**, 41 (1987). 31

[120] Åslund, N., Liljeborg, A., Forsgren, P. & Wahlsten, S. Three-dimensional digital microscopy using the phoibosl scanner. *Scanning* **9**, 227 (1987). 31

[121] Amos, W., White, J. & Fordham, M. Use of confocal imaging in the study of biological structures. *Appl. Optics* **26**, 3239 (1987). 31

[122] Pawley, J. *Handbook of biological confocal microscopy* (Springer, 1990), 3rd edn. 31

[123] Amos, B., McConnell, G. & Wilson, T. *Handbook of Comprehensive Biophysics*, chap. Confocal Microscopy (Elsevier, 2011). 31

[124] Conchello, J. & Lichtman, J. Optical sectioning microscopy. *Nat. Methods* **2**, 920 (2005). 31

[125] Lange-Asschenfeldt, S. *et al.* Applicability of confocal laser scanning microscopy for evaluation and monitoring of cutaneous wound healing. *J. Biomed. Opt.* **17**, 076016 (2012). 31

[126] Amos, W. & White, J. How the confocal laser scanning microscope entered biological research. *Biol. Cell* **95**, 335 (2003). 31, 32, 33

[127] Rietdorf, J. & Stelzer, E. H. K. *Handbook of Biological Confocal Microscopy*, chap. Special Optical Elements, 43–58 (Springer, 2006), 3rd edn. 33

[128] Toomre, D. & Pawley, J. B. *Handbook of Biological Confocal Microscopy*, chap. Disk-Scanning Confocal Microscopy, 221–238 (Springer, 2006), 3rd edn. 33, 68

[129] Plesch, A. & Bille, J. Digital laser scanning fundus camera. *Appl. Optics* **26**, 1480 (1987). 33

[130] Veilleux, I., Spencer, J., Biss, D., Côté, D. & Lin, C. In vivo cell tracking with video rate multimodality laser scanning microscopy. *IEEE J. Sel. Top. Quant.* **14**, 10 (2008). 33

[131] Goldstein, S., Hubin, T., Rosenthal, S. & Washburn, C. A confocal video-rate laser-beam scanning reflected-light microscope with no moving parts. *J. Microsc.* **157**, 29 (1990). 33

[132] Fan, G. Y. *et al.* Video-rate scanning two-photon excitation fluorescence microscopy and ratio imaging with cameleons. *Biophys. J.* **76**, 2412 (1999). URL `http://www.biophysj.org/cgi/content/abstract/76/5/2412`. 33

[133] Nguyen, Q., Callamaras, N., Hsieh, C. & Parker, I. Construction of a two-photon microscope for video-rate ca2+ imaging. *Cell Calcium* **30**, 383 (2001). 33

[134] Callamaras, N. & Parker, I. Construction of a confocal microscope for real-time xy and xz imaging. *Cell Calcium* **26**, 271 (1999). 33

[135] Dickensheets, D. & Kino, G. Silicon-micromachined scanning confocal optical microscope. *J. Microelectromech. S.* **7**, 38 (1998). 34

[136] Helmchen, F., Fee, M., Tank, D. & Denk, W. A miniature head-mounted two-photon microscope high-resolution brain imaging in freely moving animals. *Neuron* **31**, 903 (2001). 34

[137] Myaing, M., MacDonald, D. & Li, X. Fiber-optic scanning two-photon fluorescence endoscope. *Opt. Lett.* **31**, 1076 (2006). 34

[138] Delaney, P. & Harris, M. *Handbook of Biological Confocal Microscopy*, chap. Fibre-Optics in Scanning Optical Microscopy, 501–515 (Springer, 2006), 3rd edn. 34

[139] Zhang, L., Nelson, L. & Seibel, E. Spectrally enhanced imaging of occlusal surfaces and artificial shallow enamel erosions with a scanning fiber endoscope. *J. Biomed. Opt.* **17**, 076019 (2012). 34

[140] P. Xi, Y. L. & Ren, Q. *Scanning and image reconstruction techniques in confocal laser scanning microscopy in Laser Scanning, Theory and Applications* (Intech Open,, 2009). 34

[141] Aylward, R. Advanced galvanometer-based optical scanner design. *Sensor Rev.* **23** (2003). 34

[142] Girkin, J. *et al. Adaptive optics in confocal and two-photon microscopy of rat brain: a single correction per optical section*, vol. 6442 of *Multiphoton Microscopy in the Biomedical Sciences VII* (Proceedings of SPIE: The International Society for Optical Engineering, 2007). 35, 137, 139, 182

[143] Stelzer, E. H. K. *Handbook of Biological Confocal Microscopy*, chap. The Intermediate Optical System of Laser-Scanning Confocal Microscopes, 204–220 (Springer, 2006), 3rd edn. 35

[144] Carlsson, K. The influence of specimen refractive index, detector signal integration, and non-uniform scan speed on the imaging properties in confocal microscopy. *J. Microsc.* **163**, 167 (1991). 37

[145] Jacobsen, H. & Hell, S. Effect of the specimen refractive index on the imaging of a confocal fluorescence microscope employing high aperture oil immersion lenses. *Bioimaging* **3**, 39 (1995). 37

[146] White, N., Errington, R., Fricker, M. & Wood, J. Aberration control in quantitative imaging of botanical specimens by multidimensional fluorescence microscopy. *J. Microsc.* **181**, 99 (1996). 37

[147] Fwu, P., Wang, P., Tung, C. & Dong, C. Effects of index-mismatch-induced spherical aberration in pump-probe microscopic image formation. *Appl. Optics* **44**, 4220 (2005). 37

[148] Sheppard, C. & Gu, M. Axial imaging through an aberrating layer of water in confocal microscopy. *Opt. Commun.* **88**, 180 (1992). 37

[149] Hell, S., REINER, G., CREMER, C. & STELZER, E. Aberrations in confocal fluorescence microscopy induced by mismatches in refractive index. *J. Microsc.* **169**, 391 (1993). 37, 86, 173

[150] Sheppard, C. *et al.* Effects of specimen refractive index on confocal imaging. *J. Microsc.* **185**, 366 (1997). 37

[151] Frisken Gibson, S. & Lanni, F. Experimental test of an analytical model of aberration in an oil-immersion objective lens used in three-dimensional light microscopy. *J. Opt. Soc. Am. A* **8**, 1601 (1991). 37

[152] Török, P., Varga, P., Laczik, Z. & Booker, G. Electromagnetic diffraction of light focused through a planar interface between materials of mismatched refractive indices: an integral representation. *J. Opt. Soc. Am. A* **12**, 325 (1995). 37, 86, 149, 173

[153] Török, P., Varga, P., Konkol, A. & Booker, G. Electromagnetic diffraction of light focused through a planar interface between materials of mismatched refractive indices: structure of the electromagnetic field. ii. *J. Opt. Soc. Am. A* **13**, 2232 (1996). 37

[154] Török, P., Varga, P. & Németh, G. Analytical solution of the diffraction integrals and interpretation of wave-front distortion when light is focused through a planar interface between materials of mismatched refractive indices. *J. Opt. Soc. Am. A* **12**, 2660 (1995). 37

[155] Török, P., Hewlett, S. & Varga, P. The role of specimen-induced spherical aberration in confocal microscopy. *J. Microsc.* **188**, 158 (1997). 37

[156] Wiersma, S. & Visser, T. Defocusing of a converging electromagnetic wave by a plane dielectric interface. *J. Opt. Soc. Am. A* **13**, 320 (1996). 37

[157] Egner, A. & Hell, S. Equivalence of the huygens–fresnel and debye approach for the calculation of high aperture point-spread functions in the presence of refractive index mismatch. *J. Microsc.* **193**, 244 (1999). 37

[158] Sheppard, C. & Wilson, T. Effect of spherical aberration on the imaging properties of scanning optical microscopes. *Appl. Optics* **18**, 1058 (1979). 37

[159] Visser, T. & Wiersma, S. Spherical aberration and the electromagnetic field in high-aperture systems. *J. Opt. Soc. Am. A* **8**, 1404 (1991). 37

[160] Sheppard, C. Aberrations in high aperture conventional and confocal imaging systems. *Appl. Optics* **27**, 4782 (1988). 37

[161] Booth, M. & Wilson, T. Strategies for the compensation of specimen-induced spherical aberration in confocal microscopy of skin. *J. Microsc.* **200**, 68 (2000). 38

[162] Sheppard, C. & Gu, M. Aberration compensation in confocal microscopy. *Appl. Optics* **30**, 3563 (1991). 38

[163] Sheppard, C., Gu, M., Brain, K. & Zhou, H. Influence of spherical aberration on axial imaging of confocal reflection microscopy. *Appl. Optics* **33**, 616 (1994). 38, 50

[164] Sieracki, C., Levey, C. & Hansen, E. Simple binary optical elements for aberration correction in confocal microscopy. *Opt. Lett.* **20**, 1213 (1995). 38

[165] Wan, D., Rajadhyaksha, M. & Webb, R. Analysis of spherical aberration of a water immersion objective: application to specimens with refractive indices 1.33-1.40. *J. Microsc.* **197**, 274 (2000). 38

[166] O'Byrne, J. & Cogswell, C. High-resolution confocal transmission microscope: Part ii-determining image position and correcting aberrations. In *Proceedings of SPIE*, vol. 1660, 512 (1992). 38

[167] O'Byrne, J. *et al. Proceedings of the Second International Workshop on Adaptive Optics for Industry and Medicine*, chap. Adaptive optics in confocal microscopy, 85–90 (World Scientific, 2000). 38

[168] Azucena, O. *et al.* Wavefront aberration measurements and corrections through thick tissue using fluorescent microsphere reference beacons. *Opt. Express* **18**, 17521 (2010). 38, 139

[169] Schwertner, M., Booth, M., Tanaka, T., Wilson, T. & Kawata, S. Spherical aberration correction system using an adaptive optics deformable mirror. *Opt. Commun.* **263**, 147 (2006). 38

[170] Debarre, D., Booth, M. & Wilson, T. Image based adaptive optics through optimisation of low spatial frequencies. *Opt. Express* **15**, 8176 (2007). 38

[171] Neil, M., Juskaitis, R. & Wilson, T. Method of obtaining optical sectioning by using structured light in a conventional microscope. *Opt. Lett.* **22**, 1905 (1997). 38, 185

[172] Debarre, D., Botcherby, E., Booth, M. & Wilson, T. Adaptive optics for structured illumination microscopy. *Opt. Express* **16**, 9290 (2008). 38

[173] Potsaid, B., Bellouard, Y. & Wen, J. Adaptive scanning optical microscope (asom): A multidisciplinary optical microscope design for large field of view and high resolution imaging. *Opt. Express* **13**, 6504 (2005). 38

[174] Wright, A. *et al.* Dynamic closed-loop system for focus tracking using a spatial light modulator and a deformable membrane mirror. *Opt. Express* **14**, 222 (2006). 38

[175] Poland, S., Wright, A. & Girkin, J. Active focus locking in an optically sectioning microscope utilizing a deformable membrane mirror. *Opt. Lett.* **33**, 419 (2008). 38

[176] Dreher, A., Bille, J. & Weinreb, R. Active optical depth resolution improvement of the laser tomographic scanner. *Appl. Optics* **28**, 28 (1989). 45

[177] Guilhabert, B. *et al.* Integration by self-aligned writing of nanocrystal/epoxy composites on ingan micro-pixelated light-emitting diodes. *Opt. Express* **16**, 18933 (2008). 49

[178] Hecht, E. *Hecht optics*, vol. 997 (1998). 48

[179] Guilhabert, B. *Hybrid inorganic-organic micro-devices combining gallium nitride and polymers.* Ph.D. thesis, Institute of Photonics (2007). 49, 55

[180] Donovan, M., Zhang, D. & Liu, H. Step by step analysis toward optimal mtf algorithm using an edge test device. *J X-Ray Sci. Technol.* **17**, 1 (2009). 51

[181] Yin, F., Giger, M. & Doi, K. Measurement of the presampling modulation transfer function of film digitizers using a curve fitting technique. *Med. Phys.* **17**, 962 (1990). 51, 101

[182] Samei, E., Flynn, M. & Reimann, D. A method for measuring the presampled mtf of digital radiographic systems using an edge test device. *Med. Phys.* **25**, 102 (1998). 52

[183] Li, T., Feng, H. & Xu, Z. A new analytical edge spread function fitting model for modulation transfer function measurement. *Chin. Opt. Lett.* **9**, 031101 (2011). 64

[184] Zipfel, W., Williams, R. & Webb, W. Nonlinear magic: multiphoton microscopy in the biosciences. *Nat. Biotechnol.* **21**, 1369 (2003). 71, 72, 74, 76, 78

[185] So. Two-photon excitation fluorescence microscopy (2000). 72, 74, 77

[186] Kaiser, W. & Garrett, C. Two-photon excitation in $caf_2 : eu^{2+}$. *Phys. Rev. Lett.* **7**, 612 (1961). First report on TPE. 72

[187] Singh, S. & Bradley, L. Three-photon absorption in napthalene crystals by laser excitation. *Phys. Rev. Lett.* **12**, 612 (1964). 72

[188] Rentzepis, P., Mitschele, C. & Saxman, A. Measurement of ultrashort laser pulses by three-photon fluroescence. *Appl. Phys. Lett.* **17**, 122 (1970). 72

[189] Helmchen, F. & Denk, W. New developments in multiphoton microscopy. *Curr. Opin. Neurobiol.* **12**, 593 (2002). 72

[190] Denk, P. D. . W. W., W. *Handbook of Biological Confocal Microscopy*, chap. Two-photon molecular exciation in laser-scannign microscopy, 445–458 (Plenum Press, New York, 1995). 72

[191] Valleur, B. *Molecular Fluorescence* (Willey- VCH, 2002). 73

[192] Denk, W. Two-photon excitation in functional biological imaging. *J. Biomed. Opt.* **1**, 296 (1996). 74

[193] Gu, M. & Sheppard, C. Comparison of three-dimensional imaging properties between two-photon and single-photon fluorescence microscopy. *J. Microsc.* **177**, 128 (1995). 75

[194] Gauderon, R., Lukins, P. & Sheppard, J. Effect of a confocal pinhole in two-photon microscopy. *Microsc. Res. Techniq.* **47**, 210 (1999). 75

[195] Denk, W. Photon upmanship: Why multiphoton imaging is more than a gimmick. *Neuron* **18**, 351 (1997). 75

[196] Eggeling, C., Volkmer, A. & Seidel, C. A. M. Molecular photobleaching kinetics of rhodamine 6g by one- and two-photon induced confocal fluorescence microscopy. *ChemPhysChem* **6**, 791 (2005). URL `http://dx.doi.org/10.1002/cphc.200400509`. 77, 121

[197] Hopt, A. Highly nonlinear photodamage in two-photon fluorescence microscopy. *Biophys. J.* **80**, 2029 (2001). 77, 86

[198] König, K., So, P., Mantulin, W., Tromberg, B. & Gratton, E. Two-photon excited lifetime imaging of autofluorescence in cells during UVA and NIR photostress. *J. Microsc.* **183**, 197 (1996). 77

[199] König, K., Becker, T., Fischer, P., Riemann, I. & Halbhuber, K. Pulse-length dependence of cellular response to intense near-infrared laser pulses in multiphoton microscopes. *Opt. Lett.* **24**, 113 (1999). 77

[200] Sako, Y. *et al.* Comparison of two-photon excitation laser scanning microscopy with uv-confocal laser scanning microscopy in three-dimensional calcium imaging using the fluorescence indicator indo-1. *J. Microsc.* **185**, 9 (1997). 77

[201] Schönle, A. & Hell, S. Heating by absorption in the focus of an objective lens. *Opt. Lett.* **23**, 325 (1998). 77, 136

[202] Koester, H., Baur, D., Uhl, R. & Hell, S. Ca2+ fluorescence imaging with pico-and femtosecond two-photon excitation: signal and photodamage. *Biophys. J.* **77**, 2226 (1999). 77

[203] Herz, J. *et al.* Expanding two-photon intravital microscopy to the infrared by means of optical parametric oscillator. *Biophys. J.* **98**, 715 (2010). 77, 85

[204] Albota, M. *et al.* Design of organic molecules with large two-photon absorption cross sections. *Science* **281**, 1653 (1998). 78

[205] Xu, C. Multiphoton fluorescence excitation: New spectral windows for biological nonlinear microscopy. *P. Natl. Acad. Sci. USA* **93**, 10763 (1996). 78

[206] Mertz, J., Xu, C. & Webb, W. Single-molecule detection by two-photon-excited fluorescence. *Opt. Lett.* **20**, 2532 (1995). 79

[207] Sanchez, E., Novotny, L., Holtom, G. & Xie, X. Room-temperature fluorescence imaging and spectroscopy of single molecules by two-photon excitation. *J. Phys. Chem. A* **101**, 7019 (1997). 79

[208] Berland, K., So, P. & Gratton, E. Two-photon fluorescence correlation spectroscopy: method and application to the intracellular environment. *Biophys. J.* **68**, 694 (1995). 79

[209] Schwille, P., Haupts, U., Maiti, S. & Webb, W. Molecular dynamics in living cells observed by fluorescence correlation spectroscopy with one-and two-photon excitation. *Biophys. J.* **77**, 2251 (1999). 79

[210] Wang, X. *et al.* A chemically labeled cytotoxic agent: two-photon fluorophore for optical tracking of cellular pathway in chemotherapy. *P. Natl. Acad. Sci.* **96**, 11081 (1999). 79

[211] Gryczynski, I., Gryczynski, Z., Lakowicz, J., Yang, D. & Burke, T. Fluorescence spectral properties of the anticancer drug topotecan by steady-state and frequency domain fluorometry with one-photon and multi-photon excitation. *Photochem. Photobiol.* **69**, 421 (1999). 79

[212] Denk, W. Two-photon scanning photochemical microscopy: mapping ligand-gated ion channel distributions. *P. Natl. Acad. Sci.* **91**, 6629 (1994). 79

[213] Pettit, D., Wang, S., Gee, K. & Augustine, G. Chemical two-photon uncaging: a novel approach to mapping glutamate receptors. *Neuron* **19**, 465 (1997). 79

[214] Brown, E., Wu, E., Zipfel, W. & Webb, W. Measurement of molecular diffusion in solution by multiphoton fluorescence photobleaching recovery. *Biophys. J.* **77**, 2837 (1999). 79

[215] Denk, W., Holt, J., Shepherd, G. & Coreytt, D. Calcium imaging of single stereocilia in hair cells: localization of transduction channels at both ends of tip links. *Neuron* **15**, 1311 (1995). 79

[216] Maiti, S., Shear, J., Williams, R., Zipfel, W. & Webb, W. Measuring serotonin distribution in live cells with three-photon excitation. *Science* **275**, 530 (1997). 79

[217] König, K., Riemann, I. & Fritzsche, W. Nanodissection of human chromosomes with near-infrared femtosecond laser pulses. *Opt. Lett.* **26**, 819 (2001). 79, 86

[218] Cavey, M., Rauzi, M., Lenne, P. & Lecuit, T. A two-tiered mechanism for stabilization and immobilization of e-cadherin. *Nature* **453**, 751 (2008). 79

[219] Sinha, D. *et al.* Photocontrol of protein activity in cultured cells and zebrafish with one-and two-photon illumination. *ChemBioChem* **11**, 653 (2010). 79

[220] Centonze, V. E. & White, J. Multiphoton excitation provides optical sections from deeper within scattering specimens than confocal imaging. *Biophys. J.* **75**, 2015 (1998). 79

[221] Piston, D., Masters, B. & Webb, W. Three-dimensionally resolved NAD(P)H cellular metabolic redox imaging of the in situ cornea with two-photon excitation laser scanning microscopy. *J. Microsc.* **178**, 20 (1995). 79

[222] Denk, W. & Detwiler, P. B. Optical recording of light-evoked calcium signals in the functionally intact retina. *P. Natl. Acad. Sci.* **96**, 7035 (1999). URL `http://www.pnas.org/cgi/content/abstract/96/12/7035`. 79

[223] Masters, B., So, P. & Gratton, E. Optical biopsy of in vivo human skin: Multi-photon excitation microscopy. *Laser Med. Sci.* **13**, 196 (1998). 79

[224] Molitoris, B. & Sandoval, R. Intravital multiphoton microscopy of dynamic renal processes. *Am. J. Physiol.-Renal* **288**, F1084 (2005). 79

[225] Rubart, M. Two-photon microscopy of cells and tissue. *Circ. Res.* **95**, 1154 (2004). 79

[226] Fetcho, J. & O'Malley, D. Imaging neuronal networks in behaving animals. *Curr. Opin. Neurobiol.* **7**, 832 (1997). 79

[227] Denk, W., Delaney, K., Gelperin, A., Kleinfeld, D. & Strowbridge, B. Anatomical and functional imaging of neurons using 2-photon laser scanning microscopy. *J. Neurosci. Methods* **54**, 151 (1994). 79

[228] Squirrell, J., Wokosin, D., White, J. & Bavister, B. Long-term two-photon fluorescence imaging of mammalian embryos without compromising viability. *Nat. Technol.* **17**, 763 (1999). 79

[229] Bird, D. & Gu, M. Two-photon fluorescence endoscopy with a micro-optic scanning head. *Opt. Lett.* **28**, 1552 (2003). 79

[230] Jung, J. & Schnitzer, M. Multiphoton endoscopy. *Opt. Lett.* **28**, 902 (2003). 79

[231] Skoch, J., Hyckey, G., Kajdasz, S., Hyman, B. & Bacskai, B. In vivo imaging of amyloid-ß deposits in mouse brain with multiphoton microscopy. *Method. Mol. Biol.* **299**, 349 (2005). 79

[232] Bhawalkar, J., Kumar, N., Zhao, C. & Prasad, P. Two-photon photodynamic therapy. *J. Clin. Laser Med. Sur.* **15**, 201 (1997). 79

[233] Fine, S. & Hansen, W. Optical second harmonic generation in biological systems. *Appl. Optics* **10**, 2350 (1971). 80

[234] Campagnola, P. Shg microscopy for visualizing biomolecular arrays in cells, tissues and organisms. *Nat. Biotechnol.* **21**, 1356 (2003). 81, 82

[235] Mertz, J. & Moreaux, L. Second-harmonic generation by focused excitation of inhomogeneously distributed scatterers. *Opt. Commun.* **196**, 325 (2001). 81

[236] Moreaux, L. Membrane imaging by second-harmonic generation microscopy. *J. Opt. Soc. Am. B* **17**, 1685 (2000). 81, 82

[237] Mohler, W., Millard, A. & Campagnola, P. Second harmonic generation imaging of endogenous structural proteins. *Methods* **29**, 97 (2003). 81, 82

[238] Olivier, N. *et al.* Cell lineage reconstruction of early zebrafish embryos using label-free nonlinear microscopy. *Science* **329**, 967 (2010). 82, 139

[239] Franken, P., Hill, A., Peters, C. & Weinreich, G. Generation of optical harmonics. *Phys. Rev. Lett.* **7**, 118 (1961). 82

[240] Hellwarth, R. & Christensen, P. Nonlinear optical microscopic examination of structure in polycrystalline ZnSe. *Opt. Commun.* **12**, 318 (1974). 82

[241] Sheppard, C. & Choudhury, A. Image formation in the scanning microscope. *Opt. Acta* **24**, 1051 (1977). 82

[242] Gannaway, J. & Sheppard, C. Second-harmonic imaging in the scanning optical microscope. *Opt. Quant. Electron.* **10**, 435 (1978). 82

[243] Freund, I. & Deutsch, M. Second-harmonic microscopy of biological tissue. *Opt. Lett.* **11**, 91 (1986). 82

[244] Guo, Y. *et al.* Second-harmonic tomography of tissues. *Opt. Lett.* **22**, 1323 (1997). 82

[245] Campagnola, P. e. a. High-resolution nonlinear optical imaging of live cells by second harmonic generation. *Biophys. J.* **77**, 3341 (1999). 82

[246] Campagnola, P. J., Clark, H. A., Mohler, W. A., Lewis, A. & Loew, L. M. Second-harmonic imaging microscopy of living cells. *J. Biomed. Opt.* **6**, 277 (2001). 82

[247] Campagnola, P. *et al.* Three-dimensional high-resolution second-harmonic generation imaging of endogenous structural proteins in biological tissues. *Biophys. J.* **82**, 493 (2002). 82

[248] Zipfel, W. e. a. Live tissue intrinsic emission microscopy using multiphoton-excited native fluorescence and second harmonic generation. *P. Natl. Acad. Sci.* **100**, 7075 (2003). 82

[249] Zoumi, A. Imaging cells and extracellular matrix in vivo by using second-harmonic generation and two-photon excited fluorescence. *P. Natl. Acad. Sci.* **99**, 11014 (2002). 82

[250] Vanzi, F., Sacconi, L., Cicchi, R. & Pavone, F. Protein conformation and molecular order probed by second-harmonic-generation microscopy. *J. Biomed. Opt.* **17**, 060901 (2012). 82

[251] Dempsey, W., Fraser, S. & Pantazis, P. SHG nanoprobes: Advancing harmonic imaging in biology. *BioEssays* **34**, 351 (2012). 82

[252] Zielinski, M., Oron, D., Chauvat, D. & Zyss, J. Second-harmonic generation from a single core/shell quantum dot. *Small* **5**, 2835 (2009). 82

[253] Pantazis, P., Maloney, J., Wu, D. & Fraser, S. Second harmonic generating (SHG) nanoprobes for in vivo imaging. *P. Natl. Acad. Sci.* **107**, 14535 (2010). 82

[254] Barad, Y., Eisenberg, H., Horowitz, M. & Silberberg, Y. Nonlinear scanning laser microscopy by third harmonic generation. *Appl. Phys. Lett.* **70**, 922 (1997). 82

[255] Squier, J., Muller, M., Brakenhoff, G. & Wilson, K. Third harmonic generation microscopy. *Opt. Express* **3**, 315 (1998). 82

[256] Yelin, D., Oron, D., Korkotian, E., Segal, M. & Silberberg, Y. Third-harmonic microscopy with a titanium–sapphire laser. *Appl. Phys. B- Lasers O.* **74**, 97 (2002). 82

[257] Oron, D. *et al.* Depth-resolved structural imaging by third-harmonic generation microscopy. *J. Struct. Biol.* **147**, 3 (2004). 82

[258] Aviles-Espinosa, R. *et al.* Third-harmonic generation for the study of caenorhabditis elegans embryogenesis. *J. Biomed. Opt.* **15**, 046020 (2010). 82

[259] Duncan, M., Reintjes, J. & Manuccia, T. Scanning coherent anti-stokes raman microscope. *Opt. Lett.* **7**, 350 (1982). 83

[260] Oheim, M., Michael, D., Geisbauer, M., Madsen, D. & Chow, R. Principles of two-photon excitation fluorescence microscopy and other nonlinear imaging approaches. *Adv. Drug Deliver. Rev.* **58**, 788 (2006). 83

[261] Boyd, R. & Masters, B. *Biomedical Nonlinear Optical Microscopy*, chap. Nonlinear Optical Spectroscopy, 85–90 (Oxford University Press, 2008). 83

[262] Zumbusch, A., Holtom, G. & Xie, X. Three-dimensional vibrational imaging by coherent anti-stokes raman scattering. *Phys. Rev. Lett.* **82**, 4142 (1999). 83

[263] Cheng, J., Volkmer, A. & Xie, X. Theoretical and experimental characterization of coherent anti-stokes raman scattering microscopy. *J. Opt. Soc. Am. B* **19**, 1363 (2002). 83

[264] Wang, H., Fu, Y., Zickmund, P., Shi, R. & Cheng, J. Coherent anti-stokes raman scattering imaging of axonal myelin in live spinal tissues. *Biophys. J.* **89**, 581 (2005). 83

[265] X. Sunney Xie, J. C. & Potma, E. *Handbook of Biological Confocal Microscopy*, chap. Coherent Anti-Stokes Raman Scattering Microscopy, 595–606 (Springer, 2006), 3rd edn. 83

[266] Reid, D., Sun, J., Lamour, T. & Ferreiro, T. Advances in ultrafast optical parametric oscillators. *Laser Phys. Lett.* **8**, 8 (2011). 83

[267] Cerullo, G. & De Silvestri, S. Ultrafast optical parametric amplifiers. *Re. Sci. Instrum.* **74**, 1 (2003). 83

[268] Gratton, E. & vande Ven, M. J. *Handbook of Biological Confocal Microscopy*, chap. Laser Sources for Confocal Microscopy, 80–125 (Springer, 2006), 3rd edn. 83

[269] Theer, P., Hasan, M. & Denk, W. Two-photon imaging to a depth of 1000 µm in living brains by use of a ti: Al< sub> 2</sub> o< sub> 3</sub> regenerative amplifier. *Opt. Lett.* **28**, 1022 (2003). 84, 86, 135

[270] Beaurepaire, E. Ultra-deep two-photon fluorescence excitation in turbid media. *Opt. Commun.* **188**, 25 (2001). 84

[271] Sakadžic, S. *et al.* Multi-photon microscopy with a low-cost and highly efficient cr: Licaf laser. *Opt. Express* **16**, 20848 (2008). 84

[272] Andresen, V. *et al.* Infrared multiphoton microscopy: subcellular-resolved deep tissue imaging. *Curr. Opin. Biotech.* **20**, 54 (2009). 85, 99, 131

[273] Mojzisova, H. & Vermot, J. When multiphoton microscopy sees near infrared. *Curr. Opin. Genet. Dev.* **21**, 549 (2011). 85

[274] Shcherbo, D. *et al.* Near-infrared fluorescent proteins. *Nat. Methods* **7**, 827 (2010). 85

[275] Lin, M. Beyond the rainbow: new fluorescent proteins brighten the infrared scene. *Nat. Methods* **8**, 726 (2011). 85

[276] Shu, X. *et al.* Mammalian expression of infrared fluorescent proteins engineered from a bacterial phytochrome. *Science* **324**, 804 (2009). 85

[277] Vadakkan, T., Culver, J., Gao, L., Anhut, T. & Dickinson, M. Peak multiphoton excitation of mcherry using an optical parametric oscillator (opo). *J. Fluoresc.* **19**, 1103 (2009). 85

[278] Kredel, S. *et al.* mruby, a bright monomeric red fluorescent protein for labeling of subcellular structures. *PLOS* **4**, e4391 (2009). 85

[279] Kobat, D. *et al.* Deep tissue multiphoton microscopy using longer wavelength excitation. *Opt. Express* **17**, 13354 (2009). 85, 136

[280] Jacobsen, H., Hänninen, P., Soini, E. & Hell, S. Refractive-index-induced aberrations in two-photon confocal fluorescence microscopy. *J. Microsc.* **176**, 226 (1994). 85

[281] de Grauw, C., Vroom, J., van der Voort, H. & Gerritsen, H. Imaging properties in two-photon excitation microscopy and effects of refractive-index mismatch in thick specimens. *Appl. Optics* **38**, 5995 (1999). 85

[282] Gerritsen, H. & De Grauw, C. Imaging of optically thick specimen using two-photon excitation microscopy. *Microsc. Res. Techniq.* **47**, 206 (1999). 85, 86, 149

[283] Wiersma, S. & Visser, T. Defocusing of a converging electromagnetic wave by a plane dielectric interface. *J. Opt. Soc. Am. A* **13**, 320 (1996). 86, 156

[284] de Grauw, C., Vroom, J., van der Voort, H. & Gerritsen, H. Imaging properties in two-photon excitation microscopy and effects of refractive-index mismatch in thick specimens. *Appl. Optics* **38**, 5995 (1999). 86

[285] Dunn, A., Wallace, V., Coleno, M., Berns, M. & Tromberg, B. Influence of optical properties on two-photon fluorescence imaging in turbid samples. *Appl. Optics* **39**, 1194 (2000). 86

[286] Booth, M. & Wilson, T. Refractive-index-mismatch induced aberrations in single-photon and two-photon microscopy and the use of aberration correction. *J. Biomed. Opt.* **6**, 266 (2001). 86

[287] Dong, C., Koenig, K. & So, P. Characterizing point spread functions of two-photon fluorescence microscopy in turbid medium. *J. Biomed. Opt.* **8**, 450 (2003). 86

[288] Dong, C., Yu, B., Kaplan, P. & So, P. Performances of high numerical aperture water and oil immersion objective in deep-tissue, multi-photon microscopic imaging of excised human skin. *Microsc. Res. Techniq.* **63**, 81 (2004). 86

[289] Schwertner, M., Booth, M. & Wilson, T. Characterizing specimen induced aberrations for high na adaptive optical microscopy. *Opt. Express* **12**, 6540 (2004). 86, 87, 134, 139

[290] Keatings, S., Zhang, W. & McConnell, G. Characterization of microscope objective lenses from 1,400 to 1,650 nm to evaluate performance for long-wavelength nonlinear microscopy applications. *Microsc. Res. Techniq.* **71**, 517 (2008). 86

[291] König, K. Multiphoton microscopy in life sciences. *J. Microsc.* **200**, 83 (2000). 86

[292] Tung, C. *et al.* Effects of objective numerical apertures on achievable imaging depths in multiphoton microscopy. *Microsc. Res. Techniq.* **65**, 308 (2004). 86

[293] Lo, W. Spherical aberration correction in multiphoton fluorescence imaging using objective correction collar. *J. Biomed. Opt.* **10**, 034006 (2005). 87

[294] Muriello, P. & Dunn, K. Improving signal levels in intravital multiphoton microscopy using an objective correction collar. *Opt. Commun.* **281**, 1806 (2008). 87, 139

[295] Rueckel, M., Mack-Bucher, J. & Denk, W. Adaptive wavefront correction in two-photon microscopy using coherence-gated wavefront sensing. *P. Natl. Acad. Sci.* **103**, 17137 (2006). 87, 139

[296] Cha, J., Ballesta, J. & So, P. Shack-hartmann wavefront-sensor-based adaptive optics system for multiphoton microscopy. *J. Biomed. Opt.* **15**, 046022 (2010). 87, 134, 139

[297] Ji, N., Milkie, D. & Betzig, E. Adaptive optics via pupil segmentation for high-resolution imaging in biological tissues. *Nat. Methods* **7**, 141 (2009). 87

[298] Débarre, D. *et al.* Image-based adaptive optics for two-photon microscopy. *Opt. Lett.* **34**, 2495 (2009). 87, 134, 139

[299] Olivier, N., Débarre, D. & Beaurepaire, E. Dynamic aberration correction for multiharmonic microscopy. *Opt. Lett.* **34**, 3145 (2009). 88, 132, 134

[300] Leray, A. & Mertz, J. Rejection of two-photon fluorescence background in thick tissue by differential aberration imaging. *Opt. Express* **14**, 10565 (2006). 88, 139

[301] Aviles-Espinosa, R. *et al.* Measurement and correction of in vivo sample aberrations employing a nonlinear guide-star in two-photon excited fluorescence microscopy. *Biomedical optics express* **2**, 3135 (2011). 88, 135, 136, 139

[302] Azucena, O. *et al.* Adaptive optics wide-field microscopy using direct wavefront sensing. *Opt. Lett.* **36**, 825 (2011). 88, 136

[303] Tao, X. *et al.* Adaptive optics confocal microscopy using direct wavefront sensing. *Opt. Lett.* **36**, 1062 (2011). 88, 136

[304] Dashkevich, V. *et al.* Tunable optical parametric oscillator based on a ktp crystal, pumped by a pulsed ti 3+: Al 2 o 3 laser. *J. Appl. Spectrosc.* **74**, 390 (2007). 92

[305] Opti (2011). URL `http://www.opli.net/magazine/eo/2011/news/boston_mm_sp.aspx`. 94

[306] Invitrogen. URL `http://probes.invitrogen.com/media/pis/mp36909.pdf`. 97

[307] Pawley, J. *Handbook of biological confocal microscopy*, chap. Multifocal Multi-Photon Microscopy, 550–559 (Springer, 2006), 3rd edn. 97

[308] Pawley, J. *Handbook of biological confocal microscopy*, chap. Interaction of Light with Botanical Specimens, 414–442 (Springer, 2006), 3rd edn. 97

[309] Halbout, J., Blit, S., Donaldson, W. & Tang, C. Efficient phase-matched second-harmonic generation and sum-frequency mixing in urea. *IEEE J. Quantum Elect.* **15**, 1176 (1979). 98

[310] Bäuerle, D., Betzler, K., Hesse, H., Kapphan, S. & Loose, P. Phase-matched second harmonic generation in urea. *Phys. Status Solidi A* **42**, K119 (1977). 98

[311] Tsien, R. Y. Excitation and emission spectra of dyes. Laboratory website. URL `http://www.tsienlab.ucsd.edu/`. 98

[312] Timpson, P. *et al.* Organotypic collagen i assay: A malleable platform to assess cell behaviour in a 3-dimensional context. *J. Vis. Exp.* **56**, e3089 (2011). 98, 99

[313] Shaner, N. *et al.* Improved monomeric red, orange and yellow fluorescent proteins derived from discosoma sp. red fluorescent protein. *Nat. Biotechnol.* **22**, 1567 (2004). 99

[314] Bueno, J., Gualda, E. & Artal, P. Adaptive optics multiphoton microscopy to study ex vivo ocular tissues. *J. Biomed. Opt.* **15**, 066004 (2010). 134, 139

[315] Balu, M. *et al.* Effect of excitation wavelength on penetration depth in nonlinear optical microscopy of turbid media. *J. Biomed. Opt.* **14**, 010508 (2009). 135

[316] Liu, Y., Kim, Y. & Backman, V. Development of a bioengineered tissue model and its application in the investigation of the depth selectivity of polarization gating. *Appl. Optics* **44**, 2288 (2005). 135

[317] Liu, Y. *et al.* Evidence for localized cell heating induced by infrared optical tweezers. *Biophys. J.* **68**, 2137 (1995). 136

[318] Norris, G., Amor, R., Dempster, J., Amos, W. & McConnell, G. A promising new wavelength region for three-photon fluorescence microscopy of live cells. *J. Microsc.* **246**, 266 (2012). 136

[319] Yang, P. *et al.* Test and analysis of the time and space characteristics of phase aberration in a diode-side-pumped nd: Yag laser. In *Proc. SPIE*, vol. 6018, 60180M (2005). 136

[320] Bueno, J., Vohnsen, B., Roso, L. & Artal, P. Temporal wavefront stability of an ultrafast high-power laser beam. *Appl. Optics* **48**, 770 (2009). 136

[321] Lubeigt, W., Valentine, G. & Burns, D. Enhancement of laser performance using an intracavity deformable membrane mirror. *Opt. Express* **16**, 10943 (2008). 136

[322] Lubeigt, W. *et al.* Search-based active optic systems for aberration correction in time-independent applications. *Appl. Optics* **49**, 307 (2010). 136

[323] Vargas, G., Chan, E., Barton, J., Rylander, H. & Welch, A. Use of an agent to reduce scattering in skin. *Laser Surg. Med.* **24**, 133 (1999). 138, 185

[324] Ashkin, A. Optical trapping and manipulation of neutral particles using lasers. *P. Natl. Acad. Sci.* **94**, 4853 (1997). 140

[325] Neuman, K. & Block, S. Optical trapping. *Re. Sci. Instrum.* **75**, 2787 (2004). 140, 145, 154

[326] Ashkin, A. & Dziedzic, J. Optical levitation by radiation pressure. *Appl. Phys. Lett.* **19**, 283 (1971). 140

[327] Ashkin, A. Acceleration and trapping of particles by radiation pressure. *Phys. Rev. Lett.* **24**, 156 (1970). URL `http://link.aps.org/doi/10.1103/PhysRevLett.24.156`. 140

[328] Ashkin, A., Dziedzic, J., Bjorkholm, J. & Chu, S. Observation of a single-beam gradient force optical trap for dielectric particles. *Opt. Lett.* **11**, 288 (1986). 140

[329] Stevenson, D., Gunn-Moore, F. & Dholakia, K. Light forces the pace: optical manipulation for biophotonics. *J. Biomed. Opt.* **15**, 041503 (2010). 141

[330] Lang, M. & Block, S. Resource letter: Lbot-1: Laser-based optical tweezers. *Am. J. Phys.* **71**, 201 (2003). 141

[331] Čižmár, T., Mazilu, M. & Dholakia, K. In situ wavefront correction and its application to micromanipulation. *Nat. Photonics* **4**, 388 (2010). 141, 149

[332] Ashok, P. & Dholakia, K. Optical trapping for analytical biotechnology. *Curr. Opin. Biotech.* **23**, 16 (2011). 141, 148

[333] Liang, H., Wright, W., Cheng, S., He, W. & Berns, M. Micromanipulation of chromosomes in ptk2 cells using laser microsurgery (optical scalpel) in combination with laser-induced optical force (optical tweezers). *Exp. Cell Res.* **204**, 110 (1993). 141

[334] Mcleod, E. & Arnold, C. Subwavelength direct-write nanopatterning using optically trapped microspheres. *Nat. Nanotechnol.* **3**, 413 (2008). 141

[335] Kawata, S., Sun, H., Tanaka, T. & Takada, K. Finer features for functional microdevices. *Nature* **412**, 697 (2001). 141

[336] Jonáš, A. & Zemánek, P. Light at work: the use of optical forces for particle manipulation, sorting, and analysis. *Electrophoresis* **29**, 4813 (2008). 141

[337] Brau, R. *et al.* Passive and active microrheology with optical tweezers. *J. Opt. A - Pure Appl. Op.* **9**, S103 (2007). 141

[338] Grier, D. A revolution in optical manipulation. *Nature* **424**, 810 (2003). 141

[339] Svoboda, K. & Block, S. Biological applications of optical forces. *Annu. Rev. Bioph. Biom.* **23**, 247 (1994). 141, 173

[340] Molloy, J. & Padgett, M. Lights, action: optical tweezers. *Contemp. Phys,* **43**, 241 (2002). 141, 143, 144, 146

[341] Chiou, A. *et al.* Optical trapping and manipulation for biomedical applications. *Biophotonics* 249 (2008). 141

[342] Malagnino, N., Pesce, G., Sasso, A. & Arimondo, E. Measurements of trapping efficiency and stiffness in optical tweezers. *Opt. Commun.* **214**, 15 (2002). 141, 145, 172, 173, 178

[343] Friese, M., Rubinsztein-Dunlop, H., Heckenberg, N. & Dearden, E. Determination of the force constant of a single-beam gradient trap by measurement of backscattered light. *Appl. Optics* **35**, 7112 (1996). 144

[344] Rohrbach, A. Stiffness of optical traps: quantitative agreement between experiment and electromagnetic theory. *Phys. Rev. Lett.* **95**, 168102 (2005). 145, 155, 165

[345] Singer, W., Bernet, S., Hecker, N. & Ritsch-Marte, M. Three-dimensional force calibration of optical tweezers. *J. Mod. Optic.* **47**, 2921 (2000). 146, 147, 171, 172

[346] Ermilov, S. & Anvari, B. Dynamic measurements of transverse optical trapping force in biological applications. *Ann. Biomed. Eng.* **32**, 1016 (2004). 146

[347] Berg-Sørensen, K. & Flyvbjerg, H. Power spectrum analysis for optical tweezers. *Re. Sci. Instrum.* **75**, 594 (2009). 147, 171

[348] Wright, W., Sonek, G. & Berns, M. Parametric study of the forces on microspheres held by optical tweezers. *Appl. Optics* **33**, 1735 (1994). 147, 155

[349] d'Helon, C., Dearden, E., Rubinsztein-Dunlop, H. & Heckenberg, N. Measurement of the optical force and trapping range of a single-beam gradient optical trap for micron-sized latex spheres. *J. Mod. Optic.* **41**, 595 (1994). 147

[350] Visscher, K., Brakenhoff, G. & Krol, J. Micromanipulation by Şmultiple Ť optical traps created by a single fast scanning trap integrated with the bilateral confocal scanning laser microscope. *Cytometry* **14**, 105 (1993). 147

[351] Čižmár, T., Dalgarno, H., Ashok, P., Gunn-Moore, F. & Dholakia, K. Optical aberration compensation in a multiplexed optical trapping system. *J. Opt.* **13**, 044008 (2011). 147, 149

[352] Fällman, E. & Axner, O. Design for fully steerable dual-trap optical tweezers. *Appl. Optics* **36**, 2107 (1997). 147

[353] Mio, C., Gong, T., Terray, A. & Marr, D. Design of a scanning laser optical trap for multiparticle manipulation. *Re. Sci. Instrum.* **71**, 2196 (2000). 147

[354] Reicherter, M., Haist, T., Wagemann, E. & Tiziani, H. Optical particle trapping with computer-generated holograms written on a liquid-crystal display. *Opt. Lett.* **24**, 608 (1999). 147

[355] Hayasaki, Y., Itoh, M., Yatagai, T. & Nishida, N. Nonmechanical optical manipulation of microparticle using spatial light modulator. *Opt. Rev.* **6**, 24 (1999). 147

[356] Curtis, J., Koss, B. & Grier, D. Dynamic holographic optical tweezers. *Opt. Commun.* **207**, 169 (2002). 147

[357] Liesener, J., Reicherter, M., Haist, T. & Tiziani, H. Multi-functional optical tweezers using computer-generated holograms. *Opt. Commun.* **185**, 77 (2000). 147

[358] Gahagan, K. & Swartzlander, G., Jr. Optical vortex trapping of particles. *Opt. Lett.* **21**, 827 (1996). 148

[359] Dholakia, K. & Čižmár, T. Shaping the future of manipulation. *Nat. Photonics* **5**, 335 (2011). 148

[360] Heckenberg, N., McDuff, R., Smith, C. & White, A. Generation of optical phase singularities by computer-generated holograms. *Opt. Lett* **17**, 221 (1992). 148

[361] Heckenberg, N., McDuff, R., Smith, C., Rubinsztein-Dunlop, H. & Wegener, M. Laser beams with phase singularities. *Opt. Quant. Electron.* **24**, 951 (1992). 148

[362] O'Neil, A., MacVicar, I., Allen, L. & Padgett, M. Intrinsic and extrinsic nature of the orbital angular momentum of a light beam. *Phys. Rev. Lett.* **88**, 53601 (2002). 148

[363] Simpson, N., Dholakia, K., Allen, L. & Padgett, M. Mechanical equivalence of spin and orbital angular momentum of light: an optical spanner. *Opt. Lett.* **22**, 52 (1997). 148

[364] Sato, S., Ishigure, M. & Inaba, H. Optical trapping and rotational manipulation of microscopic particles and biological cells using higher-order mode nd: Yag laser beams. *Electron. Lett.* **27**, 1831 (1991). 148

[365] Padgett, M. & Bowman, R. Tweezers with a twist. *Nat. Photonics* **5**, 343 (2011). 148

[366] Galajda, P. & Ormos, P. Complex micromachines produced and driven by light. *Appl. Phys. Lett.* **78**, 249 (2001). 148

[367] Arlt, J., Garces-Chavez, V., Sibbett, W. & Dholakia, K. Optical micromanipulation using a bessel light beam. *Opt. Commun.* **197**, 239 (2001). 148

[368] Garcés-Chávez, V., McGloin, D., Melville, H., Sibbett, W. & Dholakia, K. Simultaneous micromanipulation in multiple planes using a self-reconstructing light beam. *Nature* **419**, 145 (2002). 148

[369] Mazilu, M., Stevenson, D., Gunn-Moore, F. & Dholakia, K. Light beats the spread:Ş non-diffractingŢ beams. *Laser Photonics Rev.* **4**, 529 (2010). 148

[370] Visscher, K. & Brakenhoff, G. Single beam optical trapping integrated in a confocal microscope for biological applications. *Cytometry* **12**, 486 (1991). 148

[371] Ghislain, L. & Webb, W. Scanning-force microscope based on an optical trap. *Opt. Lett.* **18**, 1678 (1993). 148

[372] Liu, Y., Sonek, G., Berns, M., Konig, K. & Tromberg, B. Two-photon fluorescence excitation in continuous-wave infrared optical tweezers. *Opt. Lett.* **20**, 2246 (1995). 148

[373] Berns, M., Tadir, Y., Liang, H. & Tromberg, B. Laser scissors and tweezers. *Method. Cell Biol.* **55**, 71 (1997). 148

[374] Block, S., Blair, D. & Berg, H. Compliance of bacterial flagella measured with optical tweezers. *Nature* **338**, 514 (1989). 148

[375] Simmons, R., Finer, J., Chu, S. & Spudich, J. Quantitative measurements of force and displacement using an optical trap. *Biophys. J.* **70**, 1813 (1996). 148

[376] Svoboda, K., Schmidt, C., Schnapp, B., Block, S. *et al.* Direct observation of kinesin stepping by optical trapping interferometry. *Nature* **365**, 721 (1993). 148

[377] Finer, J., Simmons, R., Spudich, J. *et al.* Single myosin molecule mechanics: piconewton forces and nanometre steps. *Nature* **368**, 113 (1994). 148

[378] Wang, M., Yin, H., Landick, R., Gelles, J. & Block, S. Stretching DNA with optical tweezers. *Biophys. J.* **72**, 1335 (1997). 148

[379] Ramser, K. & Hanstorp, D. Optical manipulation for single-cell studies. *J. Biophotonics* **3**, 187 (2010). 148

[380] Ashkin, A. History of optical trapping and manipulation of small-neutral particle, atoms, and molecules. *IEEE J. Sel. Top. Quant.* **6**, 841 (2002). 148

[381] Roichman, Y., Waldron, A., Gardel, E. & Grier, D. Optical traps with geometric aberrations. *Appl. Optics* **45**, 3425 (2006). 149, 175

[382] Ghislain, L., Switz, N. & Webb, W. Measurement of small forces using an optical trap. *Re. Sci. Instrum.* **65**, 2762 (1994). 149, 155, 170, 172, 173, 178

[383] Felgner, H., Müller, O. & Schliwa, M. Calibration of light forces in optical tweezers. *Appl. Optics* **34**, 977 (1995). 149, 173

[384] Rohrbach, A. & Stelzer, E. Trapping forces, force constants, and potential depths for dielectric spheres in the presence of spherical aberrations. *Appl. Optics* **41**, 2494 (2002). 149, 172, 178

[385] Fällman, E. & Axner, O. Influence of a glass-water interface on the on-axis trapping of micrometer-sized spherical objects by optical tweezers. *Appl. Optics* **42**, 3915 (2003). 149

[386] Vermeulen, K., Wuite, G., Stienen, G. & Schmidt, C. Optical trap stiffness in the presence and absence of spherical aberrations. *Appl. Optics* **45**, 1812 (2006). 149, 171, 172, 178

[387] Ota, T. *et al.* Enhancement of laser trapping force by spherical aberration correction using a deformable mirror. *Jpn. J. Appl. Phys.* **42**, 701 (2003). 150, 173, 178

[388] Nader, S., Reihani, S. & Oddershede, L. Optimizing immersion media refractive index improves optical trapping by compensating spherical aberrations. *Opt. Lett.* **32**, 1998 (2007). 150, 174, 178

[389] Ke, P. & Gu, M. Characterization of trapping force in the presence of spherical aberration. *J. Mod. Optic.* **45**, 2159 (1998). 150, 173, 174, 178

[390] Nader, S., Reihani, S., Charsooghi, M., Khalesifard, H. & Golestanian, R. Efficient in-depth trapping with an oil-immersion objective lens. *Opt. Lett.* **31**, 766 (2006). 150, 174, 178

[391] Hajizadeh, F. & S Reihani, S. Optimized optical trapping of gold nanoparticles. *Opt. Express* **18**, 551 (2010). 150

[392] Hansen, P., Bhatia, V., Harrit, N. & Oddershede, L. Expanding the optical trapping range of gold nanoparticles. *Nano Lett.* **5**, 1937 (2005). 150

[393] Wulff, K. *et al.* Aberration correction in holographic optical tweezers. *Opt. Express* **14**, 4169 (2006). 155, 168, 177, 178

[394] Bowman, R., Wright, A. & Padgett, M. An slm-based shack–hartmann wavefront sensor for aberration correction in optical tweezers. *J. Opt.* **12**, 124004 (2010). 155

[395] Török, P. & Kao, F. *Optical imaging and microscopy: techniques and advanced systems*, vol. 87 (Springer Verlag, 2003). 158

[396] Florin, E., Pralle, A., Stelzer, E. & H
"orber, J. Photonic force microscope calibration by thermal noise analysis. *Appl. Phys. A-Mater.* **66**, 75 (1998). 161, 173, 178

[397] Gibson, G., Leach, J., Keen, S., Wright, A. & Padgett, M. Measuring the accuracy of particle position and force in optical tweezers using high-speed video microscopy. *Opt. Express* **16**, 14561 (2008). 161

[398] Cheezum, M., Walker, W. & Guilford, W. Quantitative comparison of algorithms for tracking single fluorescent particles. *Biophys. J.* **81**, 2378 (2001). 161

[399] Anderson, C., Georgiou, G., Morrison, I., Stevenson, G. & Cherry, R. Tracking of cell surface receptors by fluorescence digital imaging microscopy using a charge-coupled device camera. low-density lipoprotein and influenza virus receptor mobility at 4 degrees c. *J. Cell Sci.* **101**, 415 (1992). 162

[400] Leach, J. *et al.* Comparison of faxen's correction for a microsphere translating or rotating near a surface. *Phys. Rev. E* **79**, 026301 (2009). URL `http://eprints.gla.ac.uk/32620/`. 170, 171

[401] Inouye, Y., Shoji, S., Furukawa, H., Nakamura, O. & Kawata, S. Pico-newton friction force measurements using a laser-trapped microsphere. *Jpn. J. Appl. Phys.* **37**, L684 (1998). 170

[402] Polin, M., Ladavac, K., Lee, S., Roichman, Y. & Grier, D. Optimized holographic optical traps. *Opt. Express* **13**, 5831 (2005). 173, 178

[403] Dienerowitz, M., Gibson, G., Bowman, R. & Padgett, M. Holographic aberration correction: optimising the stiffness of an optical trap deep in the sample. *Opt. Express* **19**, 24589 (2011). 174, 178

[404] Hovhannisyan, V., Su, P. & Dong, C. Characterization of optical-aberration-induced lateral and axial image inhomogeneity in multiphoton microscopy. *J. Biomed. Opt.* **13**, 044023 (2008). 177, 184

[405] Potsaid, B., Finger, F. & Wen, J. Automation of challenging spatial-temporal biomedical observations with the adaptive scanning optical microscope (asom). *Automation Science and Engineering, IEEE Transactions on* **6**, 525 (2009). 184

[406] Rivera, L., Potsaid, B. & Wen, J. Image tracking of multiple c. elegans worms using adaptive scanning optical microscope (asom). *Int. J. Optomechatron.* **4**, 1 (2010). 184

[407] Zou, W., Qi, X. & Burns, S. Wavefront-aberration sorting and correction for a dual-deformable-mirror adaptive-optics system. *Opt. Lett.* **33**, 2602 (2008). 185

[408] Chen, D., Jones, S., Silva, D. & Olivier, S. High-resolution adaptive optics scanning laser ophthalmoscope with dual deformable mirrors. *J. Opt. Soc. Am. A* **24**, 1305 (2007). 185

[409] Hell, S. W. Toward fluorescence nanoscopy (2003). 185

[410] Huang, D. *et al.* Optical coherence tomography. *Science* **254**, 1178 (1991). 185

[411] Hermann, B. *et al.* Adaptive-optics ultrahigh-resolution optical coherence tomography. *Opt. Lett.* **29**, 2142 (2004). 185

Appendices

Appendix A

Zernike Coefficients

The general formulation for the Zernike polynomials in radial coordinates with radius ρ and angle θ is given by:

$$Z_n^m(\rho,\theta) = \begin{cases} R_n^{|m|}(\rho)\cdot cos(m\theta) & \text{for } m \geq 0 \\ R_n^{|m|}(\rho)\cdot sin(m\theta) & \text{for } m < 0 \end{cases} \tag{A.1}$$

where n and m represent the radial order and azimuthal frequency respectively, and the term R_n^m which only depends on the radius ρ:

$$R_n^m(\rho) = \sum_{i=0}^{\frac{n-m}{2}} \frac{(-1)^i(n-i)!}{i!(\frac{n+m}{2}-i!)(\frac{n-m}{2}-i!)} \cdot \rho^{n-2i} \tag{A.2}$$

The mathematical notation of the Zernike polynomials up to the 4th order are presented in table A.1 while an illustration is given in Figure A.1. The last column gives the colloquial name for the respective aberration. Here, n and m represent the radial order and azimuthal frequency respectively, with

$$n, m \in \mathbb{N} \tag{A.3a}$$
$$n \geq m \tag{A.3b}$$
$$n - m = even \tag{A.3c}$$

In literature Zernike polynomials can also often be found with one index k. The change of indexation follows the equation

$$k = \frac{1}{2}(n(n+2)+m) \tag{A.4}$$

Table A.1: The Zernike polynomials up the 4th radial order.

Order n	Frequency m	Z_n^m	Z_k	$Z_k(\rho,\theta)$	aberration
0	0	Z_0^0	Z_0	1	piston
1	1	Z_1^1	Z_1	$2\rho\sin(\theta)$	y-axis tilt
	-1	Z_1^{-1}	Z_2	$2\rho\cos(\theta)$	x-axis tilt
2	2	Z_2^2	Z_3	$\sqrt{6}\,\rho^2\sin(2\theta)$	astigm. $\pm 45°$
	0	Z_2^0	Z_4	$\sqrt{3}\,(2\rho^2-1)$	defocus
	-2	Z_2^{-2}	Z_5	$\sqrt{6}\,\rho^2\cos(2\theta)$	astigm. $0°/90°$
3	3	Z_3^3	Z_6	$\sqrt{8}\,\rho^3\sin(3\theta)$	trefoil $30°$
	1	Z_3^1	Z_7	$\sqrt{8}\,(3\rho^3-2\rho)\sin\theta$	y-axis coma
	-1	Z_3^{-1}	Z_8	$\sqrt{8}\,(3\rho^3-2\rho)\cos\theta$	x-axis coma
	-3	Z_3^{-3}	Z_9	$\sqrt{8}\,\rho^3\cos(3\theta)$	trefoil $0°$
4	4	Z_4^4	Z_{10}	$\sqrt{10}\,\rho^4\sin(4\theta)$	
	2	Z_4^2	Z_{11}	$\sqrt{10}\,(4\rho^4-3\rho^2\sin(2\theta)$	2^{nd} order astigm. $0°$
	0	Z_4^0	Z_{12}	$\sqrt{5}\,(6\rho^4-6\rho^2+1)$	spherical aberration
	-2	Z_4^{-2}	Z_{13}	$\sqrt{10}\,(4\rho^4-3\rho^2\cos(2\theta)$	2^{nd} order astigm. $45°$
	-4	Z_4^{-4}	Z_{14}	$\sqrt{10}\,\rho^4\cos(4\rho)$	

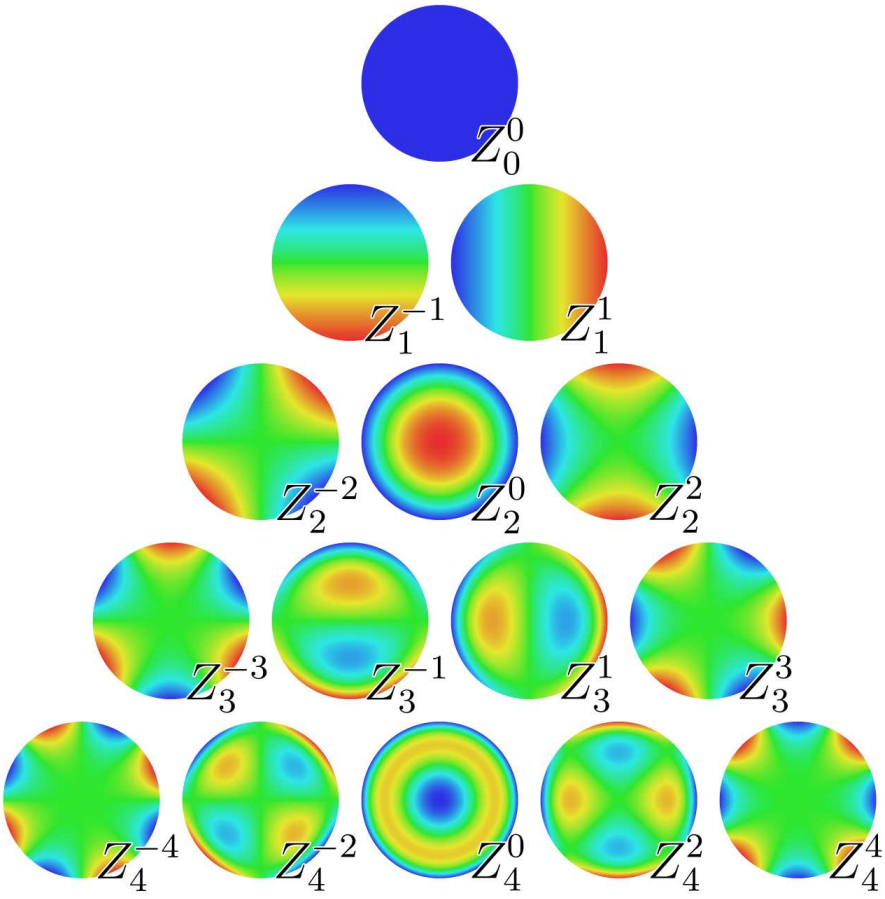

Figure A.1: Illustration of the Zernike polynomials up to the 4th order.

Appendix B

Edge Spread Function

The fitting of ESF was done according to Boone *et al.* [45] with the following function:

$$\mathrm{ESF}(x) = e + f\left\langle a\left\{1 - \exp\left(-b\left|x - x_0\right|\right)\right\} + c \cdot \mathrm{erf}(\sqrt{d}\left|x - x_0\right|)\right\rangle \qquad \text{(B.1)}$$

where $\langle\rangle$ denotes the absolute value. In this work, a purely Gaussian line spread function and thus an error function for the edge spread function was adequate to describe the blurring properties of the system. The fitting was performed with OriginPro and required a set of proper initial values for all parameters. The following is the user-defined function that was used in commercial curve fitting software:

```
double F1,F2,F3,F4,F5,F6;
F1=(x-g)*0.025;
F2=abs(F1);
F3=a*(1.0-exp(-F2*b));
F4=c*erf(F2*sqrt(d));
F5=F3+F4;
if(F1<=0)
F6=-F5;
else
F6=F5;
y=e+f*F6;
```

where F1-F6 are intermediary values in the routine. While seven parameters are used in the fitting procedure of the ESF (**a,b,c,d,e,f** and **g**) only four of these influence the shape of the LSF and the MTF (*i.e.* parameters a,b,c,d). The meaning and unit of each fitting parameter are given in table B.1. The value of 0.025 in F1 corresponds to the sampling interval (in µm) between each point in the x-axis and was adjusted for each digital zoom setting and scanning direction.

The LSF was then calculated with the fitting parameters obtained from the ESF fitting with the following analytical equation comprised of the weighted sum of exponential and Gaussian functions:

Table B.1: Fitting parameters for the ESF according to Boone *et al.* [45].

parameter	meaning	unit
a	amplitude of exponential	a.u.
b	slope of exponential	μm^{-1}
c	amplitude of Gaussian	a.u.
d	standard deviation of Gaussian	μm^{-2}
e	offset in measured data (y_{min})	a.u.
f	arbitrary range in measured data (y_{mean})	a.u.
g	offset in x (x_0)	μm

$$\mathrm{LSF}(x) = k\left(\alpha \exp(-\mu\,|x - x_0|) + \beta \exp(-\sigma\,[x - x_0]^2)\right) \tag{B.2}$$

with parameters α, β, σ, μ and k, where α and β are the weighting factors for the exponential and the Gaussian functions respectively. The parameter σ denotes the standard deviation of the Gaussian and μ the slope of the exponential function. The value of k is determined to norm the area of the LSF to unity:

$$k = \frac{1}{2}\left\{\frac{\alpha}{\mu} + \frac{1}{2}\beta\sqrt{\frac{\pi}{\sigma}}\right\}. \tag{B.3}$$

The following parameter substitutions were used:

$$\alpha = ab; \qquad \beta = 2c\sqrt{\frac{d}{\pi}}; \qquad \mu = b; \qquad \sigma = d. \tag{B.4}$$

The MTF was calculated by using the fitting parameters of the ESF according to:

$$\mathrm{MTF}(f) = \frac{c\exp(\frac{-\pi^2 f^2}{d}) + a(1 + \frac{4\pi^2 f^2}{b^2})^{-1}}{c + a}. \tag{B.5}$$

Appendix C

Acronyms

AD	achromatic doublet
AO	adaptive optics
APD	avalanche photo diode
AR	anti-reflection
BMC	Boston Micromachine Coorp.
BS	beam splitter
BSM	beam steering mirror
CARS	coherent anti-Stokes Raman scattering
CMOS	complementary metal oxide semiconductor
CSLM	confocal scanning laser microscopy
DAQ	data acquisition
DMM	deformable membrane mirror
DPSSL	diode-pumped, solid-state laser
ESF	edge spread function
FM	flipping mirror
FOV	field of view
FFT	fast Fourier transform
FWHM	full width at half maximum
IR	infra red
LSF	line spread function
LUT	look-up table
MEMS	microelectromechanical systems
MF	merit factor
MPM	multiphoton microscopy
MTF	modulation transfer function
NA	numerical aperture
NLOM	nonlinear optical microscopy
OPO	optical parametric oscillator
OT	optical trapping/tweezers
OTF	ocular transfer function
PBS	polarising beam splitter
PH	pin hole
PMT	photomultiplier tube
PSF	point spread function
RIM	refractive index mismatch
ROI	region of interest
RSA	random search algorithm
SA	spherical aberration
SHG	second harmonic generation
SHIM	second harmonic imaging microscopy
SLM	spatial light modulator
SNR	signal to noise ratio
STD	standard deviation
TPEF	two photon excited fluorescence
USAF	United States air force
WD	working distance
WFS	wave front sensor

Appendix D

Symbols

a	radius
α	half aperture angle
β	drag coefficient
c	speed of light
χ	susceptibility
Δ	pixel pitch
D	entrance pupil
η	dynamic viscosity
f	focal length
f_r	repetition rate
F_D	viscous drag force
f_N	Nyquist frequency
f_R	Rayleigh frequency
γ	hyperpolarisability
h	Plank's constant
ι	mean free path length
λ	wavelength
k	spring constant
k_B	Boltzmann constant
μ	particle motility
n	refractive index
ϕ	wavefront
Q	trapping efficiency
σ	square root of variance
T	absolute temperature
u	axial optical unit
U_c	DMM control voltage
v	lateral optical unit
v_c	critical velocity
ξ	viscous damping factor
ζ	Faxén's law surface factor

Appendix E

Publications

Oral presentations

"Adaptive multiphoton and harmonic generation microscopy for whole tissue imaging"
M. Caroline Müllenbroich, Ewan J. McGhee, Kurt I. Anderson and Amanda J. Wright,
IONS-11, Paris, France, February 2012.

"Aberration Correction in an Optical Trapping System Using a Deformable Membrane Mirror"
M. Caroline Müllenbroich, Niall McAlinden, and Amanda J. Wright,
Frontiers in Optics, San Jose, USA, October 2011.

"Adaptive Optics in Optical Trapping"
M. Caroline Müllenbroich and Amanda J. Wright,
IONS-9, Salamanca, Spain, April 2011.

Poster presentations

IONS-NA3 conference, Stanford, Palo Alto, USA, October 2011

First Annual SU2P Symposium, University of Strathclyde, Glasgow, March 2010

Laser Applications of Adaptive Optics Meeting, Edinburgh, Scotland, August 2009

FOI (Functional optical imaging), Nottingham, UK, July 2009

9th intern. ELMI meeting on advanced microscopy, Glasgow, Scotland, June 2009

KTN workshop on Adaptive Optics, Institute of Physics, London, UK, November 2008

Appendix F

Acknowledgments

The Scottish Universities Physics Alliance (SUPA) has transformed the landscape of university based research in Scotland in just a few years and has had a immense impact on post graduates at all participating universities. I am profoundly grateful for the benefits like infrastructure, the grad school, networking opportunities and financial support that I have received from SUPA.

I therefore have to thank John Girkin for encouraging me to apply for the SUPA studentship which allowed me to join the Institute of Photonics for my PhD studies. I thank my supervisor Amanda Wright for entrusting me with responsibilities and always encouraging me to do my own independent research. I am grateful to Keith Mathieson for the generous support and sound advice towards the end of my PhD but most of all for always having a open door for me.

To Niall McAlinden, Simon Poland, David Hughes and Fiona Watts I say thank you for your good humour and the time you shared with me in the lab and group meetings.

To Lisa Flanagan, Sharon Kelly and Lynda McLaughlin, many thanks for easing all the administrative barriers. Paul Thompson, Paul Hynd, thank you for lending your ears and hands to rein fractious electronics and the prompt and careful manufacture of mechanical parts. Ewan Mulhern saved the day on countless occasions when 'switching it off and on again' was not the solution to my problem. Thanks!

I enjoyed working at the Beatson Institute for Cancer Research because of the friendly working atmosphere created there: Ewan McGhee, Kurt Anderson, David Strachan, Paul Timpson, Max and Juli, thanks for making me feel welcome and help out in every possible way.

Thank you for the friendship and taking your time to share mine: Benoit Guilhabert, David Massoubre, David Burns, Peter Schlosser, David Elfström, Jonathan McKendry, Daniele Parotta and especially Caroline Foucher, Franziska Luckert and Aline Dinkelaker. This thesis would not have been finished without the regular chats that put perspective and sound female sense back to everyday life in a physics lab.

To all the IONS friends made on the way, thank you for this great sense of community making each conference such a great pleasure to attend. People from ICFO, Galway, Salamanca, Southhampton... you know who you are. May our ways cross many times more.

For countless hours shared around our kitchen table drinking wine and playing cards, fudge you all my Westminster mates, especially Johannes, Pier, Yoann, Mat, Helen, Sarah, Hannah and Ellie.

With me from the very beginning, sharing all the experiences from the excitement of the first student hall parties until the frenzy breaks loose after submission, Bram, Richard, Mariana, Franzi and Loyd.

Teaching me all I needed to know about Scottish sarcasm, self deprecation and the fine art of ranting, thanks Loyd.

I thank my sisters, my little niece Paula, and my parents who have given me evermore support and help throughout my PhD. *Ce n'est pas tant l'aide de nos amis qui nous aide que notre confiance dans cette aide. Merci mille fois!*

❦

Glasgow, December 8, 2012
Caroline Müllenbroich